

MAGNETOHYDRODYNAMIC EFFECTS ON HEAT TRANSFER IN TOKAMAK FUSION
REACTOR BLANKETS

A THESIS

Presented to
The Faculty of the Division of Graduate Studies
by
Shahid Khan

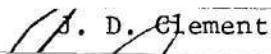
In Partial Fulfillment
of the Requirements for the Degree
Doctor of Philosophy
in the School of Nuclear Engineering

Georgia Institute of Technology
January, 1978

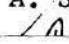
MAGNETOHYDRODYNAMIC EFFECTS ON HEAT TRANSFER IN TOKAMAK
FUSION REACTOR BLANKETS

Approved:


J. N. Davidson, Chairman


J. D. Clement


R. W. Carlson


A. Schneider

P. V. Desai

Date approved by Chairman

January 24, 1977

DEDICATION

To Eleanor

ACKNOWLEDGEMENTS

The author wishes to express his gratitude to his thesis advisor, Dr. J. N. Davidson, who besides being an intellectual whiz, is also a very human person. Thanks are also due to the reading committee, particularly Dr. R. Carlson for advice on graphics, and Dr. P. Desai for furthering his understanding of fluid mechanics. A number of fellow students have also contributed to this work in various ways. The help of Yehia Rizk, N. L. Sankar, Pak-tai Wan, Dhunjishaw Lal, Robert Kim, Adel Alapour and Amir Mikhial is acknowledged and appreciated. Mrs. J. Griffith is to be applauded for her efforts in translating the authors unreadable handwriting into type, and finally Prak, Aim-on, Fred, Pat and Aunt Francis are to be thanked for their moral support.

TABLE OF CONTENTS

| | Page |
|---|------|
| DEDICATION | ii |
| ACKNOWLEDGMENTS. | iii |
| LIST OF ILLUSTRATIONS. | vi |
| NOMENCLATURE | xx |
| SUMMARY. | xxii |
| Chapter | |
| I. INTRODUCTION. | 1 |
| Objective | |
| Background | |
| Research Overview | |
| II. MATHEMATICAL FORMULATION. | 14 |
| Geometrical Arrangement | |
| Basic Equations | |
| Dimensionless Equations and Boundary Conditions | |
| III. NUMERICAL FORMULATION | 33 |
| The Finite Difference Equations | |
| Solution of the Finite Difference Equations | |
| Boundary Conditions | |
| Order of Computation | |

TABLE OF CONTENTS (Continued)

| Chapter | Page |
|---|------|
| IV. PROGRAM CALIBRATION | 64 |
| The Purely Hydrodynamic Velocity Entry Problem | |
| The Purely Hydrodynamic Thermal Entry Problem | |
| Moving Wall Cases | |
| V. RESULTS AND DISCUSSION. | 117 |
| Case with $C = 0$ on all Walls | |
| Case with $C = \text{infinity}$ on all Walls | |
| Case with $C = 10$ on all Walls | |
| Case with $C = 1$ on all Walls | |
| Comparison of Finite and Limiting Conductivity Cases | |
| Some Mixed Wall Conductivity Cases | |
| Stability and Computer Time Requirements | |
| VI. CONCLUSIONS AND SUGGESTIONS FOR FUTURE WORK | 223 |
| APPENDIX A | 226 |
| BIBLIOGRAPHY | 232 |
| VITA | 236 |

LIST OF ILLUSTRATIONS

| Figure | | Page |
|--------|---|------|
| 1. | Conceptual Design of Argonne Tokamak Experimental Power Reactor | 3 |
| 2. | Ducted Coolant Blanket Module | 5 |
| 3. | Geometrical Arrangement of the Duct | 15 |
| 4. | Duct Cross-section. | 20 |
| 5. | Staggered Grid Structure in yz Plane. | 35 |
| 6. | Isometric View of General Control Volume. | 36 |
| 7. | yz Face of Control Volume for Equations Centered at the Main Nodes | 37 |
| 8. | yz Face of Control Volume for v Equation. | 39 |
| 9. | yz Face of Control Volume for w Equation. | 40 |
| 10. | Comparison of Center-point Axial Velocity Development with Experimental Results of Goldstein and Kreid | 74 |
| 11. | Comparison of Axial Pressure Coefficient Development with Experimental Results of Beavers, Sparrow and Magnuson | 74 |
| 12. | Axial Pressure Gradient Development | 75 |

LIST OF ILLUSTRATIONS (Continued)

| Figure | | Page |
|--------|--|------|
| 13. | Axial Velocity Contours, Surface and Development ($Re = 100$) | 76 |
| 14. | Axial Velocity and Secondary Flow Vectors ($Re = 100$) | 77 |
| 15. | w and v Velocity Profiles and Surface ($Re = 100$) . . . | 78 |
| 16. | Bulk Temperature and Nusselt Number for Constant Wall Temperature Case | 79 |
| 17. | Temperature Contours and Surface for Constant Wall Temperature Case ($L = 0.1$, $Pe = 100, 500$) | 80 |
| 18. | Temperature Contours and Surface for Constant Wall Temperature Case ($L = 0.1$, $Pe = 1000, 10000$) . . . | 81 |
| 19. | Center-line Temperature Development for Constant Wall Temperature Case ($Pe = 10, 100, 500, 1000$) . . . | 82 |
| 20. | Nusselt Number Development Surfaces along a Wall for Constant Wall Temperature Case ($Pe = 10, 100$) . . . | 83 |
| 21. | Nusselt Number Development Surfaces along a Wall for Constant Wall Temperature Case ($Pe = 500, 1000$) . . | 84 |
| 22. | Bulk Temperatures for Constant Wall Heat Flux. | 85 |
| 23. | Nusselt Number and Center-line Wall Temperature for Constant Wall Heat Flux. | 86 |

LIST OF ILLUSTRATIONS (Continued)

Figure

| | | |
|-----|--|----|
| 24. | Temperature Contours at $L = 0.1$ ($Pe = 100, 500, 1000, 10000$) | 87 |
| 25. | Center-plane Temperature Development with Constant Wall Heat Flux ($Pe = 10, 100$) | 88 |
| 26. | Center-plane Temperature Development with Constant Wall Heat Flux ($Pe = 1000, 10000$) | 89 |
| 27. | Wall Temperature Development with Constant Wall Heat Flux ($Pe = 10, 100$) | 90 |
| 28. | Wall Temperature Development with Constant Wall Heat Flux ($Pe = 500, 1000, 10000$) | 91 |
| 29. | Wall and Center-line Temperature Development at Various Values of L for Constant Wall Heat Flux Case ($Pe = 10$) | 92 |
| 30. | Wall and Center-line Temperature Development at Various Values of L for Constant Wall Heat Flux Case ($Pe = 100$) | 93 |
| 31. | Wall and Center-line Temperature Development at Various Values of L for Constant Wall Heat Flux Case ($Pe = 500$) | 94 |
| 32. | Wall and Center-line Temperature Development at Various Values of L for Constant Wall Heat Flux Case ($Pe = 1000$) | 95 |

LIST OF ILLUSTRATIONS (Continued)

| Figure | | Page |
|--------|---|------|
| 33. | Nusselt Number Development along a Wall for Constant Wall Heat Flux Case ($Pe = 10, 100$) | 96 |
| 34. | Nusselt Number Development along a Wall for Constant Wall Heat Flux Case ($Pe = 500, 1000$) | 97 |
| 35. | Mean Nusselt Number and Bulk Temperature Development for Values of Pe ($Q = 100$) | 98 |
| 36. | Temperature Contours and Surface for $Q = 100$ and $L = 0.1$ ($Pe = 100, 300$) | 99 |
| 37. | Temperature Contours and Surface for $Q = 100$ and $L = 0.1$ ($Pe = 500, 1000$) | 100 |
| 38. | Local Nusselt Number across a Wall at Values of L for $Q = 100$ ($Pe = 100, 1000$) | 101 |
| 39. | Wall Center and Wall Corner Temperature Development for Values of Internal Heat Source Q ($Pe = 100$) | 102 |
| 40. | Secondary Flow Vectors at $L = 0.1$ (Cases (a), (b), (c) and (d)) | 103 |
| 41. | w Velocity Profiles at $L = 0.1$ (Cases (a), (b), (c) and (d)) | 104 |
| 42. | v Velocity Profiles at $L = 0.1$ (Cases (a), (b), (c) and (d)) | 105 |

LIST OF ILLUSTRATIONS (Continued)

| Figure | Page |
|---|------|
| 43. Axial Velocity Contours and Surface at $L = 0.1$ (Cases (a) and (b)) | 106 |
| 44. Axial Velocity Contours and Surface at $L = 0.1$ (Cases (c) and (d)) | 107 |
| 45. Axial Velocity Development at Center-plane (Cases (a), (b), (c) and (d)) | 108 |
| 46. Axial Velocity at Various Values of L (Cases (a) and (b)) | 109 |
| 47. Axial Velocity at Values of L (Cases (c) and (d)) | 110 |
| 48. Temperature Contours and Surface at $L = 0.1$ (Cases (a) and (b)) | 111 |
| 49. Temperature Contours and Surface at $L = 0.1$ (Cases (c) and (d)) | 112 |
| 50. Temperature and Wall Nusselt Number at Values of L and Center-plane Temperature Development for all Walls Stationary. | 113 |
| 51. Center-plane Temperature Development (Cases (a), (b), (c), and (d)) | 114 |
| 52. Center-line Temperature at Various Values of L (Cases (a) and (b)) | 115 |

LIST OF ILLUSTRATIONS (Continued)

| Figure | Page |
|---|------|
| 53. Center-line Temperature at Various Values of L (Cases (c) and (d)) | 116 |
| 54. Current Density Vectors for $C = 0$ ($L = 0.001, 0.005, 0.010, 0.100$) | 139 |
| 55. Axial Induced Field Contours for $C = 0$ ($L = 0.001, 0.005, 0.010, 0.100$) | 140 |
| 56. Current Density Vectors in Axial Plane (xz at Center, xy near Wall) | 141 |
| 57. Axial Induced Field at Values of L and Axial Field Surface at $L = 0.1$ | 142 |
| 58. H_y Field at Values of L and H_y Field Surface at $L = 0.001$ | 143 |
| 59. H_z Field at Values of L and H_z Field Surface at $L = 0.001$ | 144 |
| 60. Axial Velocity at Values of L and Axial Velocity Contours and Surface at $L = 0.1$ | 145 |
| 61. v and w Velocity Profiles at $L = 0.005$ | 146 |
| 62. Nusselt Numbers at Values of L and Temperature Contours at $L = 0.1$ for Constant Wall Heat Flux . . . | 147 |
| 63. Center-line and Wall Temperatures at Values of L for Constant Wall Heat Flux | 148 |

LIST OF ILLUSTRATIONS (Continued)

| Figure | | Page |
|--------|---|------|
| 64. | Center-point Axial Velocity and Mean Nusselt Number Development ($C = 0$) | 149 |
| 65. | Axial Pressure Gradient and Axial Pressure Coefficient Development ($C = 0$) | 150 |
| 66. | Wall Center Temperature and Wall Corner Temperature Development ($C = 0$) | 151 |
| 67. | Current Density Vectors for $C = \text{infinity}$ ($L = 0.001, 0.005, 0.010, 0.100$) | 152 |
| 68. | Axial Field Contours for $C = \text{infinity}$ ($L = 0.001, 0.005, 0.010, 0.100$) | 153 |
| 69. | Current Density Vectors in Axial Plane for $C = \text{infinity}$ (xy near Wall, xz at Center, xz near Wall) | 154 |
| 70. | Axial Field at Values of L and Axial Field Surface at $L = 0.1$ ($C = \text{infinity}$) | 155 |
| 71. | H_y Field at Values of L and H_y Field Surface at $L = 0.001$ ($C = \text{infinity}$) | 156 |
| 72. | H_z Field at Values of L and H_z Field Surface at $L = 0.001$ ($C = \text{infinity}$) | 157 |
| 73. | Axial Velocity for Values of L and Velocity Contours and Surface at $L = 0.1$ ($C = \text{infinity}$) | 158 |

LIST OF ILLUSTRATIONS (Continued)

| Figure | | Page |
|--------|--|------|
| 74. | Nusselt Number at Values of L , Nusselt Number Surface along a Wall and Temperature Contours for $L = 0.1$ ($C = \text{infinity}$) | 159 |
| 75. | Wall and Center-line Temperatures for Values of L ($C = \text{infinity}$) | 160 |
| 76. | Center-point Axial Velocity and Mean Nusselt Number Development ($C = \text{infinity}$) | 161 |
| 77. | Axial Pressure Gradient and Pressure Coefficient Development ($C = \text{infinity}$) | 162 |
| 78. | Wall Center Temperature and Wall Corner Temperature Development ($C = \text{infinity}$) | 163 |
| 79. | Current Density Vectors for $C = 10.0$ ($L = 0.001$, 0.005 , 0.010 , 0.100) | 164 |
| 80. | Axial Field Contours for $C = 10.0$ ($L = 0.001$, 0.005 , 0.010 , 0.100) | 165 |
| 81. | Current Density Vectors in Axial Plane for $C = 10.0$ (xz near Wall, xz at Center, xy near Wall) | 166 |
| 82. | Center-point Axial Velocity and Mean Nusselt Number Development ($C = 10.0$) | 166 |
| 83. | Axial Pressure Gradient and Pressure Coefficient Development ($C = 10.0$) | 168 |

LIST OF ILLUSTRATIONS (Continued)

| Figure | Page |
|--|------|
| 84. Wall Center and Wall Corner Temperature Development (C = 10.0) | 169 |
| 85. Current Density Vectors for C = 1.0 (L = 0.001, 0.005, 0.010, 0.100). | 170 |
| 86. Axial Field Contours for C = 1.0 (L = 0.001, 0.005, 0.010, 0.100). | 171 |
| 87. Current Density Vectors in Axial Plane for C = 1.0 (xz near Wall, xz at Center, xy near Wall) | 172 |
| 88. Center-point Axial Velocity and Mean Nusselt Number Development (C = 1.0). | 173 |
| 89. Pressure Coefficient and Axial Pressure Gradient Development (C = 1.0). | 174 |
| 90. Wall Center and Wall Corner Temperature Development (C = 1.0). | 175 |
| 91. Axial Field at Values of L and Axial Field Surface at L = 0.1 (C = 1.0). | 176 |
| 92. Hy Field at Values of L (C = 1.0). | 177 |
| 93. Hz Field at Values of L and Hz Field Surface at L = 0.1 (C = 1.0). | 178 |

LIST OF ILLUSTRATIONS (Continued)

| Figure | | Page |
|--------|--|------|
| 94. | Comparison of Fully Developed Relative Axial Pressure Gradient with Work of Chang and Lundgrin and Work of Chu | 179 |
| 95. | Fully Developed Relative Pressure Coefficient | 179 |
| 96. | Relative Velocity Entry Length and Fully Developed Nusselt Number at $L = 0.1$ | 180 |
| 97. | Current Density Vectors for Case A ($L = 0.001, 0.005, 0.010, 0.100$) | 181 |
| 98. | Axial Field Contours for Case A ($L = 0.001, 0.005, 0.010, 0.100$) | 182 |
| 99. | Current Density Vectors in Axial Plane for Case A (xz near Wall, xz at Center, xy near Wall). | 183 |
| 100. | Current Density Vectors for Case B ($L = 0.001, 0.005, 0.010, 0.100$) | 184 |
| 101. | Axial Field Contours for Case B ($L = 0.001, 0.005, 0.010, 0.100$) | 185 |
| 102. | Current Density Vectors in Axial Plane for Case B (xz near Wall, xz at Center, xy near Wall). | 186 |
| 103. | Axial Field and Hz Field Surfaces for Case A and Case B ($L = 0.1, 0.001$) | 187 |

LIST OF ILLUSTRATIONS (Continued)

| Figure | Page |
|---|------|
| 104. Axial Field at Values of L for Case A and Case B . . . | 188 |
| 105. Axial Field at Values of L for Case A and Case B . . . | 189 |
| 106. Hy Field at Values of L for Case A and Case B. | 190 |
| 107. Hy Field at Values of L for Case A and Case B. | 191 |
| 108. Hz Field at Values of L for Case A and Case B. | 192 |
| 109. Hz Field at Values of L for Case A and Case B. | 193 |
| 110. Axial Velocity Contours and Surface for Case A and Case B (L = 0.1) | 194 |
| 111. Axial Velocity at Values of L for Case A and Case B (L = 0.1). | 195 |
| 112. v and w Velocity Profiles and Secondary Flow Vectors for Case A (L = 0.005) | 196 |
| 113. Temperature Contours for Case A and Case B(L = 0.1) . | 197 |
| 114. Current Density Vectors for Case C (L = 0.001, 0.005, 0.010, 0.100). | 199 |
| 115. Axial Field Contours for Case C (L = 0.001, 0.005, 0.010, 0.100). | 199 |
| 116. Current Density Vectors for Case D (L = 0.001, 0.005, 0.010, 0.100). | 200 |

LIST OF ILLUSTRATIONS (Continued)

| Figure | Page |
|--|------|
| 117. Axial Field Contours for Case D ($L = 0.001, 0.005, 0.010, 0.100$) | 201 |
| 118. Current Density Vectors in Axial Plane for Case D (xz near Wall, xz at Center, xy near Wall). | 202 |
| 119. Axial Field Surfaces for Case C and Case D ($L = 0.1$) and H_z and H_y Field Surfaces for Case D ($L = 0.001$) . . | 203 |
| 120. Axial Velocity Contours and Surface for Case C and Case D ($L = 0.1$). | 204 |
| 121. Center-line Axial Velocity at Values of L for Case C. . | 205 |
| 122. Wall Temperature at Values of L for Case C with Constant Wall Heat Flux. | 206 |
| 123. Temperature Contours for Case C with Constant Wall Heat Flux ($L = 0.1$) | 206 |
| 124. Case Comparison of Center-point Axial Velocity and Axial Pressure Gradient Developments. | 207 |
| 125. Case Comparison of Pressure Coefficient and Nusselt Number Development. | 208 |
| 126. Case Comparison of Wall Center Temperature and Wall Corner Temperature Development. | 209 |
| 127. Current Density Vectors for Case E ($L = 0.001, 0.005, 0.010, 0.100$) | 210 |

LIST OF ILLUSTRATIONS (Continued)

| Figure | Page |
|--|------|
| 128. Current Density Vectors in the Axial Plane for Case E (xz near Wall, xz at Center, xy near Wall) | 211 |
| 129. Axial Velocity at Values of L and Axial Velocity Contours at L = 0.1 for Case E | 212 |
| 130. Axial Field at Values of L and Axial Field Surface at L = 0.1 for Case E | 213 |
| 131. Hy Field at Values of L and Hy Field Surface at L = 0.1 for Case E | 214 |
| 132. Center-line Temperatures at Values of L for Case E (Linearly Varying Heat Generation, No Heat Generation) . | 215 |
| 133. Temperatures at Values of L and Temperature Contours at L = 0.1 for Case E (Linearly Varying Heat Generation, No Heat Generation). | 216 |
| 134. Conducting Wall Center Temperatures at Values of L for Case E (Linearly Varying Internal Heat Generation, No Internal Heat Generation). | 217 |
| 135. Bulk Temperature and Conducting Wall Center Temperature Development for Case E | 218 |
| 136. Current Density Vectors for Case F (L = 0.001, 0.005, 0.010, 0.100). | 219 |
| 137. Axial Field Contours for Case F (L = 0.001, 0.005, 0.010, 0.100) | 220 |

LIST OF ILLUSTRATIONS (Concluded)

| Figure | Page |
|--|------|
| 138. Current Density Vectors for Case G ($L = 0.001, 0.005,$ 0.010, 0.100) | 221 |
| 139. Axial Field Contours for Case G ($L = 0.001, 0.005,$ 0.010, 0.100) | 222 |

NOMENCLATURE

Vector Quantities \vec{B} Magnetic Flux Density \vec{H} Magnetic Field \vec{E} Electric Field \vec{J} Current Density \vec{V} Fluid Velocity

(These quantities may have components e.g. H_x, H_y, H_z and u, v, w in the x, y , or z directions respectively.)

Scalar Quantities B_{py} Imposed Magnetic Field in y (Poloidal) Direction B_{tx} Imposed Magnetic Field in x (toroidal) Direction D Duct Width h Heat Transfer Coefficient k Thermal Conductivity of Fluid p Pressure in Fluid q_w'' Wall Heat Flux Q Volumetric Heat Source R Axial Length of Duct μ Viscosity of Fluid μ_e Magnetic Permeability of Fluid σ Electrical Conductivity of Fluid σ_w Electrical Conductivity of Wall ρ Density of fluid γ Ratio of Imposed Fields (Toroidal/Poloidal) t Duct Wall Thickness T Temperature of FluidDimensionless Quantities C Conductance Ratio

| | |
|-----|------------------------------|
| Hap | Poloidal Hartmann Number |
| Hat | Toroidal Hartmann Number |
| Ec | Eckert Number |
| L | Dimensionless Axial Distance |
| Nu | Nusselt Number |
| Pe | Peclet Number |
| Pr | Prandtl Number |
| Re | Reynolds Number |
| Rem | Magnetic Reynolds Number |

Coefficients and Dummy Variables Associated with the Numerical Analysis

$A_i, B^j, C^k, D^j, F_l, L_m^n, S_l, T_m^n$, are coefficients where:

$i = N, S, E, W, P$

$j = \text{any dependent variable}$

$k = u, v, w$

$l = U, D \text{ (upstream or downstream)}$

$n = x, y, z$

$m = n, s, e, w$

$\psi_{i,l}$ any Dependent Variable

Γ any Transport Property

$\alpha, \beta, \epsilon, \phi, \gamma, \Omega$, are dummy variables associated with the TDMA.

SUMMARY

Magnetohydrodynamic flow in the entrance region of a square channel is considered. This flow situation is shown to be of a type found in Tokamak fusion reactor blankets with circulating lithium coolant. The presence of secondary flow in the developing region forces three dimensional modeling of the problem. The three momentum, three induction, pressure and energy equations that describe the system are cast in parabolic form and integrated numerically by the use of a marching procedure in the stream-wise direction. Mesh size limitations restrict the solutions to low Hartmann numbers.

The results show that the MHD pressure drop is strongly dependent on the electrical conductivity of the duct walls perpendicular to the imposed transverse magnetic field and relatively insensitive to the conductivity of the parallel walls. Velocity and temperature profiles are flattened and heat transfer coefficients increased with the largest increase occurring when the duct corners are electrically insulated. Hydrodynamic entry lengths are shown to decrease significantly with Hartmann number increase, and minutely with wall electrical conductivity increase.

The main conclusions are that, by judicious use of current breaks, insulated corners and walls, the MHD pumping losses should be reduceable to a tolerable level, and at the same time the benefits of blanket simplification and heat transfer enhancement can be enjoyed.

CHAPTER I

INTRODUCTION

Objective

Controlled thermonuclear fusion offers an essentially limitless energy source. Much complexity, unfortunately, is involved in harnessing this tremendous potential. Fusion reactions are well understood and have been amply demonstrated by many types of destructive nuclear weapons. While fusion energy has been profusely used by the military, unlike fission it still awaits commercial use. Design of a power producing fusion reactor is made very difficult by the need to provide containment for a super-hot plasma.

Of the various means for providing containment for the fusion plasma, the magnetic confinement concept is currently in the most advanced stages of study. A number of designs utilizing magnetic confinement have been proposed, and out of these the Tokamak type machine appears to be the most promising. In this design the plasma is confined in a toroidal geometry by a strong magnetic field. The only possible means of plasma leakage is by slow diffusion across the toroidal magnetic field lines. Since the ignition temperature for deuterium-tritium fusion is lower, the first generation of such reactors will probably operate on this fuel mixture.

Deuterium is easily extracted from sea water, of which there is no shortage, while tritium, not being naturally occurring isotope, has to be produced. The only really feasible means of tritium production is to breed it in a lithium bearing blanket in which $\text{Li}^6(n, T)$ and $\text{Li}^7(n, n'T)$ reactions will take place. The majority of the fusion reaction

energy appears in the 14 MeV neutrons, and thus the blanket has to serve the purposes of neutron moderation and heat removal as well. This blanket is placed between the plasma and the main magnetic windings and heat removed by a circulating coolant can be used for generating electricity by means of a conventional heat engine. Figure 1 shows a typical conceptual design of such a system.

This problem of heat removal from the controlled thermonuclear reactor is likely to be one of the key factors affecting the plant economics. Many important parameters such as capital costs, power plant efficiency, fuel breeding, induced activity, material and structural criteria and the reactor lifetime are affected by the choice of the coolant and the geometry of the blanket. Since the reactor size and capital costs are directly related, maximizing the first wall power loading is desirable. Even though it is clear that other factors such as radiation damage, and plasma stability may strongly affect this allowable wall loading, the ability to cool the wall appears to be one of the major factors involved in establishing its limit.¹

The most obvious and simple solution to the problem is to use lithium not only as the breeding material, but also as the heat transfer medium. Liquid lithium being metallic, has a high boiling point and excellent heat transfer characteristics. Conceptually, the blanket could be a very simple structure with the lithium in it serving all the functions of neutron moderation, tritium breeding and heat removal. However, the blanket, being inside the toroidal field coils, is subject to the intense toroidal magnetic field, generated by the coils for the purpose of plasma confinement, and also the relatively weaker, but still

OHMIC HEATING AND
EQUILIBRIUM FIELD COILS

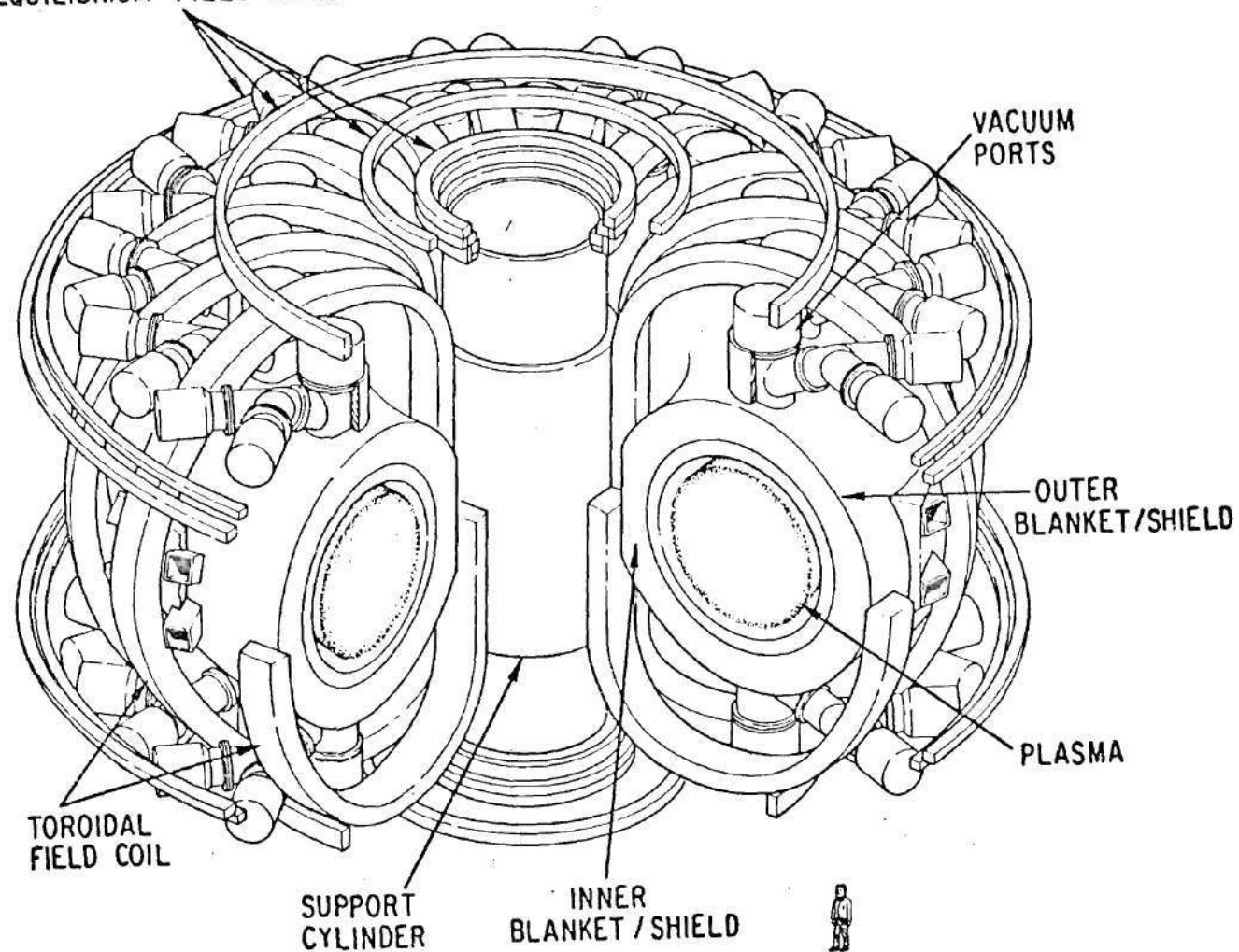


Figure 1. Conceptual Design of Argonne Tokamak Experimental Power Reactor

strong, poloidal field generated by the plasma current. Any circulating fluid in the blanket would then have to be pumped along and across magnetic field lines. If the fluid is electrically conducting, as lithium is, these magnetic fields affect the flow by the principles of magnetohydrodynamics and alter the velocity profiles in the channels. The ultimate effect being to increase the pressure drop and alter the heat removal properties of the flow.

Fears that this pressure drop may be excessive, have prompted recent reevaluations of lithium circulating blankets. The magnetohydrodynamic pressure drop is a maximum when the applied field is transverse to the flow direction and zero when the field and flow are exactly parallel. Therefore, to reduce the MHD head loss it is obvious that the flow direction should be kept aligned with the toroidal field as much as possible. This constraint results in designs such as that shown in Figure 2. The blanket is segmented into a number of modules and each has an independent coolant circuit. The main flow is only perpendicular to the toroidal field when the coolant enters within the region of the coils. Then the flow direction immediately becomes toroidal and there is no longer a retarding body force due to the toroidal field. However, the weaker poloidal field is now normal to the flow and it exerts a retarding force.

This particular situation leads to two interesting magnetohydrodynamic (MHD) flow problems, neither of which had been solved. First of all there is the problem of flow around a right angled bend in the presence of one or two imposed field components. Solutions to this problem have not been attempted. However, if it is assumed that

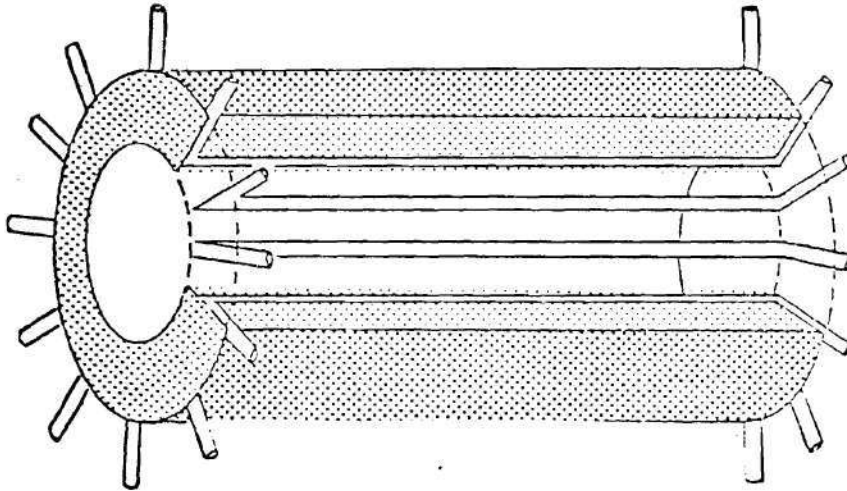


Figure 2. Ducted Coolant Blanket Module

in crossing the intense toroidal field, before the corner is turned, the flow becomes essentially slug, which is consistent with the very high toroidal Hartmann number, the second problem presents itself. When this slug flow becomes parallel to the toroidal field, there is a tendency for it to relax towards the fully developed profile that corresponds to the now transverse poloidal magnetic field. However, the toroidal field retards this development, and the result is a flow that probably never reaches a fully developed state before it has to exit from the blanket. This problem, which is the object of interest in this research, can be thought of as a MHD entry problem.

Flow in a duct develops by virtue of deceleration of the slug profile near the walls under the action of viscosity. This causes net transfer of fluid towards the center of the duct, and transverse secondary flow is generated to accomplish this task. As the transverse magnetic field has differing effects on secondary velocities parallel and perpendicular to it, this entry problem is always three dimensional, even in a circular tube. To be more in keeping with conceptual blanket designs, the duct considered was a square one. Since the problem involves simultaneously developing velocities, temperatures and induced magnetic fields, and is non-linear, the method of solution must be numerical.

Background

The literature was examined for methods relevant to the solution of the three-dimensional MHD entry problem in a square duct.

Purely Hydrodynamic Duct Flow

The momentum equation for fully developed laminar flow in a rectangular duct is linear, and an exact analytical Fourier series solution is available.² Corresponding exact³ and approximate⁴ temperature solutions are also available for both the cases of constant wall temperature around the periphery, and constant imposed peripheral heat flux. While the hydrodynamic entry problem in a circular tube can be treated as two-dimensional, the corresponding problem for a rectangular duct cannot. Because it is three-dimensional and non-linear in nature, it was not until 1972, that a satisfactory solution to this entry problem for a rectangular duct was obtained.

Generally, the entrance flow in straight ducts of constant cross-section experiences no streamwise separation, although cross flow recirculation may prevail. For these cases the Navier-Stokes equations can be parabolized with respect to the streamwise direction, and integrated numerically by a marching technique in the streamwise direction. Patankar and Spalding⁵ first introduced this assumption and successfully employed it to solve the entry problem in square ducts with all stationary walls as well as with one laterally moving wall. Their results showed excellent agreement with the painstaking experimental analyses of Goldstein et al.,⁶ and Beavers et al.⁷ Soon afterwards, Caretto et al.⁸ and Curr et al.⁹ developed alternate numerical solution techniques for the parabolized equations in terms of primitive variables, or in terms of vorticity and velocity. All of these formulations yielded accurate solutions for the stationary boundary and one moving wall cases.

Briley¹⁰ modified the original technique of Patankar and Spalding by including some of the off diagonal elements in the coefficient matrices for the velocity and pressure corrections. However, this improvement did not seem to have appreciable effects. Ghia et al.¹¹ applied Briley's method to polar ducts, again with good results. The original method of Patankar and Spalding has been extended to include the magnetic induction equations and used to solve the postulated problem in the research.

Magnetohydrodynamic Duct Flow

The classical work in the area, of course, was that of Hartmann¹² who first solved for the effect of a transverse magnetic field on an electrically conducting fluid flowing between parallel plates. He obtained the well known Hartmann profile after having assumed steady, uniformly conducting, incompressible laminar flow with no variations in the flow direction. Shercliff¹³ solved the same problem for rectangular ducts with non conducting walls. The case for rectangular ducts with perfectly conducting walls was solved by Chang and Lundgren,¹⁴ and Gold¹⁵ obtained the solution for circular pipes with non conducting walls. Shercliff¹⁶ postulated a boundary condition applicable to thin finitely conducting walls. Using this result and rather involved mathematics, Ihara et al.¹⁷ and Chu¹⁸ solved the arbitrary conductivity problem for circular and rectangular ducts respectively. Hunt,^{19,20} after making the high Hartmann number approximation, used boundary layer analyses to solve for the mixed wall rectangular duct cases. This involved various combinations of non conducting, perfectly conducting, and finitely conducting walls.

The principal result stemming from all the above work is that for a transverse field and laminar flow, the effect of the field is to induce currents resulting from the $\vec{V} \times \vec{B}$ induced emf. These currents flow in one direction in the core of the flow and return either through the walls (normal to the field) if the walls are conducting or along the slower moving boundary layers on these walls. The currents, in turn, give rise to a $\vec{J} \times \vec{B}$ Lorentz force, which acts parallel to the fluid motion, retarding the core and accelerating the boundary layers if the walls are non conducting or merely retarding the flow if the walls provide return paths for the currents. The result is a thinning of the boundary layers on walls normal to the field, a flattening of the velocity profile in the core, and, for conducting walls, a large net force opposing fluid motion. In the case of insulating walls, the currents lie entirely within the fluid and there is no net Lorentz force, but the velocity profile is flattened and viscous resistance is increased owing to steeper gradients near the walls. The boundary layers on walls parallel to the field are not affected to the same degree.

The major conclusion is that if the ducts cannot be made insulating the magnetic pressure drop is proportional to the square of the Hartmann number. Since the electrical conductivity of most refractory metals is somewhat similar to liquid metals, these pressure drops could be minimized by insulating the inner and/or outer surfaces of coolant channels by perhaps a ceramic coating covered, in turn with a material compatible with lithium.

All of the MHD papers referenced above have been analytical and their solutions are generally in awkward series form. Hoffman and

Carlson²¹ have approximated these results by the following expression for the fully developed pressure gradient in circular and rectangular ducts,

$$\frac{-D^2}{\mu U_o} \frac{dP}{dx} = K \left(\frac{Ha^2 \tanh Ha}{Ha - \tanh Ha} - 3 + \frac{D^2}{\mu U_o} \frac{dP}{dx} \right)_{B=0} + \frac{Ha^2 C}{1+C}$$

where all the symbols are as defined in the nomenclature and K is a dimensionless parameter that equals 1.0 for rectangular and 1.3 for circular ducts. This expression simplifies further for the limiting cases of C equal zero and C equal infinity, and it has seen wide use in the calculation of pressure drops in fusion blanket systems.

Strangely enough there has not been much application of numerical analysis to the solution of MHD problems. For fully developed rectangular duct flow, Chu²² has reconfirmed his earlier Fourier series solution by use of a finite difference net and a relaxation procedure. Wu²³ has shown the applicability of the finite element method to one dimensional, unsteady, rectangular duct flow of low magnetic Reynolds number. The low magnetic Reynolds number assumption allowed him to neglect the induced field calculation.

Shercliff,¹⁶ using various approximations, tried to manipulate the MHD entry problem in two dimensions for a circular pipe. However, he was unable to arrive at the developing velocity profiles explicitly. Shohet et al.^{24,25} numerically solved the MHD entry problem for a parallel plate channel and a cylindrical annulus. Besides their analyses being two dimensional, they also assumed a low magnetic Reynolds number

and thus avoided the induced field calculation. Thus, besides its possible application to the Tokamak blanket situation, the three-dimensional MHD entry problem, including induced field computation, stood out as one that had not even been attempted. It was the primary purpose of this research to solve this outstanding problem.

For an aligned field there is no interaction with the velocity and the pressure drop is purely hydrodynamic and thus much less than a hydromagnetic pressure drop. It is this fact that forces blanket designers to orient the main flow in the toroidal direction so that it only crosses the relatively weak poloidal field. Another effect of the aligned magnetic field is to delay the full flow development. This development requires lateral motion in the duct and such fluid motion is impeded by the field.²⁶

Magnetohydrodynamic Effects on Duct Heat Transfer

In the absence of a magnetic field the heat transfer to single phase liquid metals is relatively well established.^{27,28} To the extent that it steepens the velocity profile at the wall, a transverse magnetic field may be expected to increase the heat transfer in laminar flow. The problem in its various forms has been the subject of a number of analytical treatments involving flat ducts, circular pipes, constant wall heat flux, constant wall temperatures, insulating and conducting walls. The most recent papers appear to be those of Gardner²⁹ on the circular pipe problem and of Michiyoshi and Matsumoto³⁰ and Back³¹ on the flat duct problem. Most of the work is reviewed and referenced in a paper by Regier.³² For Hartmann numbers below about 5, the effect of the magnetic field is not very significant. Above Hartmann numbers

of 100, the Nusselt numbers approach asymptotic values.

Research Overview

The three-dimensional MHD entry problem required the simultaneous solution of three momentum, three induction, one pressure correction and one energy equation. By exploiting certain similarities between this family of equations, it was possible to cast them into a parabolic form amenable to the application of streamwise marching integration. Since the finite difference mesh used was uniformly spaced throughout the transverse plane, the solutions were limited to low Hartmann number. This is a direct consequence of the steepening of gradients near the walls, and the resulting need of finer grid in these regions to obtain proper resolution as the Hartmann number is increased.

Due to the low Hartmann number of the solutions, no claim is made as to having explicitly solved the Tokamak blanket problem. However, besides setting up a sound computational framework for many possible future problems, these solutions provide much insight into the effects of wall conductivity on developing and fully developed MHD duct flows. Various means of combating high MHD pumping requirements, such as insulating corners, inserting wall current breaks, having some walls conducting and some non conducting, have also been studied in this work. The effect of the magnetic field strength on heat transfer has also been observed, and some conclusions and recommendations directly applicable to Tokamak blankets, have been made in the last chapter.

Mathematical formulation and derivation of the basic equations is presented in Chapter II, while the numerical methods used to obtain

their solution are detailed in Chapter III. Extensive testing of the computer program and its calibration against known solutions and experimental results was carried out, and some of these results are shown in Chapter IV. Chapter V presents the current results obtained for the three-dimensional MHD entry problem, and Chapter VI concludes this work and contains some suggestions and recommendations.

CHAPTER II

MATHEMATICAL FORMULATION

Geometrical Arrangement

The problem of interest is to be solved in a square duct. The orientation of the axes with respect to the duct is shown in Figure 3. The main flow is along the x direction which is also the toroidal direction. The poloidal direction is then labeled y . Velocity components along the x , y and z axes are u , v and w , respectively. Induced magnetic field components are H_x , H_y and H_z , respectively. The length of the duct, R , is assumed to be much greater than the width of a side, D . This duct could be part of the first wall, in which case one side would be exposed to the plasma. This would result in a heat flux being imposed on that wall, and an internal heat generation term that would vary across the duct cross-section.

Basic Equations

The equations that define the problem are the continuity equation, the Navier-Stokes equations, the energy equation, and Maxwell's equations. Steady, newtonian, laminar, incompressible and constant property flow is assumed. For strong magnetic fields, laminar flow has been shown to persist even at Reynolds numbers much higher than those found in fusion blanket channels,³³ due to the turbulence damping effects of such fields. Coolant temperature rises of about 200°C are expected in fusion blankets, and this temperature difference results in lithium properties such as the density, specific heat, thermal conductivity changing by a few

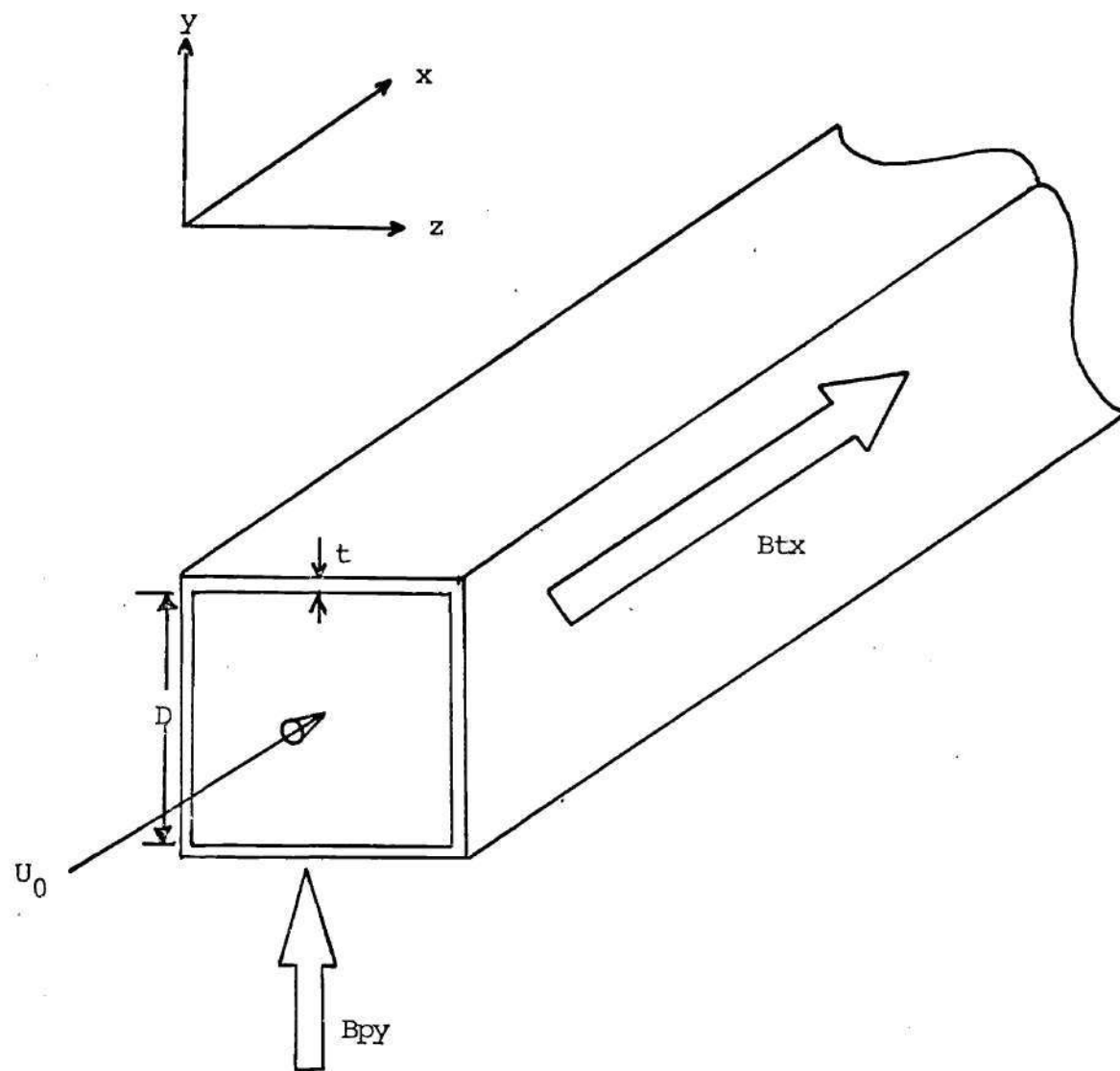


Figure 3. Geometrical Arrangement of the Duct

percent. The viscosity is the most temperature sensitive, and over this range (300°C - 500°C) shows a variation of about 10%.²⁸ Thus, the laminar flow assumption is good, and the constant property assumption reasonable. The MKS system of units is used wherever units are required in the following formulations.

Based on these assumptions the continuity equation becomes,

$$\bar{\nabla} \cdot \bar{V} = 0 \quad (1)$$

The Navier-Stokes equations are,

$$\rho \bar{V} \cdot \nabla \bar{V} = -\nabla P + \mu \nabla^2 \bar{V} + \bar{J} \times \bar{B} \quad (2)$$

where the $\bar{J} \times \bar{B}$ term is simply the Lorentz body force.

Maxwell's equations and the appropriate constitutive equations for the steady state are,

$$\bar{\nabla} \times \bar{E} = 0 \quad (3)$$

$$\bar{\nabla} \times \bar{B} = \mu_e \bar{J} \quad (4)$$

$$\bar{\nabla} \cdot \bar{B} = 0 \quad (5)$$

$$\bar{J} = \sigma(\bar{E} + \bar{V} \times \bar{B}) \quad (6)$$

$$\bar{B} = \bar{B}_0 + \mu_e \bar{H} \quad (7)$$

Hall current has been neglected in equation (6) which is Ohm's law. Assuming an isotropic medium allowed the writing of equation (7).

Now that the basic equations have been stated, the magnetic induction equations need to be derived. Taking the curl of Ohm's law (eq. 6) and using equation (3) gives,

$$\begin{aligned}
\bar{\nabla} \times \bar{J} &= \sigma(\bar{\nabla} \times \bar{E}) + \sigma \bar{\nabla} \times (\bar{\nabla} \times \bar{B}) \\
&= \sigma(\bar{B} \cdot \bar{\nabla} \bar{\nabla}) - \sigma(\bar{\nabla} \cdot \bar{\nabla} \bar{B}) .
\end{aligned} \tag{8}$$

The curl of equation (4) yields,

$$\bar{\nabla} \times \bar{J} = \frac{1}{\mu_e} \bar{\nabla} \times (\bar{\nabla} \times \bar{B}) . \tag{9}$$

Use of equations (5), (7) and (9), and the fact that the imposed magnetic field \bar{B}_0 is uniform, results in,

$$\bar{\nabla} \times \bar{J} = \bar{\nabla}(\bar{\nabla} \cdot \bar{H}) - \nabla^2 \bar{H} = -\nabla^2 \bar{H} . \tag{10}$$

Combining equations (8) and (10) leads to,

$$\sigma(\bar{B} \cdot \bar{\nabla} \bar{\nabla}) - \sigma(\bar{\nabla} \cdot \bar{\nabla} \bar{B}) + \nabla^2 \bar{H} = 0 . \tag{11}$$

Use of equation (7) and the uniform field assumption gives,

$$(\bar{\nabla} \cdot \bar{\nabla}) \bar{H} - (\bar{H} \cdot \bar{\nabla}) \bar{\nabla} = \frac{1}{\sigma \mu_e} \nabla^2 \bar{H} + \frac{1}{\mu_e} (\bar{B}_0 \cdot \bar{\nabla}) \bar{\nabla} \tag{12}$$

which is the general form for the magnetic induction equation.

It is illuminating to consider the similarities between the induction equation (12) and the momentum equation (2). The first set of terms on the left hand side of the induction equation is similar in form and character to the convection terms in the momentum equation. These terms correspond to a convection of the induced magnetic field. The first set of terms on the right hand side of the induction equation corresponds to the viscous terms in the momentum equation. Finally, the second set of terms on the right hand side of equation (12), being source terms whose magnitudes are dependent on the imposed magnetic field, directly

correspond to body force terms in the momentum equation. It shall be seen later that it is because of these similarities that the same generalized numerical procedure can be used to solve the momentum, induction and energy equations.

The only equation remaining is the energy equation,

$$\rho C_p (\bar{V} \cdot \bar{\nabla} T) = k(\nabla^2 T) + J^2/\sigma + Q_n''' \quad (13)$$

where J^2/σ is the contribution due to Ohmic heating, Q_n''' the nuclear heating term, and the Viscous dissipation function has been neglected. Again, the diffusion and convection terms correspond to the similar terms in the momentum and induction equations.

It is obvious that equations (2), (12) and (13) are elliptic in their full forms. The cause of this, of course, is the diffusive terms $\nabla^2 \Psi$, where Ψ can be velocity, temperature or induced magnetic field. Parabolizing these equations in the axial coordinate involves neglection of the axial diffusive terms. The ellipticity in the other two coordinate directions is retained. It must be mentioned that this approximation is possible only when:⁵ (a) there exists a predominant direction of flow (i.e. there is no reverse flow in that direction), (b) the diffusion of momentum, heat and induced field is negligible in that direction, and (c) the downstream pressure field has little or no influence on the upstream flow conditions.

When these conditions are satisfied, the coordinate in the main flow direction becomes a one-way coordinate, i.e. the upstream conditions can determine the downstream flow properties, but not vice-versa. As

shall be more fully explained in the next chapter, it is this convenient behavior that enables the employment of marching integration from an upstream station to a downstream one. Since the flow is strongly convective, the above stipulations are almost identically satisfied for the momentum equations. Only at very low Reynolds numbers is axial viscous diffusion of any significance. The importance of axial conduction in the energy equation is measured by the magnitude of the Peclet number. It has been shown that eliminating axial conduction for Peclet numbers of about 10 causes errors in the heat transfer coefficients of a few percent, while the errors associated with Peclet numbers of around 100 or more are essentially negligible.²⁷ Most practical applications correspond to Peclet numbers of about 100 or higher. Except for very near the entrance, the induced field variations are expected to be small in the axial direction, and especially since there is essentially no axial current flow, setting all axial second derivatives to zero in the induction equations seems a reasonable assumption. Here the magnetic Reynolds number determines the relative strength of the diffusive and convective terms.

Boundary Conditions

Figure 4 shows a crosssection of the duct of interest. Region 1 is the interior which is occupied by the fluid. Region 2 is the wall itself, with finite thickness t , where t is much less than the side D . Region 3 is vacuum extending up to infinity where a constant, uniform magnetic field B_{py} acts in the y -direction.

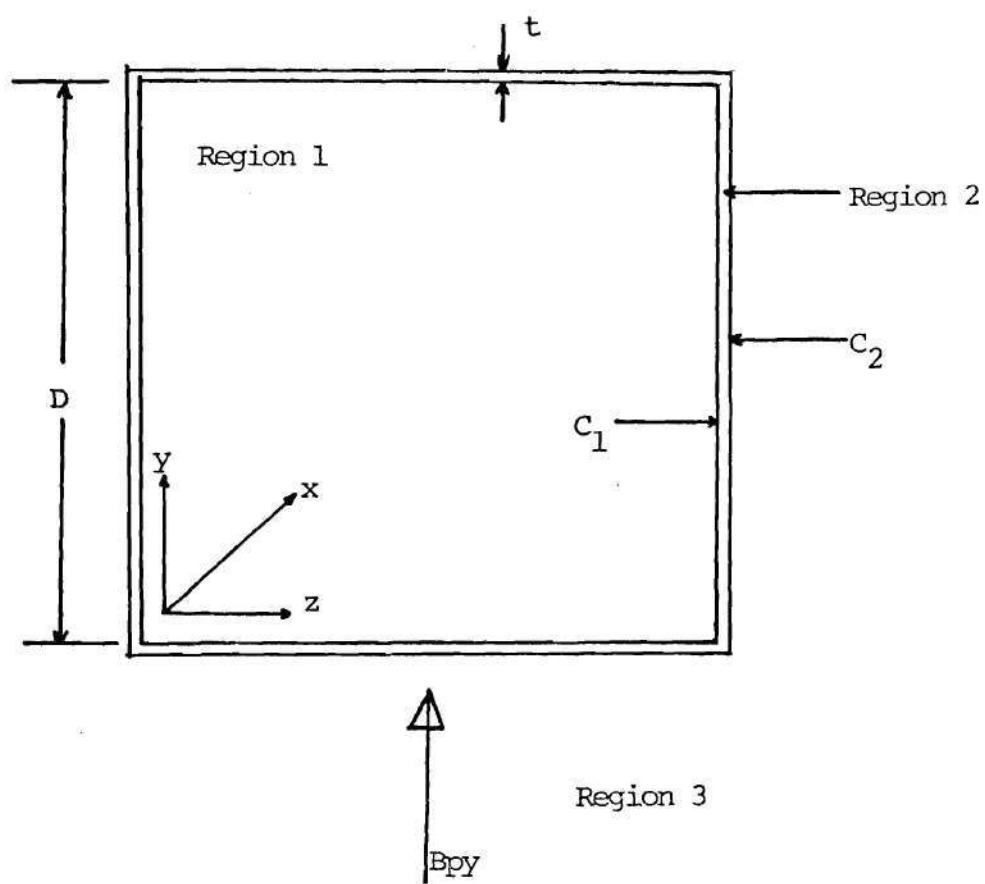


Figure 4. Duct Cross-section

The momentum and energy equations have to be satisfied only in region 1, whereas Maxwell's equations (3) to (7) have to be satisfied in all space. Zero velocities at the duct walls are specified as boundary conditions on the momentum equations. Boundary conditions for the walls being at a constant temperature or subject to a constant heat flux are imposed on the energy equation. These are of a standard form and will be stated in more detail later. The description of the system is completed by imposing continuity of tangential components of electric potential \bar{E} , and of normal and tangential components of magnetic field \bar{B} , at interfaces, plus boundary conditions on \bar{B} and \bar{E} at infinity. It should be mentioned that continuity of tangential components of \bar{B} implies no surface currents. This is appropriate, since in non-magnetic materials, surface currents occur only in the presence of unsteady magnetic fields.

H_x , the axial induced field component, will be much larger than H_z or H_y since it is generated by the primary motion, while they are generated by the secondary flow. In region 3, σ_3 is equal to zero, thus the current is zero and equation (4) forces the curl of \bar{H} to be zero. Since H_y and H_z are virtually negligible, this means that H_x is essentially a constant here. However, since H_x must go to zero at infinity, H_x must be zero in region 3.

In the wall all velocities are identically zero, and so Ohm's law states the continuity of tangential electric field at the interface C_1 as,

$$E_{t1} = E_{t2} \text{ at } C_1$$

or,

$$\frac{J_{t1}}{\sigma_1} = \frac{J_{t2}}{\sigma_2} \quad (14)$$

Also, zero velocities in the wall result in the induction equation (12) becoming,

$$\nabla^2 \bar{H}_2 = 0 \quad (15)$$

in region 2. Expanding equation (14) results in the following expressions for the currents,

$$J_x = \frac{\partial H_z}{\partial y} - \frac{\partial H_y}{\partial z} \quad (16)$$

$$J_y = \frac{\partial H_x}{\partial z} - \frac{\partial H_z}{\partial x} \quad (17)$$

$$J_z = \frac{\partial H_y}{\partial x} - \frac{\partial H_x}{\partial y} \quad (18)$$

Since the induction equation of most importance is that for the H_x component, explicit boundary conditions for this equation are derived first. From equations (17) and (18), if H_y and H_z are much smaller than H_x , it is possible to write,

$$J_y = \frac{\partial H_x}{\partial z} \quad (19)$$

$$J_z = - \frac{\partial H_x}{\partial y} \quad (20)$$

Under the assumption of no axial currents, it is possible to write,

$$J_t = \frac{\partial H_x}{\partial n} \quad (21)$$

and from equation (14),

$$\frac{1}{\sigma_1} \frac{\partial H_{x_1}}{\partial n} = \frac{1}{\sigma_2} \frac{\partial H_{x_2}}{\partial n} \quad (22)$$

where t is the tangential direction and n the normal. Equation (22) holds at the interface 1.

So far it is possible to state the boundary conditions on H_x as follows: $H_{x_2} = 0$ on C_2 the boundary between regions 2 and 3; $H_{x_1} = H_{x_2}$, $\sigma_2 \frac{\partial H_{x_1}}{\partial n} = \sigma_1 \frac{\partial H_{x_2}}{\partial n}$ on C_1 the boundary between regions 1 and 2. This is a rather difficult problem since it involves two domains and two sets of boundary conditions. The two domains being, of course, the duct interior where equation (12) applies, and the duct wall where equation (15) holds. For certain special cases this problem can be simplified. If the duct wall is a perfect insulator (σ_2 equal zero) then $H_{x_2} = 0$ so that it is only necessary to solve equation (12) with $H_{x_1} = 0$ on C_1 . If the duct wall is a perfect conductor ($\sigma_2 = \infty$) the boundary conditions on equation (12) become $\partial H_{x_1} / \partial n = 0$ on C_1 . There is another limiting case first derived by Shercliff¹⁶ for which the problem reduces to solving equation (12) in region 1 with boundary conditions given on C_1 . Using the fact that the thickness of the duct wall is much less than the duct width allows the x component of equation (15) to be approximated by,

$$\frac{\partial^2 H_{x_2}}{\partial n^2} = 0 \quad (23)$$

For a thin wall, the solution to equation (23) is locally linear and can be represented as,

$$Hx_2 \approx \alpha(n-t) \quad (\text{on } C_1, n=0) \quad (24)$$

and thus,

$$\left(\frac{\partial Hx_2}{\partial n} \right) \Big|_{C_1} = \alpha$$

giving,

$$\alpha = - \frac{1}{t} (Hx_2) \Big|_{C_1}$$

$$\left(\frac{\partial Hx_2}{\partial n} \right) \Big|_{C_1} = - \frac{1}{t} (Hx_2) \Big|_{C_1} = - \frac{1}{t} (Hx_1) \Big|_{C_1}$$

and with equation (22), results finally in,

$$\left(\frac{\partial Hx_1}{\partial n} \right) \Big|_{C_1} + \frac{\sigma_1}{\sigma_2 t} (Hx_1) \Big|_{C_1} = 0 \quad (25)$$

This is Shercliff's thin wall boundary condition and can be used for walls of finite conductivity. The limiting cases for σ_2 equal zero and σ_2 equal infinity are included in this statement.

For the other field components, H_y and H_z , boundary conditions are difficult to specify explicitly. Except for very near the entrance, these fields, which are generated by the secondary flow, are expected to be very small. Thus, a reasonable approximation seems to be to allow

these fields to vary linearly within the wall as in equation (25) for tangential walls, and let the fields go to zero at all normal walls.

Components of the Lorentz Force

The Lorentz force components can easily be shown to take on the following forms.

x-Component

$$\left[-B_{py} \left(\frac{\partial H_y}{\partial x} - \frac{\partial H_x}{\partial y} \right) \right] \quad (26)$$

y-Component

$$\left[B_{tx} \left(\frac{\partial H_y}{\partial x} - \frac{\partial H_x}{\partial y} \right) \right] \quad (27)$$

z-Component

$$\left[B_{py} \left(\frac{\partial H_z}{\partial y} - \frac{\partial H_y}{\partial z} \right) - B_{tx} \left(\frac{\partial H_x}{\partial z} - \frac{\partial H_z}{\partial x} \right) \right] \quad (28)$$

The expanded forms of the momentum, induction and energy equations then become the following.

Momentum,

$$\rho \left(\frac{\partial(u \cdot u)}{\partial x} + \frac{\partial(u \cdot v)}{\partial y} + \frac{\partial(u \cdot w)}{\partial z} \right) = - \frac{\partial P}{\partial x} + \mu \left(\frac{\partial^2 u}{\partial y^2} + \frac{\partial^2 u}{\partial z^2} \right) - B_{py} \left(\frac{\partial H_y}{\partial x} - \frac{\partial H_x}{\partial y} \right) \quad (29)$$

$$\rho \left(\frac{\partial(v \cdot u)}{\partial x} + \frac{\partial(v \cdot v)}{\partial y} + \frac{\partial(v \cdot w)}{\partial z} \right) = - \frac{\partial P}{\partial y} + \mu \left(\frac{\partial^2 v}{\partial y^2} + \frac{\partial^2 v}{\partial z^2} \right) + B_{tx} \left(\frac{\partial H_y}{\partial x} - \frac{\partial H_x}{\partial y} \right) \quad (30)$$

$$\rho \left(\frac{\partial(w \cdot u)}{\partial x} + \frac{\partial(w \cdot v)}{\partial y} + \frac{\partial(w \cdot w)}{\partial z} \right) = - \frac{\partial P}{\partial z} + \mu \left(\frac{\partial^2 w}{\partial y^2} + \frac{\partial^2 w}{\partial z^2} \right) + B_{py} \left(\frac{\partial H_z}{\partial y} - \frac{\partial H_y}{\partial z} \right) - B_{tx} \left(\frac{\partial H_x}{\partial z} - \frac{\partial H_z}{\partial x} \right) \quad (31)$$

With the no-slip boundary condition on all rigid walls.

Induction,

$$\begin{aligned} \frac{\partial(v \cdot H_x)}{\partial y} + \frac{\partial(w \cdot H_x)}{\partial z} &= \frac{1}{\sigma \mu_e} \left(\frac{\partial^2 H_x}{\partial y^2} + \frac{\partial^2 H_x}{\partial z^2} \right) + \frac{1}{\mu_e} \left(B_{tx} \frac{\partial u}{\partial x} + B_{py} \frac{\partial u}{\partial y} \right) \\ &\quad + \frac{\partial(u \cdot H_y)}{\partial y} + \frac{\partial(u \cdot H_z)}{\partial z} \end{aligned} \quad (32)$$

$$\frac{\partial(u \cdot Hy)}{\partial x} + \frac{\partial(w \cdot Hy)}{\partial z} = \frac{1}{\sigma \mu_e} \left(\frac{\partial^2 Hy}{\partial y^2} + \frac{\partial^2 Hy}{\partial z^2} \right) + \frac{1}{\mu_e} \left(B_{tx} \frac{\partial v}{\partial x} + B_{py} \frac{\partial v}{\partial y} \right) + \frac{\partial(v \cdot Hx)}{\partial x} + \frac{\partial(v \cdot Hz)}{\partial z} \quad (33)$$

$$\frac{\partial(u \cdot Hz)}{\partial x} + \frac{\partial(v \cdot Hz)}{\partial y} = \frac{1}{\sigma \mu_e} \left(\frac{\partial^2 Hz}{\partial y^2} + \frac{\partial^2 Hz}{\partial z^2} \right) + \frac{1}{\mu_e} \left(B_{tx} \frac{\partial w}{\partial x} + B_{py} \frac{\partial w}{\partial y} \right) + \frac{\partial(w \cdot Hx)}{\partial x} + \frac{\partial(w \cdot Hy)}{\partial y} \quad (34)$$

with the boundary conditions described by equation (25) and its limiting cases.

Energy,

$$\rho C_p \left(\frac{\partial(u \cdot T)}{\partial x} + \frac{\partial(v \cdot T)}{\partial y} + \frac{\partial(w \cdot T)}{\partial z} \right) = k \left(\frac{\partial^2 T}{\partial y^2} + \frac{\partial^2 T}{\partial z^2} \right) + \frac{1}{\sigma} \left[\left(\frac{\partial Hz}{\partial y} - \frac{\partial Hy}{\partial z} \right)^2 + \left(\frac{\partial Hx}{\partial z} - \frac{\partial Hz}{\partial x} \right)^2 + \left(\frac{\partial Hy}{\partial x} - \frac{\partial Hx}{\partial y} \right)^2 \right] + Q_n''' \quad (35)$$

with either a fixed temperature boundary condition, $T = T_{\text{wall}}$, or a specified heat flux boundary condition such as,

$$-k \frac{dT}{dn} = q_w'' \quad (36)$$

where q_w'' can be zero for thermal insulation.

Dimensionless Equations and Boundary Conditions

To non-dimensionlize the above equations, the following dimensionless quantities are defined,

$$u' = u/U_0, \quad v' = v/U_0, \quad w' = w/U_0,$$

$$x' = x/D, \quad y' = y/D, \quad z' = z/D, \quad P' = P/\rho U_0^2,$$

$$Hx' = \frac{\mu_e Hx}{Bpy}, \quad Hy' = \frac{\mu_e Hy}{Bpy}, \quad Hz' = \frac{\mu_e Hz}{Bpy}.$$

Here U_0 is the velocity of initial slug flow at the duct entrance, D is the width of the duct, and Bpy is the imposed magnetic field in the y -direction. For the temperature equation, it is appropriate to have the non-dimensionalization compatible with the specified boundary condition. The constant wall temperature case requires,

$$\theta = \frac{T - T_i}{T_w - T_i}, \quad [Q_n''']' = \frac{Q_n''' D^2}{k(T_w - T_i)},$$

while for the constant wall heat flux case it is preferable to define,

$$\theta = \frac{T - T_i}{q_w'' D/k}, \quad [Q_n''']' = Q_n''' D/q_w''.$$

Here, T_i is the uniform inlet temperature and q_w'' the uniform wall heat flux. T_w , the wall temperature, is no longer constant for the specified wall flux case, and thus can no longer be used in the non-dimensionalization.

The following standard non-dimensional parameters are also introduced:

$$\begin{aligned}
 \text{Reynolds number} &= \text{Re} = U_o D \rho / \mu \\
 \text{Hartmann number} &= \text{Ha} = BD(\sigma/\mu)^{1/2} \\
 \text{Magnetic Reynolds number} &= \text{Rem} = U_o D \sigma \mu_e \\
 \text{Nusselt number} &= \text{Nu} = h D / k \\
 \text{Prandtl number} &= \text{Pr} = \mu C_p / k \\
 \text{Conductance Ratio} &= C = \sigma_w t / \sigma D \\
 &\quad (\text{Conductance of duct wall / conductance of fluid}) \\
 \text{Eckert number} &= \text{Ec} = \frac{U_o^2}{C_p (t_w - T_i)} = \frac{U_o^2 k}{C_p q_w'' D}
 \end{aligned}$$

After performing the non-dimensionalization, the following equation set is obtained.

Continuity:

$$\frac{\partial u}{\partial x} + \frac{\partial v}{\partial y} + \frac{\partial w}{\partial z} = 0 \quad (37)$$

Momentum:

$$\frac{\partial(u \cdot u)}{\partial x} + \frac{\partial(u \cdot v)}{\partial y} + \frac{\partial(u \cdot w)}{\partial z} = \frac{1}{\text{Re}} \left(\frac{\partial^2 u}{\partial y^2} + \frac{\partial^2 u}{\partial z^2} \right) - \frac{\text{Ha} p^2}{\text{Re Rem}} \left(\frac{\partial H_y}{\partial x} - \frac{\partial H_x}{\partial y} \right) + \frac{\partial p}{\partial x} \quad (38)$$

$$\frac{\partial(v \cdot u)}{\partial x} + \frac{\partial(v \cdot v)}{\partial y} + \frac{\partial(v \cdot w)}{\partial z} = \frac{1}{\text{Re}} \left(\frac{\partial^2 v}{\partial y^2} + \frac{\partial^2 v}{\partial z^2} \right) + \frac{\gamma \text{Ha} p^2}{\text{Re Rem}} \left(\frac{\partial H_y}{\partial x} - \frac{\partial H_x}{\partial y} \right) - \frac{\partial p}{\partial y} \quad (39)$$

$$\begin{aligned}
 \frac{\partial(w \cdot u)}{\partial x} + \frac{\partial(w \cdot v)}{\partial y} + \frac{\partial(w \cdot w)}{\partial z} &= \frac{1}{\text{Re}} \left(\frac{\partial^2 w}{\partial y^2} + \frac{\partial^2 w}{\partial z^2} \right) + \frac{\text{Ha} p^2}{\text{Re Rem}} \left(\frac{\partial H_z}{\partial y} - \frac{\partial H_y}{\partial z} \right) \\
 &\quad - \frac{\gamma \text{Ha} p^2}{\text{Re Rem}} \left(\frac{\partial H_x}{\partial z} - \frac{\partial H_z}{\partial x} \right) - \frac{\partial p}{\partial z} \quad (40)
 \end{aligned}$$

Here $u = v = w = 0$ are the boundary conditions at the duct walls, $\gamma = B_{tx}/B_{py}$, and H_{ap} is the Hartmann number based on the transverse (poloidal) field B_{py} .

Induction:

$$\frac{\partial(v \cdot H_x)}{\partial y} + \frac{\partial(w \cdot H_x)}{\partial z} = \frac{1}{\text{Rem}} \left(\frac{\partial^2 H_x}{\partial y^2} + \frac{\partial^2 H_x}{\partial z^2} \right) + \gamma \frac{\partial u}{\partial x} + \frac{\partial u}{\partial y} + \frac{\partial(H_y \cdot u)}{\partial y} + \frac{\partial(H_z \cdot u)}{\partial z} \quad (41)$$

$$\frac{\partial(u \cdot H_y)}{\partial x} + \frac{\partial(w \cdot H_y)}{\partial z} = \frac{1}{\text{Rem}} \left(\frac{\partial^2 H_y}{\partial y^2} + \frac{\partial^2 H_y}{\partial z^2} \right) + \gamma \frac{\partial v}{\partial x} + \frac{\partial v}{\partial y} + \frac{\partial(H_x \cdot v)}{\partial x} + \frac{\partial(H_z \cdot v)}{\partial z} \quad (42)$$

$$\frac{\partial(u \cdot H_z)}{\partial x} + \frac{\partial(v \cdot H_z)}{\partial y} = \frac{1}{\text{Rem}} \left(\frac{\partial^2 H_z}{\partial y^2} + \frac{\partial^2 H_z}{\partial z^2} \right) + \gamma \frac{\partial w}{\partial x} + \frac{\partial w}{\partial y} + \frac{\partial(H_x \cdot w)}{\partial x} + \frac{\partial(H_y \cdot w)}{\partial y} \quad (43)$$

The boundary conditions being the dimensionless form of equation (25) and its limiting cases,

$$\left. \frac{\partial H_t}{\partial n} \right|_{\text{wall}} + \left. \frac{H_t}{C} \right|_{\text{wall}} = 0 \quad (44)$$

and,

$$\left. H_n \right|_{\text{wall}} = 0$$

Energy:

$$\begin{aligned} \frac{\partial(u \cdot \theta)}{\partial x} + \frac{\partial(v \cdot \theta)}{\partial y} + \frac{\partial(w \cdot \theta)}{\partial z} = & \frac{1}{\text{Re Pr}} \left(\frac{\partial^2 \theta}{\partial y^2} + \frac{\partial^2 \theta}{\partial z^2} \right) + \frac{H_{ap}^2 \text{Ec}}{\text{Re Rem}^2} \left(\left(\frac{\partial H_z}{\partial y} - \frac{\partial H_y}{\partial z} \right)^2 \right. \\ & \left. + \left(\frac{\partial H_x}{\partial z} - \frac{\partial H_z}{\partial x} \right)^2 + \left(\frac{\partial H_y}{\partial x} - \frac{\partial H_x}{\partial y} \right)^2 \right) + Q_n''' / \text{Re Pr} \end{aligned} \quad (45)$$

The constant wall temperature boundary condition being, simply $\theta = 1.0$ on the wall, and the constant wall heat flux boundary condition being the non-dimensional form of equation (36),

$$\frac{d\theta}{dn} = -1.0 \quad . \quad (46)$$

Equation (46) is obtained by performing a simple heat balance at the wall,

$$q_w'' = h (T_w - T_b)$$

and using Fourier's law,

$$q_w'' = -k \left. \frac{dT}{dn} \right|_{\text{wall}} \quad .$$

Recalling $\theta = (T - T_i) / (q_w'' D / k)$ gives,

$$-\frac{k}{D} \frac{q_w'' D}{k} \frac{d\theta}{dn} = q_w''$$

or,

$$\frac{d\theta}{dn} = -1 \quad , \quad \text{which is equation (46).}$$

It should be mentioned that in the above equations and boundary conditions, the dimensionless variables should have primes on them, i.e. x should be x' , and so on. However, in the interest of brevity, the primes have been left out.

All that needs to be added to equations (37) through (46) to complete the mathematical formulation of the problem is a statement on the entry conditions. Since the equation set is parabolic in the axial direction, no exit conditions are required and in fact cannot be tolerated. At the duct entrance, uniform slug flow is specified and all other quantities, temperature, pressure and induced magnetic field components are constant or zero.

CHAPTER III

NUMERICAL FORMULATION

The Finite Difference Equations

Inspection of equations (38), (39), (40), (41), (42), (43), and (45) reveals that they can all be written in the following general form,

$$\frac{\partial(u \cdot \Psi)}{\partial x} + \frac{\partial(v \cdot \Psi)}{\partial y} + \frac{\partial(w \cdot \Psi)}{\partial z} = \Gamma \frac{\partial^2 \Psi}{\partial y^2} + \Gamma \frac{\partial^2 \Psi}{\partial z^2} + S_{\Psi} \quad (47)$$

where Ψ is any of the dependent variables, Γ is the appropriate transport property such as viscosity or thermal conductivity, and S is a source term. For dimensionless equations, Γ simply becomes the suitable combination of non-dimensional parameters, e.g. $1/\text{Re Pr}$ for the energy equation and $1/\text{Rem}$ for the induction equations. The source terms for the momentum and energy equations are body forces and heat generation functions respectively, while for the induction equations they include imposed field components and some convective type terms. If eq. (47) represents a momentum equation, an extra pressure gradient term is needed. Since the pressure is treated as an unknown, the gradient is written separately and not included in the source.

Equation (47) needs to be transformed into a finite difference equation. In so doing, the approach of Patankar et al⁵ is followed. A three-dimensional staggered grid is imposed on the flow field. This is basically the MAC grid structure of Harlow and Welch,³⁴ and has the v and w velocity components stored midway between the main points where all other variables (u velocity, pressure, induced field components and

temperature) are stored. The staggered grid has the advantage of convenience in the computing of convective terms for variables placed at the cell center and pressure gradients for the v and w momentum equations. Figure 5 displays the grid structure.

The usual way to obtain a finite difference equation from a partial difference equation is to substitute for the individual terms in the equation, expressions obtained from Taylor series expansions of these terms. However, in this work the control volume approach has been used to formulate the finite difference equations since it always ensures total conservation of properties in all points in the domain.³⁵ An integral equation can be constructed over the control volume shown in Fig. 6, and by the use of the assumptions regarding the nature of the variation of Ψ between the grid points, the finite difference equation can be obtained. In other words, the finite difference equation is obtained by expressing each term in the parent partial differential equation as an integrated average over a small control volume.

Figure 6 portrays the control volume of interest for equations centered at the main nodes. The yz face of this same control volume is displayed by Fig. 7. The N, S, E and W points are the next adjacent nodes where the variable under computation is stored. The n , s , e and w points are on the boundary of the control volume itself. The dimensions of the control volume are Δx , Δy and Δz , while δy_n , δy_s , δz_e and δz_w are distances in the respective directions to the next point at which the variable under computation is stored. For a uniform grid, δy_n , δy_s , δz_e and δz_w will all be equal to Δy and Δz . Since the v and w velocity components are stored at different locations, the positioning of their

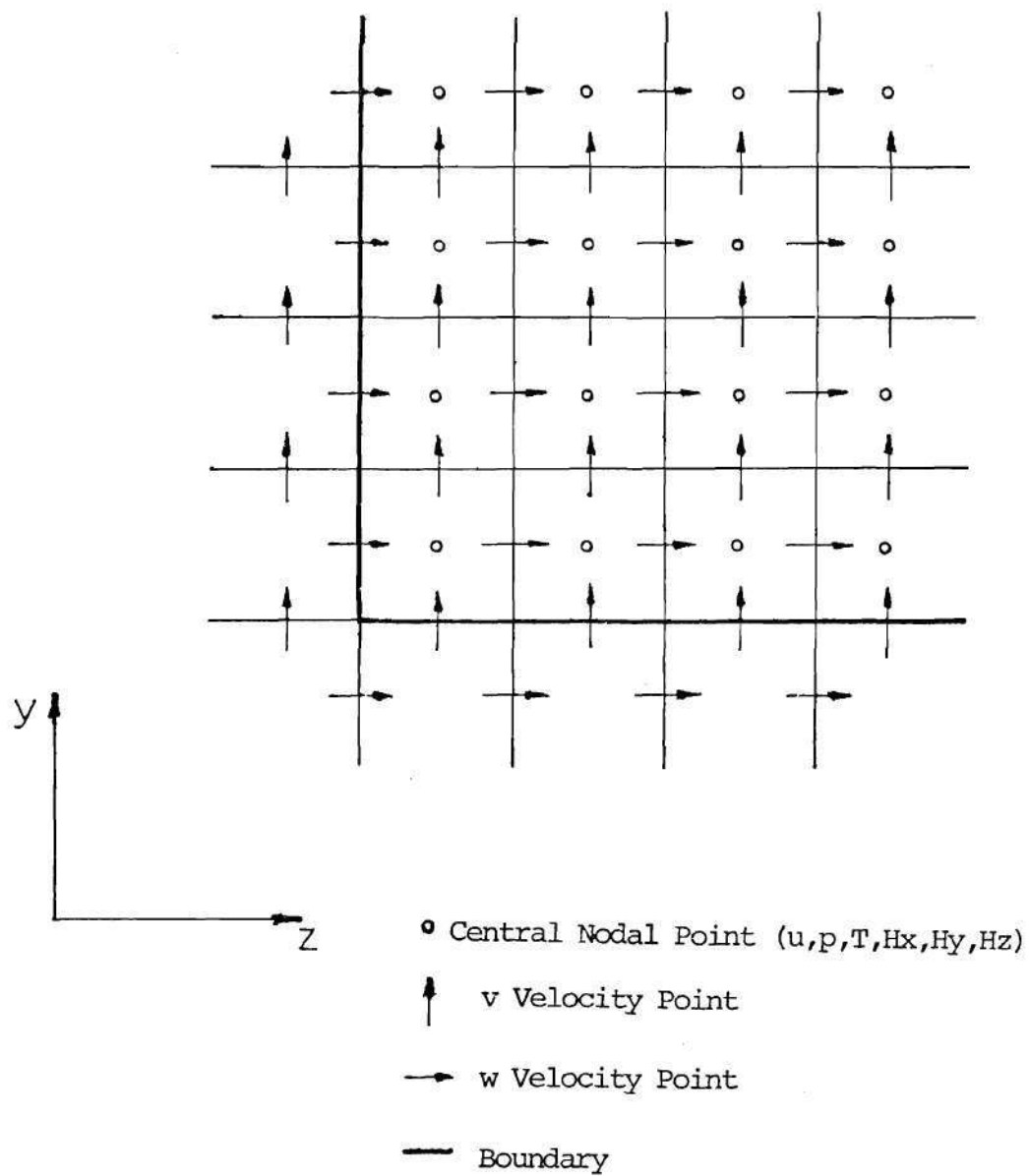


Figure 5. Staggered Grid Structure in yz Plane

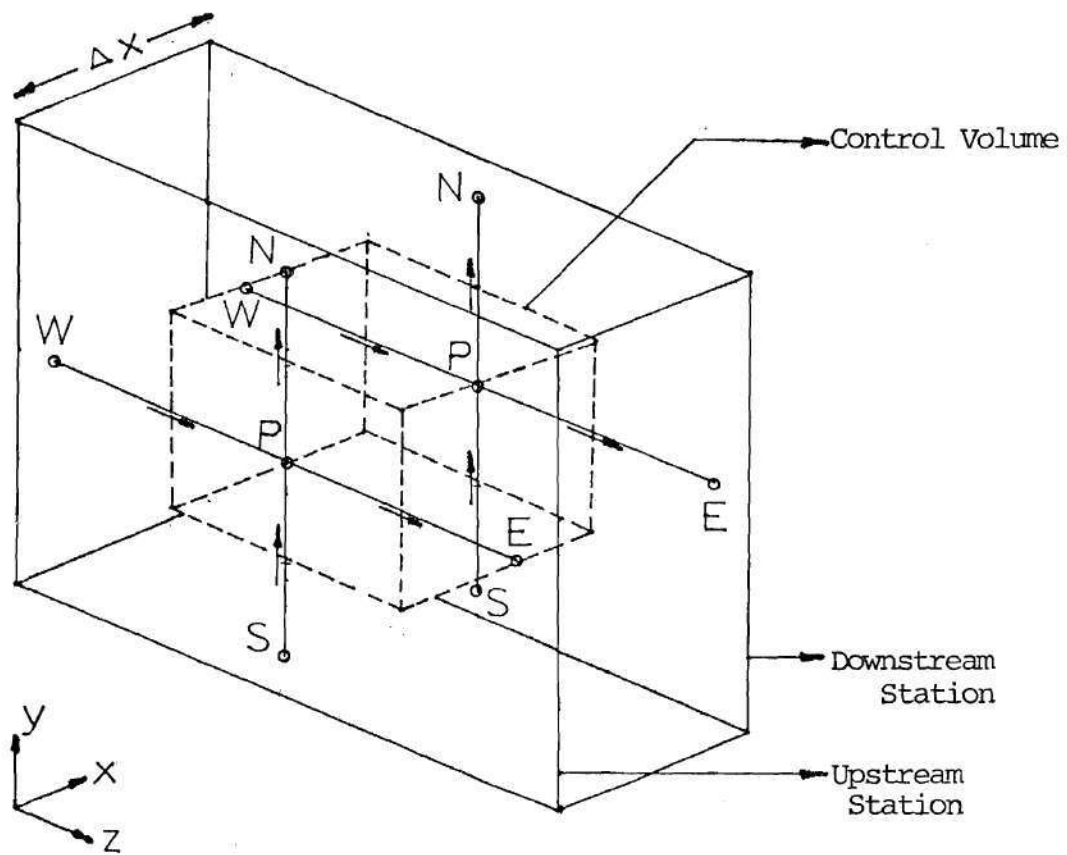


Figure 6. Isometric View of General Control Volume

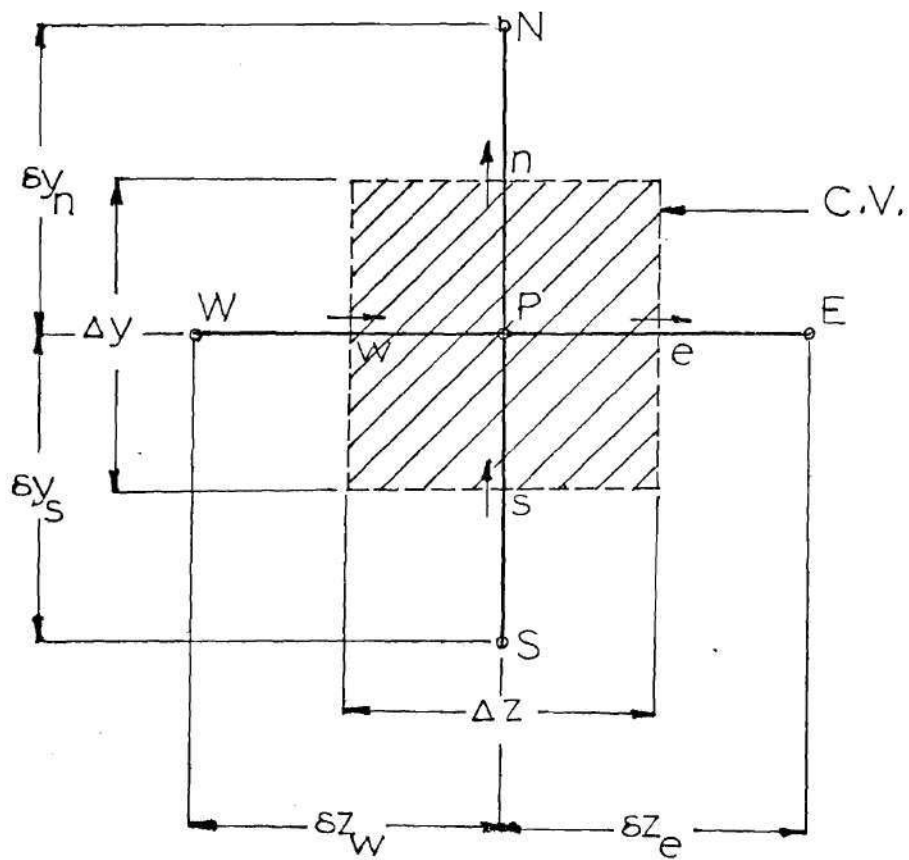


Figure 7. yz Face of Control Volume for Equations Centered at the Main Nodes (u, p, T, H_x, H_y, H_z)

respective control volumes will be different. The yz faces of these control volumes are shown in Figs. 8 and 9. It should be noted that in programing the equations, the same index value (J,K) is used for variables stored at a particular central node, and for the v and w velocities stored at the halfway points immediately south or west of that node.

In order to proceed with the integration of the equations over the control volume, the nature of the variation of the dependent variable Ψ between the grid points must now be specified, as previously noted. In the x direction, Ψ varies in a stepwise manner, i.e. the downstream ($x=x_D$) values of Ψ are supposed to prevail over the interval from x_U to x_D , except at x_U where U represents the upstream station. This assumption, called upwind differencing, is needed to make the finite difference scheme a fully implicit one and ensure numerical stability. For the calculation of the x direction convection and of source terms that may depend on Ψ , the variation of Ψ in the yz plane is also taken to be stepwise. Thus, in the yz plane the value of Ψ is assumed to remain uniform and equal to Ψ_P over the dotted rectangle shown in Fig. 7 surrounding the point P, and to change sharply to Ψ_N , Ψ_S , Ψ_E or Ψ_W outside the rectangle. For the cross-stream convection from the xy and xz faces of the control volume, the value of Ψ convected is taken to be the arithmetic mean of the Ψ values on either side of that face. Thus, a convenient combination of the central-difference and upwind-difference formulae for the first order derivatives has been used. For diffusion across the xy and xz faces of the control volume, it is assumed that Ψ varies linearly between grid points.

Consider the general eq. (47) term by term. The convective terms will be integrated first in accord with the assumptions that have just

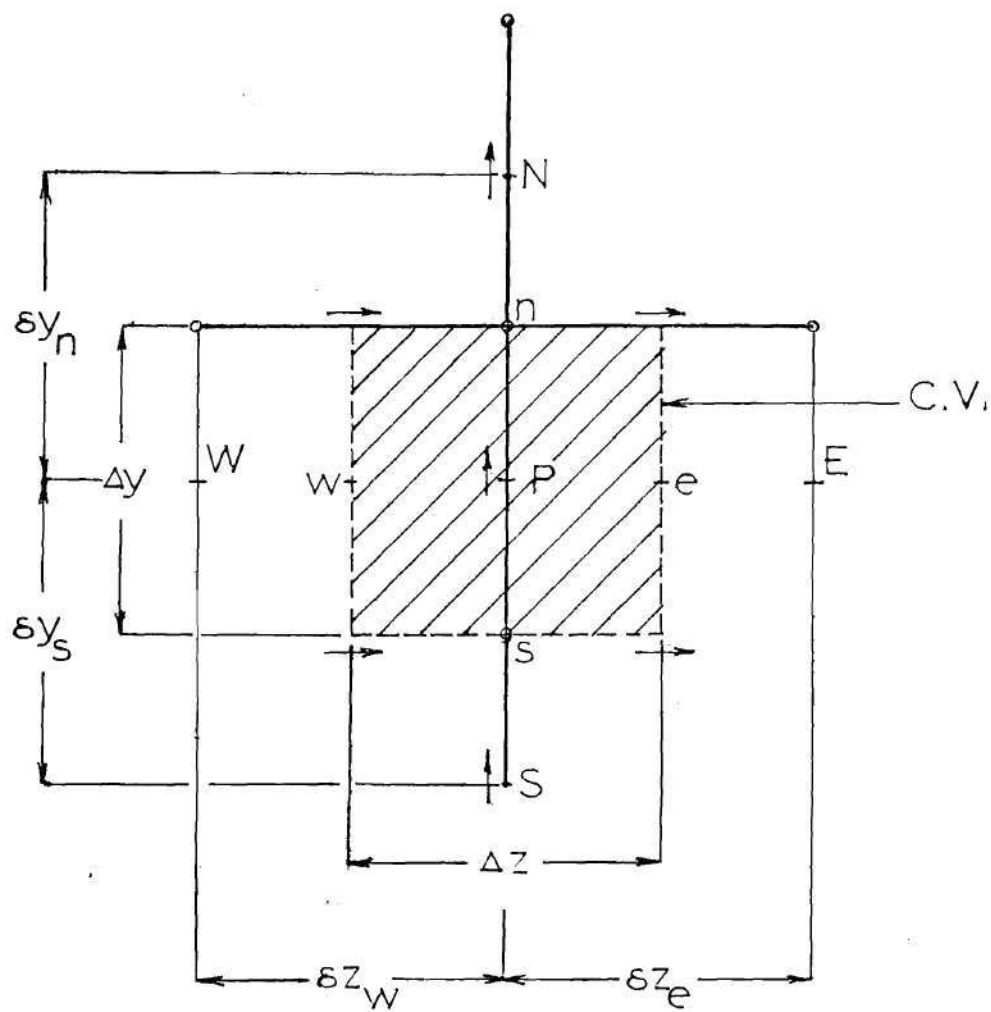


Figure 8. yz Face of Control Volume for v Equation

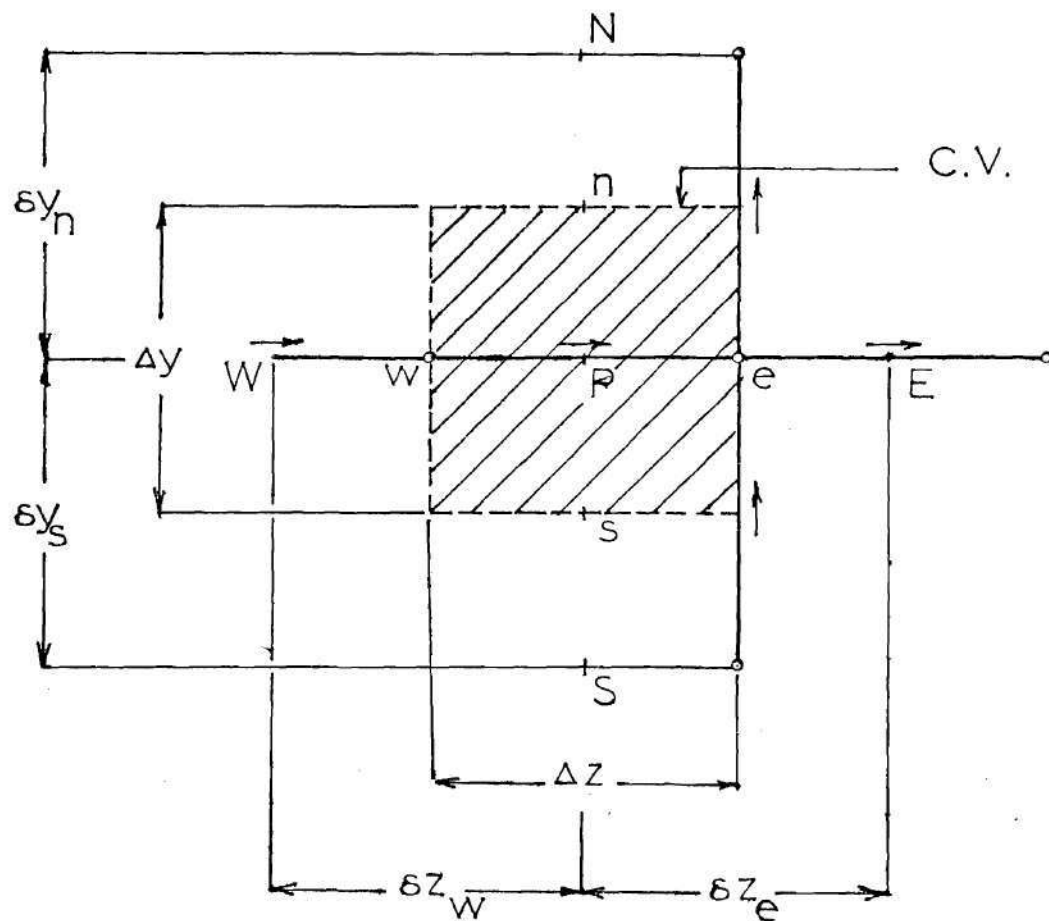


Figure 9. yz Face of Control Volume for w Equation

been made. Integrating them over the control volume, and dividing by Δx , one obtains,

$$\frac{1}{\Delta x} \left\{ \int_{Cv} \frac{\partial}{\partial x} (u \cdot \Psi) dV + \int_{Cv} \frac{\partial}{\partial y} (v \cdot \Psi) dV + \int_{Cv} \frac{\partial}{\partial z} (w \cdot \Psi) dV \right\}$$

which is,

$$\begin{aligned} & \left[(u \Psi)_{P,D} - (u \Psi)_{P,U} \right] \frac{\Delta y \Delta z}{\Delta x} + \left[\frac{v_n}{2} (\Psi_N + \Psi_P) - \frac{v_s}{2} (\Psi_S + \Psi_P) \right]_U \Delta z \\ & + \left[\frac{w_e}{2} (\Psi_E + \Psi_P) - \frac{w_w}{2} (\Psi_W + \Psi_P) \right]_U \Delta y . \end{aligned}$$

In order to keep the scheme implicit, the downstream value $u_{P,D}$ in $(u \Psi)_{P,D}$ must be expressed in terms of $u_{P,U}$ the upstream value. This is achieved by applying the continuity equation about the control volume. In the present formulation this equation can be expressed as,

$$[u_{D,P}] - u_{U,P} \frac{\Delta y \Delta z}{\Delta x} + [v_n - v_s] \Delta z + [w_e - w_w] \Delta y = 0 . \quad (48)$$

The above integration of the convective terms then yields,

$$\begin{aligned} & \left[u_{P,U} \frac{\Delta y \Delta z}{\Delta x} - \Delta z [v_n - v_s]_U - \Delta y [w_e - w_w]_U \right] \Psi_P - \left[u \Psi_{P,U} \right] \frac{\Delta y \Delta z}{\Delta x} \\ & + \left[\left\{ \frac{v_n}{2} \right\}_U \left\{ \Psi_N + \Psi_P \right\}_D - \left\{ \frac{v_s}{2} \right\}_U \left\{ \Psi_S + \Psi_P \right\}_D \right] \Delta z \\ & + \left[\left\{ \frac{w_e}{2} \right\}_U (\Psi_E + \Psi_P)_D - \left\{ \frac{w_w}{2} \right\}_U (\Psi_W + \Psi_P)_D \right] \Delta y . \end{aligned}$$

This expression can be written as,

$$F_D \Psi_{P,D} - F_U \Psi_{P,U} + L_n^y (\Psi_N + \Psi_P)_D - L_s^y (\Psi_S + \Psi_P)_D + L_e^z (\Psi_E + \Psi_P)_D - L_w^z (\Psi_W + \Psi_P)_D$$

which is the integrated convective terms divided by Δx , where,

$$F_U = \frac{\Delta y \Delta z}{\Delta x} (u_{P,U})$$

$$L^y = \frac{\Delta z}{2} (v)_U, \quad L^z = \frac{\Delta y}{2} (w)_U$$

$$F_D = F_U - 2 L_n^y + 2 L_s^y - 2 L_e^z + 2 L_w^z.$$

For the diffusive terms, it is assumed that Ψ varies linearly between grid points. Integrating them as before, the terms become,

$$\int_{Cv} \left(\Gamma \frac{\partial^2 \Psi}{\partial y^2} + \Gamma \frac{\partial^2 \Psi}{\partial z^2} \right) dV$$

and after dividing by Δx one obtains,

$$\Gamma \left[\frac{\Psi_N - \Psi_S}{\delta y_n} - \frac{\Psi_P - \Psi_S}{\delta y_s} \right]_D \Delta z + \Gamma \left[\frac{\Psi_E - \Psi_P}{\delta z_e} - \frac{\Psi_P - \Psi_W}{\delta z_w} \right]_D \Delta y.$$

If the quantities T^y and T^z are defined as,

$$T^y = \frac{\Gamma \Delta z}{\delta y} \quad \text{and} \quad T^z = \frac{\Gamma \Delta y}{\delta z},$$

then the diffusive terms divided by Δx become,

$$T_n^y(\psi_N - \psi_P)_D - T_s^y(\psi_P - \psi_S)_D + T_e^z(\psi_E - \psi_P)_D - T_w^z(\psi_P - \psi_W)_D .$$

For the source term components that depend on ψ , the variation of ψ in the yz plane is also taken to be stepwise. As before, one obtains,

$$\int_{Cv} S_\psi dV$$

and after division by Δx , this yields,

$$S_\psi \Delta y \Delta z .$$

This source term is separated into two parts equal to $S_U + S_D \psi_D$. The first part (S_U) is computed from upstream conditions, while the second part depends on ψ_D and is thus part of the current implicit calculation.

The source terms in the momentum and induction equations are complicated and will now be discussed. In the dimensionless axial momentum eq. (38), the source terms are,

$$- \frac{Hap^2}{Re Rem} \left[\frac{\partial Hy}{\partial x} - \frac{\partial Hx}{\partial y} \right] .$$

As before, these terms are integrated over the control volume and the result divided by Δx , giving

$$S_U = \frac{Hap^2}{Re Rem} \left[[Hx_n - Hx_s] \Delta z - [Hy_{P,D} - Hy_{P,U}] \frac{\Delta y \Delta z}{\Delta x} \right] . \quad (49)$$

The second term of the above result, which arises from the integration of $(\partial Hy / \partial x)$, is a potential troublemaker. Since the momentum

equations are solved first in the order of computation, the current downstream value of H_y is not known yet. The only recourse is to evaluate the entire derivative at the upstream station, with the help of the two station upstream values. Since H_y , being a transverse component, is small near the entrance, and Δx , the axial step, is also small (especially near the entrance) this is not a bad approximation.

For the v and w momentum equations, the source terms are,

$$\frac{\gamma \text{Hap}^2}{\text{Re Rem}} \left[\frac{\partial H_y}{\partial x} - \frac{\partial H_x}{\partial y} \right]$$

and,

$$\frac{\text{Hap}^2}{\text{Re Rem}} \left[\frac{\partial H_z}{\partial y} - \frac{\partial H_y}{\partial z} \right] - \frac{\gamma \text{Hap}^2}{\text{Re Rem}} \left[\frac{\partial H_x}{\partial z} - \frac{\partial H_z}{\partial x} \right] ,$$

respectively.

Again the same problem associated with the $(\partial H_y/\partial x)$ and $(\partial H_z/\partial x)$ derivatives arises. The remedy is as before, namely evaluation at the upstream station. Integration over the control volume followed by division by Δx yields,

$$S_U = \frac{\gamma \text{Hap}^2}{\text{Re Rem}} \left[(H_{y_{P,D}} - H_{y_{P,U}}) \frac{\Delta y \Delta z}{\Delta x} + (H_{x_n} - H_{x_s}) \Delta z \right] \quad (50)$$

and,

$$S_U = \frac{\gamma \text{Hap}^2}{\text{Re Rem}} \left[(H_{z_n} - H_{z_s}) \Delta z - (H_{y_e} - H_{y_w}) \Delta y \right] - \frac{\gamma \text{Hap}^2}{\text{Re Rem}} \left[(H_{x_e} - H_{x_w}) \Delta y - (H_{z_{P,D}} - H_{z_{P,U}}) \frac{\Delta y \Delta z}{\Delta x} \right] , \quad (51)$$

for the v and w equations respectively. It should be noted that since none of the source terms are dependent on u , v or w , then for the momentum equations, S_D is zero.

The source term for the axial induction eq. (41) is,

$$\gamma \frac{\partial u}{\partial x} + \frac{\partial u}{\partial y} + \frac{\partial (u \cdot H_y)}{\partial y} + \frac{\partial (u \cdot H_z)}{\partial z} .$$

This term is integrated over the control volume using, again, the assumptions that were made about the nature of the property variation. After performing the integration and dividing the result by Δx , one obtains

$$S_U = \gamma \left[u_{P,D} - u_{P,U} \right] \frac{\Delta y \Delta z}{\Delta x} + (u_n - u_s) \Delta z \\ + \left((H_y \cdot u)_n - (H_y \cdot u)_s \right) \Delta z + \left((H_z \cdot u)_e - (H_z \cdot u)_w \right) \Delta y .$$

Since S_U is calculated from upstream values, use must be made of the continuity equation to obtain an expression for $u_{P,D}$ in terms of $(\partial v / \partial y)$ and $(\partial w / \partial z)$ which are evaluated upstream. This process is the same as was used in the derivation of the general difference equation. Proceeding, one obtains

$$S_U = \gamma \left(-\Delta z (v_n - v_s) - \Delta y (w_e - w_w) \right) + (u_n - u_s) \Delta z \\ + \left((H_y \cdot u)_n - (H_y \cdot u)_s \right) \Delta z + \left((H_z \cdot u)_e - (H_z \cdot u)_w \right) \Delta y . \quad (52)$$

The source terms for the transverse field components H_y and H_z are obtainable from eqs. (42) and (43) as

$$\gamma \frac{\partial v}{\partial x} + \frac{\partial v}{\partial y} + \frac{\partial (Hx \cdot v)}{\partial x} + \frac{\partial (Hz \cdot v)}{\partial z}$$

and,

$$\gamma \frac{\partial w}{\partial x} + \frac{\partial w}{\partial y} + \frac{\partial (Hx \cdot w)}{\partial x} + \frac{\partial (Hy \cdot w)}{\partial y} ,$$

respectively.

Integration gives,

$$S_U = \left(\gamma \{v_{P,D} - v_{P,U}\} + \{Hx_{P,D} v_{P,D} - Hx_{P,U} v_{P,U}\} \right) \frac{\Delta y \Delta z}{\Delta x} \\ + (v_n - v_s) \Delta z + (Hz_e v_e - Hz_w v_w) \Delta y$$

and,

$$S_U = \left(\gamma \{w_{P,D} - w_{P,U}\} + \{Hx_{P,D} w_{P,D} - Hx_{P,U} w_{P,U}\} \right) \frac{\Delta y \Delta z}{\Delta x} \\ + (w_n - w_s) \Delta z + (Hy_n w_n - Hy_s w_s) \Delta z$$

for these two equations.

By use of the continuity of magnetic flux, it is possible to express $Hx_{P,D}$ in the above two equations in terms of transverse derivatives evaluated at the upstream station. Continuity of magnetic flux implies:

$$(Hx_{P,D}) \frac{\Delta y \Delta z}{\Delta x} = Hx_{P,U} \frac{\Delta y \Delta z}{\Delta x} - \Delta z \{Hy_n - Hy_s\} - \{Hz_e - Hz_w\} \Delta y$$

and inserting this into the above two expressions for S_U yields,

$$\begin{aligned}
S_U = & \left\{ Hx_{P,U} \frac{\Delta y \Delta z}{\Delta x} - \Delta z (Hy_n - Hy_s) - (Hz_e - Hz_w) \Delta y \right\} v_{P,D} \\
& - Hx_{P,U} v_{P,U} \frac{\Delta z \Delta y}{\Delta x} + \gamma (v_{P,D} - v_{P,U}) \frac{\Delta y \Delta z}{\Delta x} + (v_n - v_s) \Delta z \\
& + (Hz_e v_e - Hz_w v_w) \Delta y
\end{aligned} \tag{53}$$

for the Hy equation, and for the Hx equation,

$$\begin{aligned}
S_U = & \left\{ Hx_{P,U} \frac{\Delta y \Delta z}{\Delta x} - \Delta z (Hy_n - Hy_s) - (Hz_e - Hz_w) \Delta y \right\} w_{P,D} \\
& + Hx_{P,U} w_{P,U} \frac{\Delta y \Delta z}{\Delta x} + \gamma (w_{P,D} - w_{P,U}) \frac{\Delta y \Delta z}{\Delta x} + (w_n - w_s) \Delta z \\
& + (Hy_n w_n - Hy_s w_s) \Delta z .
\end{aligned} \tag{54}$$

In the above two expressions, the $(\partial v / \partial x)$ and $(\partial w / \partial x)$ derivatives call for downstream $v_{P,D}$ and $w_{P,D}$ values. As was done for the momentum equations, these derivatives could be evaluated entirely at the upstream station. However, since the velocities are computed before the induced fields, these new downstream values are used.

In summary, the general finite difference equation can be written as,

$$\begin{aligned}
& F_D \Psi_{P,D} - F_U \Psi_{P,U} + L_n^y \{ \Psi_N + \Psi_P \}_D - L_s^y \{ \Psi_S + \Psi_P \}_D + L_e^z \{ \Psi_E + \Psi_P \}_D - L_w^z \{ \Psi_W + \Psi_P \}_D \\
& = T_n^y \{ \Psi_N - \Psi_P \}_D - T_s^y \{ \Psi_P - \Psi_S \}_D + T_e^z \{ \Psi_E - \Psi_P \}_D - T_w^z \{ \Psi_P - \Psi_W \}_D \\
& + S_U + S_P \Psi_{P,D} .
\end{aligned} \tag{55}$$

Rearrangement of the terms yields,

$$\psi_{P,D} = A_N \psi_{N,D} + A_S \psi_{S,D} + A_E \psi_{E,D} + A_W \psi_{W,D} + B_P \quad (56)$$

where,

$$A_N = A'_N / A'_P$$

$$A_S = A'_S / A'_P$$

$$A_E = A'_E / A'_P$$

$$A_W = A'_W / A'_P$$

$$B_P = B'_P / A'_P$$

and,

$$A'_N = T_n^y - L_n^y \quad , \quad A'_S = T_s^y + L_s^y$$

$$A'_E = T_e^z - L_e^z \quad , \quad A'_W = T_w^z + L_w^z$$

$$B'_P = F_U \psi_{P,U} + S_U + (\text{pressure term for momentum eqs.})$$

$$A'_P = A'_N + A'_S + A'_E + A'_W + F_U - S_P$$

The complete set of momentum, induced field and energy equations, cast in the above form, along with all the respective coefficients are given in Appendix A.

Nothing has been said about the treatment of pressure up to this point. This is deliberate since the pressure computation, as always, requires special attention. The axial and transverse pressure gradients are uncoupled by introducing a deliberate inconsistency into the pressure treatment. The axial gradient is written as $(\partial \bar{p} / \partial x)$, while the transverse gradients are $(\partial p / \partial y)$ and $(\partial p / \partial z)$. The quantity \bar{p} can be thought of as a space averaged pressure which is constant over the duct cross-section. The value of $(\partial \bar{p} / \partial x)$ must be known in order to calculate $(\partial p / \partial y)$ and $(\partial p / \partial z)$. This practice is implicit in two dimensional boundary layer theories also, but it escapes notice there because it is not necessary to solve the momentum equation for the cross-stream direction. Here, there are two cross-stream directions, and the momentum equations must be solved for both of them in order to find out how the fluid distributes itself between these two directions.

This practice is a necessary consequence of the intention to exploit the boundary-layer nature of the flow; it is the final step in preventing downstream influences from propagating upstream. If this step is omitted, the result is not increased in accuracy as one might naively expect; it is rather a solution which may be wholly unrealistic physically. The inconsistency in the treatment of pressure, it may be said, is one part of the price that is paid for making the equations parabolic. The gain is the freedom to employ marching integration, and to use two-dimensional storage, even though the flow is three-dimensional and the full equations are elliptic.

The actual pressure computation itself is performed by the guess and correct method of Amsden and Harlow.³⁶ A pressure field is first

guessed at, and is then used to calculate a first approximation to the velocity field. This velocity will, of course, not satisfy the continuity equation. The guessed pressure is then corrected in such a way as to make the velocity field conform to the continuity equation. The conservation of total mass flow in the duct is used to correct the axial (space averaged) pressure gradient, while the local continuity equation applied to each control volume is used to correct the transverse pressure field.

Assume for the moment that $(\partial \bar{p} / \partial x)$ is known and that the downstream value of u has been obtained from the axial momentum equation. Then a preliminary set of v 's and w 's can be obtained from the equations:

$$v_p^* = A_N v_N^* + A_S v_S^* + A_E v_E^* + A_W v_W^* + B_P + D^v (p_P^* - p_S^*) \quad (57)$$

$$w_P^* = A_N w_N^* + A_S w_S^* + A_E w_E^* + A_W w_W^* + B_P + D^w (p_P^* - p_W^*) \quad (58)$$

where the superscript $*$ given to v and w denotes approximate values, based on an estimated pressure field p^* . These v^* 's, and w^* 's will not satisfy the continuity equation for each control volume, but will produce a net mass source emerging from each control volume. The pressure needs to be corrected so as to eliminate this mass source. The mass source is defined by,

$$m_P = C^v (v_n^* - v_P^*) + C^w (w_E^* - w_P^*) + C^u (u_{P,D} - u_{P,U}) \quad (59)$$

where C^v , C^w and C^u represent appropriate coefficients from the continuity eq. (48). The pressure is now written as

$$p = p^* + p' \quad (60)$$

where p^* is the uncorrected portion, and p' the correction. From eqs. (57), (58) and the original forms of the v and w momentum equations, it becomes possible to write,

$$v_P = v_P^* + D^V(p_P' - p_S') + A_N(v_N - v_N^*) + A_S(v_S - v_S^*) + A_E(v_E - v_E^*) + A_W(v_W - v_W^*) \quad (61)$$

$$w_P = w_P^* + D^W(p_P' - p_W') + A_N(w_N - w_N^*) + A_S(w_S - w_S^*) + A_E(w_E - w_E^*) + A_W(w_W - w_W^*) \quad (62)$$

It should be noted that the mass source has been annihilated in writing the above two equations. The guessed pressure field to be used is simply the one at the immediately upstream station. Since this will be very near to the true pressure, the starred velocities will be very close to the unstarred ones. This allows the last four terms in eqs. (61) and (62) to be safely dropped and the velocity corrections become,

$$v_P = v_P^* + D^V(p_P' - p_S') \quad (63)$$

$$w_P = w_P^* + D^W(p_P' - p_W') \quad (64)$$

Substituting eqs. (63) and (64) for the corresponding velocities into the continuity equation yields,

$$\begin{aligned}
& p'_P (2C^V_D V + 2C^W_D W) - C^V_D V p'_N - C^V_D V p'_S - C^W_D W p'_E \\
& \quad - C^W_D W p'_W \\
& = C^V (v_N^* - v_P^*) + C^W (w_E^* - w_P^*) + C^U (u_{P,D} - u_{P,U}) \quad . \quad (65)
\end{aligned}$$

The right hand side of the above equation is the mass source of eq. (59).

To cast this equation into the general form, the coefficients are defined as,

$$\begin{aligned}
A_N &= \frac{C^V_D V}{A'_P} = A_S \\
A_E &= \frac{C^W_D W}{A'_P} = A_W \\
B_P &= \left\{ C^V (v_N^* - v_P^*) + C^W (w_E^* - w_P^*) + C^U (u_{P,D} - u_{P,U}) \right\} / A'_P
\end{aligned}$$

where,

$$A'_P = 2C^V_D V + 2C^W_D W \quad .$$

The pressure correction equation then becomes,

$$p'_P = A_N p'_N + A_S p'_S + A_E p'_E + A_W p'_W + B_P \quad . \quad (66)$$

It should be recalled that by taking the divergence of the momentum equations, it is possible to obtain a Poisson equation for the pressure. This equation is elliptic in all three space coordinates, and will not permit employment of a marching integration technique in the axial direction. To be able to march in this direction, the $(\partial^2 p / \partial x^2)$

term must be treated as known and the equation regarded as elliptic in only the y and z directions. This is why $(\partial \bar{p}/\partial x)$ must be obtained before p' is obtained from the solution of eq. (66). Incidentally, eq. (66) is like a two-dimensional Poisson equation with a source term that relates it to the three dimensionality of the situation. Solution of eq. (66) throughout the domain results in a pressure correction distribution which is used in eqs. (63) and (64) to obtain the corrected transverse velocities.

Up until now it has been assumed that the longitudinal pressure gradient $(\partial \bar{p}/\partial x)$ was known. This quantity is obtained before the computation of the transverse velocities by application of the conservation of integral mass flow through the duct. Again, the quantity is split into a guessed value and a correction,

$$\frac{\partial \bar{p}}{\partial x} = \frac{\partial \bar{p}^*}{\partial x} + \frac{\partial \bar{p}'}{\partial x} \quad (67)$$

At this point it may again be mentioned that a good approximation to the axial pressure gradient already exists in the form of the immediately upstream value. Approximations to the axial velocities can be obtained from the equation:

$$u_P^* = A_N u_N^* + A_S u_S^* + A_E u_E^* + A_W u_W^* + B_P + D^u (\partial \bar{p}/\partial x)^* \quad (68)$$

The mass flow rate due to this approximate velocity can be calculated as,

$$\dot{m}^* = \sum \rho u^* \Delta y \Delta z \quad ,$$

while the true mass flow rate should be the one present at the duct inlet,

$$\dot{m} = \sum \rho U_o \Delta y \Delta z \quad . \quad (69)$$

As before, the axial velocity correction equation can be obtained as,

$$u_p = u_p^* + D^u (\partial \bar{p} / \partial x)^* \quad . \quad (70)$$

To obtain the transverse pressure correction equation, the velocity corrections were substituted into the local continuity equation. Here the axial velocity correction eq. (70) is substituted into the total continuity eq. (69) to give:

$$\dot{m} = \sum \left(u_p^* + D^u \left(\frac{\partial \bar{p}}{\partial x} \right)^* \right) \rho \Delta y \Delta z \quad ,$$

which can be written as,

$$\left(\frac{\partial \bar{p}}{\partial x} \right)^* = \frac{\dot{m} - \sum u_p^* \rho \Delta y \Delta z}{\sum D^u \rho \Delta y \Delta z} \quad . \quad (71)$$

By this means, the axial pressure correction can be obtained. It should be pointed out that there is only one value of $(\partial \bar{p} / \partial x)^*$ per axial station as $(\partial \bar{p} / \partial x)$ is treated as a constant across the cross section, while for the transverse directions there is a different pressure correction value for each point. Thus, the u^* values obtained by using a guessed pressure gradient $(\partial \bar{p} / \partial x)^*$ can be corrected by the use of eqs. (70) and (71). This must be done before the transverse velocities are

computed. Once all three velocity components have been obtained, the induced field equations and energy equation can be solved without undue difficulty.

Solution of the Finite Difference Equations

All the relevant equations have been shown to be expressible in the form of the general eq. (56). This equation represents a pentadiagonal system. Two sweeps of a tridiagonal matrix algorithm (TDMA) are used to solve the system. The first sweep is in the y direction, followed by the second in the z direction.

Equation (56) is,

$$\Psi_P = A_N \Psi_N + A_S \Psi_S + A_E \Psi_E + A_W \Psi_W + B_P$$

or,

$$\Psi_j = \chi_j \Psi_{j+1} + \beta_j \Psi_{j-1} + \epsilon_j \quad (72)$$

where,

$$\epsilon_j = (A_E \Psi_E + A_W \Psi_W + B_P)_U,$$

$$\chi_j = A_N, \quad \beta_j = A_S$$

and j is an index that increases in the y direction, i.e. Ψ_N is Ψ_{j+1} and Ψ_S is Ψ_{j-1} when Ψ_P is Ψ_j .

Equation (72) represents the y direction sweep. It should be observed that the values of Ψ used in the ϵ_j term are the upstream values.

More will be said about this later. For eq. (72), Ψ_1 and Ψ_N are known boundary values while Ψ_2 through Ψ_{N-1} have to be calculated. Consider the expansions of eq. (72) for the first few values of j :

$$\Psi_3 = \chi_3 \Psi_4 + \beta_3 \Psi_2 + \epsilon_3$$

$$\Psi_4 = \chi_4 \Psi_5 + \beta_4 (\chi_3 \Psi_4 + \beta_3 \Psi_2 + \epsilon_3) + \epsilon_4$$

or,

$$\Psi_4 = \frac{\chi_4 \Psi_5 + \beta_4 (\beta_3 \Psi_2 + \epsilon_3) + \epsilon_4}{1 - \beta_4 \chi_3}$$

In general, these expressions can be expressed as,

$$\Psi_j = \chi'_j \Psi_{j+1} + \beta'_j, \quad j = 2, 3, \dots, N-1 \quad (73)$$

where,

$$\chi'_j = \frac{\chi_j}{1 - \beta_j \chi'_{j-1}}, \quad \beta'_j = \frac{\beta_j \beta'_{j-1} + \epsilon_j}{1 - \beta_j \chi'_{j-1}}$$

and,

$$\chi'_2 = \chi_2, \quad \beta'_2 = \beta_2 \Psi_1 + \epsilon_2.$$

If the known boundary value, Ψ_N , is started with, eq. (73) can be used to obtain all Ψ 's between $j = 2$, and $j = N-1$. The boundary value Ψ_1 is used in the calculation of Ψ_2 , as a part of β'_2 . This essentially completes the y direction sweep.

The z direction sweep is represented as,

$$\psi_P^{II} = A_E \psi_E^{II} + A_W \psi_W^{II} + A_N \psi_N^I + A_S \psi_S^I + B_P \quad (74)$$

where the I's refer to values obtained in the y-sweep, while the II's refer to those obtained in the z-sweep. Equation (74) can be rewritten as,

$$\psi_k = \phi_k \psi_{k+1} + \Omega_k \psi_{k-1} + \zeta_k \quad (75)$$

where,

$$\zeta_k = A_N \psi_N^I + A_S \psi_S^I + B_P$$

and,

$$\phi_k = A_E, \quad \Omega_k = A_W.$$

The index k is the z direction equivalent of j, and it should be noted that ζ_k is composed of the results from the preceeding y-sweep. Equation (75) can be written as,

$$\psi_k = \phi'_k \psi_{k-1} + \Omega'_k, \quad k = 2, 3, \dots, N-1 \quad (76)$$

where,

$$\phi'_k = \frac{\phi_k}{1 - \Omega_k \phi'_{k-1}}, \quad \Omega'_k = \frac{\Omega_k \Omega'_{k-1} + \zeta_k}{1 - \Omega_k \Omega'_{k-1}}$$

and,

$$\phi'_2 = \phi_2, \quad \Omega'_2 = \Omega_2 \psi_1 + \zeta_2.$$

The mechanics of the z-sweep are essentially the same as those of the y-sweep. It was found necessary to repeat this double sweep procedure about N times when $N \times N$ was the size of the mesh.

While it is true that the above procedure does not give the exact solution to the finite difference equations, its use is advocated by a number of reasons. Firstly, it is inherently simple. Secondly, it can be easily seen that when A_N and A_S are much smaller or much larger in magnitude than A_E and A_W the above procedure does give a nearly correct solution. Thirdly, when the forward step Δx is small, the equation is dominated by B_P which contains the upstream value $\psi_{P,U}$, and the use of slightly approximate values of ψ_N , ψ_S , ψ_E , ψ_W introduces only a very small error in ψ_P .

Numerical procedures for solving the partial differential equations in fluid dynamics tend to be iterative for three main reasons. Firstly, the equations are non-linear. Secondly, the pressure renders the continuity and momentum equations strongly linked, and thirdly, a direct solution of the implicit finite difference equations, even when they are linear, is time consuming. The procedure that has been used has been made essentially non-iterative by: (i) the calculation of the coefficients in the finite difference equations from values at the upstream station, thus forcing the equations to be linear; (ii) the use of approximate forms of the momentum eqs. (63), (64) and (70); and (iii) the solution of the finite difference equations by two sweeps of the TDMA. It is true that these three tricks introduce some errors into the solution compared to a solution produced by a fully iterative procedure.

But, first, these errors are of the same kind as the truncation errors in any finite difference procedure; and second, it is possible at the end of each forward step to calculate the error in satisfying each conservation equation, and then to make a corresponding correction at the next step downstream. Thus, by leaving errors which can be detected, and if necessary, corrected, the benefits of a non-iterative procedure are enjoyed without serious penalty. A further bonus of this method is the fact that the solution is available at a large number of axial stations. For an iterative procedure, the number of axial stations would have been much less as it would have been possible to take larger forward steps, and in fact this would have been made necessary due to the increased computer time needed to perform the iterations at each step.

Boundary Conditions

The continuous forms of the boundary conditions were given in the previous chapter. Translating them into numerical forms is a fairly simple procedure.

Velocity

The no-slip boundary condition is enforced at all the walls. The u velocity points lie on the actual boundary and are simply set to zero. Referring to Fig. 5 it can be seen that transverse velocity points also lie on the walls that are normal to the respective velocity component. However, for parallel walls, adjacent transverse velocity points straddle the boundary, and so the no-slip condition has to be enforced in between the two points. This is achieved by simply imaging the velocities, i.e. making the point external to the wall the negative of the one internal

to the wall. The average of the two will then add up to zero on the wall itself. Thus, the velocity boundary conditions for the axial velocity u , and the transverse velocities v and w become,

$$u_{\text{wall}} = 0 \quad (77)$$

$$v_{\text{wall}} = 0 \quad (\text{normal walls}) \quad (78)$$

$$v_{\text{ext}} = -v_{\text{int}} \quad (\text{parallel walls}) \quad (79)$$

$$w_{\text{wall}} = 0 \quad (\text{normal walls}) \quad (80)$$

$$w_{\text{ext}} = -w_{\text{int}} \quad (\text{parallel walls}) \quad (81)$$

Induction

The dimensionless form of the boundary condition, eq. (44), is applied at all walls for the axial field and at parallel walls for the transverse fields. At normal walls the transverse field components are always set to zero. For the axial H_x field, the condition is,

$$H_{x_{\text{wall}}} = \left(H_{x_{\text{wall}-1}} \right) / \left(1 + \Delta n / C \right) \quad (82)$$

where Δn is equal to Δy or Δz depending on which is the normal direction. For the transverse H_y field, the condition is,

$$H_{y_{\text{wall}}} = \left\{ H_{y_{\text{wall}-1}} \right\} / \left\{ 1 + \Delta z / C \right\} \quad (83)$$

for parallel walls, and

$$H_{y_{\text{wall}}} = 0 \quad (84)$$

for normal walls. For the transverse H_z field, the condition is,

$$H_{z_{wall}} = \left\{ H_{z_{wall-1}} \right\} \left\{ 1 + \Delta y / C \right\} \quad (85)$$

for parallel walls, and

$$H_{z_{wall}} = 0 \quad (86)$$

for normal walls.

Temperature

Temperature boundary conditions for the energy equation are specified by eq. (46) for the constant wall heat flux case. For the constant wall temperature case, the non-dimensional wall temperature is simply set to 1 or 0, depending on whether heat is being added or removed by the walls. In summary, these conditions are,

$$\theta_{wall} = 0 \quad (\text{heat removal by walls}) \quad (87)$$

$$\theta_{wall} = 1 \quad (\text{heat addition by walls}) \quad (88)$$

for the constant wall temperature case, and

$$\theta_{wall} = \theta_{wall-1} + \Delta n \quad (89)$$

for the constant wall heat flux case, where Δn is equal to either Δy or Δz depending on which is the normal direction.

Pressure Correction Equation

Since all velocities are zero at the walls, the velocity correction eqs. (63) and (64) indicate that the normal gradient of the pressure correction must be zero at the wall. Thus,

$$p'_{\text{wall}} = p'_{\text{wall}-1} \quad (90)$$

is the boundary condition.

The above boundary conditions, eqs. (77) to (90), are of a simple form, however, these boundary treatments can always be improved by such techniques as the incorporation of slip values at the wall³⁷ or by the use of higher order property variations (e.g. quadratic instead of linear). This sort of experimentation is deemed beyond the scope of this work.

Order of Computation

At each axial step the following procedure is followed:

- (1) The coefficient matrix for the u momentum equation is obtained using upstream properties.
- (2) The u momentum equation is solved using a guessed (upstream) axial pressure gradient.
- (3) The axial pressure gradient is corrected by forcing conservation of integral mass flow in the duct.
- (4) By using the axial pressure gradient correction, the axial velocities are corrected.
- (5) The coefficient matrix for the v momentum equation is obtained using upstream properties.

- (6) Solution to the v momentum equation is obtained using a guessed (upstream) transverse pressure field.
- (7) The coefficient matrix for the w momentum equation is obtained using upstream properties.
- (8) Solution to the w momentum equation is obtained using a guessed (upstream) transverse pressure field.
- (9) The coefficient matrix for the transverse pressure correction equation is obtained using current (downstream) velocity values.
- (10) The transverse pressure correction equation is solved.
- (11) The coefficient matrix for the axial H_x induction is obtained based on upstream properties.
- (12) The axial H_x induction equation is solved.
- (13) The coefficient matrix for the transverse H_y induction equation is obtained based on upstream properties.
- (14) The transverse H_y induction equation is solved.
- (15) The coefficient matrix for the transverse H_z induction equation is obtained based on upstream properties.
- (16) The transverse H_z induction equation is solved.
- (17) The coefficient matrix for the energy equation is obtained based on upstream properties.
- (18) The energy equation is solved for the temperatures.
- (19) The above steps are repeated for each axial position.

The above 19 steps specify the basic computational procedure. Boundary conditions must be applied in appropriate places.

CHAPTER IV

PROGRAM CALIBRATION

Whenever a computer program is to be used to simulate a physical phenomenon, it is of utmost importance that a set of preliminary runs, modeling problems for which results are available, be made. That is the purpose of this chapter on program calibration.

The Purely Hydrodynamic Velocity Entry Problem

The purely hydrodynamic, i.e. no MHD effects, velocity entry problem was run for a Reynolds number of 100, and the total duct length covered was equal to 10 duct widths. Asymptotically increasing accuracy was observed as the transverse mesh size was decreased. For a mesh of 20×20 in the transverse plane, the axial velocity and pressure coefficient developments were deemed close enough to the experimental results of references 6 and 7, so as to make further mesh refinement unnecessary. These comparisons are shown in Figs. 10 and 11. It should be noted that the pressure coefficient of Fig. 11 is simply $(\bar{p}_{in} - \bar{p}) / (\rho U_0^2)$, i.e. the total non-dimensional axial pressure difference between any axial location and the inlet. In the axial direction a little experimentation led to the choice of 216 axial steps to represent the 10 duct widths. The axial step Δx was 0.01 for the first twenty steps, and 0.05, the same as the transverse mesh spacing, for the remaining 196 steps. A small axial step right near the entrance was chosen because of the rather rapid changes in all the quantities over small axial distances in this region.

Axial variation of the results can be made universal by defining an axial parameter $L = (x/D)/Re$. The axial pressure gradient shown in Fig. 12 begins with a little peak and then decreases to a fully developed value of $Re(\partial p/\partial x)$ equal to 28.81. This compares favorably with the analytical value of 28.12 quoted by Miller.³⁸ For theoretical slug flow, i.e. uniform velocity throughout the duct interior and zero velocity on the walls, the driving axial pressure gradient must be infinite because of the infinite shear force in the infinitely thin boundary layer. However, since the numerical approximations involve a mesh of finite size, the thickness of this infinitely thin boundary layer immediately becomes finite, i.e., the mesh size adjacent to the wall. Thus, the maximum axial pressure gradient in the computation is dependent on the transverse mesh size. After the first few steps, however, the mesh spacing is sufficient to provide adequate resolution of the problem, and the axial pressure gradient behaves as it should. The little peak at the beginning represents the region of insufficient resolution. It may be mentioned at this point that these inlet conditions are singular. However, parabolic equations have the useful characteristic of recovering from the effects of a singularity once the integration has proceeded a few steps beyond the singular region.

Figure 13(a) qualitatively shows the development process. If an entry length is defined as the distance at which the center-point axial velocity achieves 95% of its fully developed value, then this length in terms of L is about 0.04. Velocity contours and the corresponding velocity surface for the fully developed condition are shown by Figs. 13(b) and 13(c), respectively. Quantitative information about the axial

velocity development across the center plane can be obtained from Fig. 14(a). Some more measurements of Goldstein and Kreid for $L = 0.1$, which for $Re = 100$ means 10 duct widths, are compared with the developed profile in Fig. 14(a). Again, the agreement is excellent.

It is also noticable from Fig. 14(a) that the area under the velocity profile curve seems to increase as the value of L associated with that particular profile increases. This reflects the transference of mass from the sides of the duct towards the center as the profile develops. This transference is accomplished by the secondary flow that exists in the developing region. Vectors representing this inward flow are plotted in Fig. 14(b). The transverse v and w profiles that correspond to these vectors are displayed in Figs. 15(a) and (b). As the axial velocity develops, these transverse components asymptotically approach zero. This process can be portrayed as a surface along an axial plane, as shown in Fig. 15(c). It should be noted that the axial scale in this figure is not linear, but piece-wise linear.

It is possible to conclude that the program is successful in predicting three-dimensional hydrodynamic entry flow.

The Purely Hydrodynamic Thermal Entry Problem

The energy equation, in the present formulation, is dependent on the momentum equations, but not vice-versa, and so it is possible to obtain different temperature solutions corresponding to the previous velocity solution. These different solutions occur when various temperature boundary conditions and internal heat sources are specified. Of the many possible combinations of temperature boundary conditions and heat

sources, three will be considered in this section. These three cases are the constant wall temperature boundary condition, the constant wall heat flux boundary condition, and the latter case with uniform internal heat generation. Since there is a definite scarcity in the literature of complete investigations of the simultaneously developing velocity and temperature fields in the entry region of square ducts, rather extensive temperature results are presented in this section.

Constant Wall Temperature Case

Figures 16 through 21 show the results for this case. The fluid enters the duct with a uniform dimensionless temperature of 1. (Recall that for this case $\theta = (T - T_w) / (T_i - T_w)$). The duct walls are kept at a constant temperature of zero. This corresponds to heat removal from the fluid until the wall and interior temperatures all become zero.

Figure 16 shows the bulk temperature and Nusselt number developments for Peclet numbers of 10, 100, 1000 and 10,000. Since the Reynolds number is kept fixed at 100, these Peclet numbers correspond to Prandtl numbers of 0.1, 1.0, 10.0 and 100.0. The bulk temperature is seen to approach zero most quickly for the lower Prandtl numbers. A few points taken from the computations of Ghia et al.¹¹ are also plotted in Fig. 16 for comparison. Good agreement is observed. The Nusselt number plotted in Fig. 16 is simply the mean of all the local Nusselt numbers, which directly relate to the local temperature gradients, around the duct periphery at a particular axial position. The fully developed Nusselt number predicted by the present computation, for the constant wall temperature boundary condition, is 2.96. This compares very well with the 2.98 computed analytically by Kays.³⁹ If the approach of the Nusselt

number to the fully developed value is used as the criterion for judging the thermal development, then it is seen that as expected the lower the Prandtl number the swifter the development. It must be kept in mind that these results are for simultaneously developing temperature and velocity, and not for the Graetz type problem which refers to thermal development alone.

Temperature contours and surfaces at $L = 0.1$ are shown in Figs. 17 and 18 for different Peclet (Prandtl) numbers. For a Peclet number of 100 the temperature surface is well advanced towards a uniform value of zero, while at the other extreme, the surface with a Peclet number of 10,000 is still near the uniform entry condition of one. Similar conclusions can be reached from Fig. 19 which qualitatively displays the center-line temperature development for different Peclet numbers. Development of the Nusselt number is best portrayed as a surface along the wall. From Figs. 20 and 21 it can be seen that the initial local Nusselt numbers are very high compared to the fully developed values. As was the case with the axial pressure gradient, the initial local Nusselt number magnitudes are fixed by the mesh size at the entrance. For the constant wall temperature boundary condition, the heat transfer is always zero at the duct corners, and maximum at the wall centers. This too can be observed from Figs. 20 and 21 by referring to the variations in the transverse y direction. Again it is obvious that the lower the Prandtl number, the quicker the development.

Constant Wall Heat Flux Case

The non-dimensional temperature, θ , is now defined as $(T-T_i)/(q_w'' D/k)$, where q_w'' is the constant wall heat flux. The situation dealt

with corresponds to heating of the fluid by the walls, and results for this case are presented in Figs. 22 through 34.

A linear increase in the bulk temperature for this case is seen in Fig. 22. This is expected since the heat input per unit axial length is fixed once the constant wall heat flux is specified. However, the heat transferred away from the wall is dependent on the Prandtl number, and so the slope of the bulk temperature rise is strongly dependent on this parameter. The higher the Prandtl number, the slower the bulk temperature rise.

Figure 23(a) shows the mean Nusselt number development. The fully developed value of 3.55 shows a deviation of about 2% from the value of 3.63 quoted for this case by Kays.³⁹ Since there is always more error associated in the numerical modeling of Neumann boundary conditions than with Dirichlet conditions, this discrepancy is understandable. A quantity of importance for the wall heat flux case is the wall temperature, since the usual purpose of the fluid flow is to cool the wall. Center-line wall temperature development is plotted in Fig. 23(b). These curves do not start from zero, as the wall heat flux, which is present even at the entrance, numerically forces the walls to have a little higher temperature than the interior fluid which is at zero.

Temperature contours at $L = 0.1$ for different Peclet numbers are shown in Fig. 24. As before, those for $Pe = 100$ are much more developed than those for $Pe = 10,000$. If these contours are compared with the ones for the constant wall temperature case, it is seen that the current contours are rounder. This is a direct consequence of the wall temperature no longer being uniform around the periphery. Qualitative pictures

of the center-line and wall temperature developments are presented in Figs. 25 through 28. It should be noted in these figures that the root of the arrow associated with each profile specifies the axial position at which the profile occurs. It is observed that the wall temperature is maximum at the corners. This is an obvious result of the fact that though the wall heat flux is constant around the periphery, the heat transfer to the fluid is minimum at the corners. Quantitative information about the center-line and wall temperature development for various Prandtl numbers is presented in Figs. 29 through 32. Nusselt number surfaces are plotted in Figs. 33 and 34. The local Nusselt number is maximum at the wall center and minimum (not zero) at the corner.

Constant Wall Heat Flux with Internal Heat Generation Case

Figures 35 through 39 represent this case. The internal heat generation is uniform throughout the duct. Recall that the internal heat source Q is made dimensionless by defining it as QD/q_w'' . An important quantity for this case is the wall temperature, θ_w , minus the bulk temperature, θ_b . The Nusselt number for the constant wall heat flux case is equal to $1/(\theta_w - \theta_b)$. Thus, even though the Nusselt number plotted in Fig. 35(a) loses its usual meaning, it still has relevance as the inverse of the above quantity. Figure 35(a) shows that this difference achieves a constant value which agrees with the parallel plate channel predictions of Ref. 40.

Observation of the temperature contours and surfaces of Figs. 36 and 37 suggests that the high temperature region at the corners extends a fair bit inwards. This stems directly from the fact that even though

the heat generation is constant throughout the duct, the heat transfer is poorest at the corners because the velocities there are low.

Figure 38 shows the axial and transverse variations of the Nusselt number $1/(\theta_w - \theta_b)$. Obviously $(\theta_w - \theta_b)$ is largest at the corners and smallest at the wall centers. Wall corner and wall center temperature developments for different values of Q and a constant value of the Peclet number are shown in Fig. 39.

It is possible to conclude from the results of the previous three cases that the program is accurately predicting solutions to the combined velocity and thermal entry problem.

Moving Wall Cases

Up until this point, all convective movements in the transverse directions have been small when compared to similar axial quantities. It is desirable to test the program under conditions where the lateral and axial fluxes are comparable. One such way of obtaining strong transverse flow is by allowing duct walls to move laterally. Physically, duct flow with one laterally moving wall is found in such devices as screw extruders, bearing lubricators, etc. In regions of fully developed flow, the cross-stream velocity and pressure fields are identical to those in steady two dimensional flow in a square cavity with a moving wall. The later problem has been analysed by Burggraf.⁴¹

Results for four moving wall cases are presented in Figs. 40 through 53. The first two cases, (a) and (b) in each figure, involved one moving wall with wall Reynold's numbers of 100 and 200, respectively. The Reynolds number of the main flow remained at 100. Thus, a wall

Reynolds number of 100 is brought about by a wall moving at the same velocity as the inlet flow. As can be seen from Figs. 40(a) and (b), this wall motion created a vortex which is centered towards a corner. The secondary velocity profiles that produce this swirling motion are shown in Figs. 41(a) and (b), and 42(a) and (b). The effect of this swirl on the fully developed axial velocity contours is shown in Figs. 43(a) and (b). Notice that the Vortex center and the maximum axial velocity point do not occur at the same position. The maximum axial velocity values of 2.03 and 1.98 for the wall Reynolds numbers of 100 and 200 respectively, are 5% larger than the similar values computed in Ref. 5. This discrepancy is not large enough to be significant, especially since qualitative agreement is excellent. Development of these skewed axial velocity distributions are displayed by Figs. 45(a) and (b), and 46(a) and (b).

Cases (c) and (d) are for two moving walls. These walls are situated opposite each other, and in case (c) move in the same direction, while in case (d) they move in opposing directions. These cases are more of academic than practical interest. Moving two walls in the same lateral direction produced two vortices, each of a nature similar to the ones in the previous case. Axial velocity profiles become double humped with the maximum value for each hump being 1.80. Moving two walls in opposite directions generated a strong central vortex. This was the only case where the vortex center and the maximum axial velocity point coincided. Results for the above two cases are shown in Figs. 40-47(c) and (d).

The temperature problem for the above moving wall cases had three walls thermally insulated and one wall at a fixed temperature of zero. The wall that had been moved in cases (a) and (b) was the one chosen to carry the fixed temperature. The effect of the fluid swirl on the temperature distribution is of interest here, and this is shown by the contours of Figs. 48(a) and (b), and Figs. 49(c) and (d). Results for the above temperature problem with all stationary walls are presented in Fig. 50 as a basis for comparison. Center-plane temperature developments for the moving wall cases are shown in Figs. 51 through 53. Streamwise vortex effects on the temperature are easily observable by comparison of Fig. 50(i), representing the stationary case with Figs. 52(a), 52(b), 53(c) and 53(d). The (a), (b), (c), and (d) are for the corresponding moving wall cases.

Based on all the results examined in this chapter, it is possible to conclude that the program functions will and should provide accurate predictions of the MHD phenomena which are discussed in the next chapter.

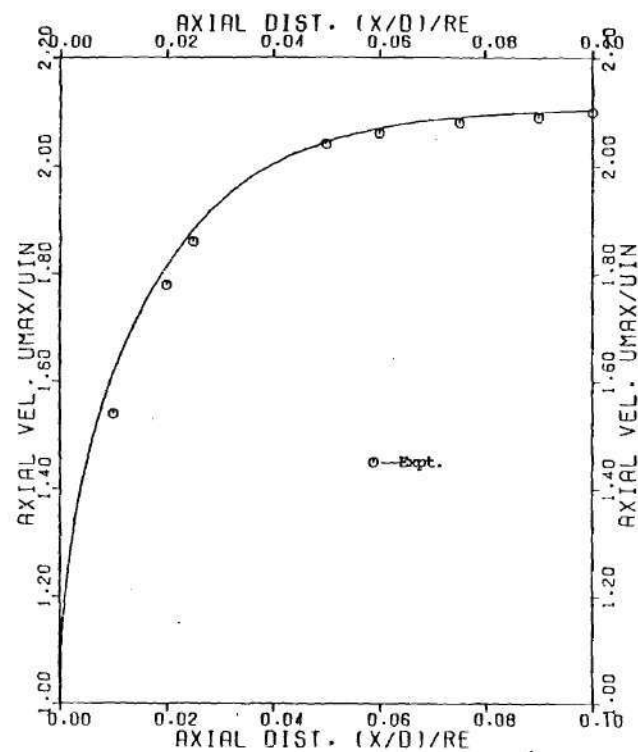


Figure 10.

Comparison of Center-point
Axial Velocity Development with
Experimental Results of Goldstein
and Kreid

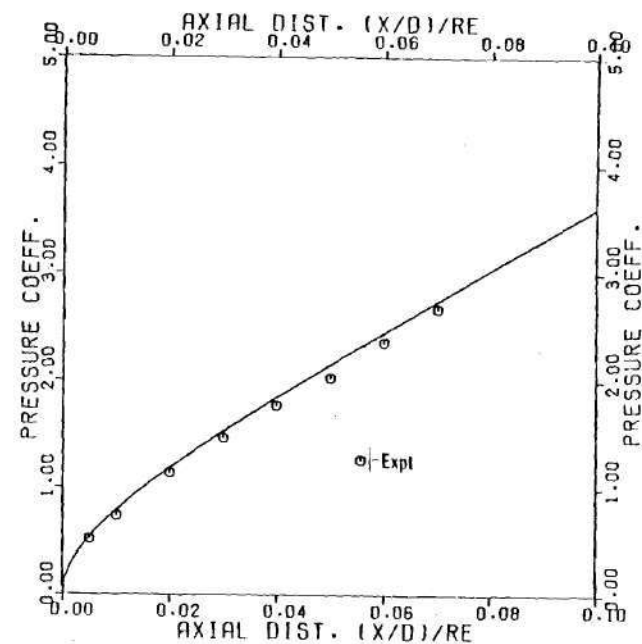


Figure 11.

Comparison of Axial Pressure
Coefficient Development with Experimental
Results of Beavers, Sparrow and Magnuson

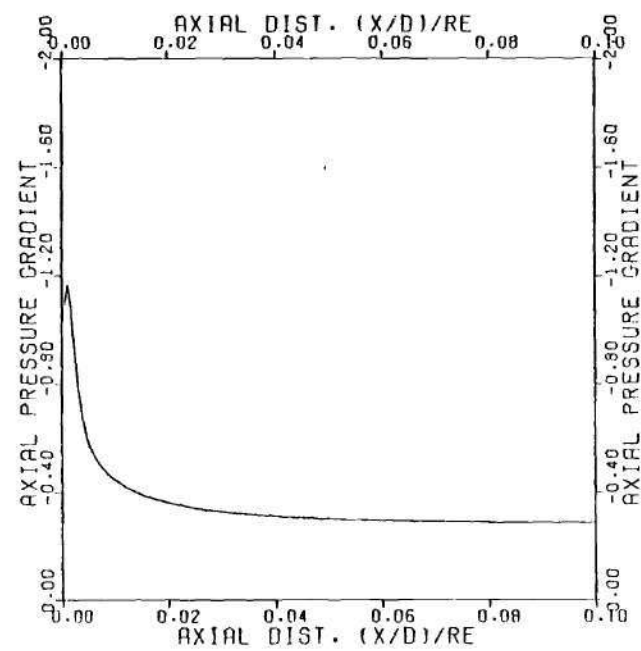


Figure 12. Axial Pressure Gradient Development

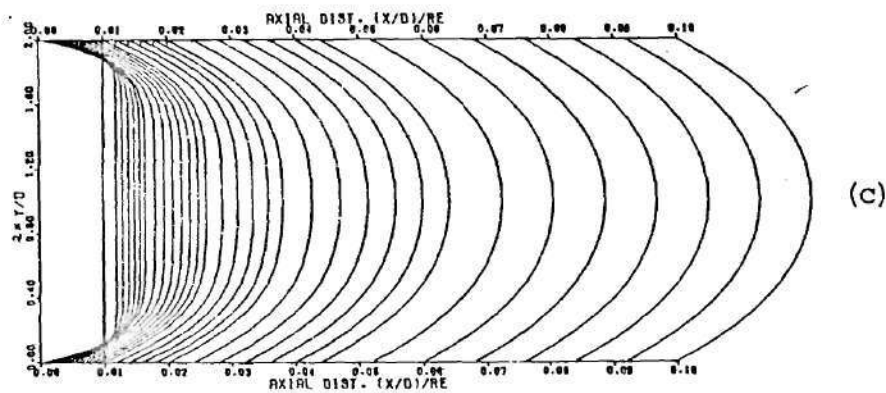
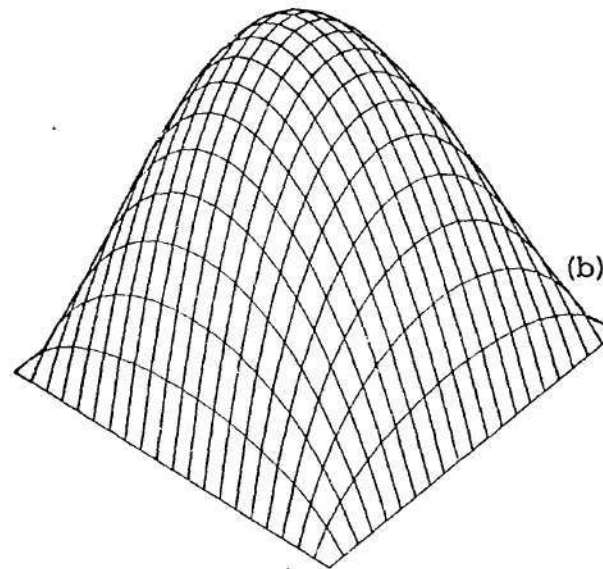
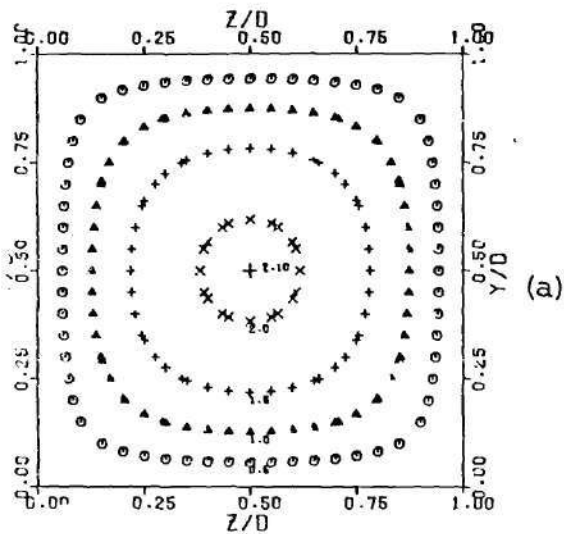


Figure 13. (a) Axial Velocity Contours at $L = 0.1$
 (b) Axial Velocity Surface at $L = 0.1$

(c) Axial Velocity Development
 $Re = 100$

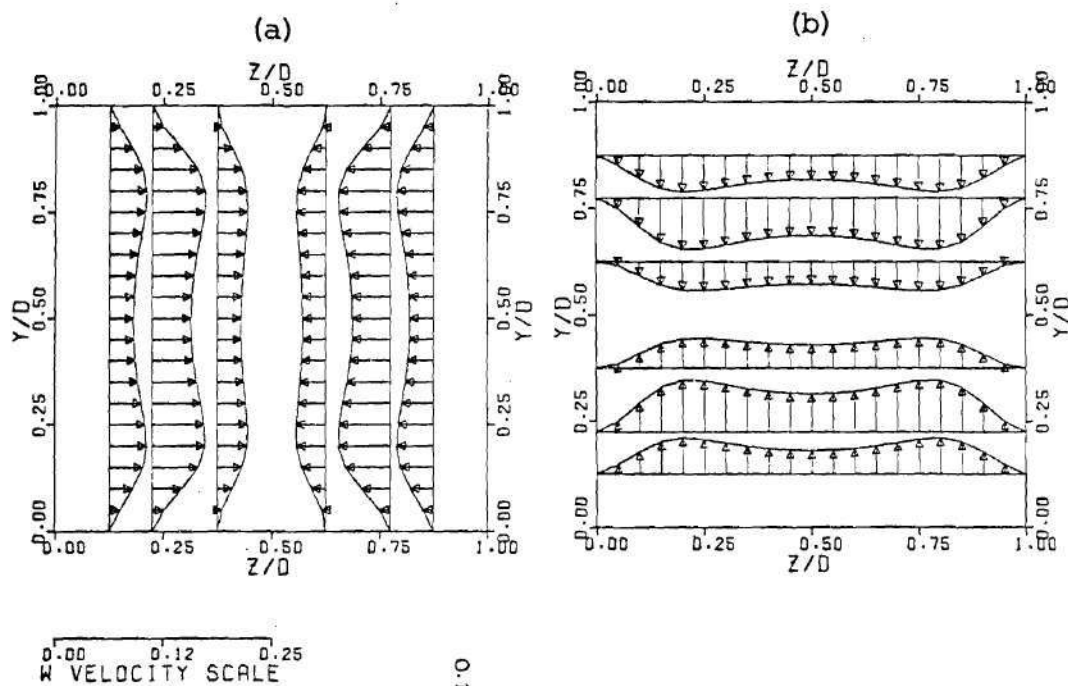
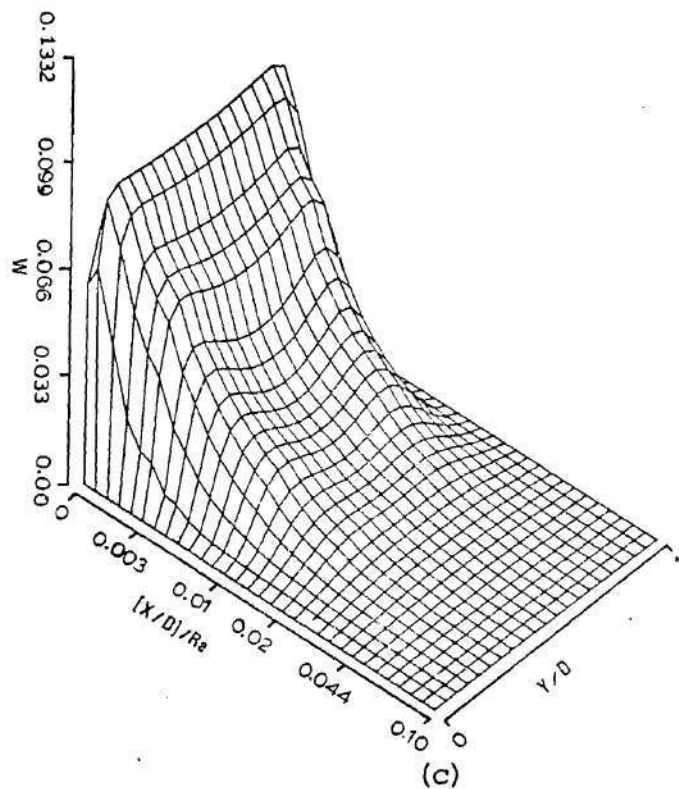


Figure 15.
 (a) w Velocity Profiles at $L=0.005$
 (b) v Velocity Profiles at $L=0.005$
 (c) w Velocity Surface along $Z/D=0.25$
 $Re = 100$



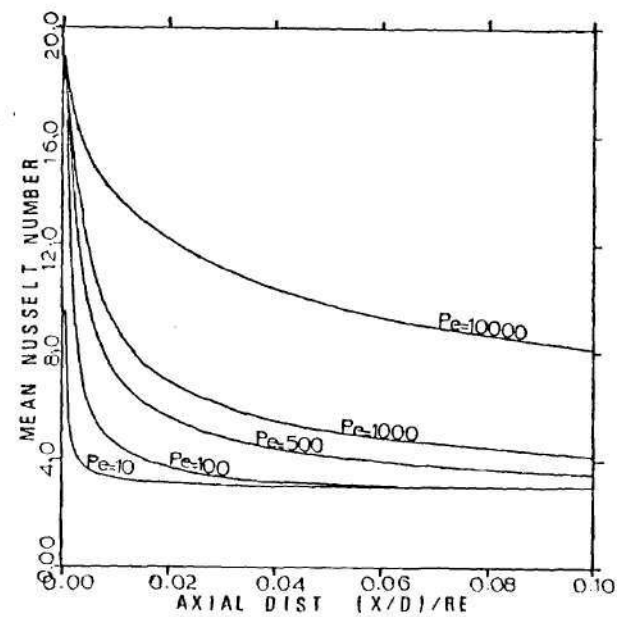
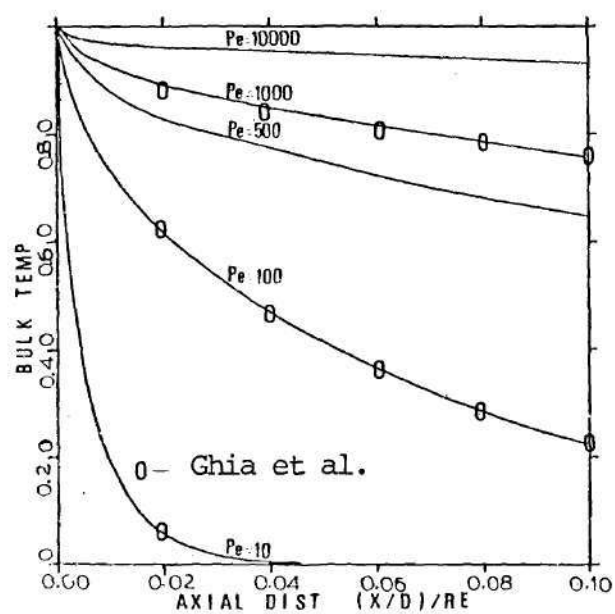


Figure 16. Bulk Temperature and Nusselt Number for Constant Wall Temperature Case

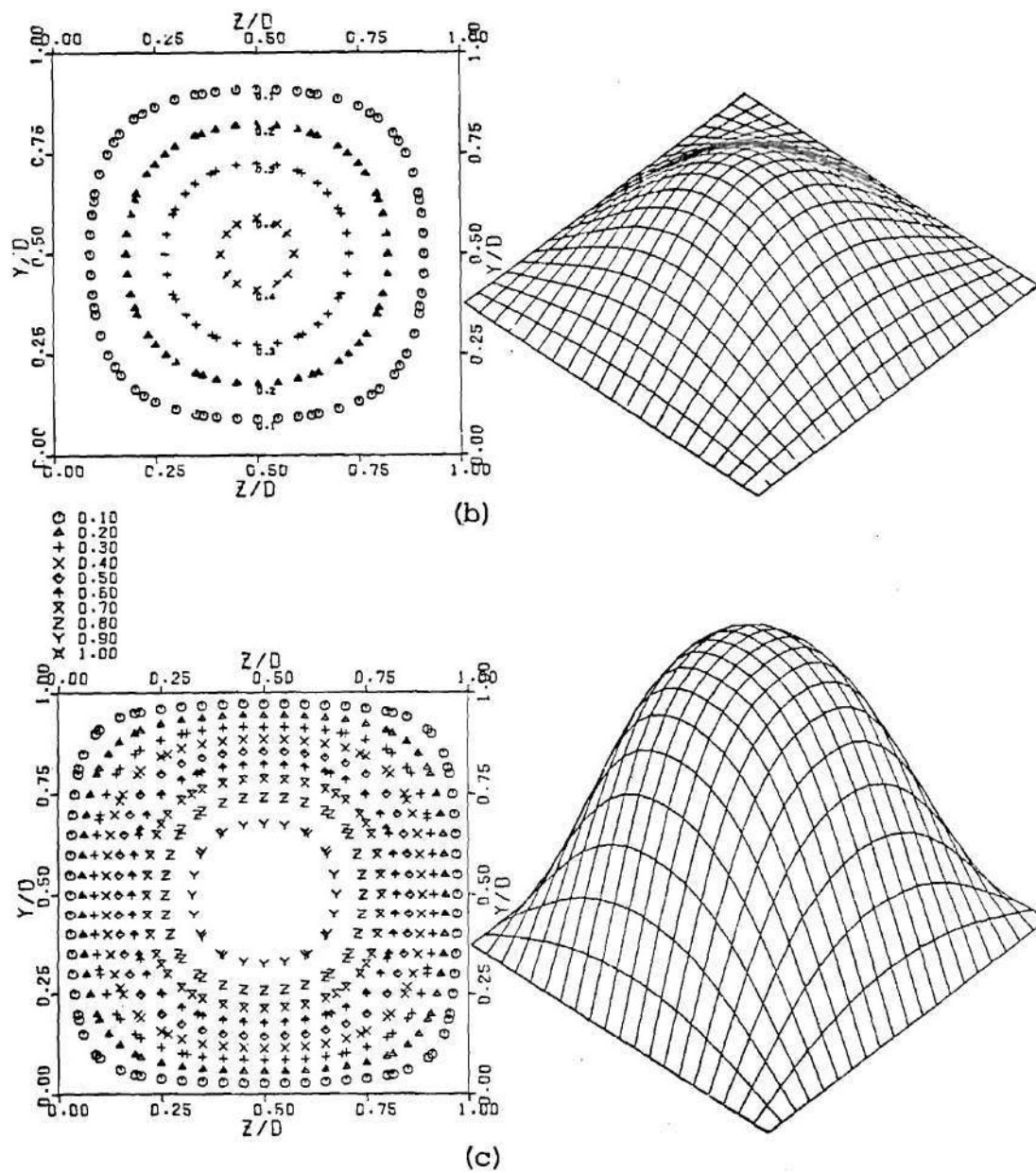


Figure 17. Temperature Contours and Surface at $L = 0.1$ for
 Constant Wall Temperature Case and (b) $Pe = 100$
 (c) $Pe = 500$

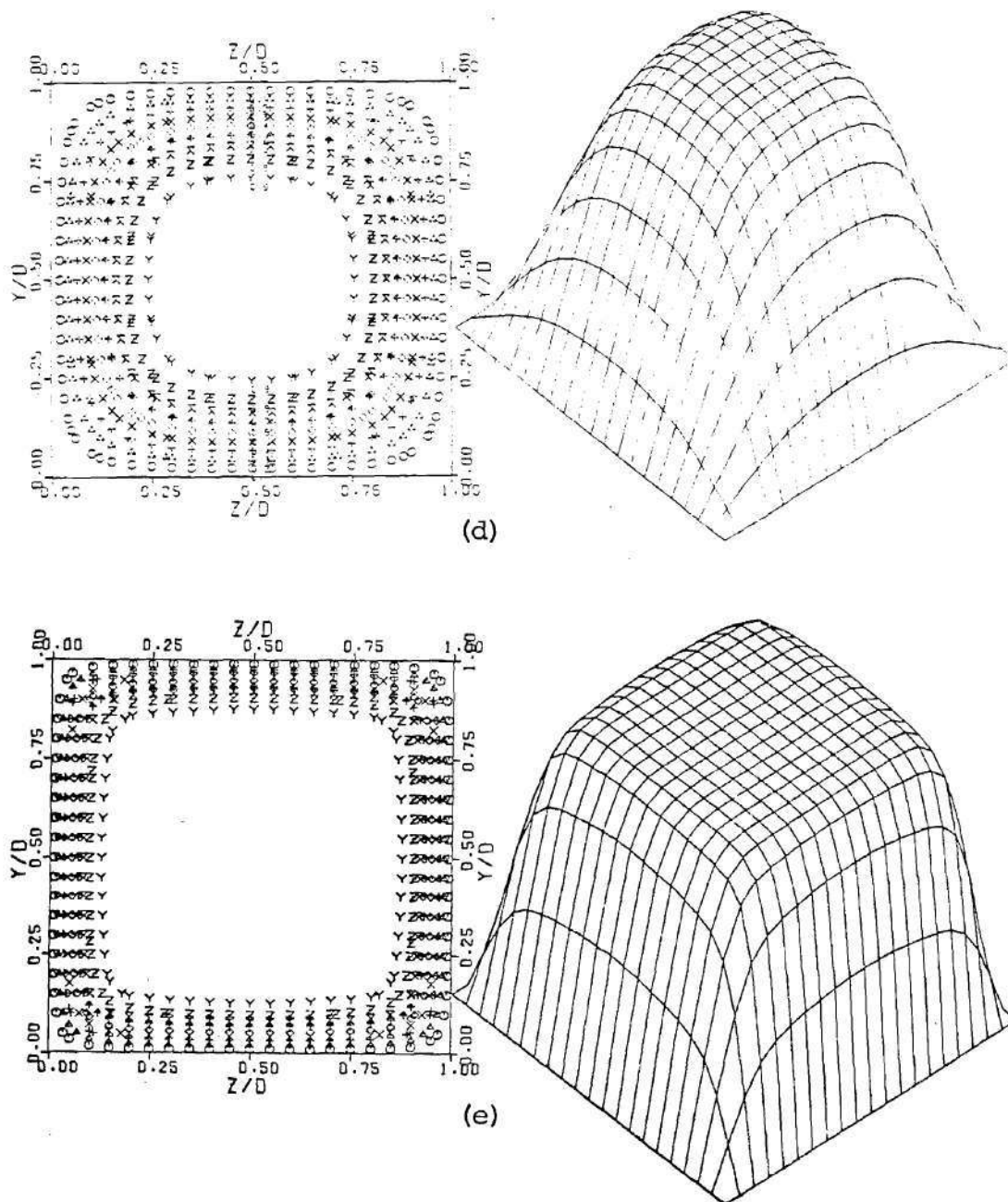


Figure 18. Temperature Contours and Surface at $L = 0.1$ for
 Constant Wall Temperature Case with (d) $Pe = 1000$
 (e) $Pe = 10000$

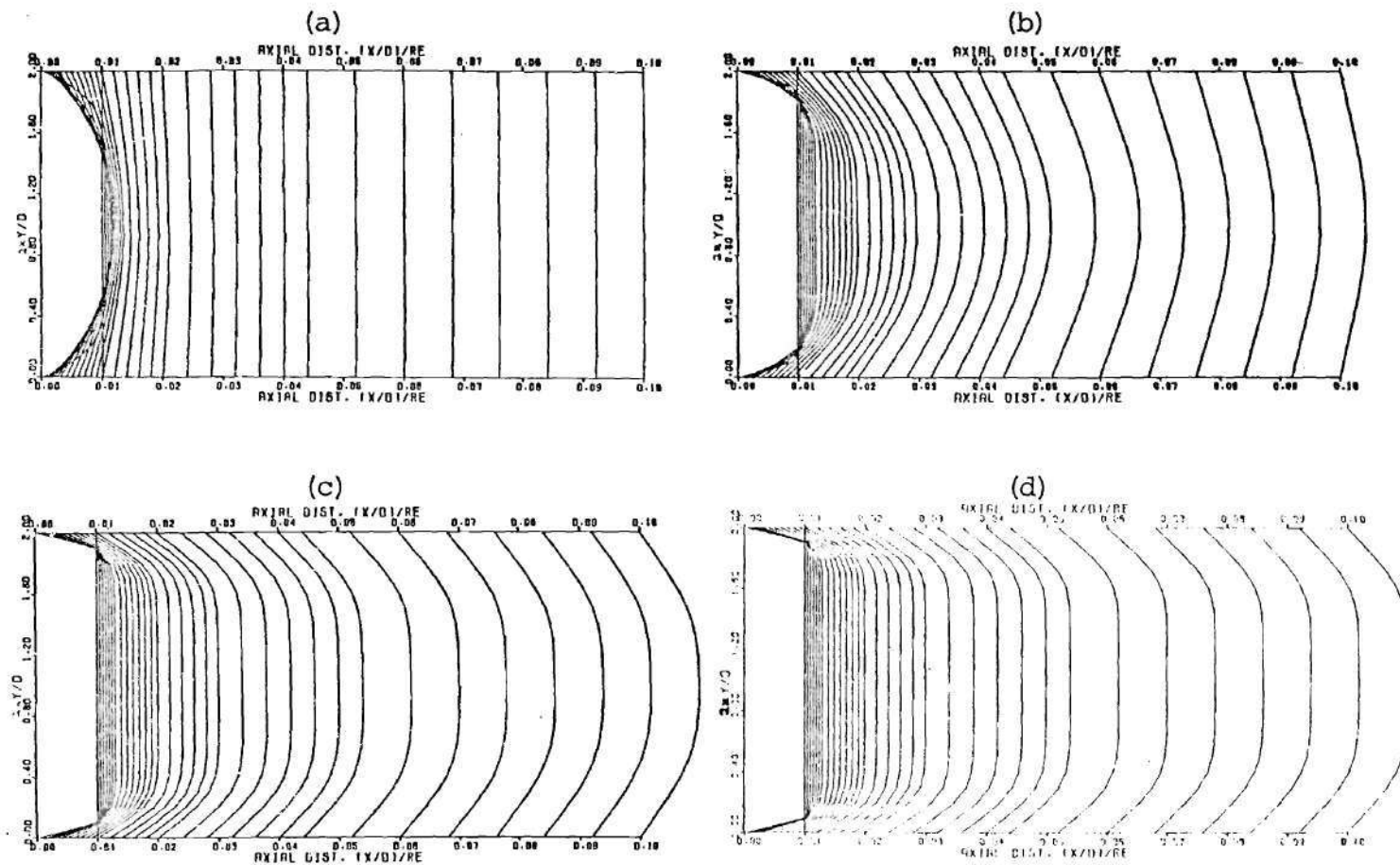


Figure 19. Center-line Temperature Development for Constant Wall Temperature Case and
 (a) $Pe = 10$, (b) $Pe = 100$, (c) $Pe = 500$, (d) $Pe = 1000$

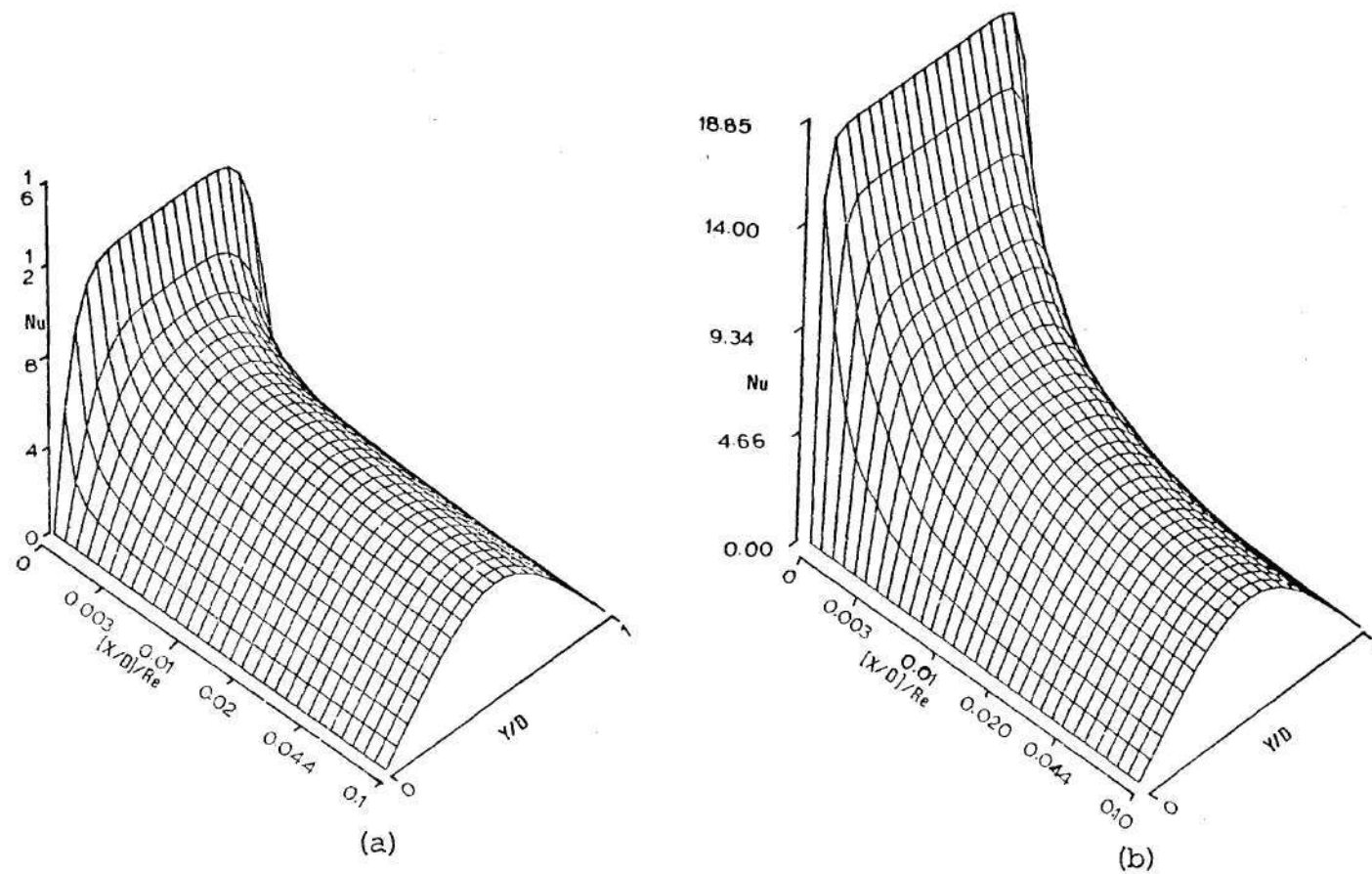


Figure 20. Nusselt Number Development Surfaces along a Wall for Constant Wall Temperature Case with (a) $Pe = 10$, (b) $Pe = 100$

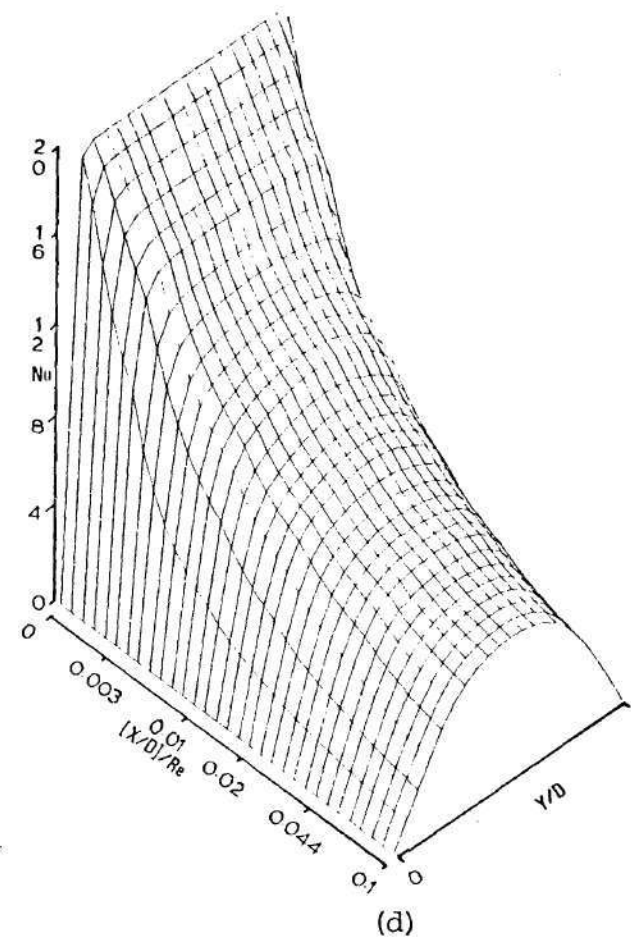
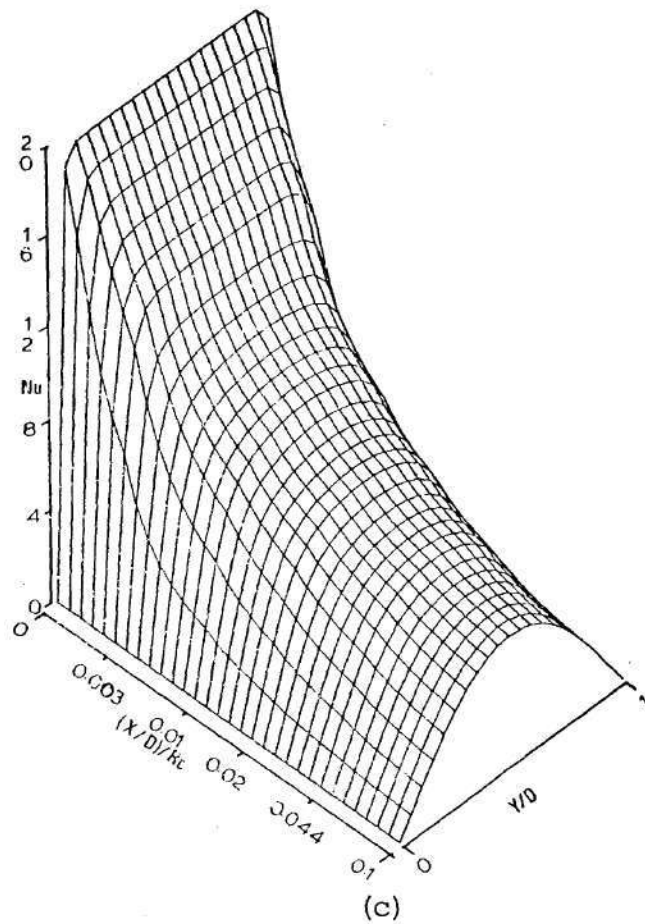


Figure 21. Nusselt Number Development Surfaces along a Wall for Constant Wall Temperature Case and with (c) $Pe = 500$, (d) $Pe = 1000$

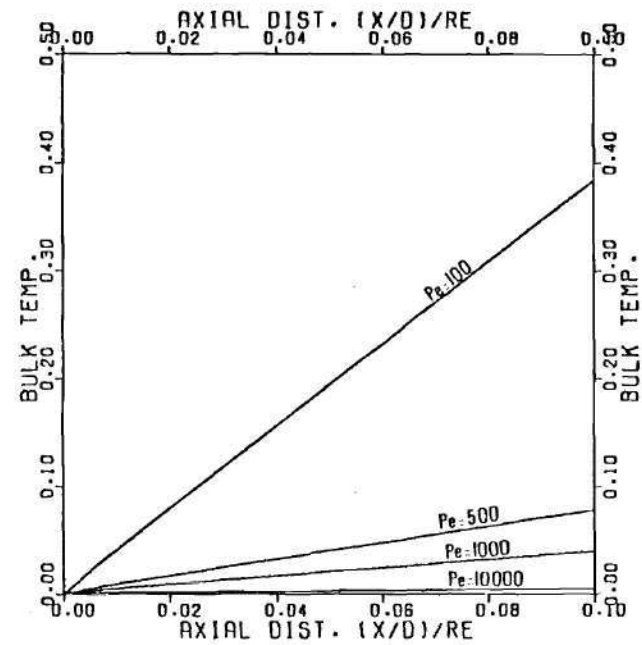
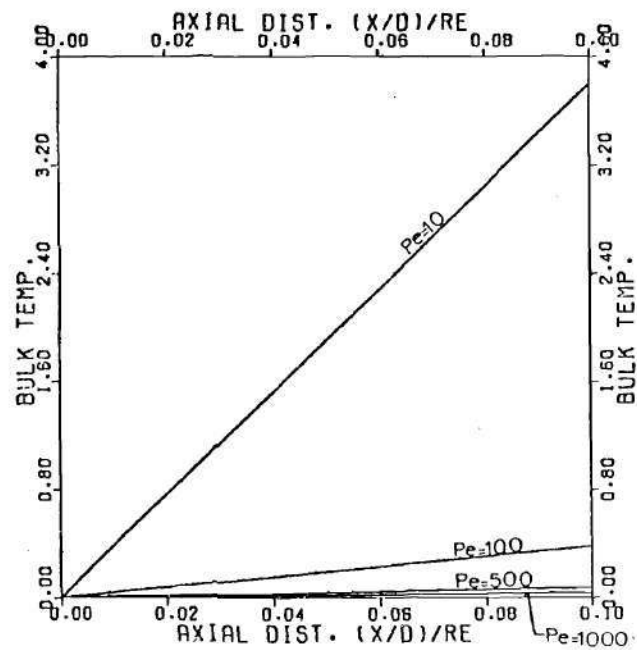
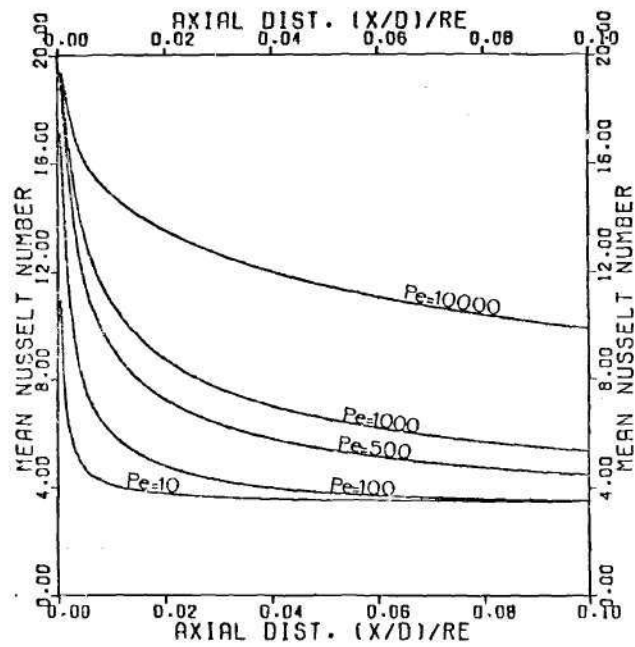
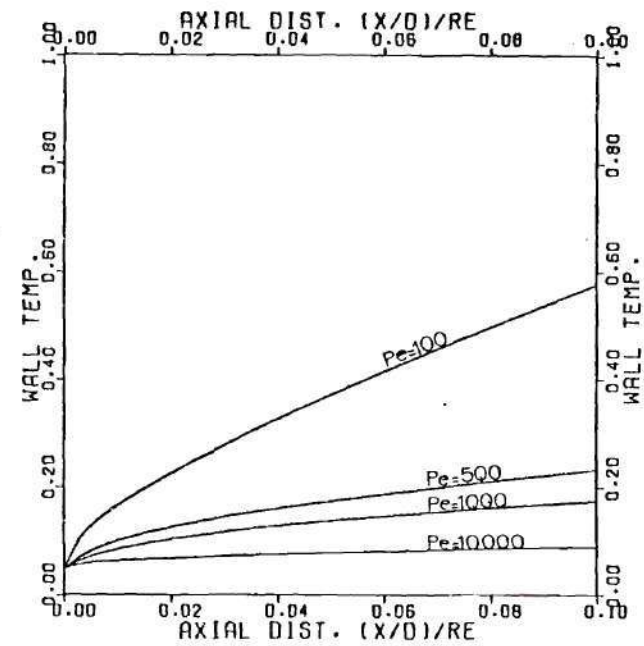


Figure 22. Bulk Temperatures for Constant Wall Heat Flux



(a)



(b)

Figure 23. (a) Nusselt Number for Constant Wall Heat Flux
(b) Center-line Wall Temperature for Constant Wall Heat Flux

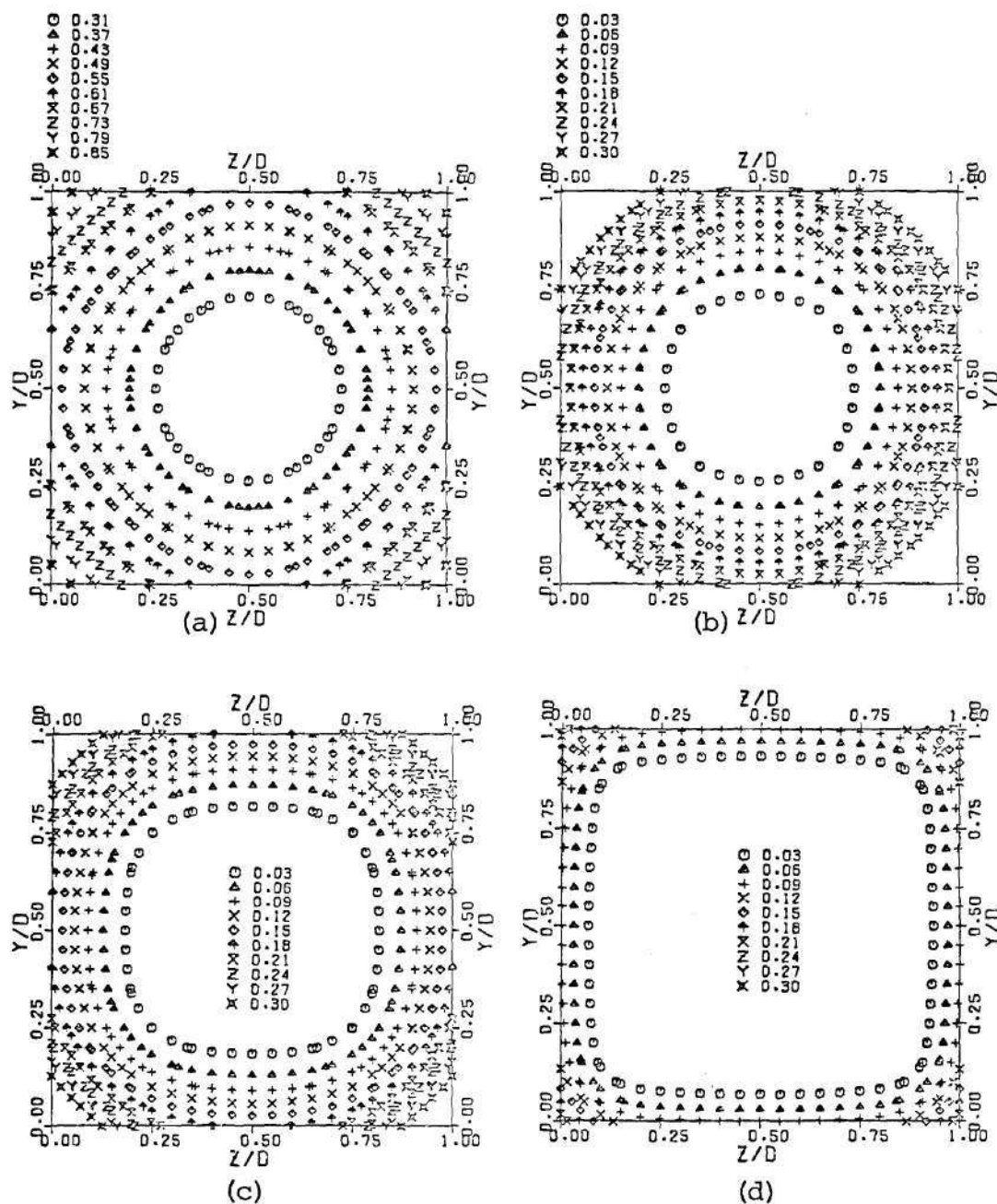


Figure 24. Temperature Contours at $L = 0.1$ for (a) $Pe = 100$,
(b) $Pe = 500$, (c) $Pe = 1000$, (d) $Pe = 10000$

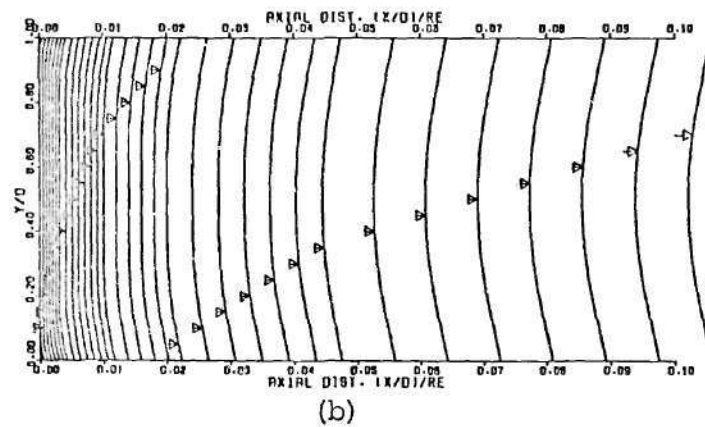
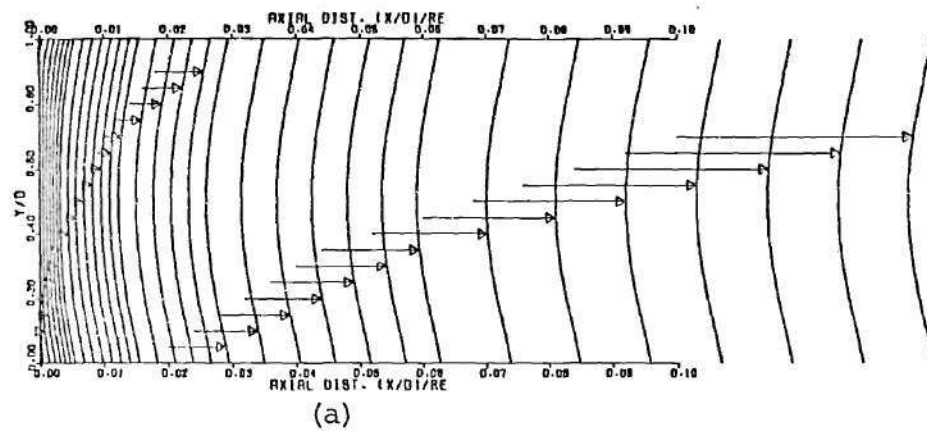


Figure 25. Center-plane Temperature Development with Constant Wall Heat Flux for (a) $Pe = 10$
(b) $Pe = 100$

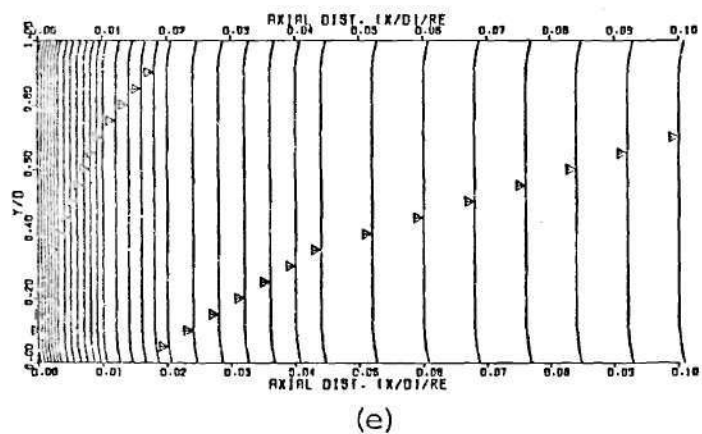
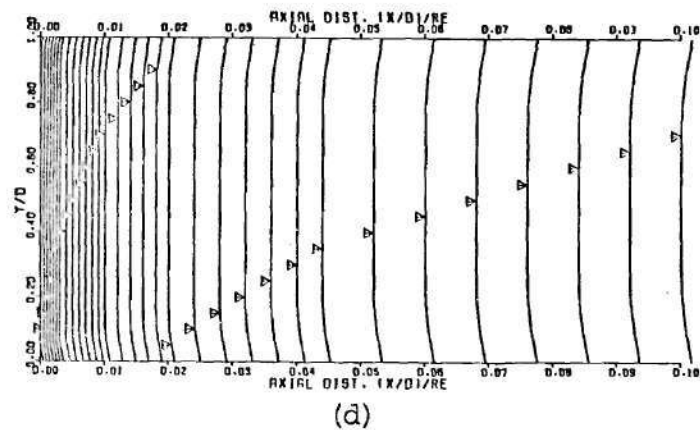
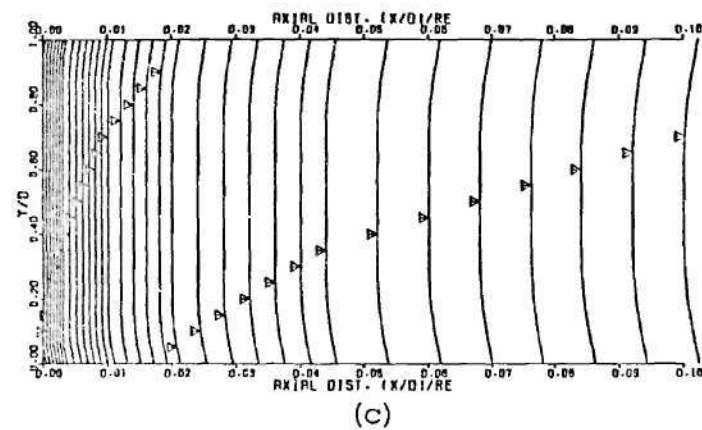


Figure 26. Center-plane Temperature Development with Constant Wall Heat Flux for (c) $Pe = 500$,
(d) $Pe = 1000$, (e) $Pe = 10000$

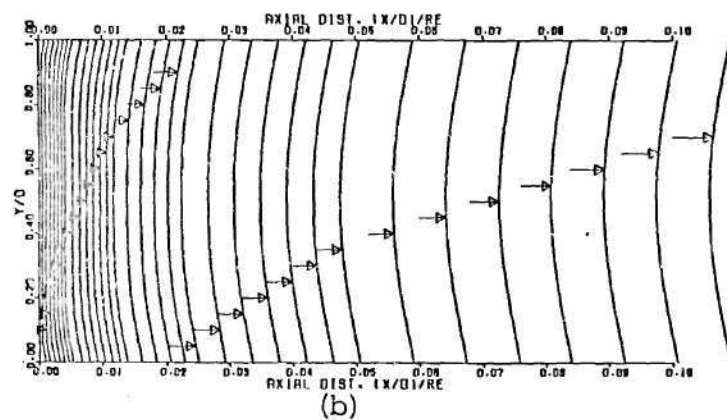
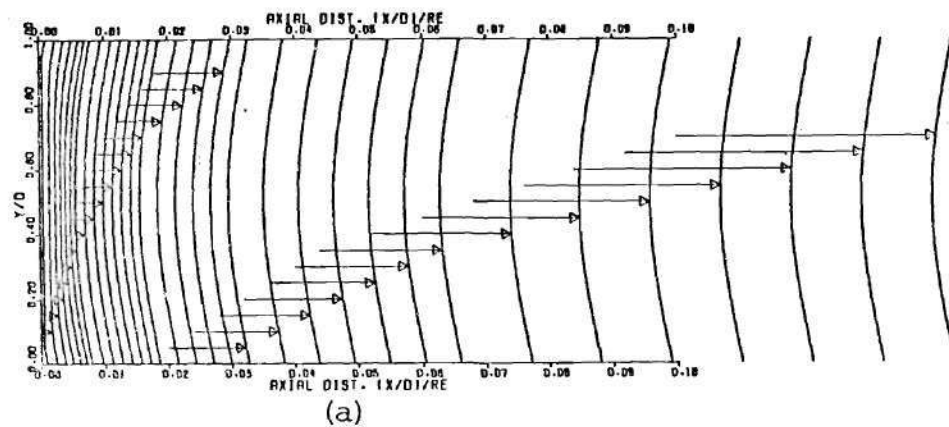


Figure 27. Wall Temperature Development with Constant Wall Heat Flux for (a) $Pe = 10$
(b) $Pe = 100$

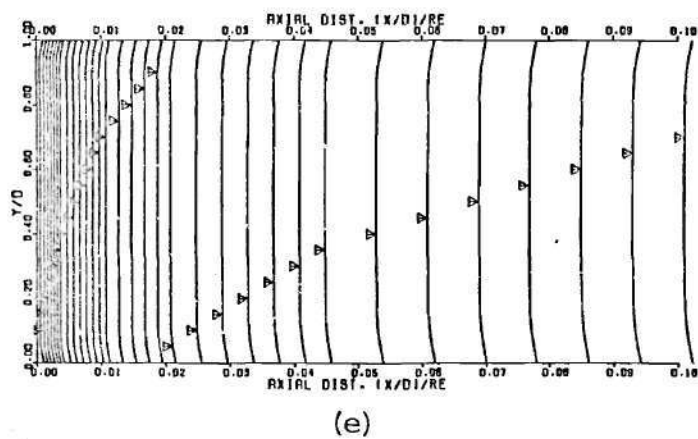
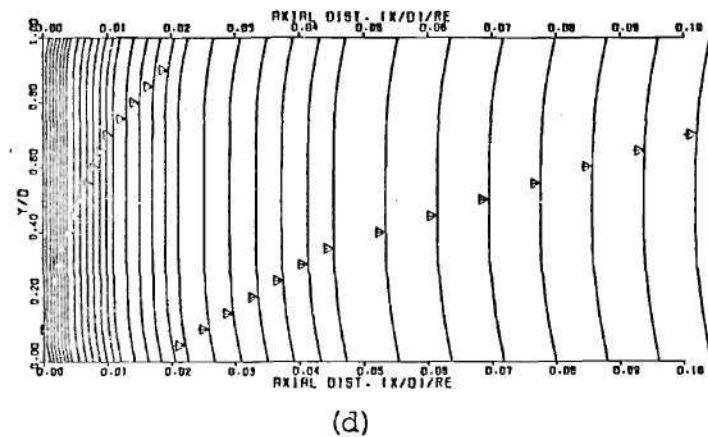
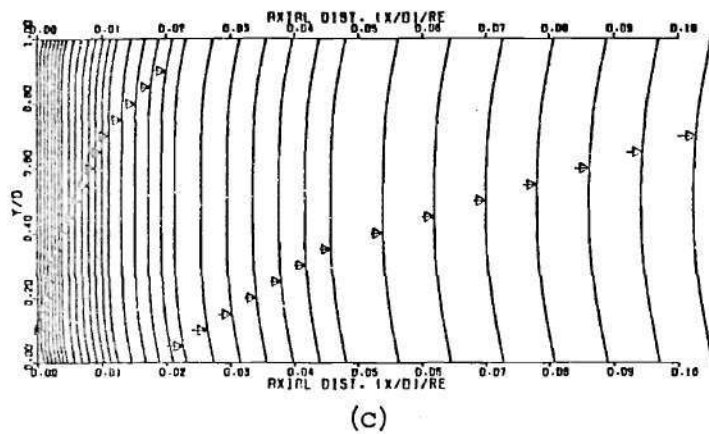


Figure 28. Wall Temperature Development with Constant Wall Heat Flux for (c) $Pe = 500$,
(d) $Pe = 1000$, (e) $Pe = 10000$

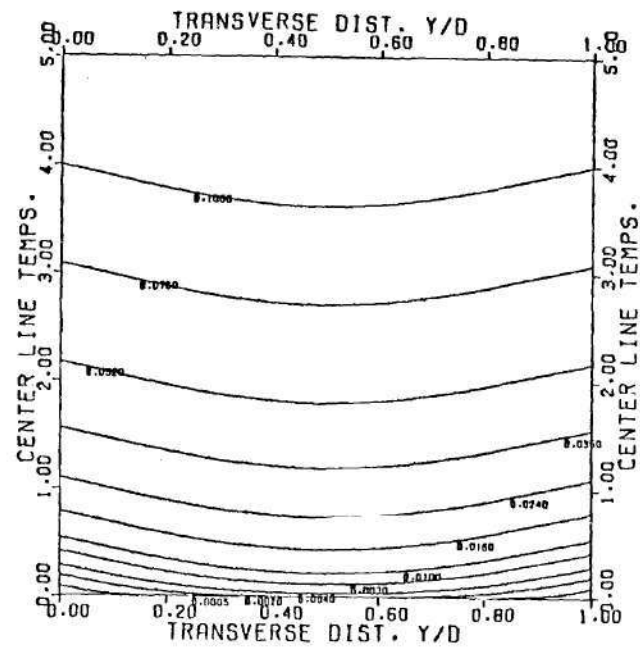
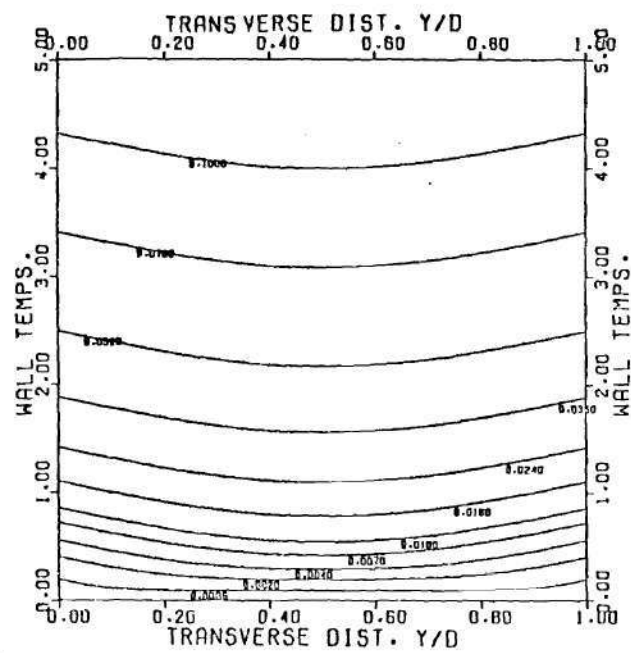


Figure 29. Wall and Center-line Temperatures at Various Values of L for Constant Wall Heat Flux Case with $Pe = 10$

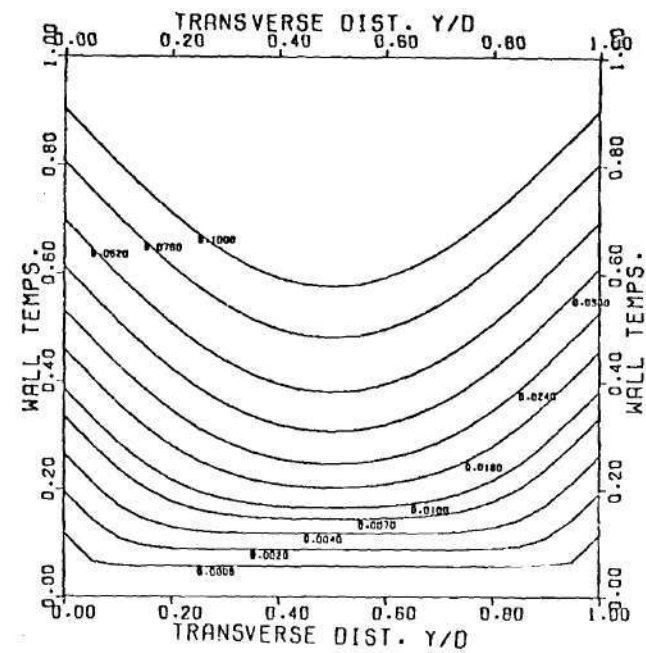
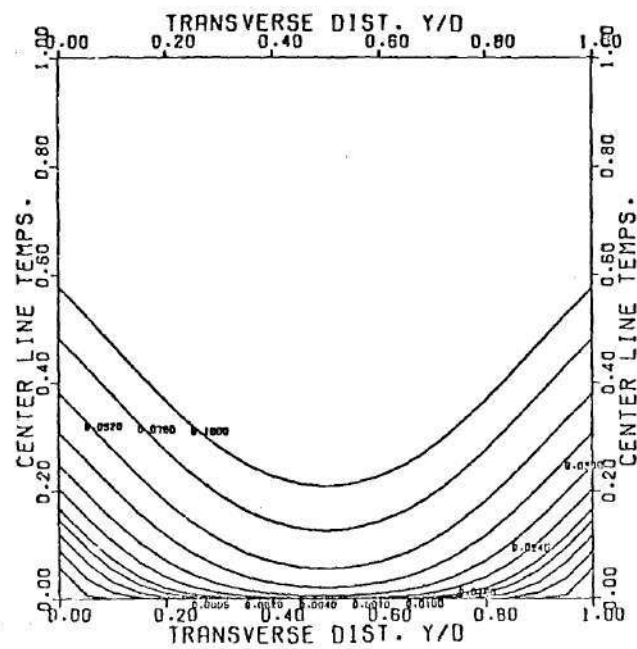


Figure 30. Wall and Center-line Temperatures for Various Values of L for Constant Wall Heat Flux Case with $Pe = 100$

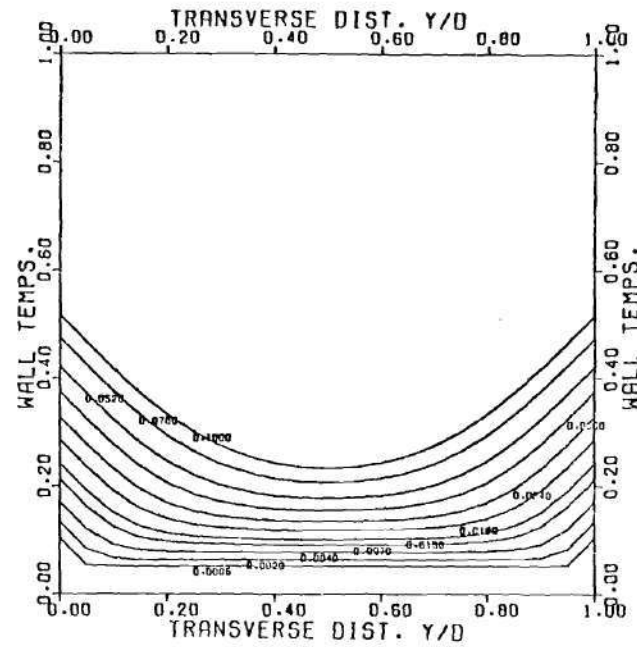
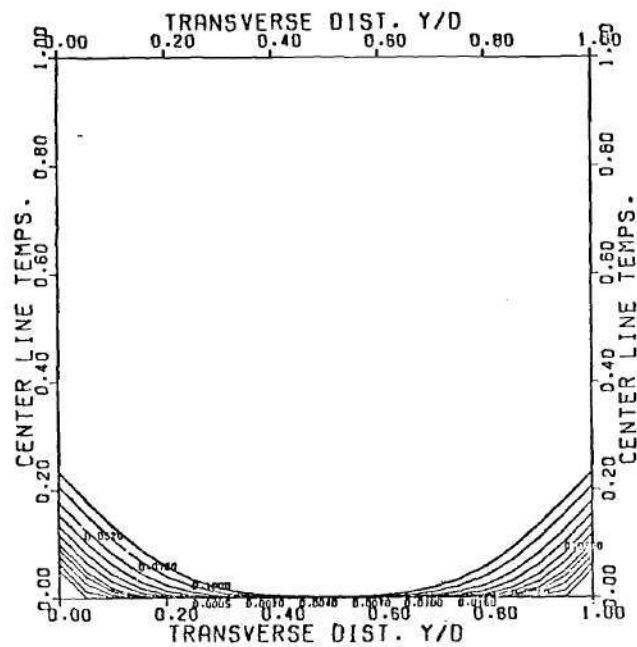


Figure 31. Wall and Center-line Temperatures for Various Values of L for Constant Wall Heat Flux Case with $Pe = 500$

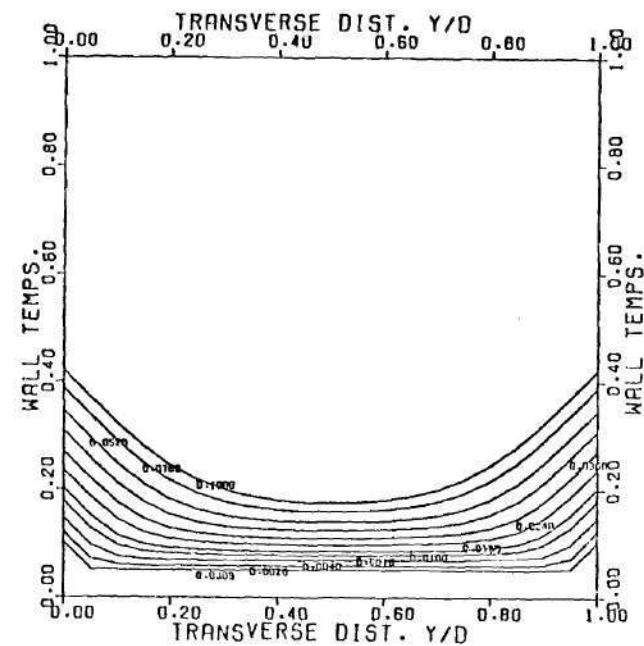
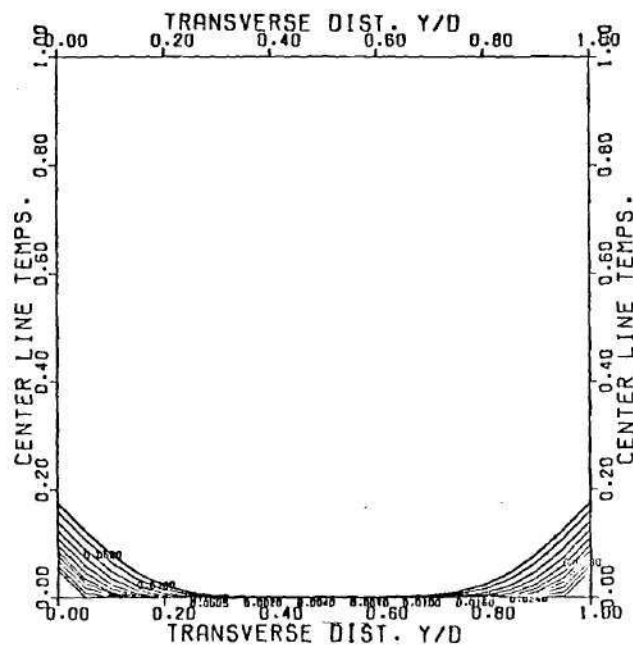


Figure 32. Wall and Center-line Temperatures at Various Values of L for Constant Wall Heat Flux Case with $Pe = 1000$

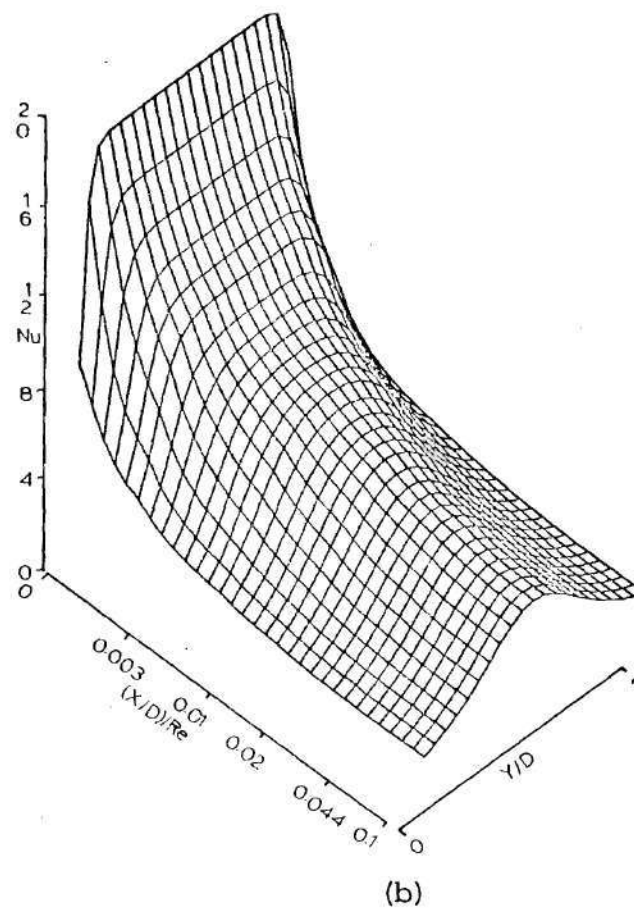
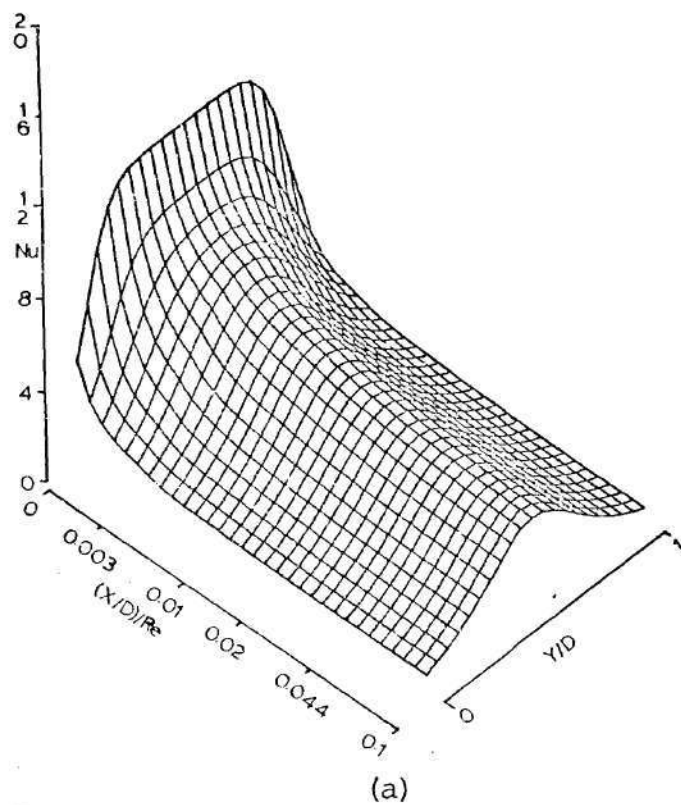


Figure 33. Nusselt Number Development Surfaces along a Wall for Constant Wall Heat Flux Case with (a) $Pe = 10$, (b) $Pe = 100$

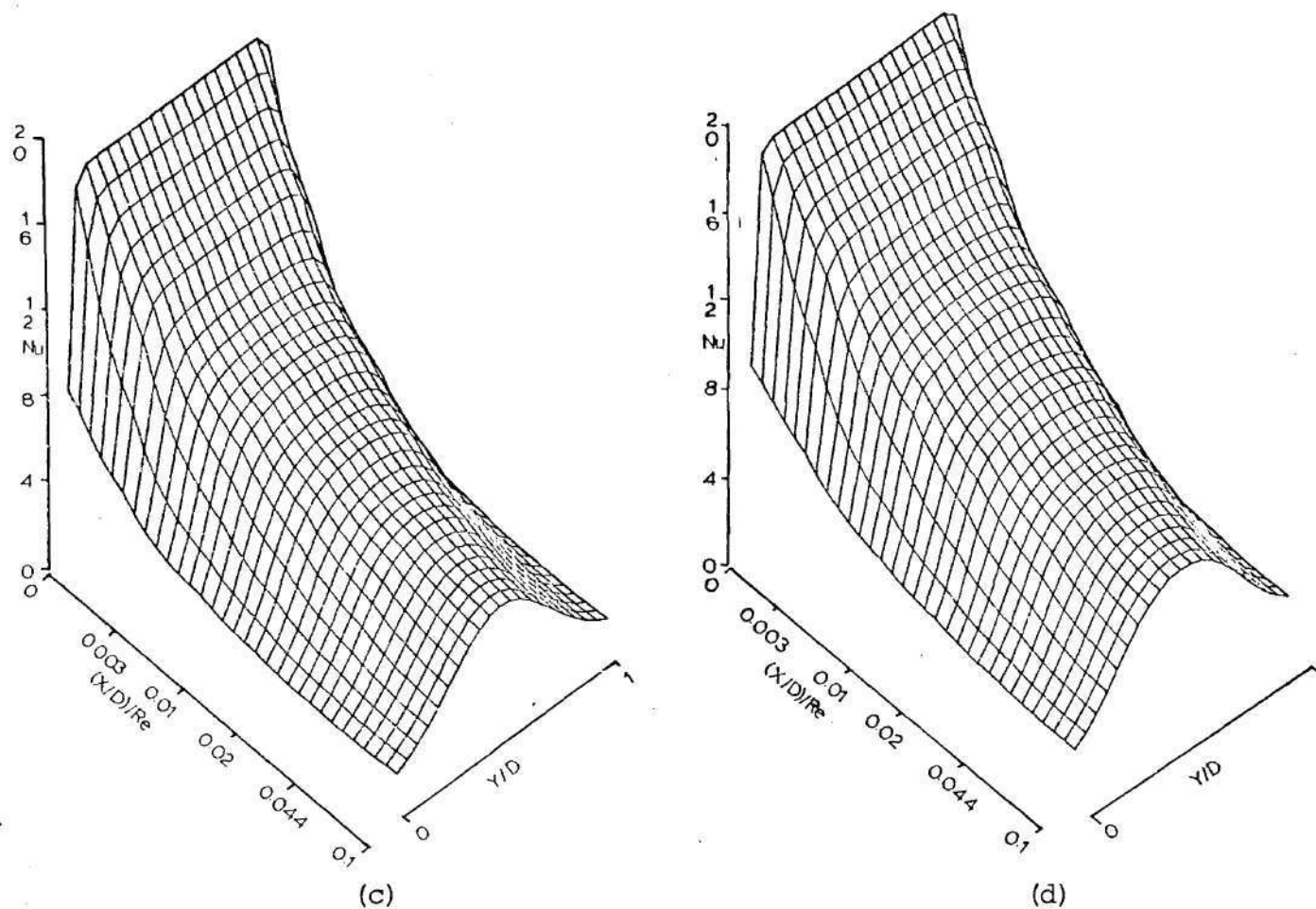


Figure 34. Nusselt Number Development Surfaces along a Wall for Constant Wall Heat Flux
Case with (c) $Pe = 500$, (d) $Pe = 1000$

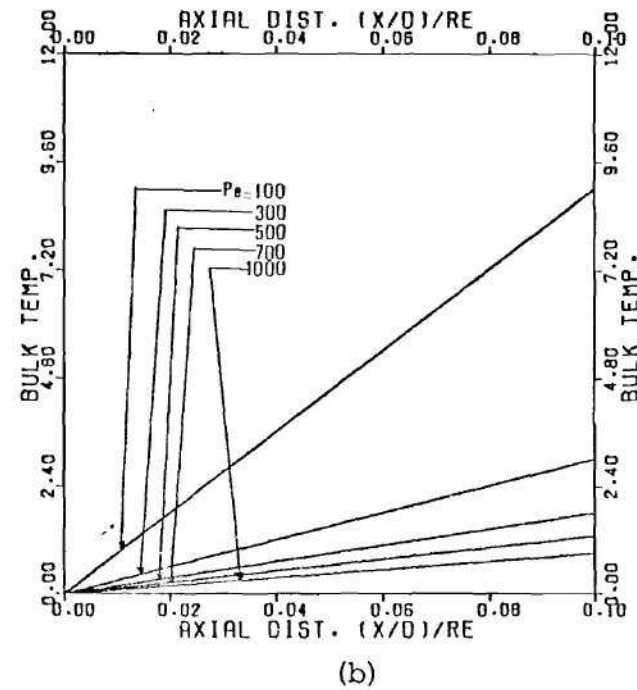
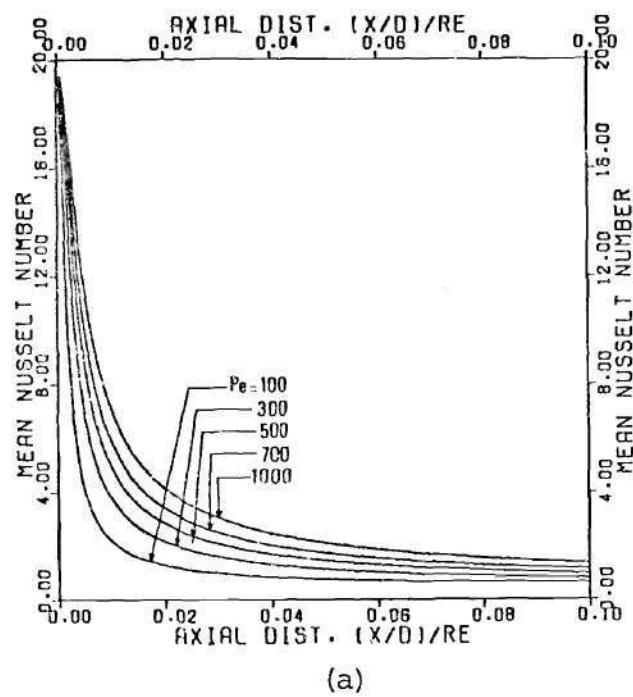


Figure 35. For $Q=100$

(a) Mean Nusselt Number Development for Values of Pe

(b) Bulk Temperature Development for Values of Pe

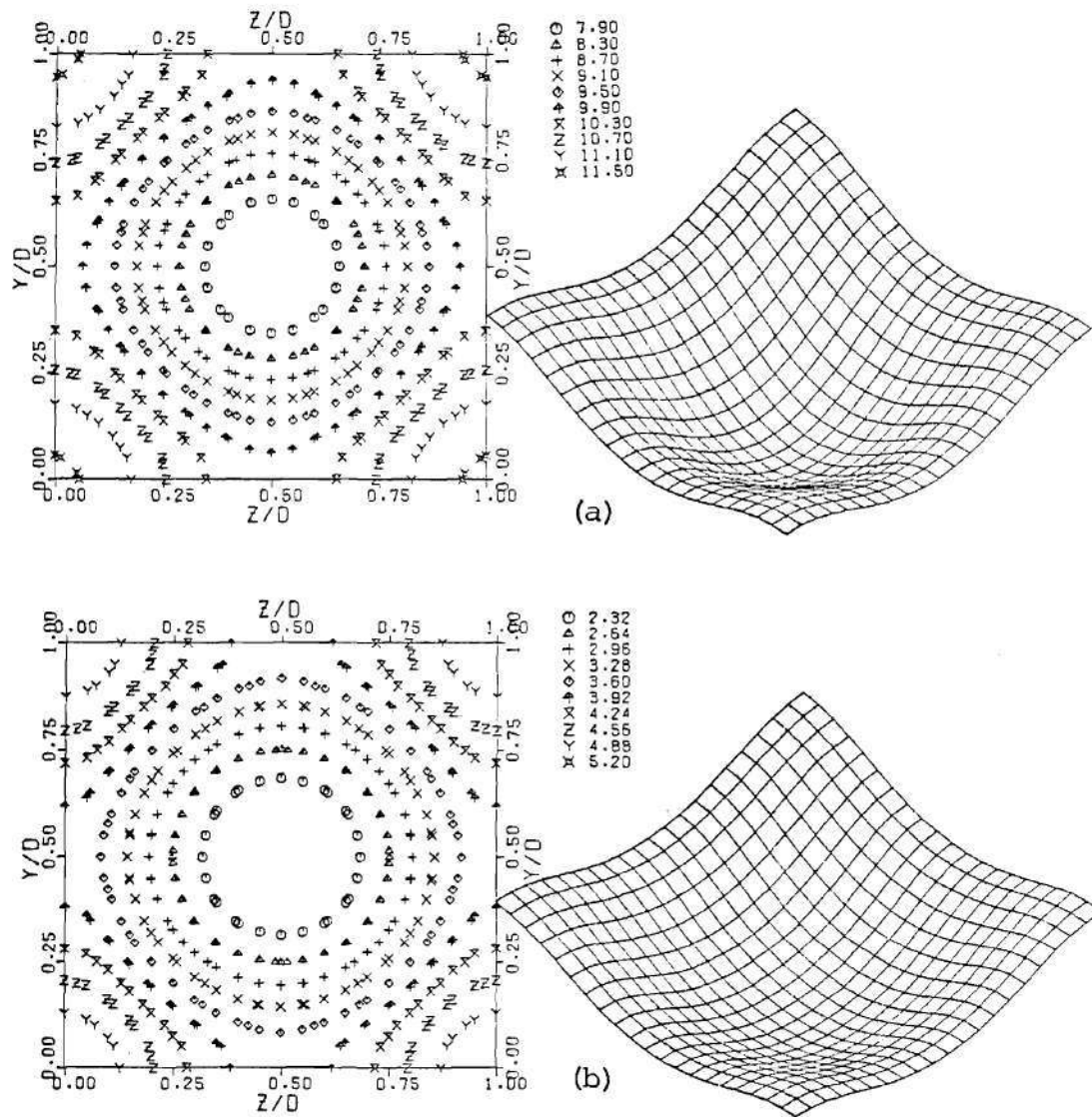


Figure 36. Temperature Contours and Surface for $Q=100$ and $L=0.1$ for
(a) $Pe=100$, (b) $Pe=300$

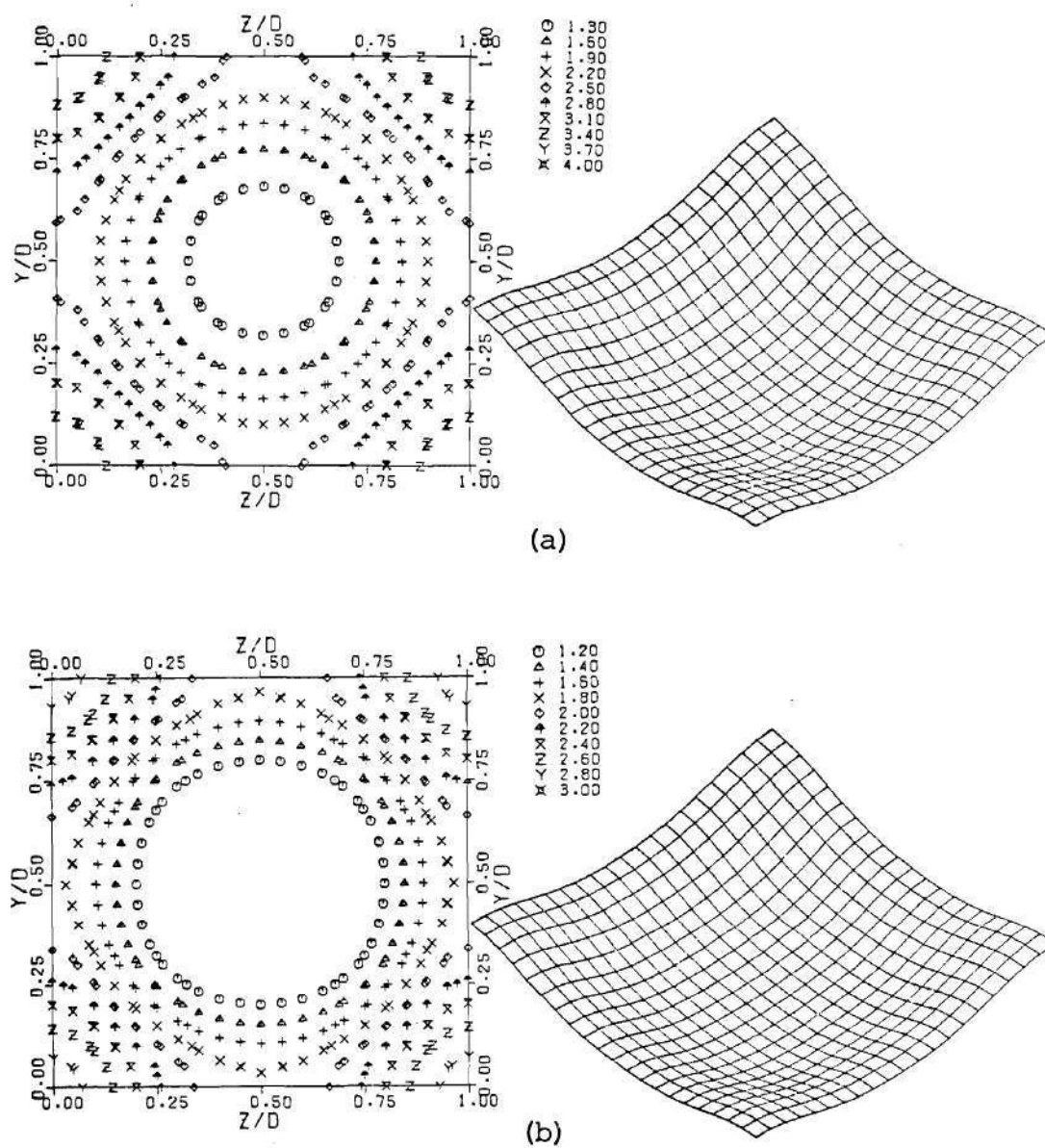
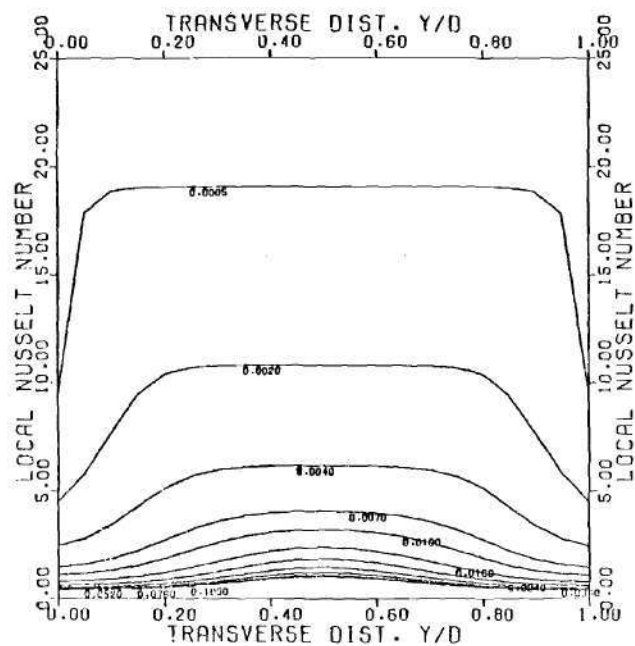
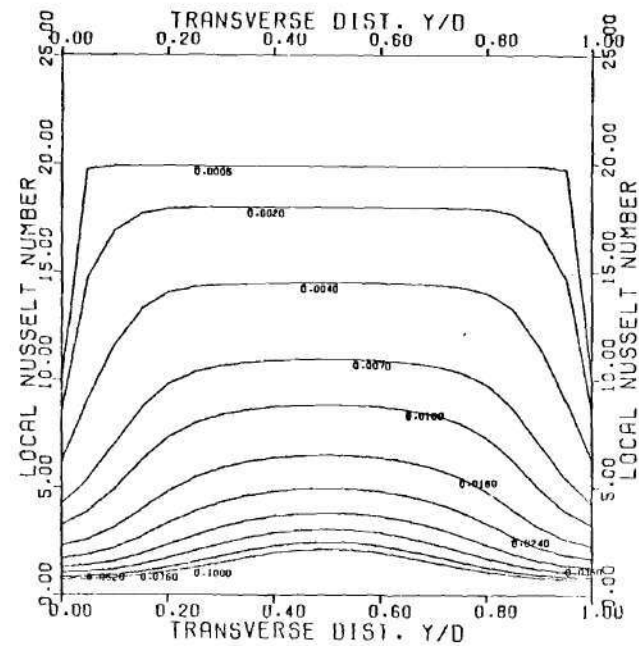


Figure 37. Temperature Contours and Surface at $L=0.1$ and $Q=100$ for
 (a) $Pe=500$, (b) $Pe=1000$



(a)



(b)

Figure. 38. Local Nusselt Number across a Wall at Values of L for $Q=100$ and
(a) $Pe=100$, (b) $Pe=1000$

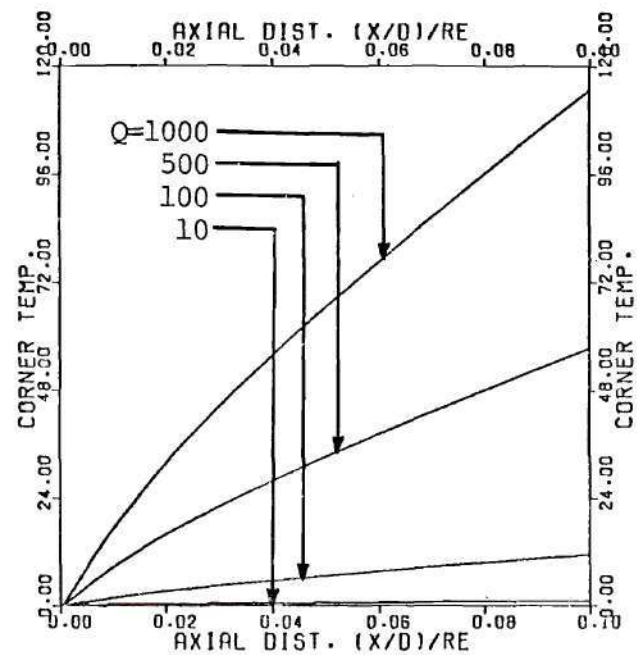
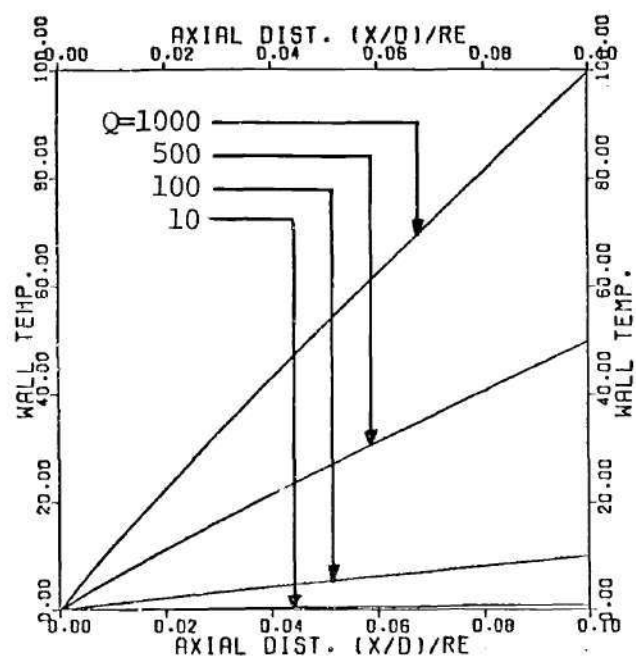


Figure 39. Wall Center and Wall Corner Temperature Development for Values of Internal Heat Source Q and $Pe=100$

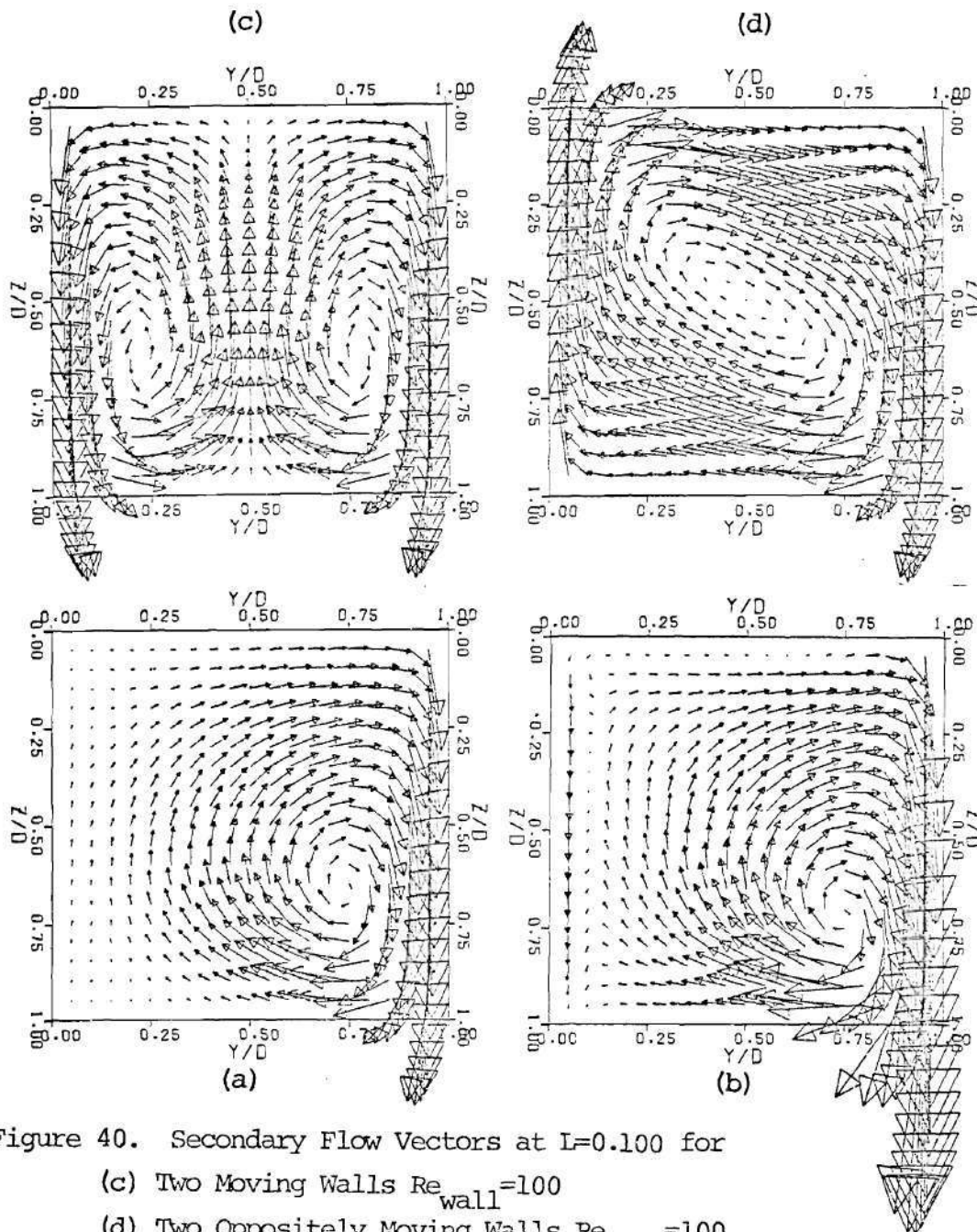


Figure 40. Secondary Flow Vectors at $L=0.100$ for
 (c) Two Moving Walls $Re_{wall}=100$
 (d) Two Oppositely Moving Walls $Re_{wall}=100$
 (a) One Moving Wall $Re_{wall}=100$
 (b) One Moving Wall $Re_{wall}=200$

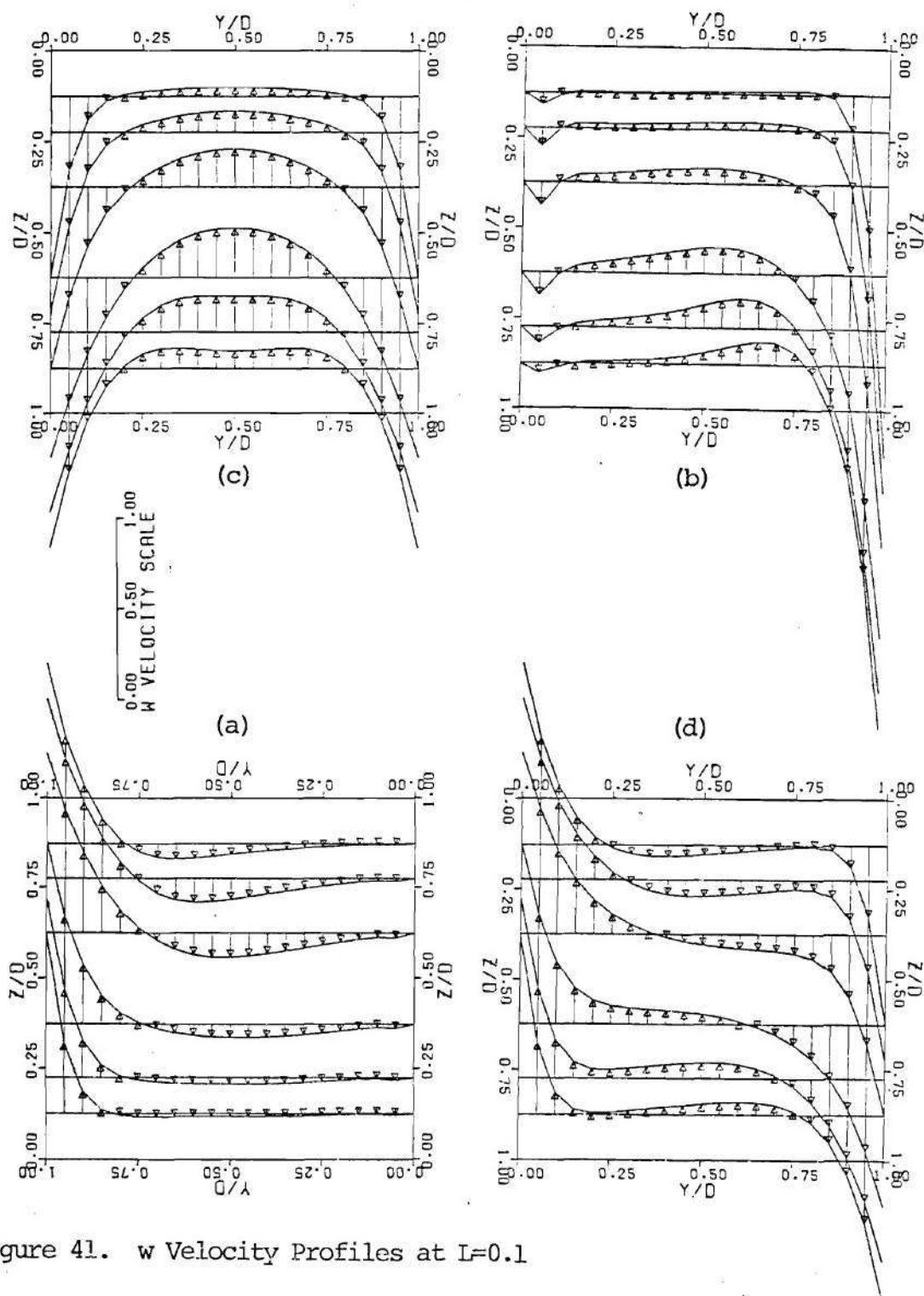


Figure 41. w Velocity Profiles at $L=0.1$

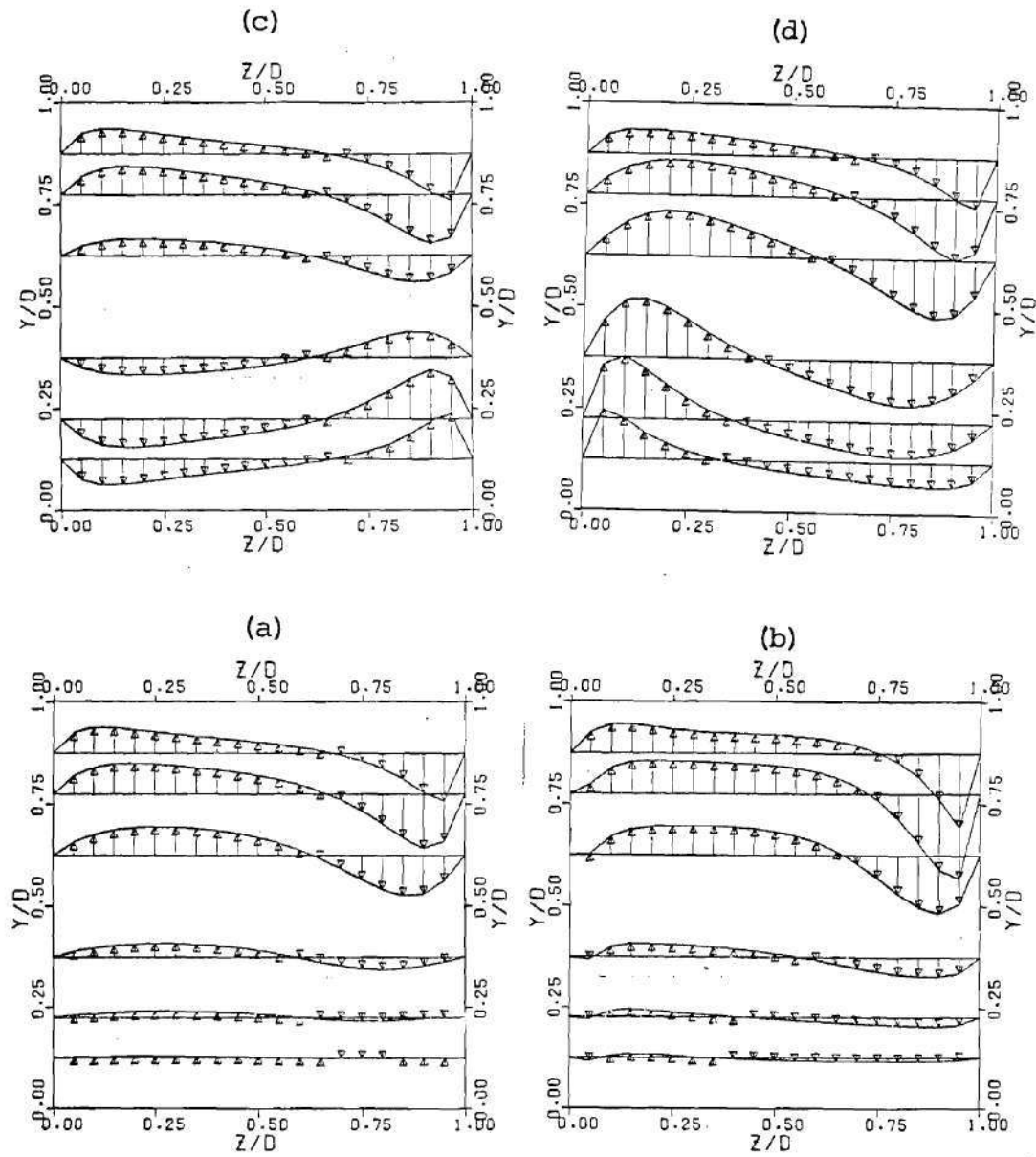


Figure 42. v Velocity Profiles at $L=0.1$

Y VELOCITY SCALE
0.00
0.50
1.00

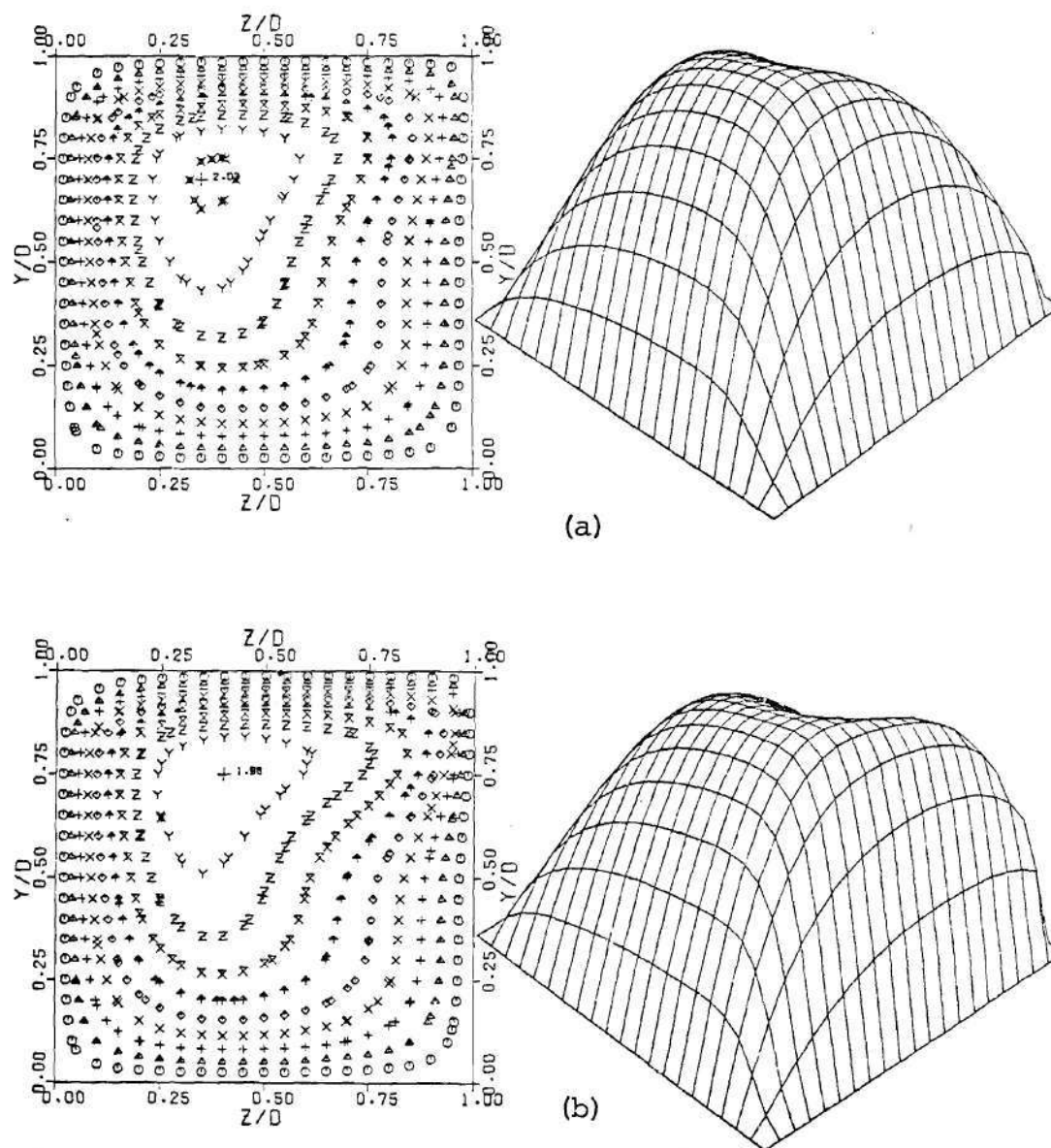


Figure 43. Axial Velocity Contours and Surface at $L=0.1$

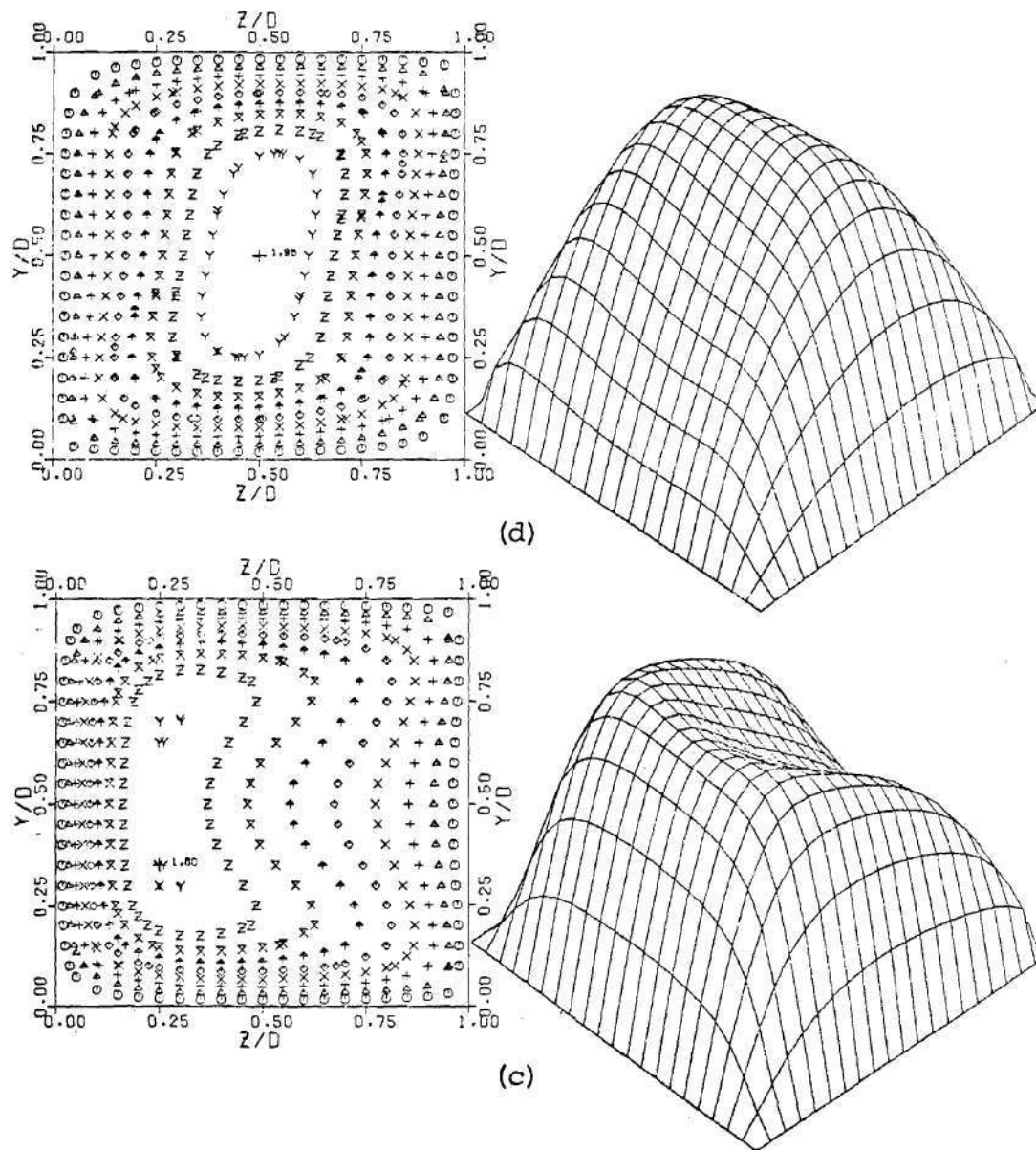


Figure 44. Axial Velocity Contours and Surface at $L=0.1$

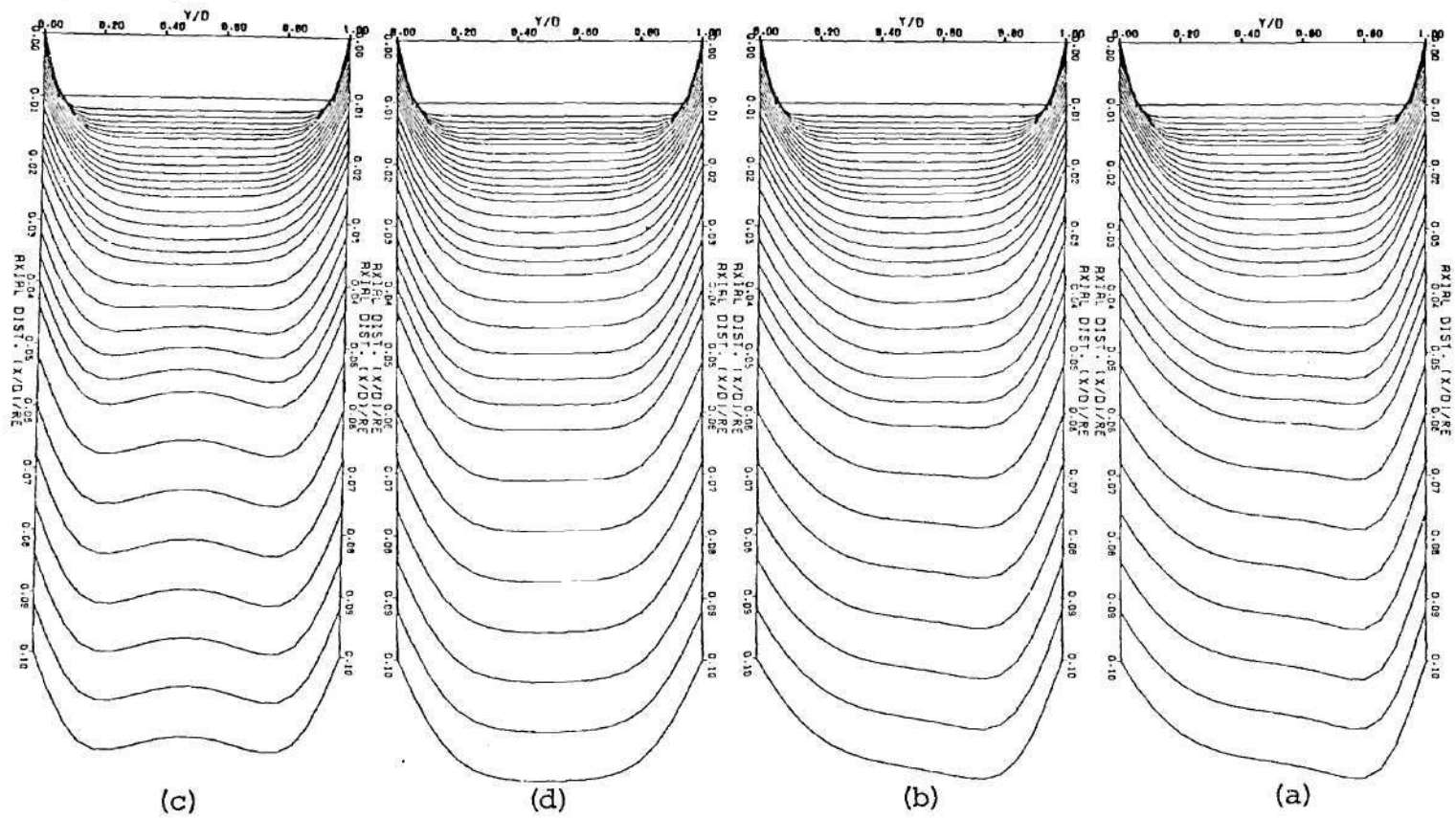
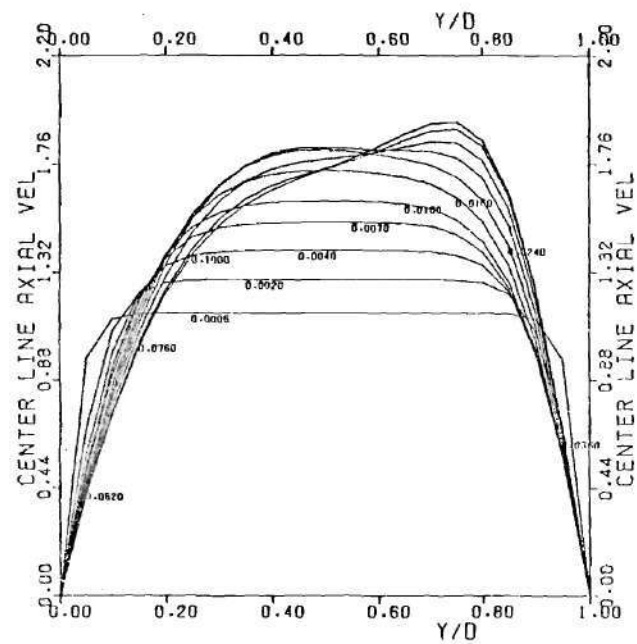
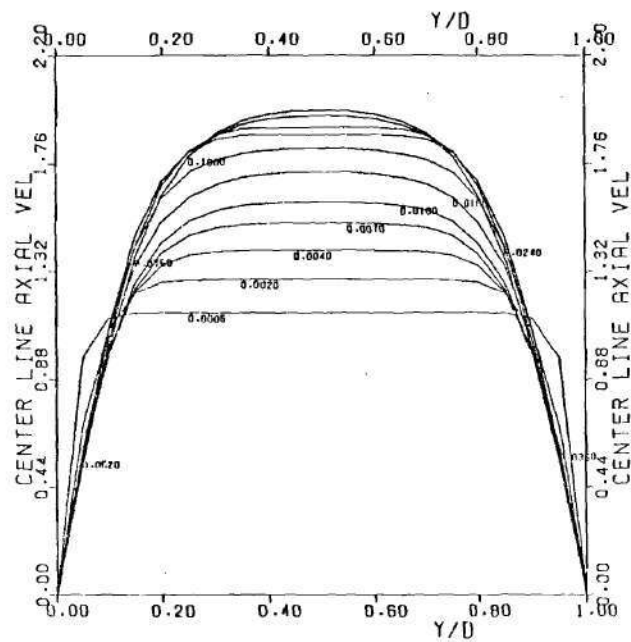
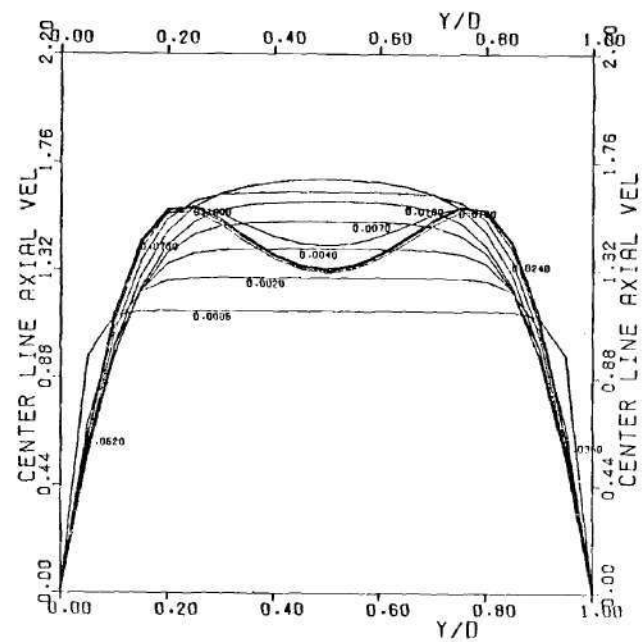


Figure 45. Axial Velocity Development at Center-plane





(d)



(c)

Figure 47. Axial Velocity at Various Values of L

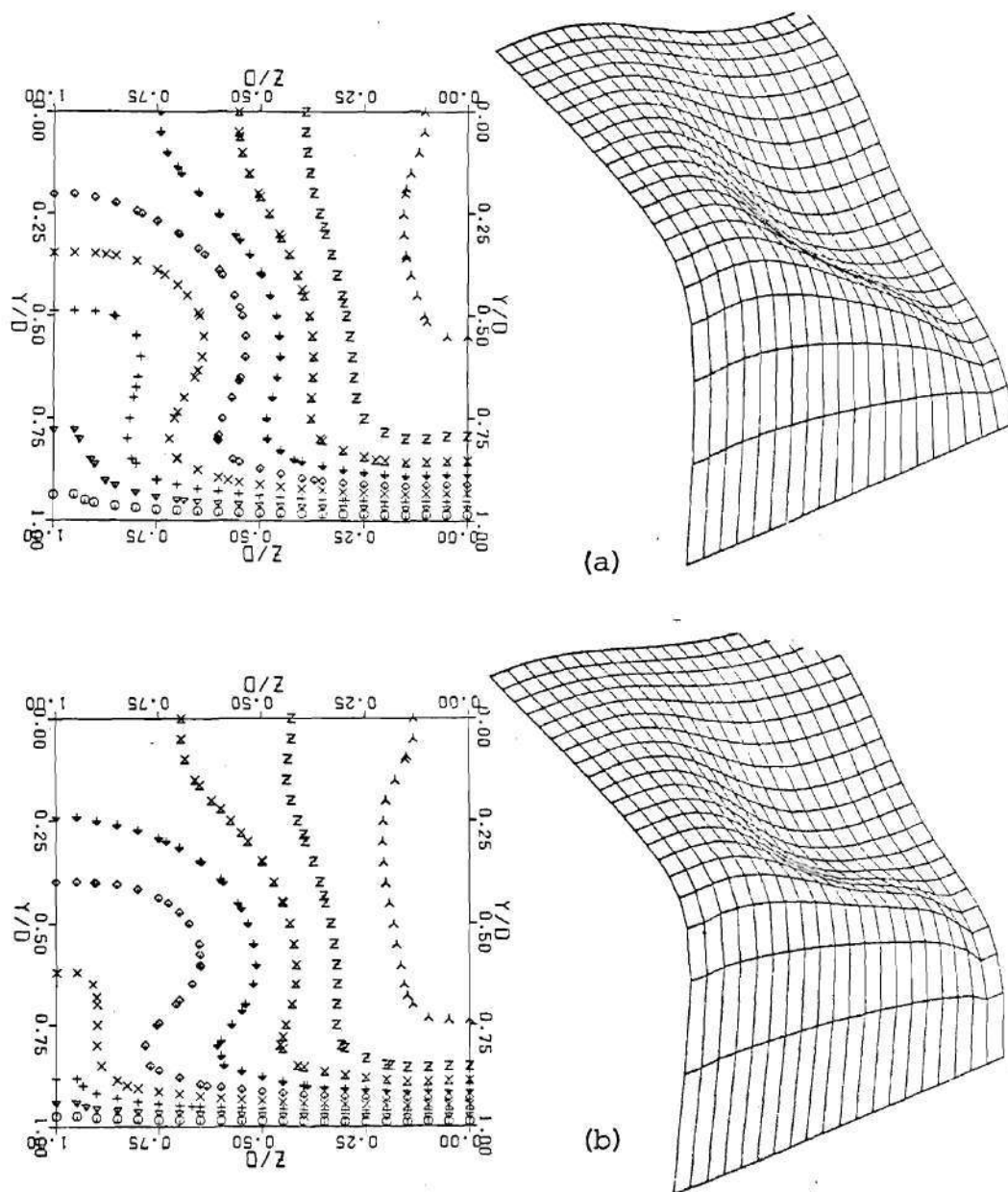


Figure 48. Temperature Contours and Surface at $L=0.1$

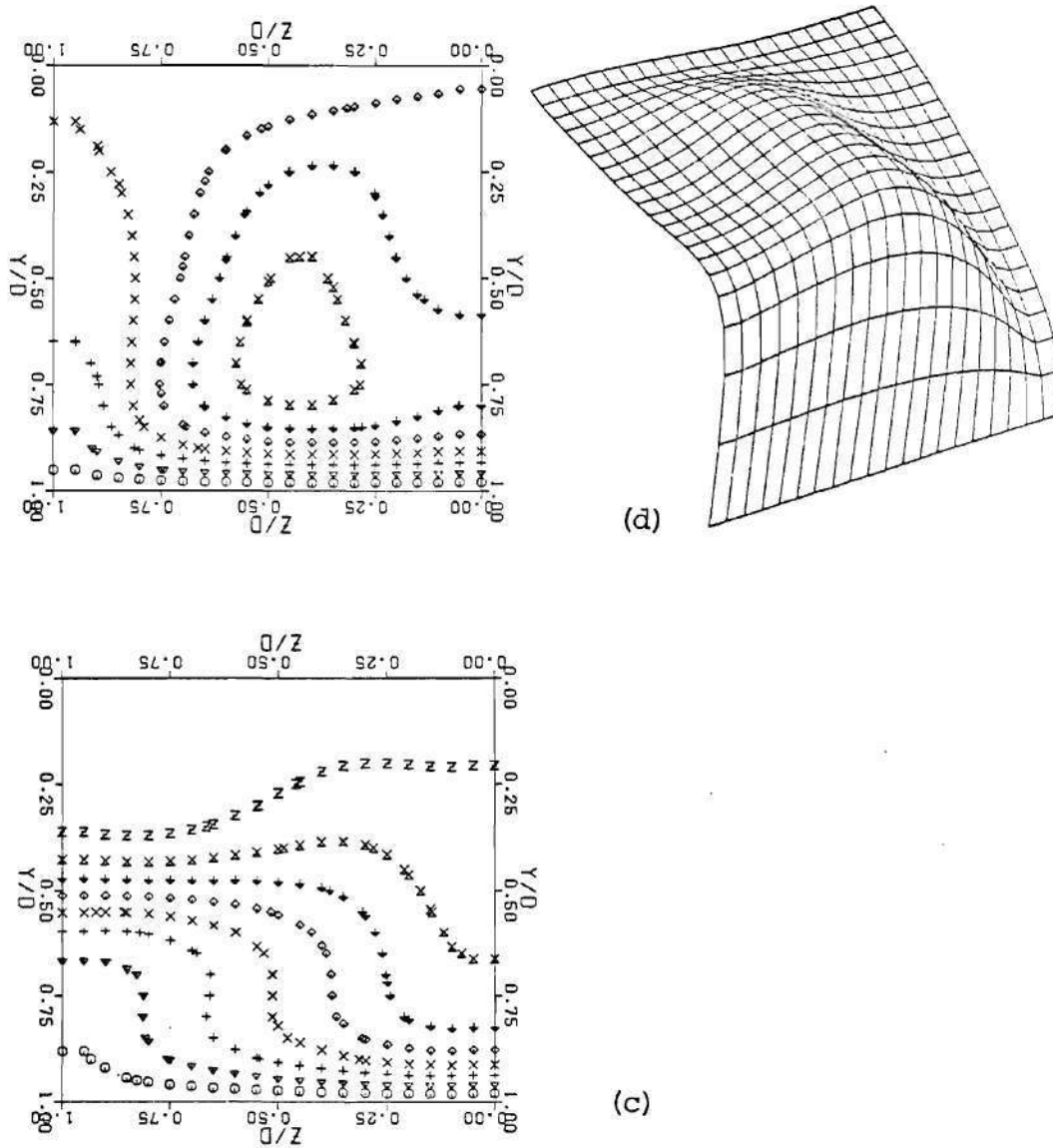


Figure 49. Temperature Contours and Surface at $L=0.1$

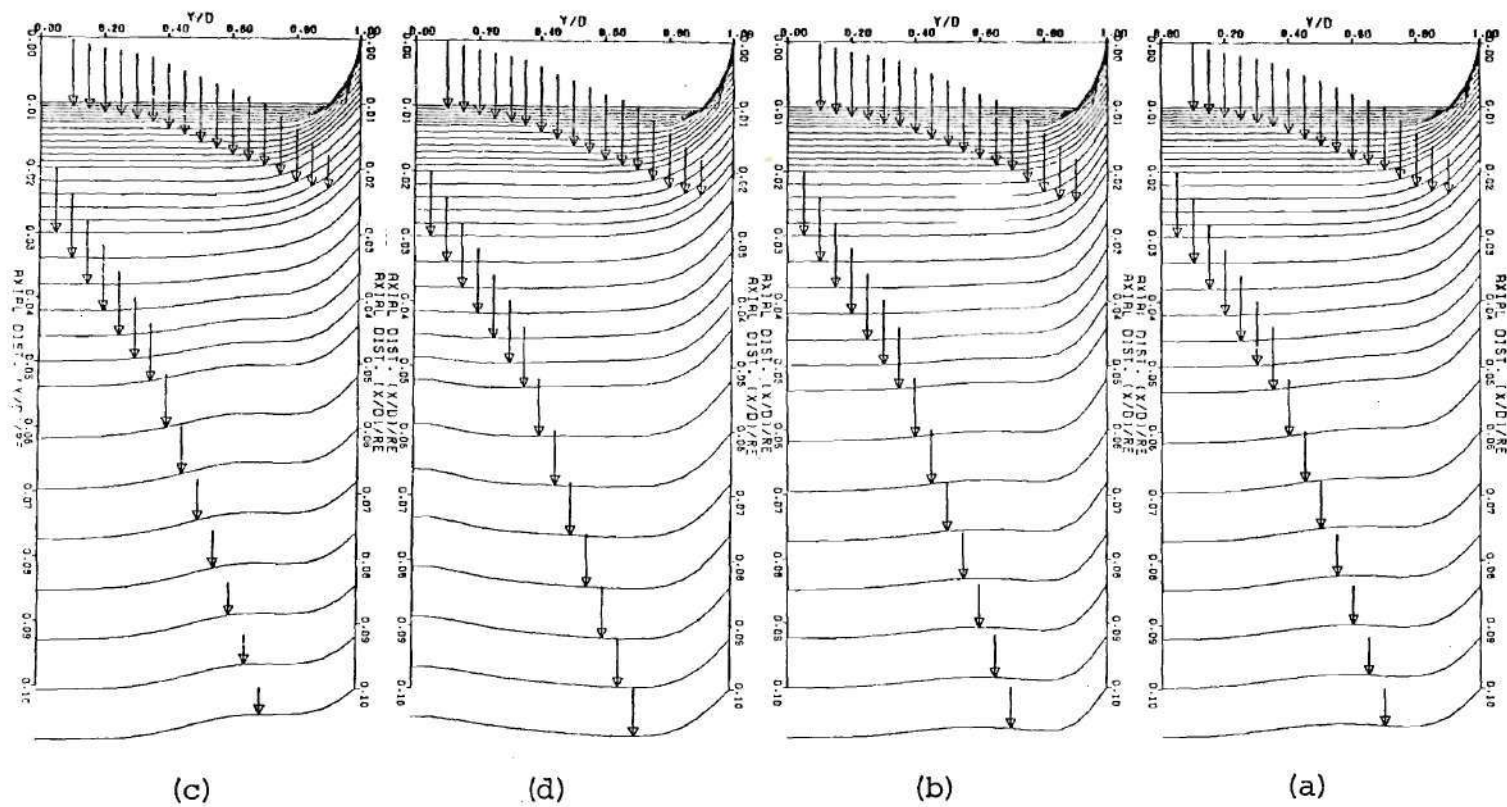


Figure 51. Center-plane Temperature Development
(The arrows indicate the axial position of the profiles.)

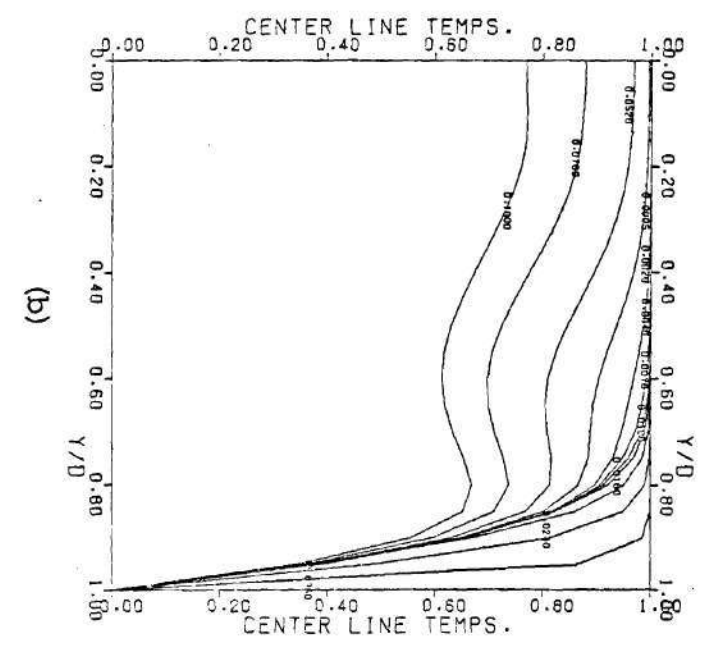
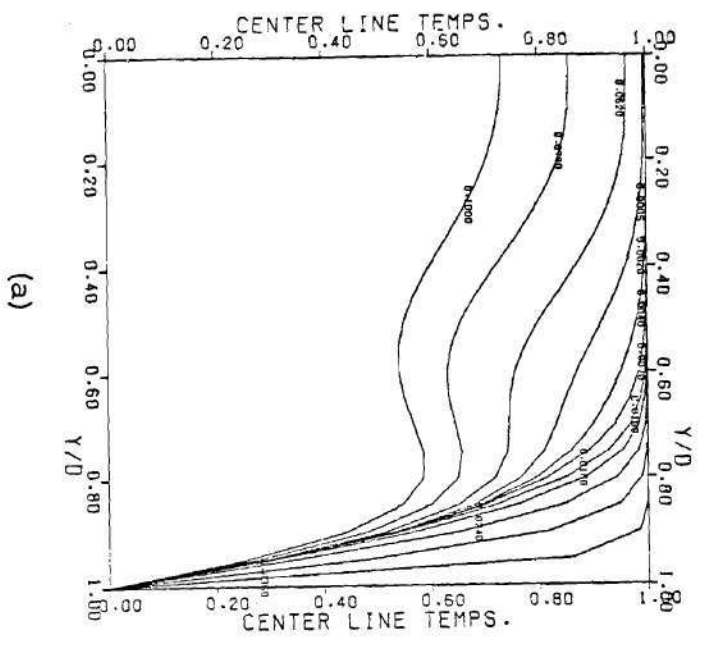
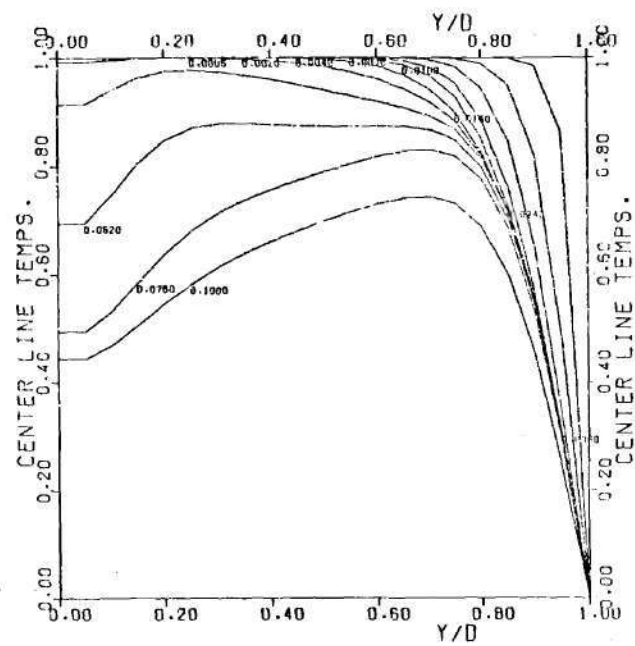
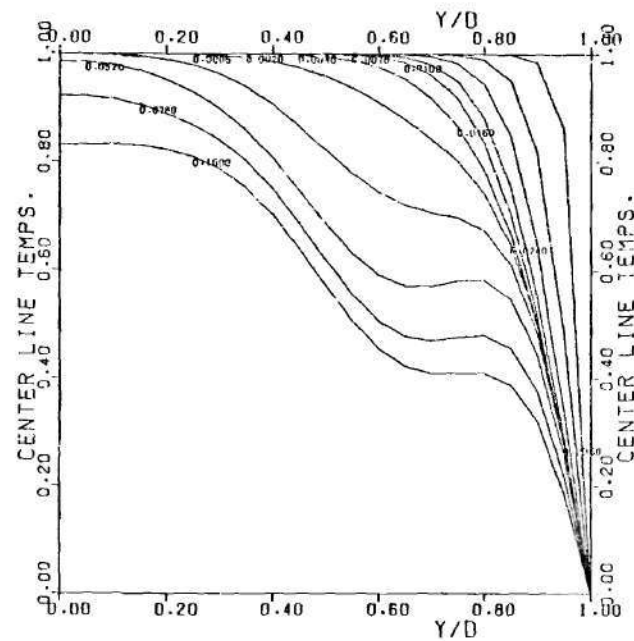


Figure 52. Center-line Temperature at Various Values of L



(d)



(c)

Figure 53. Center-line Temperature at Various Values of L

CHAPTER V

RESULTS AND DISCUSSION

Ducts with perfectly electrically insulating ($C = 0$) walls and perfectly electrically conducting walls ($C = \text{infinity}$) are the basic cases, and these are examined first. Then two finite conductivity cases ($C = 10$) and ($C = 1$) shall be considered. These are followed by two mixed problems, i.e. walls parallel to the imposed field being electrically non-conducting while walls perpendicular to the imposed field are infinitely electrically conducting and vice versa. Then the effects of insulated corners and current breaks on a perfectly conducting duct are studied. Finally the case of three walls being non-conducting electrically and one wall being infinitely or finitely electrically conducting, with and without electrically insulated corners is considered.

In Tokamak blankets the Peclet number is of the order of 10^2 and the magnetic Reynolds number is of the order of unity.³³ Thus it was decided to fix the Reynolds number at 100, the magnetic Reynolds number at 1, and the Prandtl number at 1. The constant wall heat flux boundary condition (except for the last few cases) was enforced on all four walls.

At this point a comment is made about the abundance of figures in this work. It has been said that when presented with numbers the mind can, at best, think linearly. However, when presented with a picture it can grasp the whole situation and think much more creatively. In the computer modeling of three-dimensional flows, enormous amounts of numbers are generated, and the only way for the trends represented by these numbers, to be deduced, is to plot them. The advanced graphics capabilities

of modern computer systems allows the facilitous plotting of the contours, vectors and surfaces that best represent three-dimensional variations. These capabilities have been put to good use in this work.

Case with $C = 0$ on all Walls

Results for this problem, with a Hartmann number of 10, are presented in Figs. 54 through 66. It should be noted that all the plotted results in this chapter are for Hartmann numbers of 10 (except for the parametric studies). Current density vectors, calculated from $\bar{J} = \bar{\nabla} \times \bar{H}$, for the transverse plane are shown in Fig. 54. Axial induced magnetic field contours for the same plane are shown in Fig. 55. It may be noted that the orientation of the axes in Fig. 54 is rotated 90° . This was done so as to make the figures fit within the page format. When the two transverse induced field components are very small i.e., near and in the developed region, the transverse currents are,

$$J_y = \frac{\partial H_x}{\partial z} \quad \text{and} \quad J_z = - \frac{\partial H_x}{\partial y} ,$$

and so H_x , the induced axial field component, can be considered as a stream function for J , which means that the currents flow along lines of constant H_x . Thus, near and in the developed region, the contours of Fig. 55 should trace the current vector loops observable in Fig. 54.

Figure 54(a) shows the currents right near the entrance, where the H_y and H_z components are significant, as they are generated by secondary flow which is appreciable here. A sort of source and sink activity is discerned in the center and this implies out of plane current vectors. Figure 56(a) shows the existence of a current loop in the axial xz plane

at the center. This loop, which is a result of the flow development, is the cause for the activity of Fig. 54(a). The contours of Fig. 55(a) cannot show this activity as they can only represent the current loops when H_y and H_z are small. Rather quick development of the current density vectors is seen and the developed distributions exactly follow the H_x contour loops for the corresponding axial position.

The forms of these current loops is easily explainable. Currents always seek the path of least resistance and since the walls are non-conducting, the current loops are forced to lie entirely in the fluid region. The return path of least resistance for the currents generated by the core motion is through the areas of lowest fluid velocity, i.e. the boundary regions.

In the fully developed region, current flow in the duct center is so oriented that the $\vec{J} \times \vec{B}$ Lorentz force is acting in a direction that opposes fluid motion. In regions near walls that are perpendicular to the imposed field, the direction of current flow is opposite and so the Lorentz force now acts in the flow direction. This serves to accelerate the fluid in these boundary regions, flattening out the velocity profile. Even though the net electromagnetic force on the fluid is zero, the flattened profile experiences increased viscous forces due to steeper velocity gradients at the walls. Current flow immediately adjacent to perpendicular walls is much stronger than that adjacent to parallel walls. Thus, a flatter axial velocity profile across the perpendicular, or z , direction is to be expected.

Current flow in two axial planes is displayed in Fig. 56. The plane in Fig. 56(a) lies along $Y/D = 0.5$, i.e. the centerline. Except

for the initial loop, the current flow in this plane is essentially unidirectional and appears to decrease to zero at the walls. The currents themselves are not disappearing, but simply leaving the plane of representation. This is the result of current direction changes in the transverse plane. Figure 56(b) represents a plane near a parallel wall and shows initial loop associated activity in the developing region, followed by an axially invariant distribution that seems to show currents emerging from the walls and going to zero at the center of the plane. Again, this distribution is the product of current direction changes in the transverse plane.

Figures 57, 58 and 59 display the three induced field components, H_x , H_y and H_z that produced the above current flows. One full cycle of sinusoidal type variation across the y direction and one half cycle across the z direction is observed for the axial field. Also, the magnitude of the distribution increases until the flow is developed, and the fully developed values are plotted as a surface in Fig. 57(c). The surface is a little hard to interpret as the negative portion of the sinusoid can not be seen due to hidden line removal by the plotting program. The maximum value of this field is observed to be about 0.08 and is thus 8% of the imposed transverse field relative to which it is non-dimensionalized. The y component of the induced field plotted across the two center lines is shown in Fig. 58, and except for a small positive overshoot near the entrance, is entirely negative. As a surface it is like a negative paraboloid as shown in Fig. 58(c). Again, due to hidden line removal, the entire interior of the surface cannot be seen. This field component has maximum values near the entrance and asymptotically

approaches zero as the flow develops. At its maximum it has a value of about 2% of the imposed field. The z component of the induced field, which is plotted along the $Z/D = 0.25$ and $Y/D = 0.25$ lines in Fig. 59, has a ragged sinusoidal type distribution in the y direction and a smoother, though smaller in amplitude, distribution across the z direction. Again, H_z approaches zero as the developed condition is reached and the maximum value is only about 0.3% of the imposed field.

Reasons for these H_y and H_z distributions do not immediately present themselves. However, clues to their origin can be deduced from the profile shapes of the secondary velocity components that induce them. The main source terms in the H_y and H_z induction equations are $B_{py}(\partial v/\partial y)$ and $B_{py}(\partial w/\partial y)$ respectively. If one can recall the shapes of the v and w profiles in the y direction and visualize their derivatives, these derivatives would roughly follow the H_y and H_z distributions. The v and w velocity profiles are similar in their respective directions, but it is the fact that both the above derivatives are with respect to y (the imposed field direction) that causes the differences between H_y and H_z .

As previously mentioned, axial velocity in the transverse plane is no longer expected to be symmetric. Figure 60 displays this fact well. From the contours of Fig. 60(b) it is observable that the profiles are clearly flattened, more across the y direction than the z , and the maximum velocity value at the center is reduced to 1.76. This asymmetric axial velocity distribution can only be produced by unequal transverse velocity components as it is this secondary flow which transfers fluid from wall regions inwards for flow development. Since the u profile is flatter along the y coordinate, it is closer to the slug entry profile,

and thus less fluid has to be moved in the y direction during development. For this reason it is expected that the v component should now be smaller in magnitude than the w . This fact is displayed clearly in Fig. 61.

Magnetic fields can have no direct effects on temperature distributions (except, perhaps, through Ohmic heating), but can have secondary effects through the coupling between the momentum and energy equations. Temperature fields in duct flow tend to follow the existing velocity fields, and so the temperature contours in Fig. 62(b) are slightly elongated in the same direction as the axial velocity contours. Local Nusselt numbers, wall and centerline temperatures, are also presented in Figs. 62 and 63, and show distributions similar to the non-magnetic case.

The non-conducting wall problem is completed by an investigation of the variation of certain important quantities with Hartmann number change. These quantities are plotted in Figs. 64 through 66. As the Hartmann number increases from 0 to 10, the following fully developed effects are observed:

- (1) Center-point axial velocity decreases from 2.10 to 1.76.
- (2) Velocity entry length decreases from an L value of 0.040 to 0.022.
- (3) Axial pressure gradient increases from -0.29 to -0.41.
- (4) Axial total pressure coefficient increases from 3.61 to 4.60.
- (5) Mean Nusselt number increases from 3.55 to 3.99.
- (6) Wall center and corner temperatures decrease from 0.57 and 0.90 to 0.54 and 0.87 respectively.

The last two temperature effects occur due to the temperature distribution becoming flatter and represent heat transfer enhancement.

Case with $C = \text{infinity}$ on all Walls

Figures 67 through 78 present the case of infinitely electrically conducting walls. An infinite wall conductivity parameter implies that the wall is infinitely more electrically conductive than the fluid. Thus, the path of least resistance for current return becomes the duct walls themselves rather than the fluid boundary regions as was in the $C = 0$ case. Figure 67 displays the transverse plane current vectors, and it is directly observable that the current loops are completed through the walls. A similar observance is possible from the contours of Fig. 68. The sharpness of some of the bends in the contours is a result of the linear interpolation used by the contour plotting routine, and also the fact that it used straight line segments to construct the contours. The entry region source and sink type activity that was discerned in the previous case is absent here and the currents at the duct center flow directly from one wall to the other. Equivilient current density vectors in axial planes are shown in Fig. 69. In the previous case there was a region of zero current, where the two sets of current loops met, extending down the duct center. This is absent here and current flow is essentially from one parallel wall to the other. For the perpendicular walls, currents leaving one side of the wall return to the other side of the same wall.

Since $C = \text{infinity}$, axial field gradients in the normal direction at the walls are zero. Figure 70 shows the axial field plotted across

center and quarter line. The maximum value of this field occurs at the perpendicular walls and has a magnitude equal to about 40% of the imposed field. For transverse fields, it should be recalled that the boundary conditions force the field to become zero at normal walls, and to suffer a linear variation within the other two walls, i.e., the thin wall boundary condition is used. Thus, H_y goes to zero at $Y/D = 0$ and 1 and its normal gradient goes to zero at $Z/D = 0$ and 1 . The correspondingly opposite situation holds for H_z . These two field distributions are plotted in Figs. 71 and 72. In Fig. 72(a), the forcing of the normal gradient of H_z at $Y/D = 0$ and $Y/D = 1$ to be zero seems unnatural. This casts suspicion on the appropriateness of using the thin wall boundary condition here. Again, since H_z is a secondary quantity, the resulting error is not expected to be significant.

Fully developed axial center-point velocity is 1.72 which is a little less than the 1.76 for the previous case. The profile, as observed from Fig. 73, is still more flattened in the parallel direction, but the difference between the two directions is less. The axial velocity contours appear a little less elongated because the currents are now returning through the walls, and thus they do not accelerate the fluid in the wall regions. Core velocity, however, is still retarded and as mass flow must be conserved this causes the flattening of the profile. In this case, since the currents return through the walls, there is a downstream electromagnetic force on them with a corresponding net upstream force on the fluid. The pressure gradient has to counteract this as well as the viscous shear forces at the wall. This pressure gradient is then much larger than that for the $C = 0$ case where there is no net electro-

magnetic force on the fluid.

Temperature results for this case are presented in Figs. 74 and 75, and are not very different from the $C = 0$ results. The mean Nusselt number of 4.09 is a little higher than the 3.99 for the $C = 0$ case. This corresponds to the slightly flatter profile in both transverse directions. Figures 76, 77 and 78 show the Hartmann number study, with trends similar to the last case being displayed. Varying the Hartmann number from 0 to 10 causes the center-point velocity to go from 2.10 to 1.72, the mean Nusselt number from 3.55 to 4.09, the axial pressure gradient from -0.29 to -1.22, the pressure coefficient from 3.61 to 12.52, the wall center temperature from 0.57 to 0.54, and the wall corner temperature from 0.90 to 0.86. All the above values occur at $L = 0.1$.

Case with $C = 10$ on all Walls

Magnitudes of the results for this case are not very different from the $C = \text{infinity}$ results. All differences stem from the fact that wherever the thin wall boundary condition is applied, the normal gradient of the field is no longer zero, but now has a finite value of H/C . Thus, the current vectors leave and enter the walls at different angles whose values are dependent on the local field magnitudes.

Figures 79, 80 and 81 display the current vectors and the corresponding axial field contours. Hartmann number variation effects are shown in Figs. 82, 83 and 84.

Case with $C = 1$ on all Walls

Results for this case are presented in Figs. 85 through 93. Even for this conductivity ratio, the vectors of Fig. 85 appear closer to the

$C = 0$ case. However, the approach towards the $C = 0$ case as C is reduced is visible by comparison of this case with the $C = \text{infinity}$ and $C = 10$ results. In fact, close inspection of Fig. 87(b) reveals the beginnings of the entrance region axial current loop associated with the $C = 0$ case.

Figures 88, 89 and 90 present the parametric study for this case, while Figs. 91, 92 and 93 portray the induced field distributions which appear to be in-between those for the two limiting cases.

Comparison of the Finite and Limiting Conductivity Cases

Four quantities are compared in Figs. 94 through 96. The relative pressure gradient of Fig. 94 is simply the fully developed axial pressure gradient (at $L = 0.1$) for a particular case, normalized to the non-hydromagnetic pressure gradient. As the Hartmann number and the conductivity parameter increase, so does the pressure gradient. Also, it can be seen that even a little wall conductivity causes large increases in the pressure gradient (note how close the $C = \text{infinity}$ and $C = 10$ curves are). For the limiting cases ($C = \text{infinity}$ and $C = 0$) the results of Chang and Lundgren,¹⁴ and for one finite conductivity case ($C = 1$) the results of Chu¹⁸ have been used for comparison. Both of these works were analytical and involved only the fully developed problem, i.e. one field and velocity component only. Agreement for the $C = 0$ curve is perfect, for the $C = 1$ good, and for the $C = \text{infinity}$ curve not so good at higher Hartmann number. The $C = \text{infinity}$ case involves forcing a gradient to be zero on the boundary, which is similar to forcing a wall heat flux to attain a prescribed value, and it should be recalled the mean Nusselt number for the wall heat flux case was in error by a few

percent. The rather unsophisticated treatment of the variables near the walls is the cause of these errors. Thus, for a Hartmann number of 10 and infinitely conducting walls, the fully developed axial pressure gradient is 4.21 times the non-hydromagnetic one, and for perfectly insulating walls this ratio is only 1.41.

Figure 95 compares the fully developed, relative total pressure coefficients at $L = 0.1$, and trends similar to those in the previous figure are observed. For a Hartmann number of 10 and infinitely conducting walls, the pressure coefficient at $L = 0.1$ is 3.46 times the non-hydromagnetic one, and for perfectly insulating walls this ratio is 1.27. The magnitudes of these variations are less than those for the pressure gradients because the entry lengths decrease with Hartmann number increase, and the higher entry region pressure gradients exist for shorter axial distances. Thus, the entry length reduction and pressure gradient increase work against each other and produce a small variation in the total axial pressure drop as the Hartmann number is increased.

Entrance length variation with Hartmann number and conductivity is seen in Fig. 96(a). It is observed that the relative velocity entry length i.e., magnetohydrodynamic over the hydrodynamic, decreases with increasing Hartmann number, as was expected from the plane channel analysis of Shohet et al. Increasing the conductivity parameter from zero to infinity also cause a slight decrease in this length owing to the fact that the $C = \text{infinity}$ profiles are slightly flatter, and thus nearer in form to the initial slug profile. For a Hartmann number of 10 and $C = 0$, the relative velocity entry length is 0.224, while for $C = \text{infinity}$ it is 0.212.

The mean Nusselt number of Fig. 96(b) is seen to increase with Hartmann number and conductivity increase. The conductivity variations quickly reach an asymptotic condition and there is essentially no difference between the $C = \text{infinity}$ and $C = 10$ curves. Increase with Hartmann number is quite significant and is again the result of flatter temperature profiles and steeper wall temperature gradients. For a Hartmann number of 10 and $C = \text{infinity}$, the Nusselt number is seen to be 4.09, while for $C = 0$ it is 3.99. The similar value for the non-hydromagnetic case is 3.55. Thus, though a price for higher Hartmann numbers is paid by way of larger pressure drops, the benefit of heat transfer enhancement is reaped.

Some Mixed Wall Conductivity Cases

In the previous problems, wall conductivity was constant throughout the duct and for finite values of C the pressure drops were significantly higher than for the corresponding non-magnetic cases. This effect is even more exaggerated in the fusion blanket situation since at very high Hartmann numbers hydromagnetic pressure drops are expected to be a few orders of magnitude higher. As a direct result of this, an unacceptable proportion of the reactor output is required for pumping power. If the duct walls are fabricated from an electrical non-conductor, this problem would be greatly reduced. However, since a non-conductor of electricity is usually a poor conductor of heat, the heat transfer capabilities of such a blanket could be impaired.

Possible solutions to this problem involve having some of the walls be electrical insulators, and some be electrical conductors. Since the

heat flow in the blanket will essentially be in the radial direction away from the plasma, the walls perpendicular to this direction could be made of metal, while the remaining two walls could be made of an electrical insulator, e.g. a ceramic. Thus, the two possible combinations of infinite conductivity on two walls and zero on the other two are studied here as Cases A and B. Hunt¹⁹ has suggested that the conductivity of the duct corners may play an important role in determining the pressure drop. This problem is investigated in Case C, while Case D deals with the same problem but with the addition of two non-conducting current breaks to each wall.

Cases A and B

Case A involves $C = 0$ on walls parallel to the imposed field and $C = \text{infinity}$ on walls perpendicular to the imposed field, while Case B is the reverse. Figures 97 and 98 show that the currents leave conducting walls, and form a semicircular loop eventually returning to the same walls from which they originated. As expected these currents can only flow parallel to the non-conducting walls and not enter them. Representation of the current vectors in the axial plane is provided by Fig. 99. The loop that is observable in the central xz plane is caused, as before, by currents in this entry region being unable to return through the parallel non-conducting walls. Corresponding vectors and contours for Case B are shown in Figs. 100 to 102. The magnitudes of the currents are definitely smaller for this case. Currents near the center flow directly from one conducting wall to the other, but have to return via the boundary region fluid along the non-conducting walls. Complete current loops

lying entirely in the fluid also exist near each non-conducting wall. Figure 100(a) shows core current flow in a reverse direction from the fully developed flow. This is essentially the equivalent of the loop observable in Case A, only now the ends of the loop lie in the conducting walls. Figure 102(b) shows this clearly. Induced field distributions for Cases A and B are shown in Figs. 103 to 109. The differences between them for the two cases are direct consequences of the boundary conditions. The peak values for the axial field of Case A are about four times higher than those for Case B. This was the cause of the stronger currents observed for Case A. In fact, the field values for Case A appear to be similar to those for the case with C equal to infinity on all the walls, while those for Case B appear to be near the case with C equal to zero on all the walls. This leads one to suspect that it is the conductivity of the walls perpendicular to the imposed field that is important.

Axial velocity contours and surfaces are presented in Fig. 110, and the contours are elongated in the direction of the non-conducting walls for both cases. To explain these contours it must be recalled that the Lorentz force is $\bar{J} \times \bar{B}$. The largest component of \bar{B} is the imposed one, which is along the y direction. Thus, any current flow along this parallel direction creates little or no $\bar{J} \times \bar{B}$ force, while current flow along the positive z direction produces a strong retarding force. From the current diagrams for Case A it was seen that currents leave the conducting walls in the y direction, turn, follow the positive z direction, turn again, and complete the semicircular loop by returning along the y direction to the conducting wall of origin. Thus the Lorentz force

is essentially retarding and acts on the core region where the currents are along the positive z direction. The regions where the velocity contours are elongated are those regions where the currents are either still completely in the y direction, or turning, thus creating comparatively small Lorentz force action which results in higher axial velocities and hence the elongated contour. Since there is no current flow along the negative z direction, and thus no accelerating Lorentz force component, the pressure gradient for this case is expected to be comparable to the case with all walls having C equal infinity. The magnitude of this gradient is discussed in the upcoming case comparison.

For Case B the current density pictures show strong return currents flowing in the negative z direction within the fluid adjacent to the non-conducting perpendicular walls. These currents produce an accelerating Lorentz component, while the core regions still produce a retarding component. Higher axial velocities near the non-conducting walls are the result and this explains the contour elongation of Case B. The pressure gradient for this case should be much lower than for Case A due to the Lorentz accelerating component, and the fact that some of the current loops lie entirely within the fluid region.

Axial velocity profile development across the y direction for both these cases is shown in Fig. 111. It is readily observable that the profiles for Case B are flatter across this coordinate. Axial velocity distributions like those for Case A would have required larger mass transfer from the duct edge to the center in the y direction, and so the v velocity component should be larger than the corresponding w component in the developing region. The profiles of Figs. 112(a) and (b) clearly

demonstrate this fact, and the vectors of Fig. 112(c) also show a flow biased towards the y direction. Case B would show a similar but reversed effect.

In the temperature solutions for these two cases, the constant heat flux boundary condition was imposed on all four walls. This assumes the use of a material that is a good thermal conductor while being an electrical insulator as well. Such materials, though rare, do exist. Berilium oxide, which is an electrical insulator and has a thermal conductivity higher than most metals, is one such example. Fully developed temperature contours for these two cases are shown in Fig. 113, and again suffer the same elongations as the corresponding velocity contours.

Cases C and D

From all the previous results, it is evident that the less current there is flowing within the walls, the lower is the pressure drop. Insulating the corners of a perfectly conducting duct (Case C) is a step in this direction. Also, sections of the same duct wall can be insulated from each other by inserting current breaks into the wall. These breaks can be thought of as axial lines of insulation at various positions along the periphery of the duct (Case D). Current breaks, while having substantial effect on the pressure drop, are not expected to have much effect on the heat transfer as the principal directions of heat flux are normal to these lines of insulation. Numerically, the insulated corners were achieved by specifying the electrical insulation condition at two points on either side of each corner. Two current breaks on each wall were inserted again by specification of the same condition at the 6th mesh point from each corner.

Current density vectors and axial field contours for both these cases are shown in Figs. 114 through 117. These vectors and contour loops show distinct avoidance of the insulated corners, having to jump these regions by re-entering the fluid. This same effect is observed with the current breaks especially on the perpendicular walls. The current loops must re-enter the fluid to bypass the breaks. It is also seen that the breaks on the parallel walls are less effective in their present positions, and that their performance would be improved if they were a little closer to the corners. The axial plane vectors of Fig. 118 appear confusing at first, but on comparing them with the transverse plane vectors of Fig. 116, it is seen that their distribution is a result of abrupt direction changes the currents must undergo to jump the insulated breaks and corners. Induced field surfaces are portrayed by Fig. 119, and the corners and breaks are easily seen as the regions where all the fields are forced to zero.

Effects on the axial velocity, represented by Fig. 120, are interesting. The corner velocities have been increased and the contours are quite a bit squarer. For Case D, the breaks cause these contours to bow out a little bit in the region corresponding to the breaks on the perpendicular walls, which are the most effective. Axial velocity profiles are flatter along the z direction, and they are shown along both z and y centerlines in Fig. 121 for Case C. The centerline profiles for Case D are similar. Contours and wall temperature profiles for Case C are shown in Figs. 122 and 123.

Case comparisons of A, B, C and D are plotted in Figs. 124 through 126. In these figures, $H_{ap} = 0$ refers to the non-hydromagnetic case

which is included for comparison. Cases A and C have essentially the same pressure drop, and this is about 60% of the pressure drop for a fully $C = \infty$ duct. This leads to the interesting conclusion that insulating the corners alone is equivalent in pressure drop reduction to insulating both parallel walls entirely. Addition of the current breaks in Case D reduces the fully developed pressure drop a further 20% or so. Case B, however, experiences the lowest pressure drop of all the four cases, and is only slightly higher than the totally $C = 0$ case. Recalling that Case B represented $C = \infty$ on parallel walls and $C = 0$ on perpendicular walls, one can conclude that the pressure drop in particular is strongly dependent on the conductivity of the walls that are perpendicular to the imposed field direction.

Maximum center-point axial velocity occurs for Case B, followed by D, A and C in that order. Case D is larger than C due to the accelerating effects of the current breaks, and B is larger than A due to the accelerating effects in the boundary regions. Maximum fully developed mean Nusselt number occurs for Case C (4.29) followed by D (4.17), A (4.13) and B (4.02), and it should be recalled that the corresponding non-hydromagnetic value was 3.55. Thus, Case C shows about a 25% increase over this value and is the highest because of the squaring of the velocity contours by the electrically insulating corners. Wall center and corner temperature comparisons are shown in Fig. 126.

Cases E, F and G

These last three cases relate directly to Tokamak blankets. As it has been previously mentioned, the duct under consideration could have one of its sides as part of the first wall and is thus exposed to a heat flux corresponding to radiation and neutron heating along that wall. If it

is assumed that the three ducts adjacent to this duct have similar temperature distributions, then adiabatic temperature boundary conditions can be used on the other three walls. The poloidal field is in the y direction, and so one of the walls parallel to this direction must be the one exposed to the plasma, i.e. the constant wall heat flux. These thermal boundary conditions lead directly to the induction boundary conditions of $C = 0$ on the three adiabatic walls, and $C = \text{infinity}$ (Case E) or more appropriately $C = 0.1$ (Case F) on the heat flux wall. The value $C = 0.1$ corresponds more directly to the fusion blanket case as it is obtained by assuming $\sigma_w/\sigma_f = 2$, which is about the proper conductivity ratio for steel and lithium, and $t/D = 0.05$, which is a reasonable wall thickness to duct width ratio. Finally Case G investigates the effect of extending the electrical insulation to include the corner regions of the conducting wall in Case F.

Figure 127 represents current density vectors for Case E. Currents leave the conducting wall, travel through the fluid core and return via the boundary regions adjacent to the perpendicular non-conducting walls. Near the duct entrance, the core current flows in the opposite direction to the fully developed current. This flow is simply the top of the axial current loop seen in Fig. 128(b). Velocity contours shown in Fig. 129 are again elongated towards the non-conducting walls (velocity profiles along the z direction are slightly skewed) being smaller on the side towards the one conducting wall. This is not due so much to the currents flowing near the non-conducting parallel wall, as $\bar{J} \times \bar{B} = 0$ for the parallel direction, but to the currents emerging from the conducting wall for which the Lorentz force is retarding.

Induced field distributions for Case E are displayed in Figs. 130 and 131 and are reflective of the imposed boundary conditions. In a Tokamak blanket, the neutrons provide an internal heat generation whose magnitude is dependent on the distance from the first wall. If a duct width of 10cm is assumed, a neutron heat deposition curve from the Wisconsin Tokamak Design Report⁴² leads to the use of a heat generation that linearly decreases from 1 at the first wall (i.e. the conducting wall) to 0.7 at the opposite wall. Figures 132 and 133 represent center-line temperatures and contours with and without this heat generation function. Temperatures across the conducting wall are shown in Fig. 134 and this distribution is almost flat. This is desirable for uniform cooling of the first wall. The bulk temperature and wall temperature developments are shown in Fig. 135.

For Case F the conducting wall has $C = 0.1$ to correspond to a steel wall and lithium fluid. Figures 136 and 137 show that this finite conductivity causes some of the loops to pass through the conducting wall. However, most lie entirely within the fluid, and the fully developed axial pressure gradient and velocity are essentially the same as for the case with $C = 0$ on all four walls. This is as expected since it has already been concluded that the pressure drop is strongly dependent on the conductivity of the perpendicular walls and relatively insensitive to the conductivity of the parallel walls. Thus, having one metallic wall for heat transfer and three non-conducting walls, i.e. ceramic, involves no higher pressure drop than for all non-conducting walls.

Case G is simply the above case with the electrical insulation extended to include the corners of the $C = 0.1$ wall. Figures 138 and 139

show how the currents again avoid the corner regions. However, there is very little variation between mean parameters for this and the previous case.

Stability and Computer Time Requirements

Before this chapter is closed some comments on the numerical stability and computer time requirements of the previous problems need to be made. The numerical scheme, being implicit in the transverse plane is inherently stable. The accuracy of the representation, however, is strongly dependent on the size of the forward axial step as the upwind differencing that has been used is essentially first order. As previously mentioned, 216 axial steps were used to represent an axial length equivalent to 10 duct widths. The axial step-size was 0.01 for the first 20 and 0.05 for the remaining 196 steps. The transverse mesh spacing was also 0.05. It is desirable to have Δy and Δz the same size as Δx , since the scheme is first order in the axial direction and so the truncation errors are proportional to Δx . This holds no matter how small Δy and Δz are made.

Initial runs of the program were made on a 10 x 10 mesh with 80 axial steps, and though the results were less accurate, there were no stability problems for these cases either. The main requirement for stability is that the number of sweeps of the Tri-diagonal Matrix Algorithm should be increased as the number of points in the transverse plane is increased. For the 10 x 10 mesh, 10 sweeps were required, while for the 20 x 20 mesh, 15 were necessary. If the number of sweeps is not sufficient, the calculation diverges explosively.

These problems were run on a Control Data Corporation Cyber 74 multi-processor system located at the Georgia Institute of Technology. For a 20 x 20 mesh, and 216 axial steps, the run times were about 8 minutes for the velocity, 10 minutes for the temperature and velocity, and 15 minutes for the temperature, induction and velocity problem.

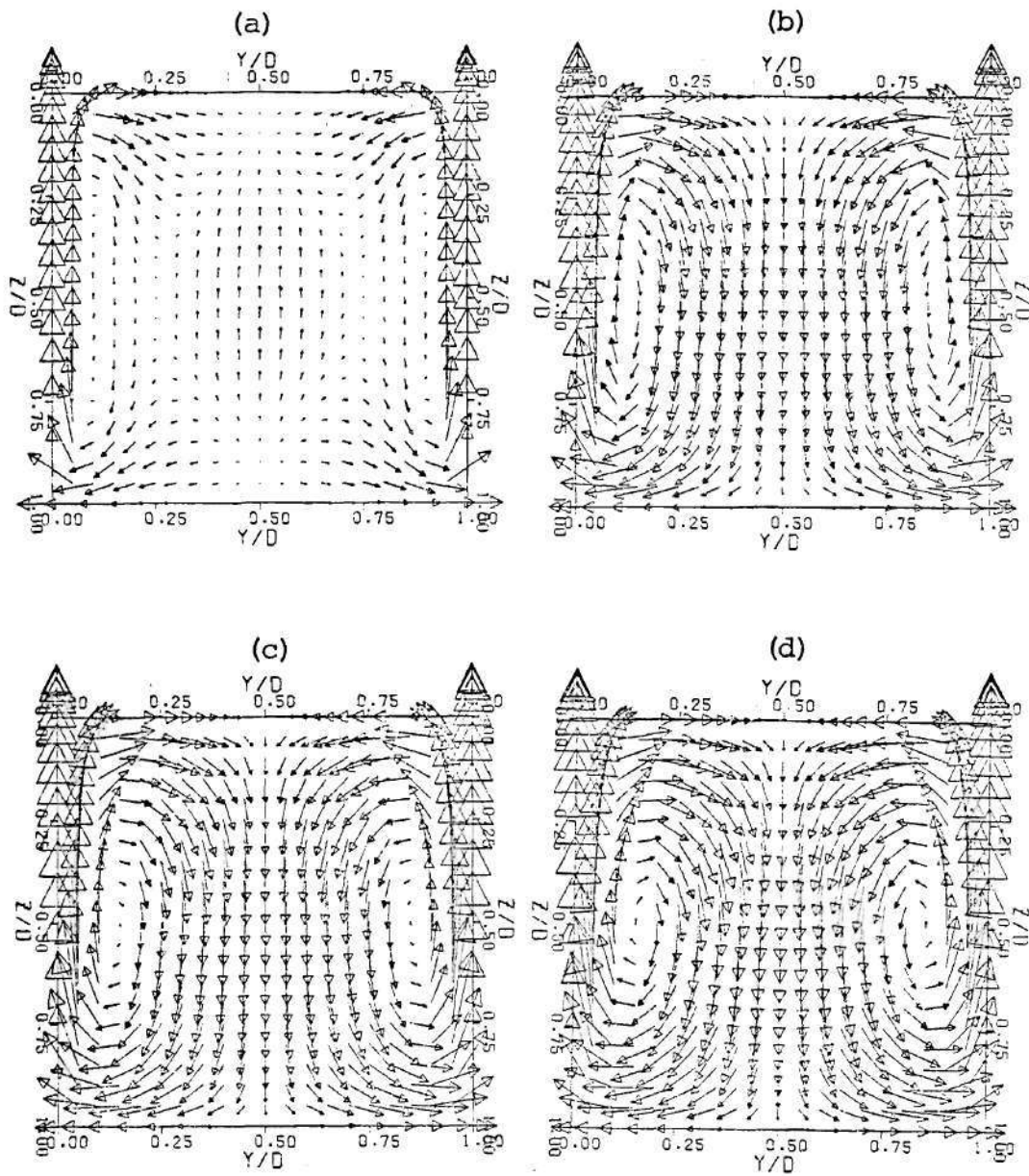


Figure 54. Current Density Vectors for $C=0$ at

- (a) $L=0.001$
- (b) $L=0.005$
- (c) $L=0.010$
- (d) $L=0.100$

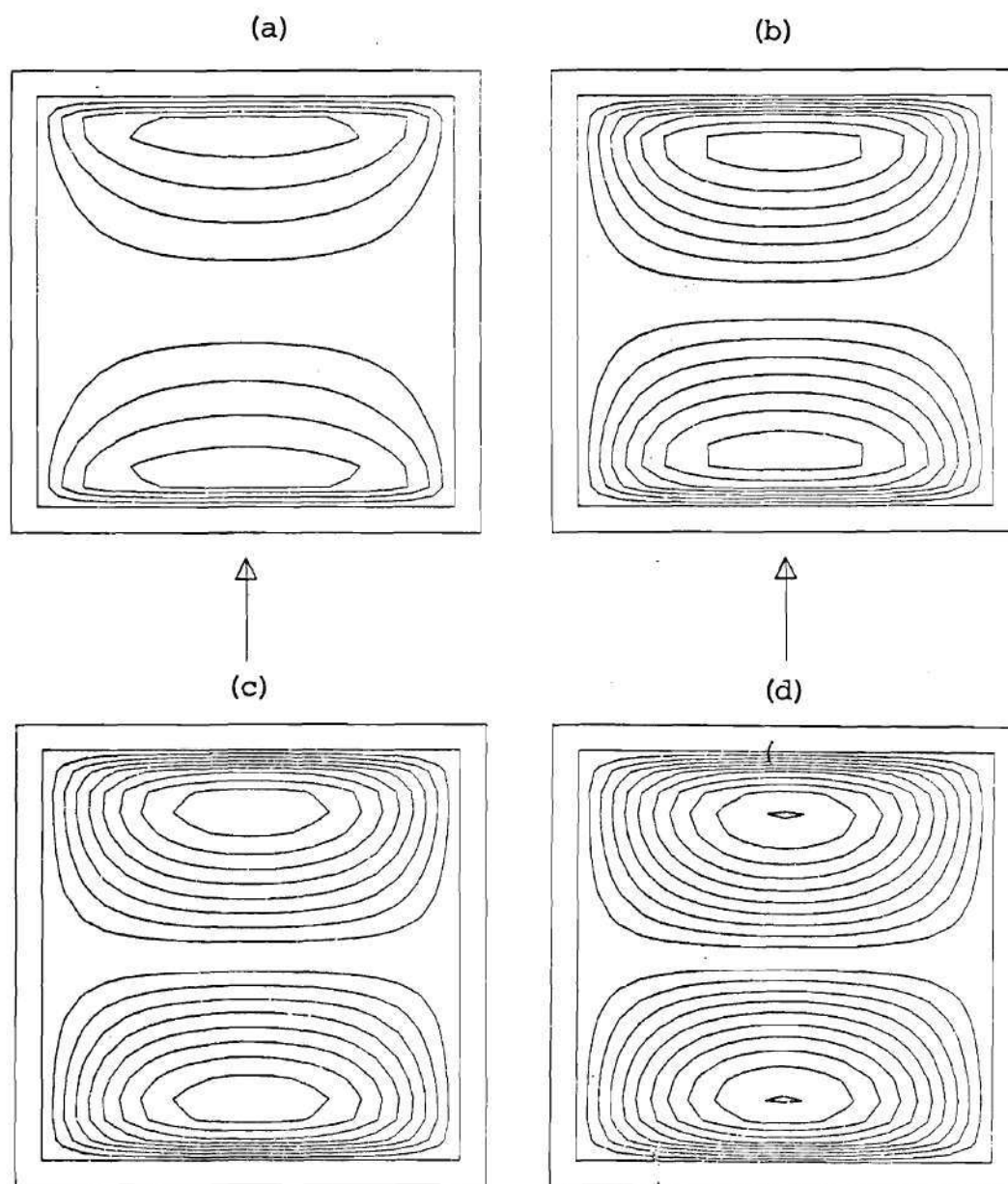
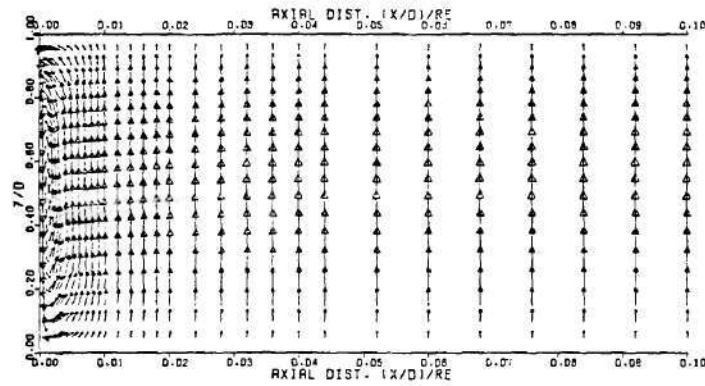


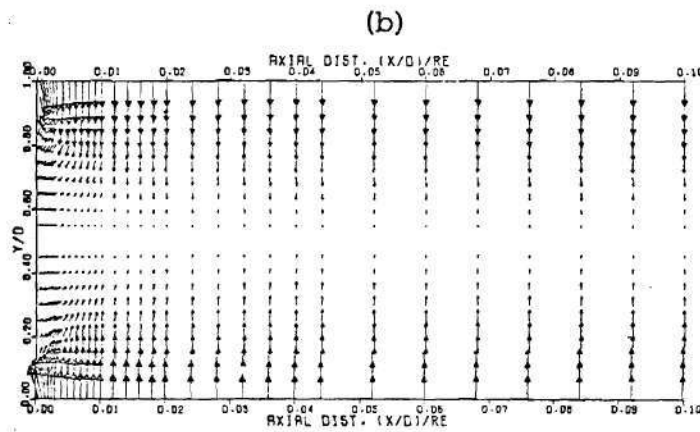
Figure 55. Axial Induced Field Contours for $C=0$ and at

(a) $L=0.001$, (b) $L=0.005$,

(c) $L=0.010$, (d) $L=0.100$



(a)

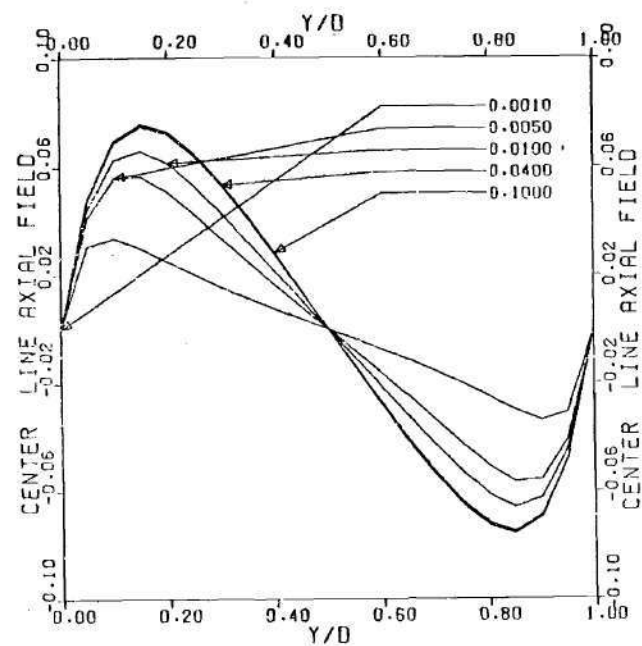


(b)

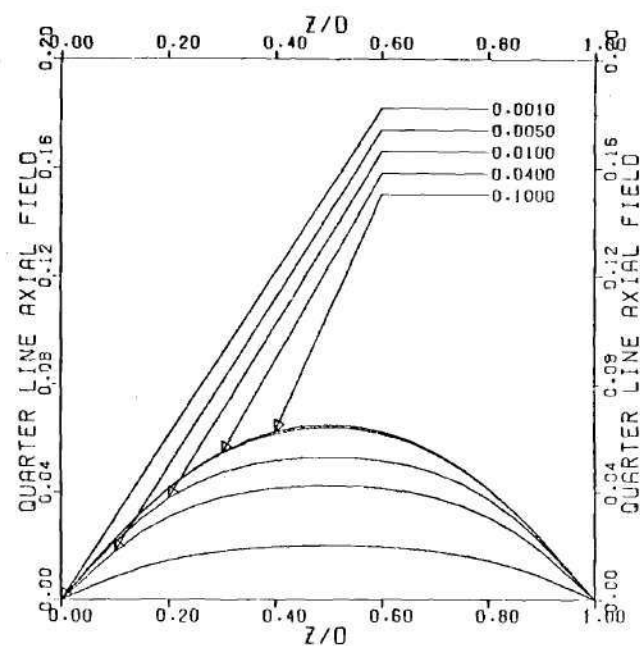
Figure 56. Current Density Vectors in Axial Plane

(a) xz at Center

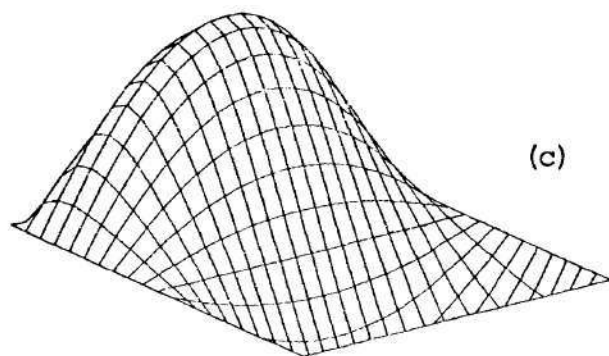
(b) xy near Wall ($Z/D=0.05$)



(a)

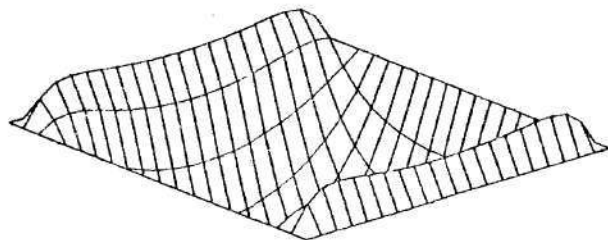
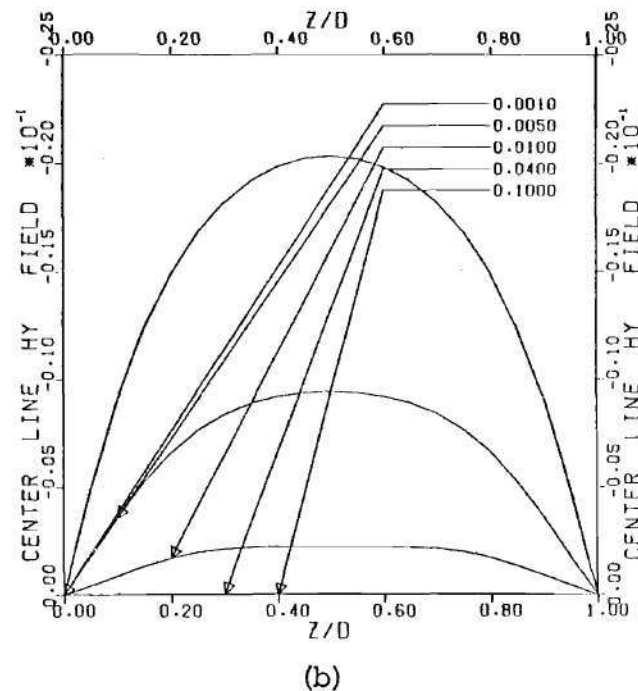
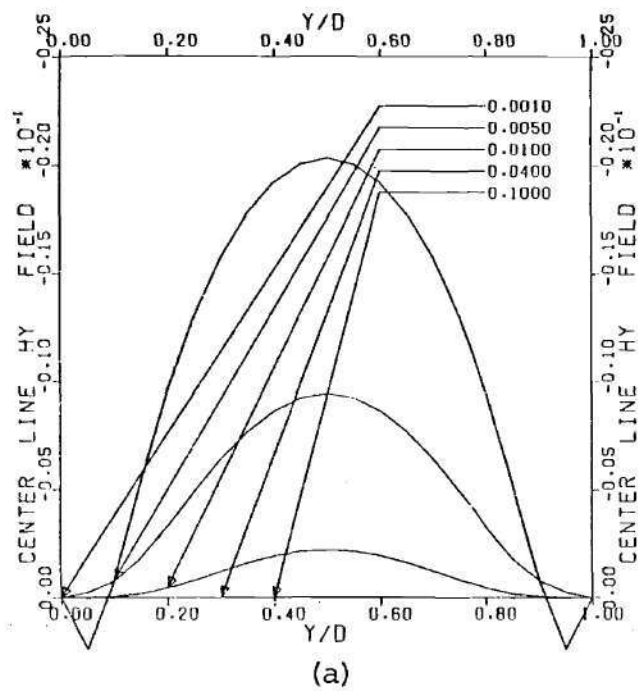


(b)

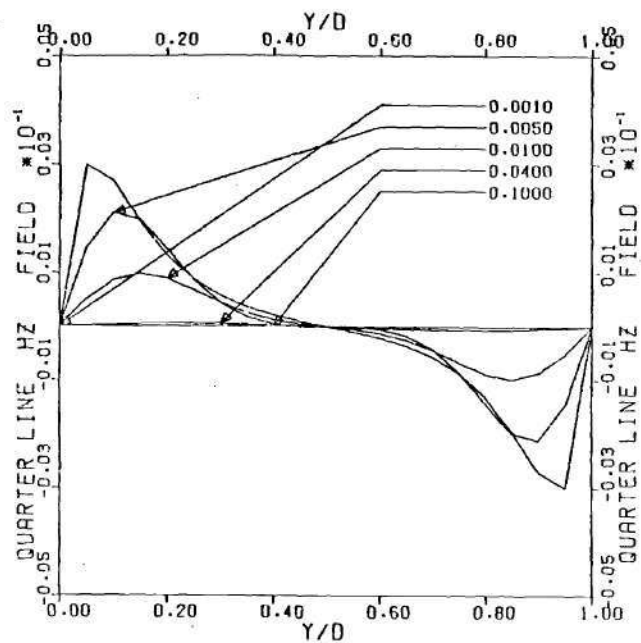


(c)

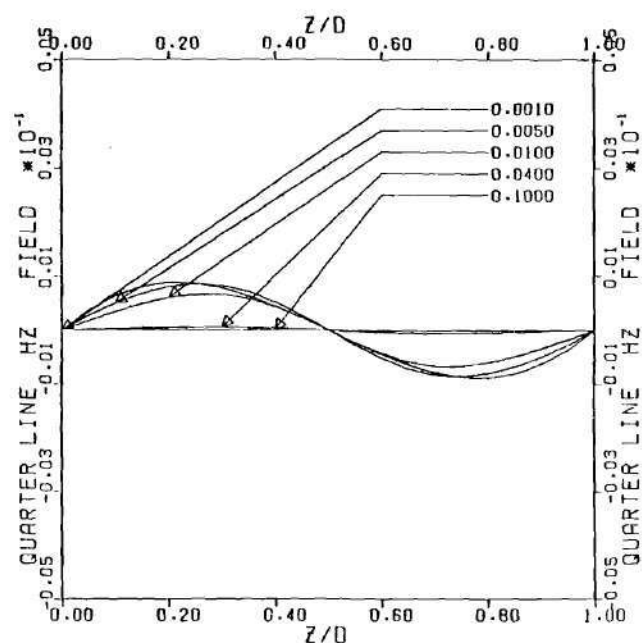
Figure 57. (a) and (b) Axial Induced Field for Values of L
(c) Axial Field Surface at $L=0.1$



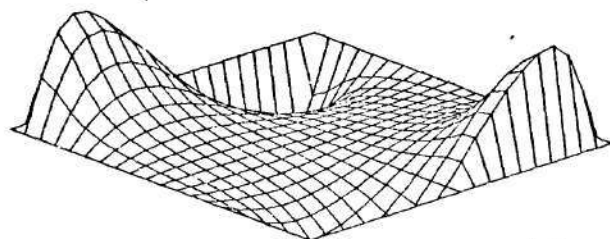
(c) Figure 58. (a) and (b) Hy Field for
Values of L
(c) Hy Field Surface at
 $L=0.001$



(a)



(b)



(c)

Figure 59. (a) and (b) Hz Field at
Values of L
(c) Hz Field Surface at
 $L=0.001$

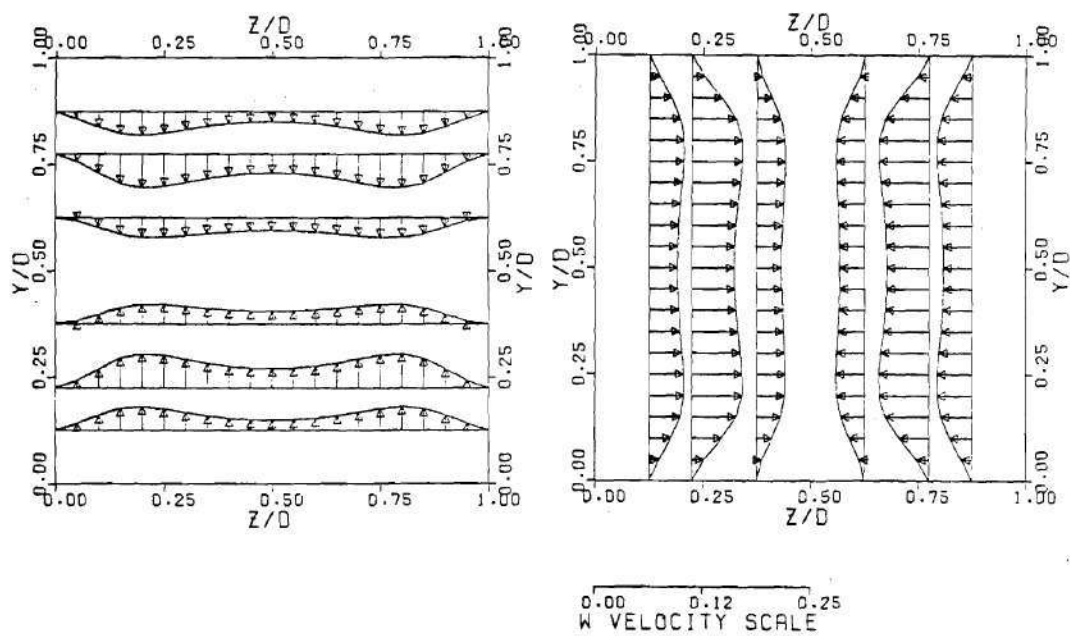
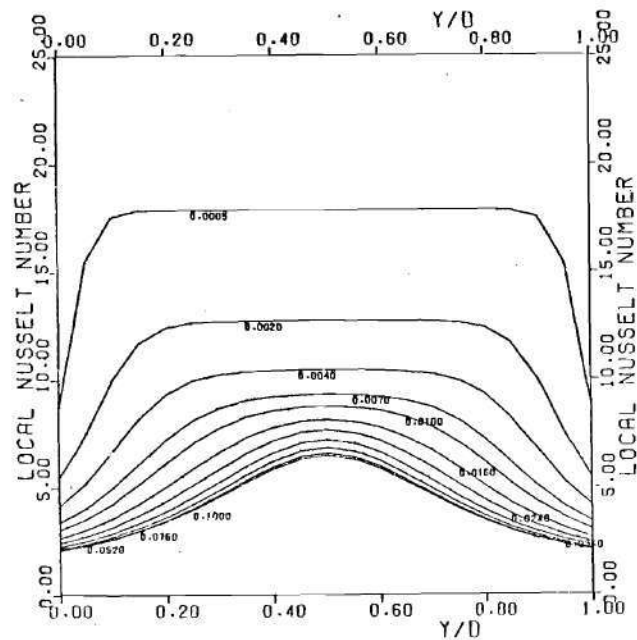
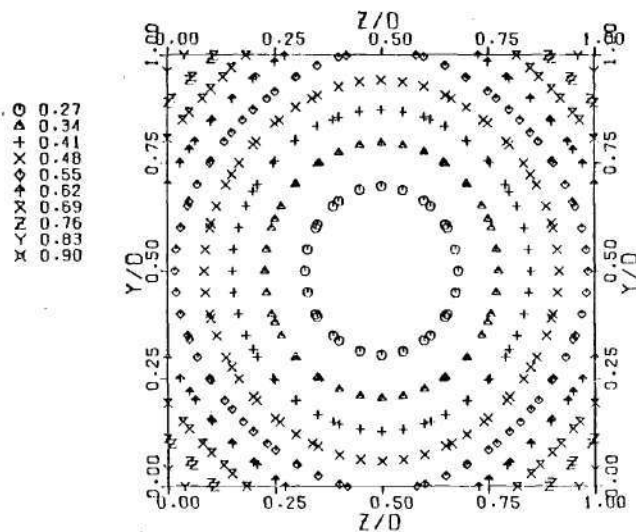


Figure 61. v Velocity Profiles at $L=0.005$ (a)

w Velocity Profiles at $L=0.005$ (b)

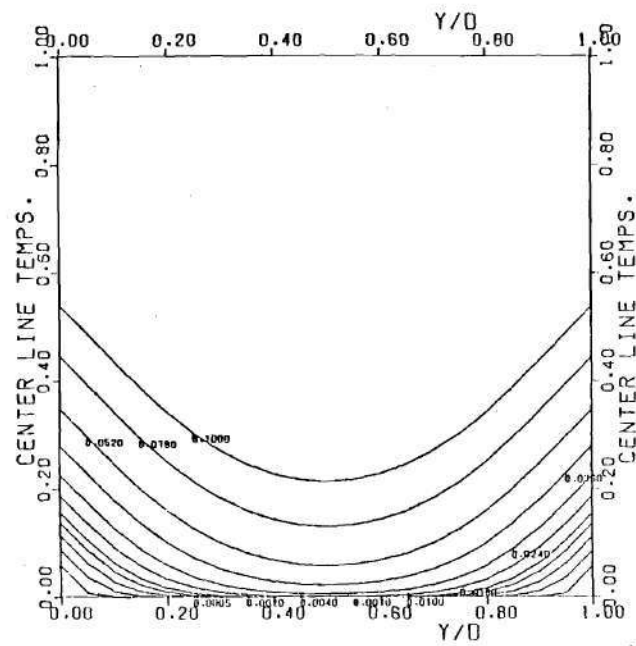


(a)

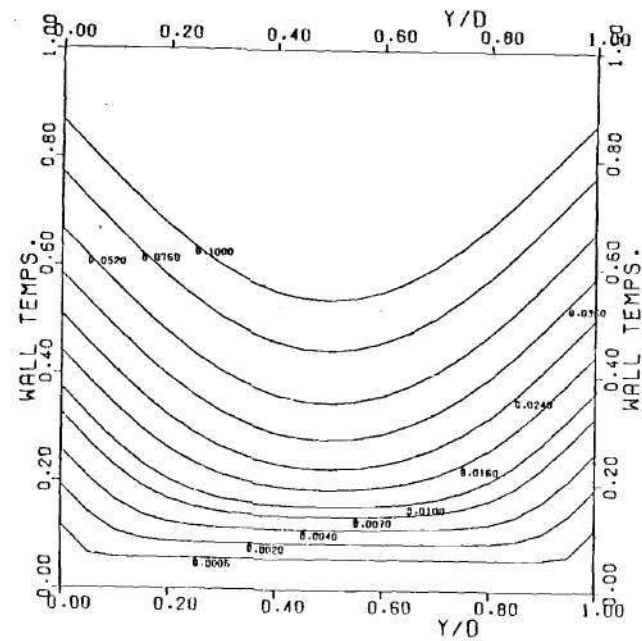


(b)

Figure 62. (a) Nusselt Numbers at Values of L
 (b) Temperature Contours at $L=0.1$
 Constant Wall Heat Flux



(a)

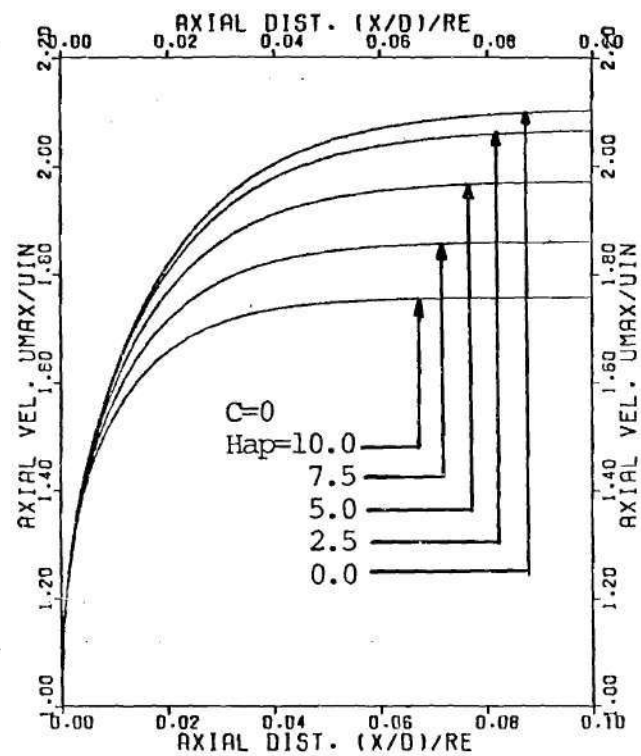


(b)

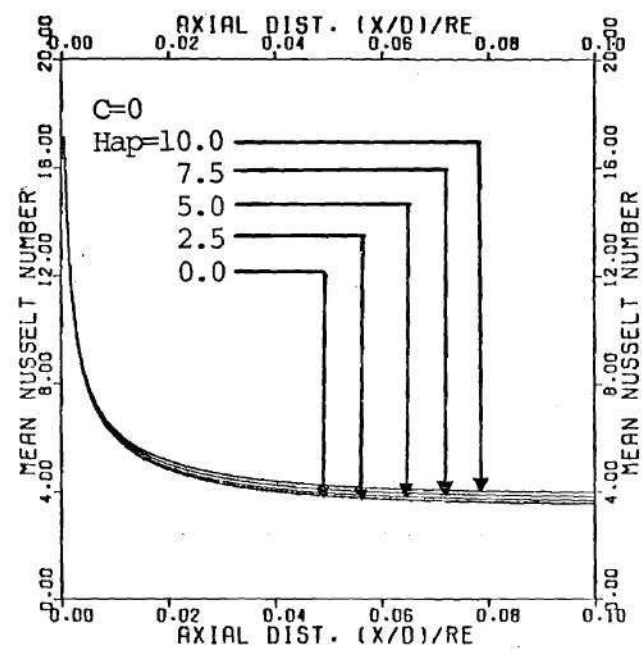
Figure 63. (a) Center-line Temperatures at Values of L

(b) Wall Temperatures at Values of L

Constant Wall Heat Flux



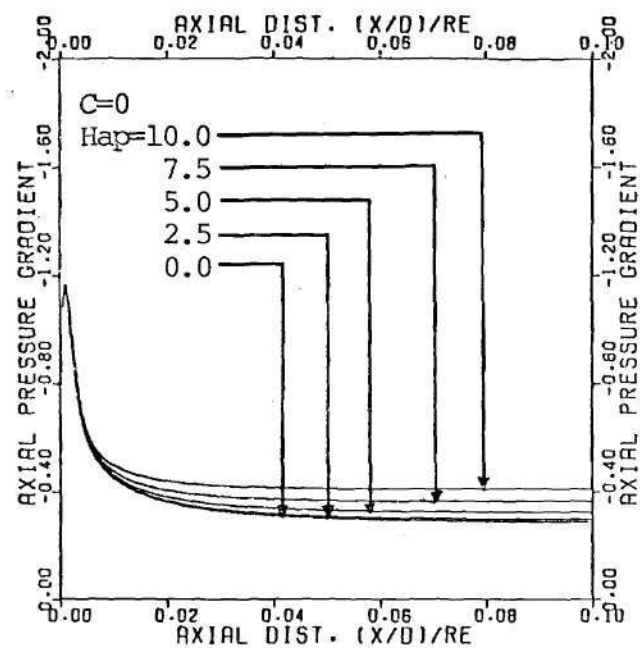
(a)



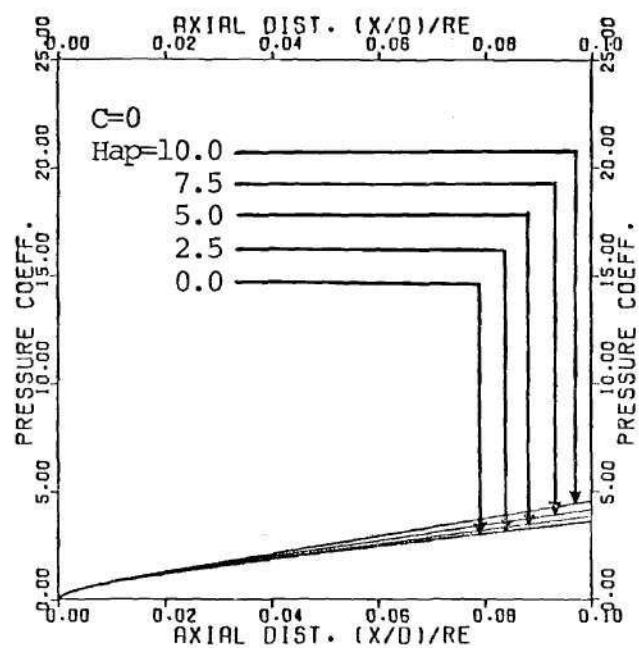
(b)

Figure 64. (a) Center-point Axial Velocity Development
(b) Mean Nusselt Number Development

$C=0$



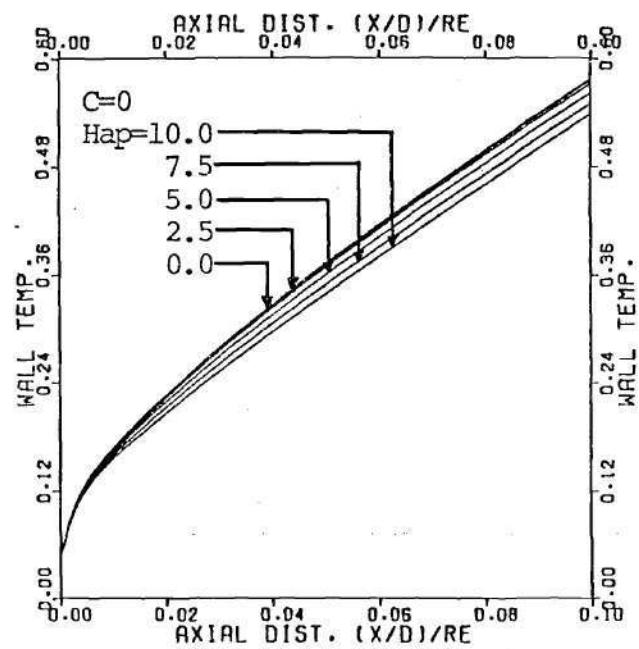
(a)



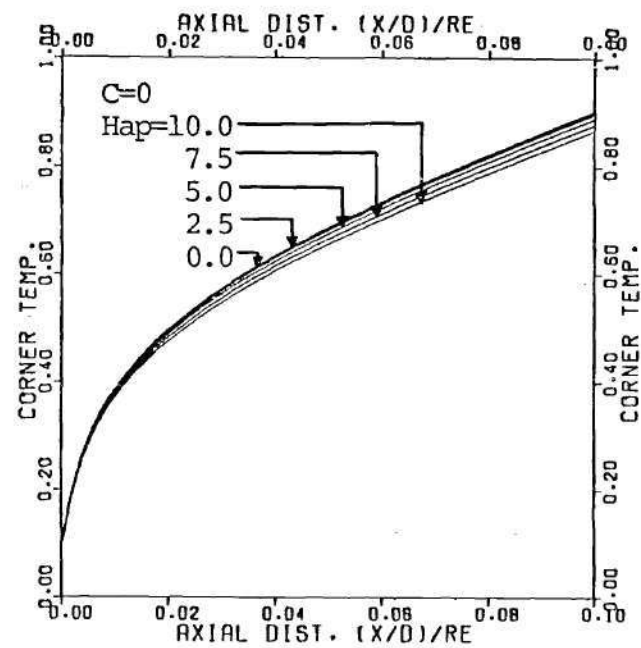
(b)

Figure 65. (a) Axial Pressure Gradient Development
(b) Pressure Coefficient Development

$C=0$



(a)



(b)

Figure 66. (a) Wall Center Temperature Development

(b) Wall Corner Temperature Development

$C=0$

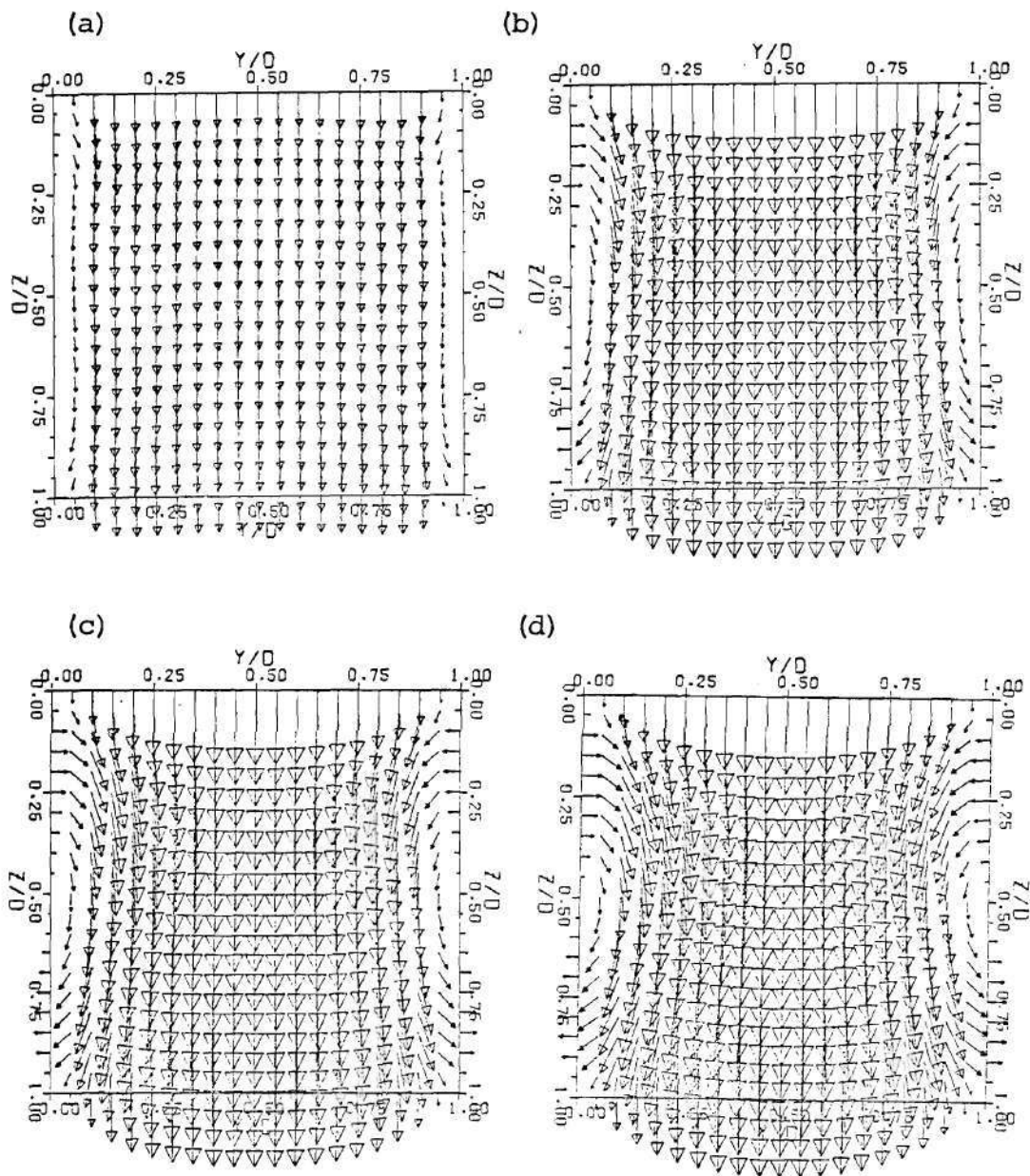


Figure 67. Current Density Vectors at
 (a) $L=0.001$, (b) $L=0.005$,
 (c) $L=0.010$, (d) $L=0.100$
 $C=\text{infinity}$

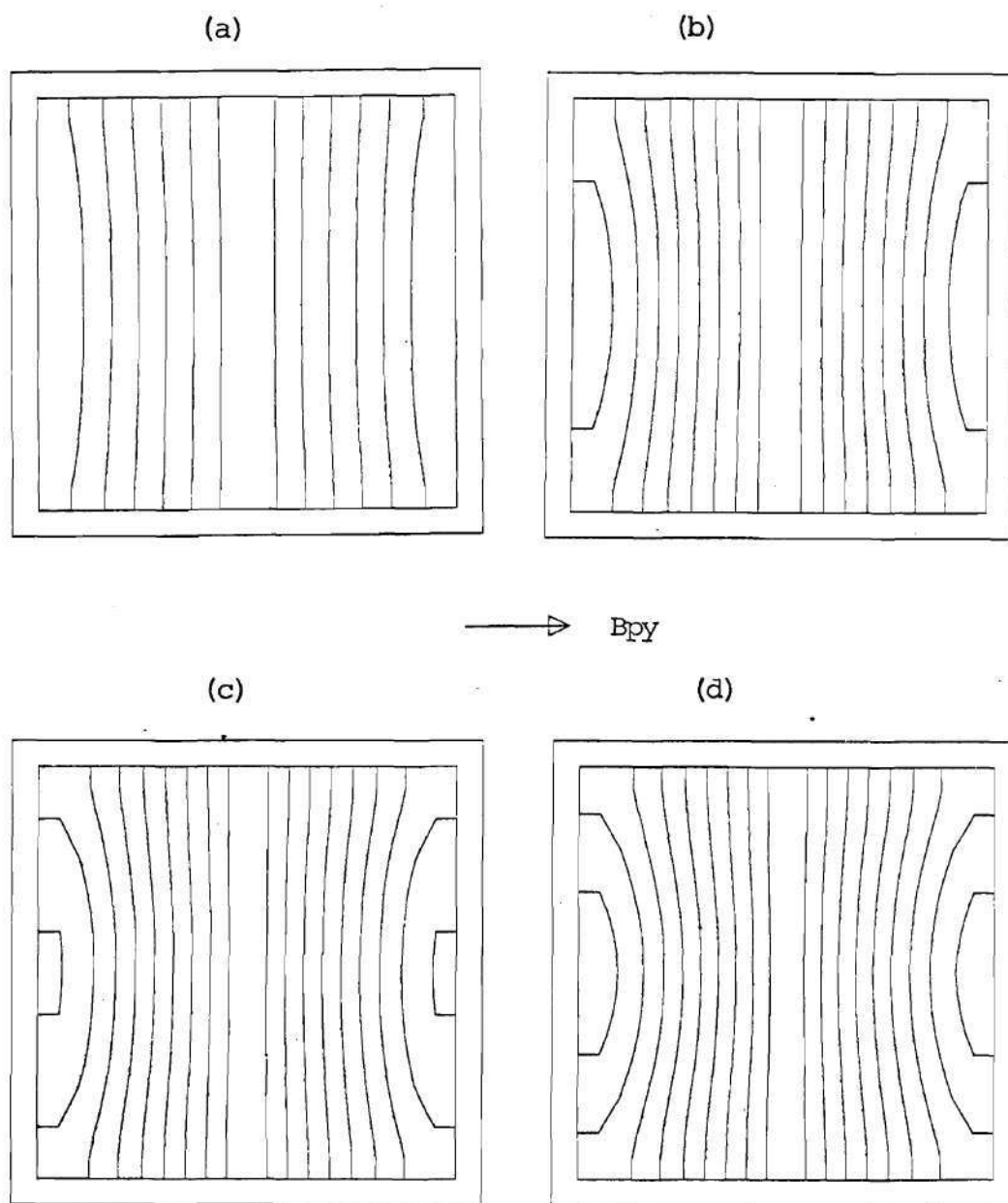
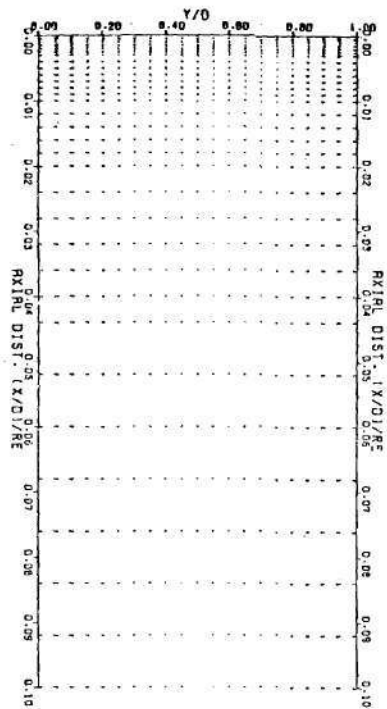
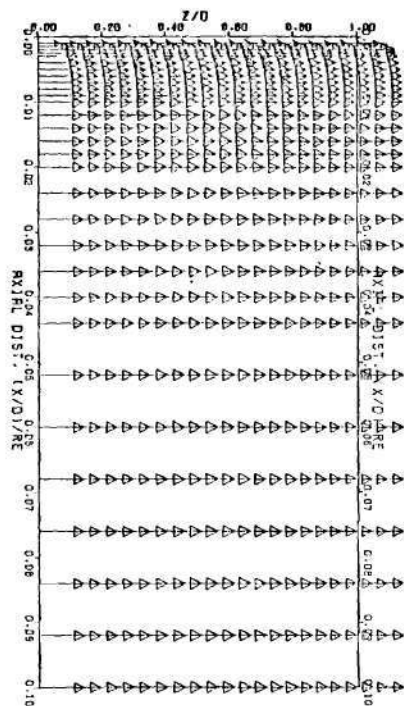


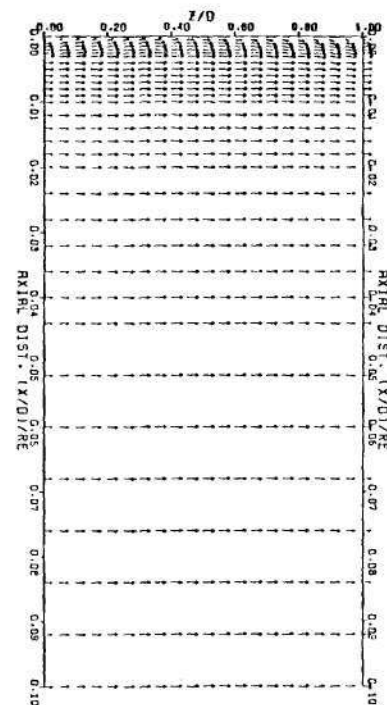
Figure 68. Axial Field Contours at
 (a) $L=0.001$, (b) $L=0.005$
 (c) $L=0.010$, (d) $L=0.100$
 $C=\infty$



(a)



(b)



(c)

Figure 69. Current Density Vectors in Axial Plane

(a) xy near Wall ($Z/D=0.05$) , (b) xz at Center

(c) xz near Wall ($Z/D=0.05$)

$C=\infty$

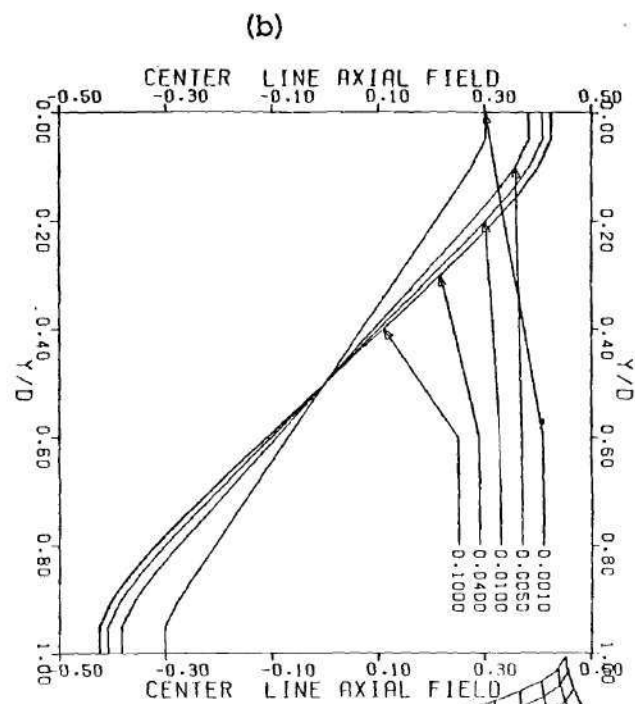
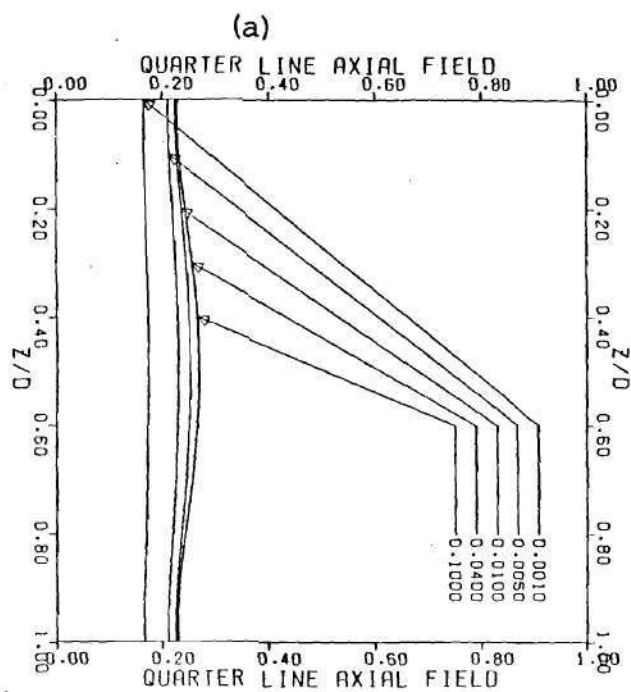
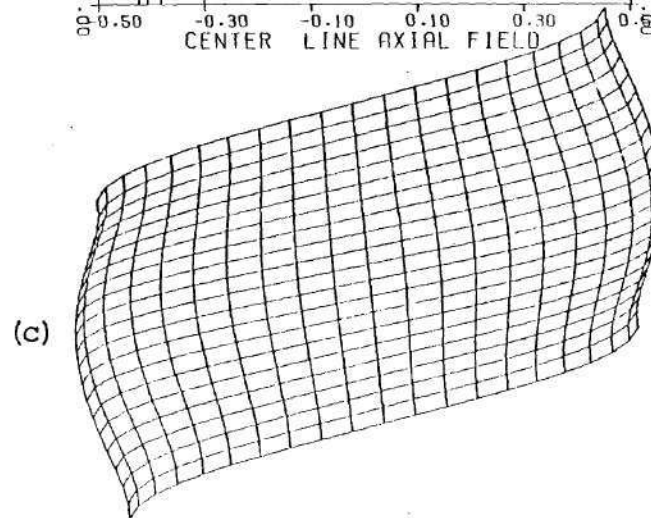


Figure 70. (a) and (b) Axial Field at
Values of L
(c) Axial Field Surface at
 $L=0.1$
 $C=\infty$



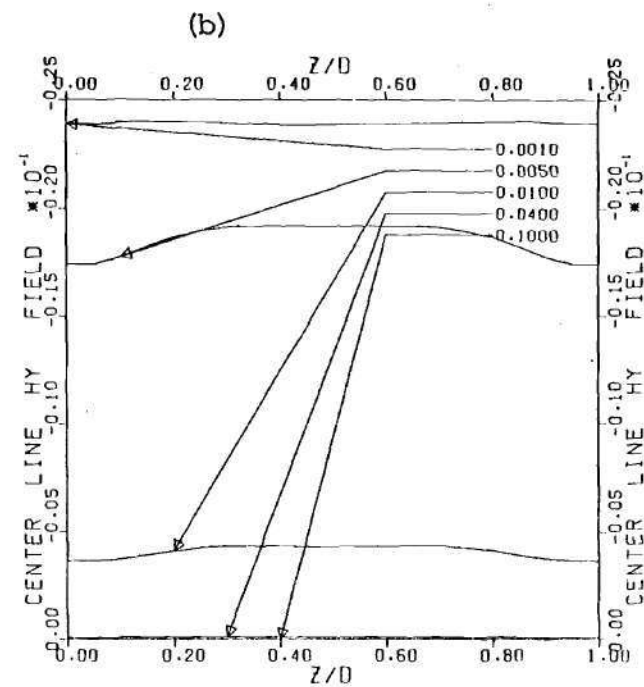
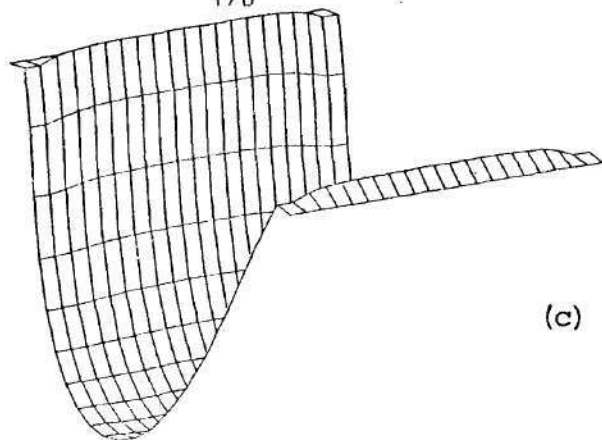
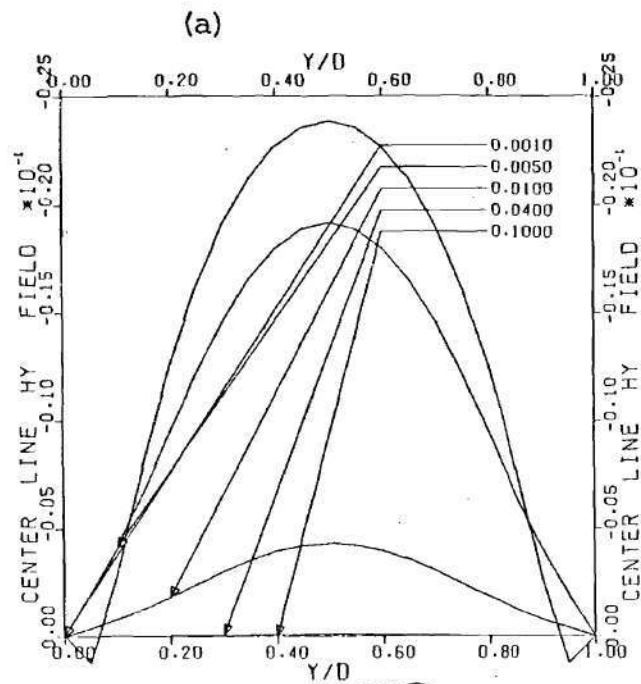


Figure 71. (a) and (b) Hy Field at
Values of L
(c) Hy Field Surface at
 $L=0.001$

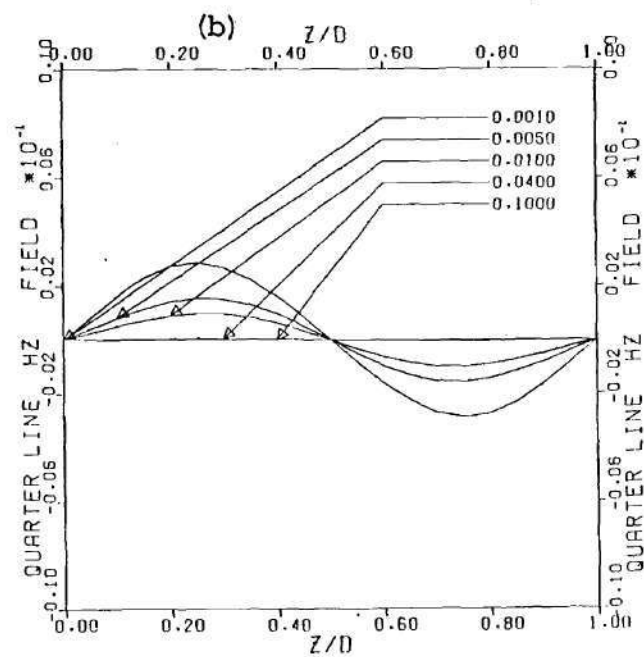
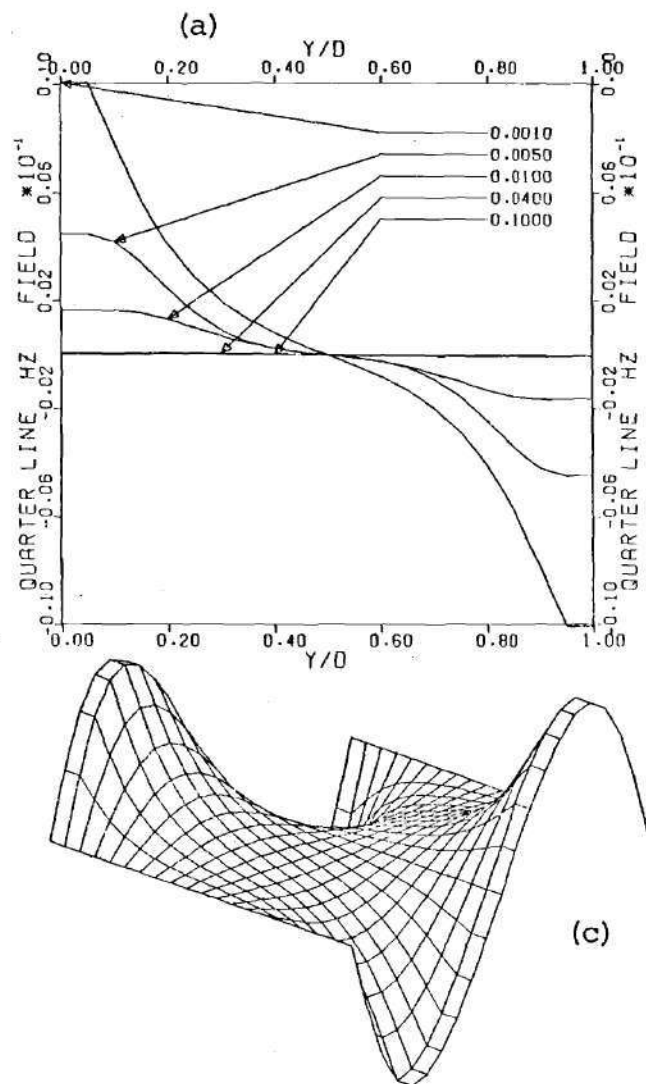
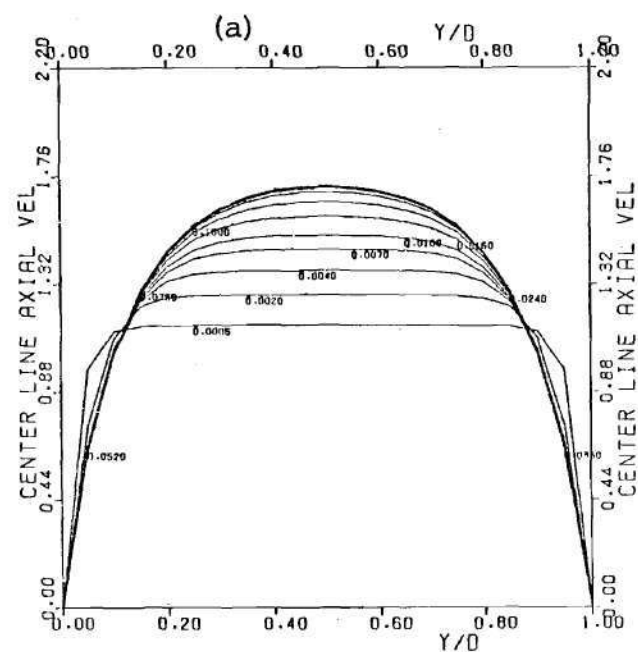


Figure 72. (a) and (b) Hz Field at
Values of L
(c) Hz Field Surface at
 $L=0.001$

$C=\infty$



O 0.20
 A 0.40
 + 0.60
 x 0.80
 x 1.00
 x 1.20
 x 1.40
 x 1.60
 x 1.80
 x 2.00

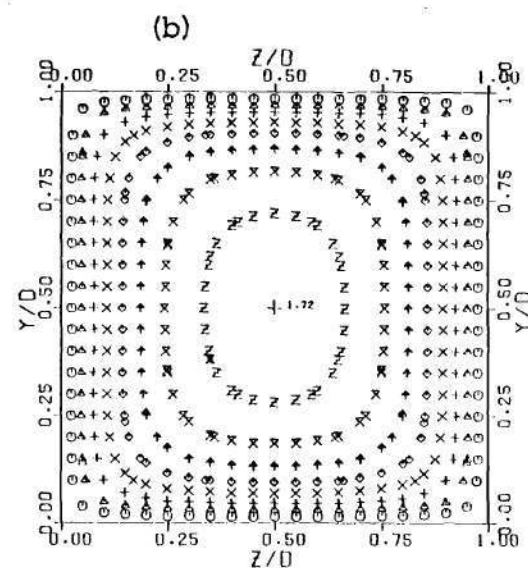
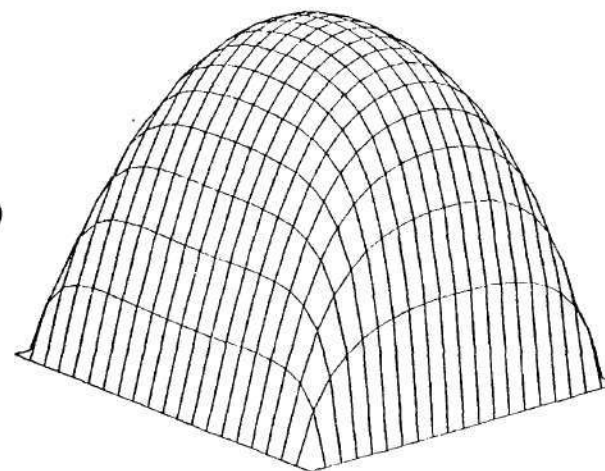


Figure 73. (a) Axial Velocity for Values of L
 (b) and (c) Velocity
 Contours and Surface
 at $L=0.1$

$C=\infty$

(c)



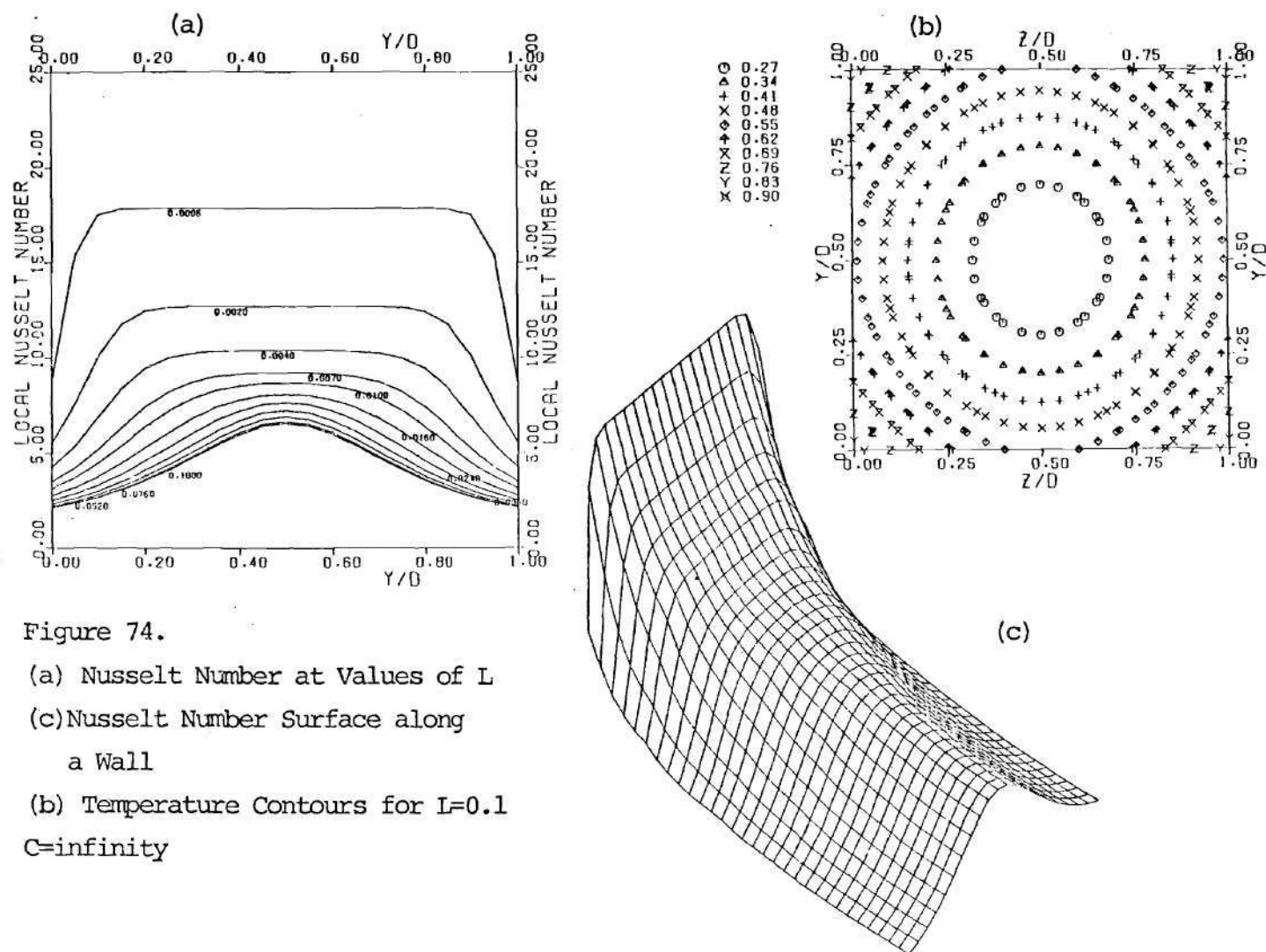


Figure 74.

(a) Nusselt Number at Values of L

(c) Nusselt Number Surface along
a Wall

(b) Temperature Contours for $L=0.1$
 $C=\infty$

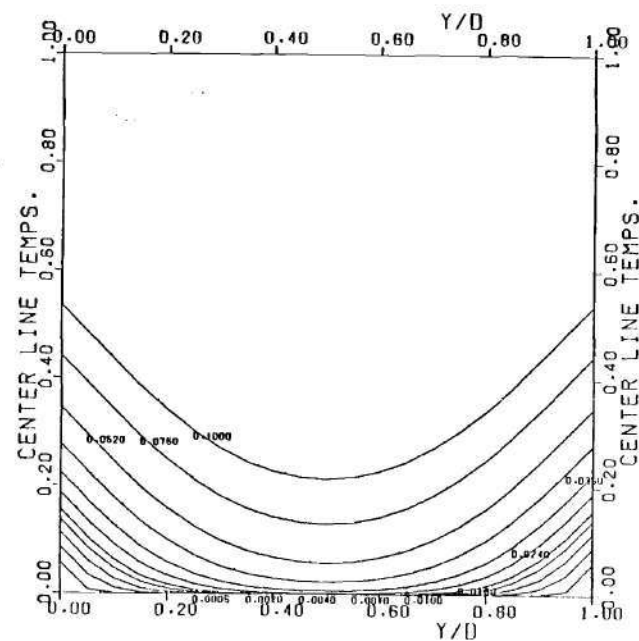
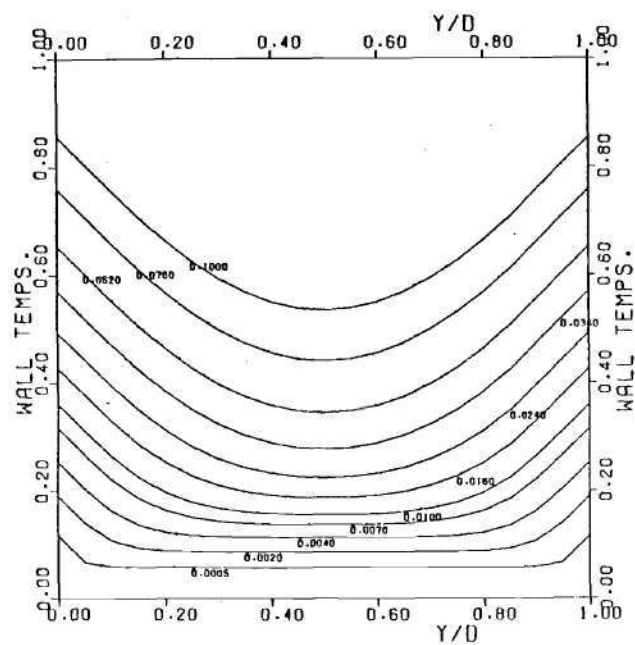
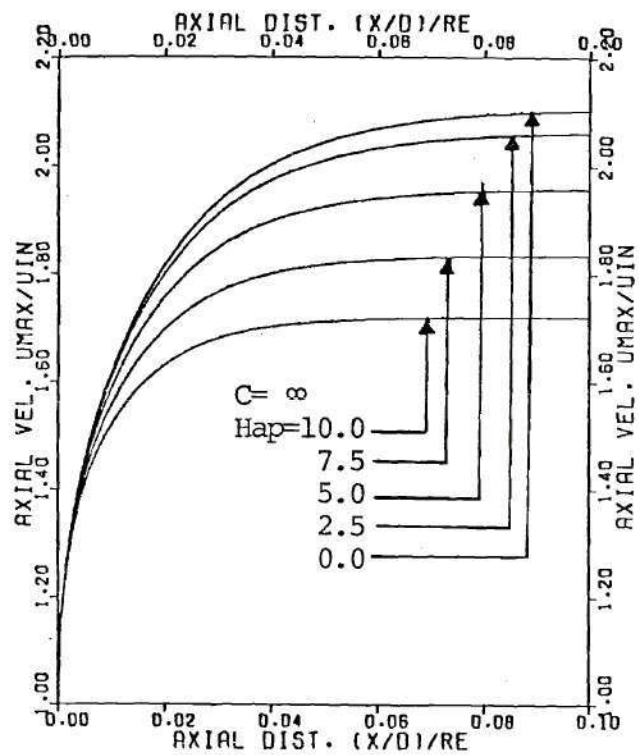
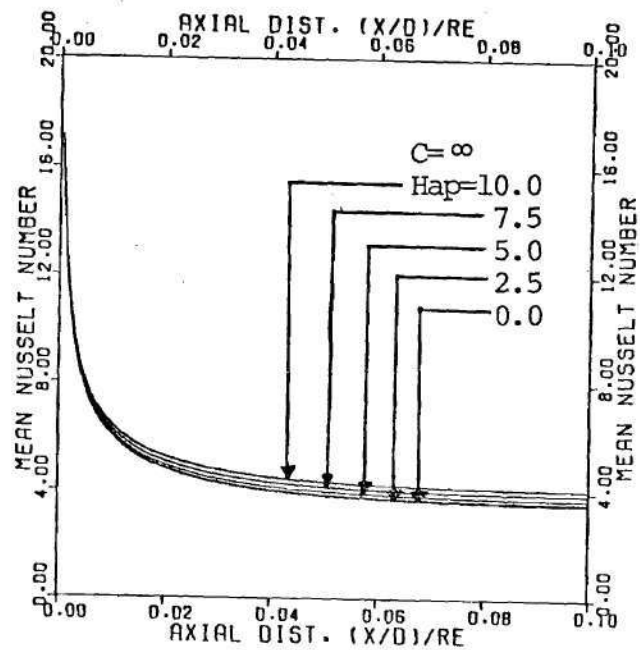


Figure 75. Wall and Center-line Temperatures for Values of L
 $C=\infty$



(a)

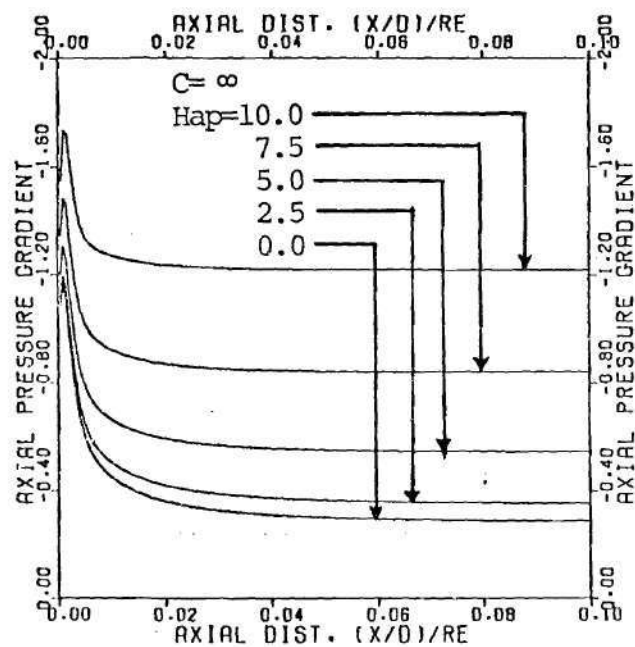


(b)

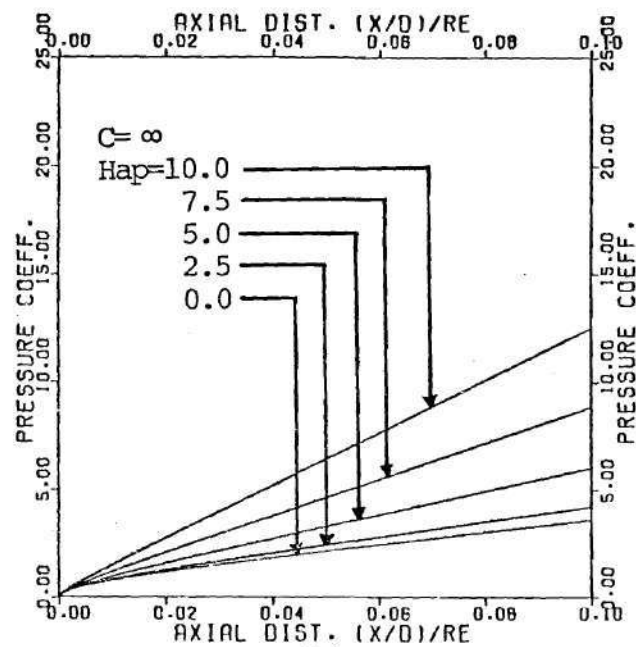
Figure 76. (a) Center-point Axial Velocity Development

(b) Mean Nusselt Number Development

$C=\infty$



(a)

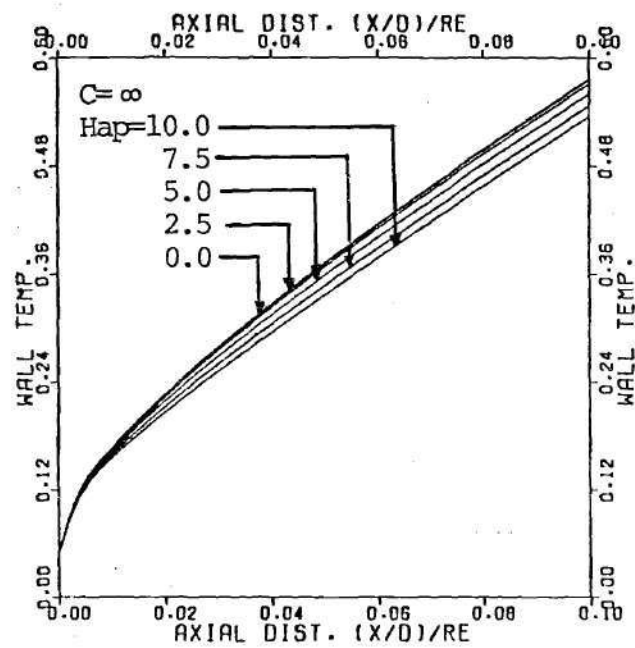


(b)

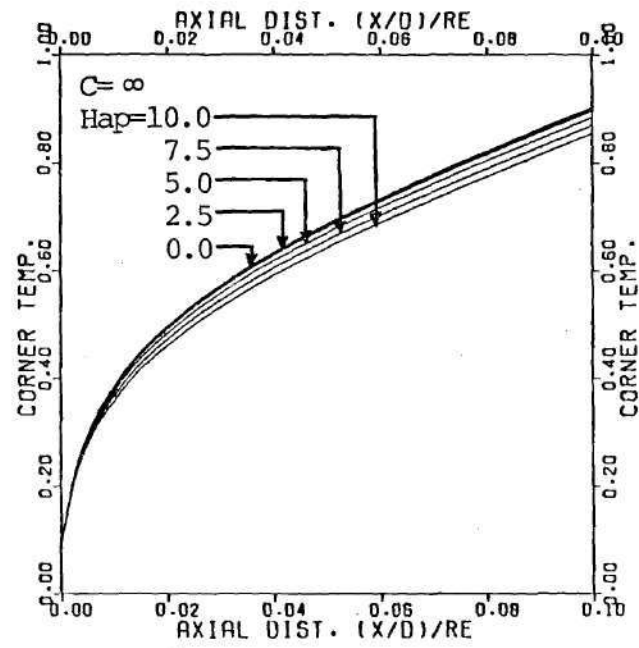
Figure 77. (a) Axial Pressure Gradient Development

(b) Pressure Coefficient Development

$C = \text{infinity}$



(a)



(b)

Figure 78. (a) Wall Center Temperature Development
(b) Wall Corner Temperature Development
 $C = \text{infinity}$

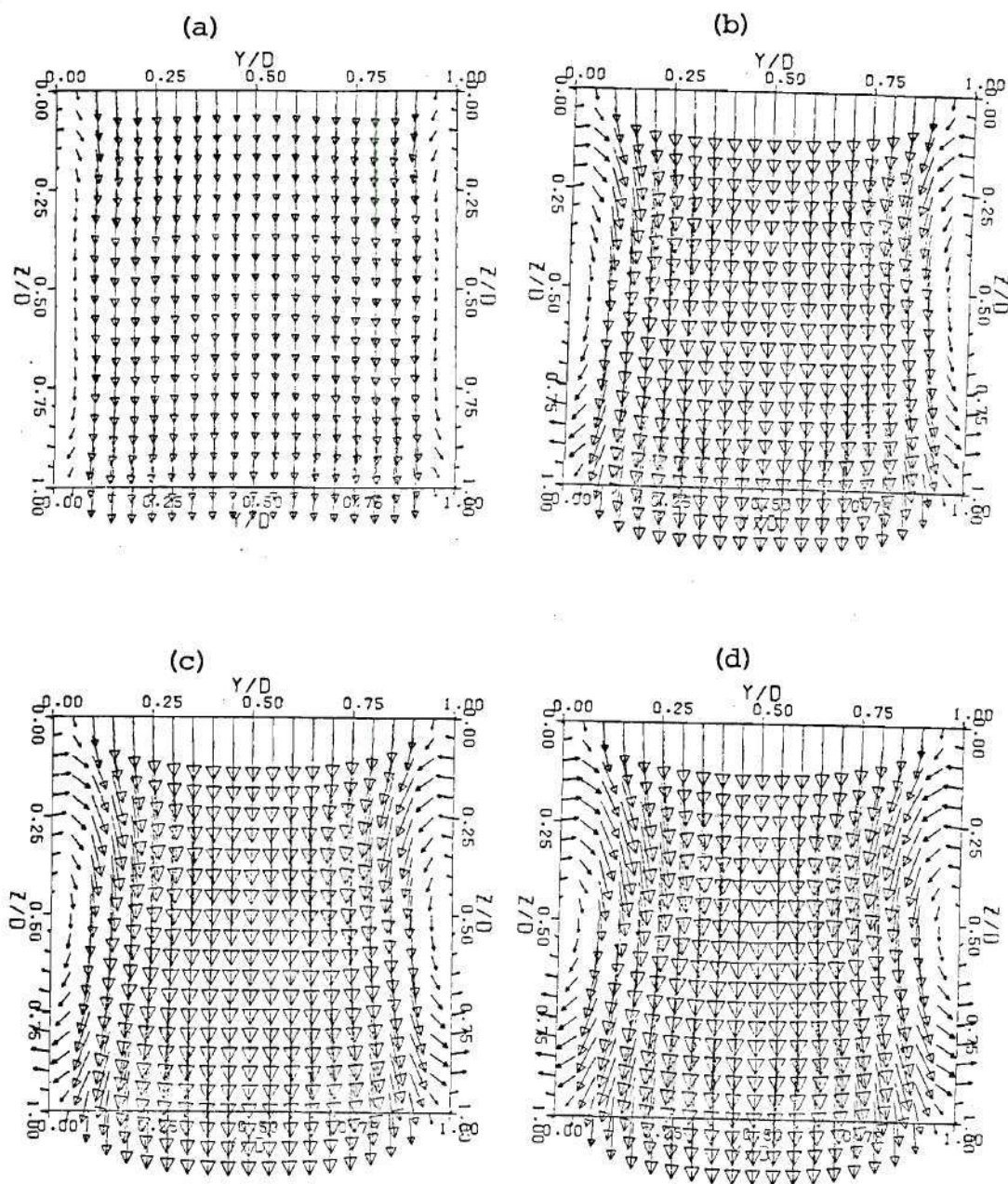


Figure 79. Current Density Vectors at
 (a) $L=0.001$, (b) $L=0.005$,
 (c) $L=0.010$, (d) $L=0.100$
 $C=10.0$

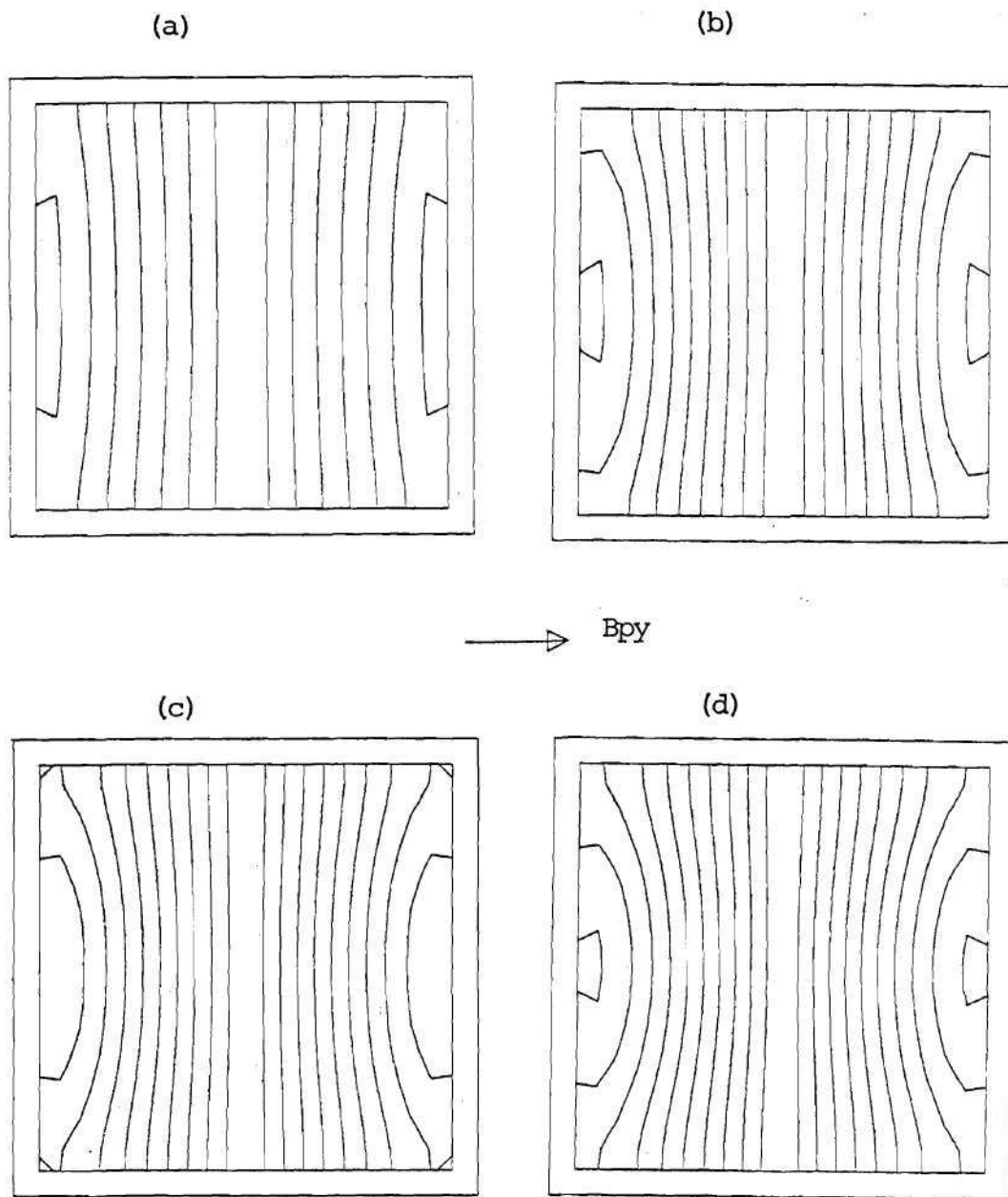


Figure 80. Axial Field Contours at
(a) $L=0.001$, (b) $L=0.005$,
(c) $L=0.010$, (d) $L=0.100$

$C=10.0$

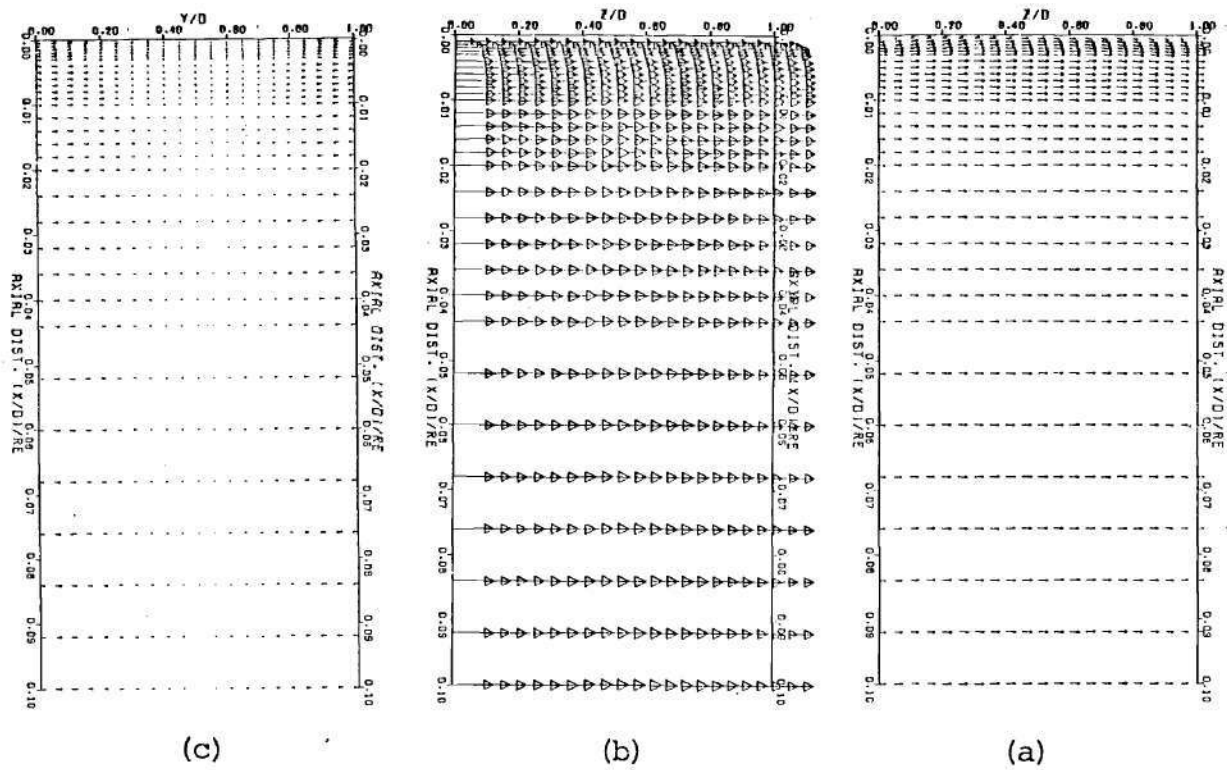


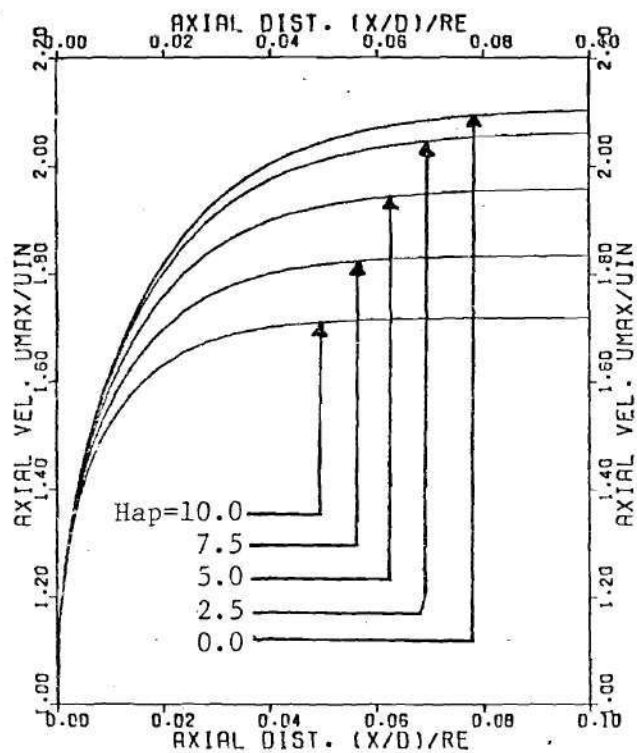
Figure 81. Current Density Vectors in Axial Plane

(a) xz near wall ($Y/D=0.05$)

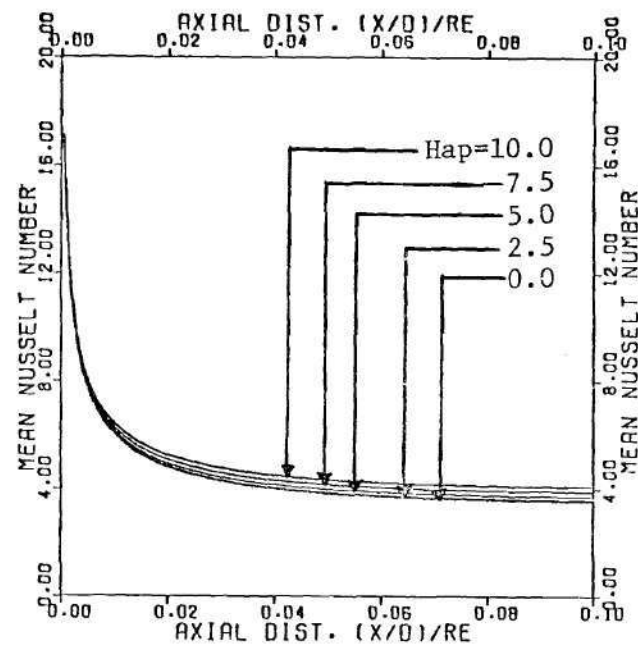
(b) xz at Center

(c) xy near wall ($Z/d=0.05$)

$C=10.0$



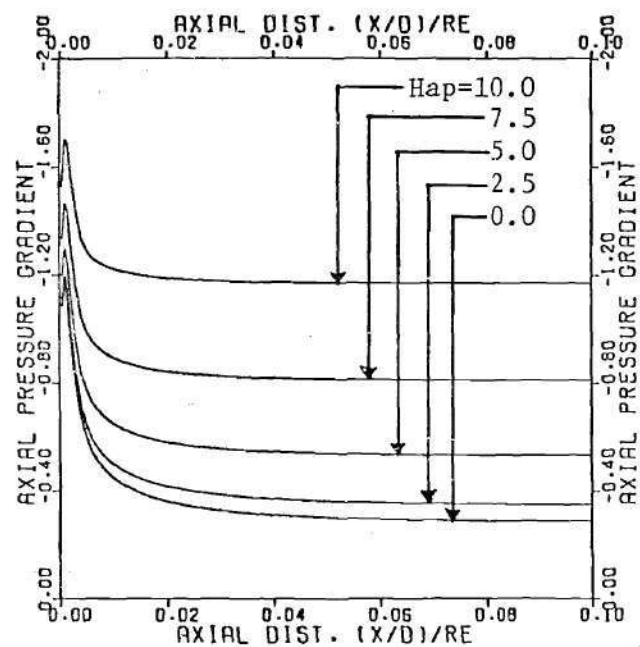
(a)



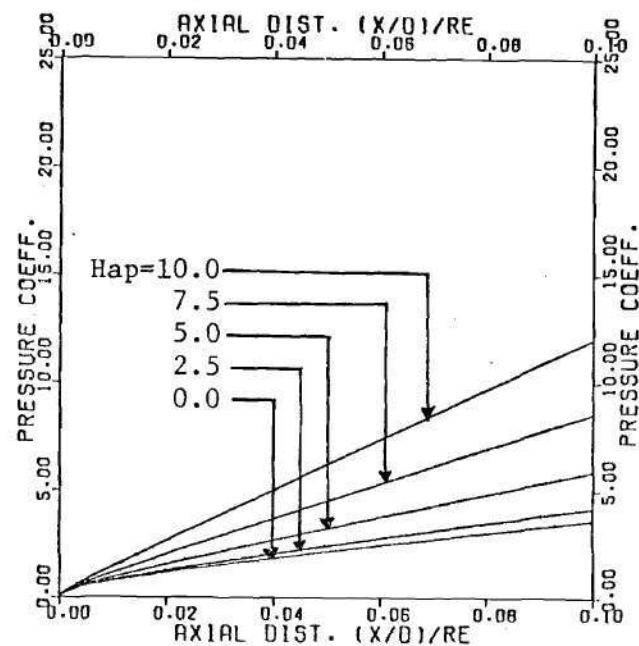
(b)

Figure 82. (a) Center-point Axial Velocity Development
(b) Mean Nusselt Number Development

$C=10.0$



(a)



(b)

Figure 83. (a) Axial Pressure Gradient Development

(b) Pressure Coefficient Development

$C=10.0$

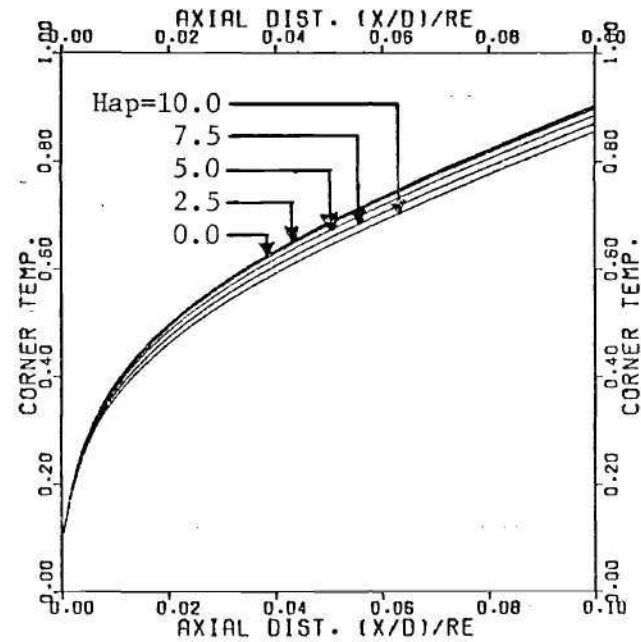
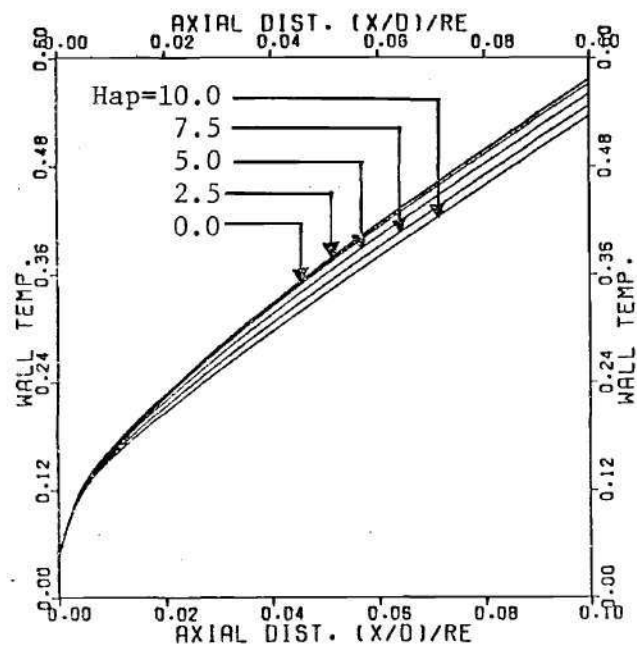


Figure 84. Wall Center and Wall Corner Temperature Development

$C=10.0$

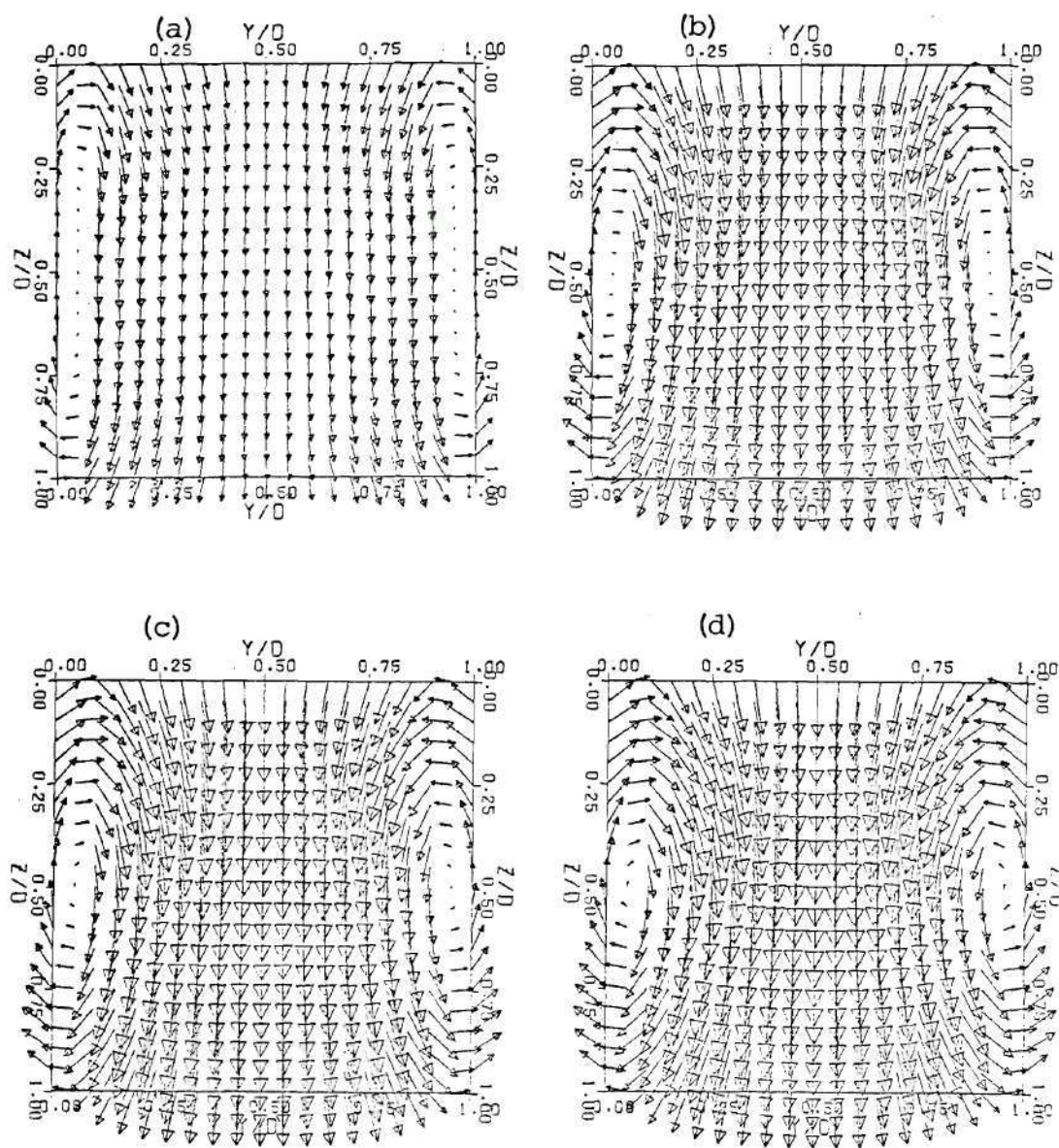


Figure 85. Current Density Vectors at
 (a) $L=0.001$, (b) $L=0.005$,
 (c) $L=0.010$, (d) $L=0.100$

$C=1.0$

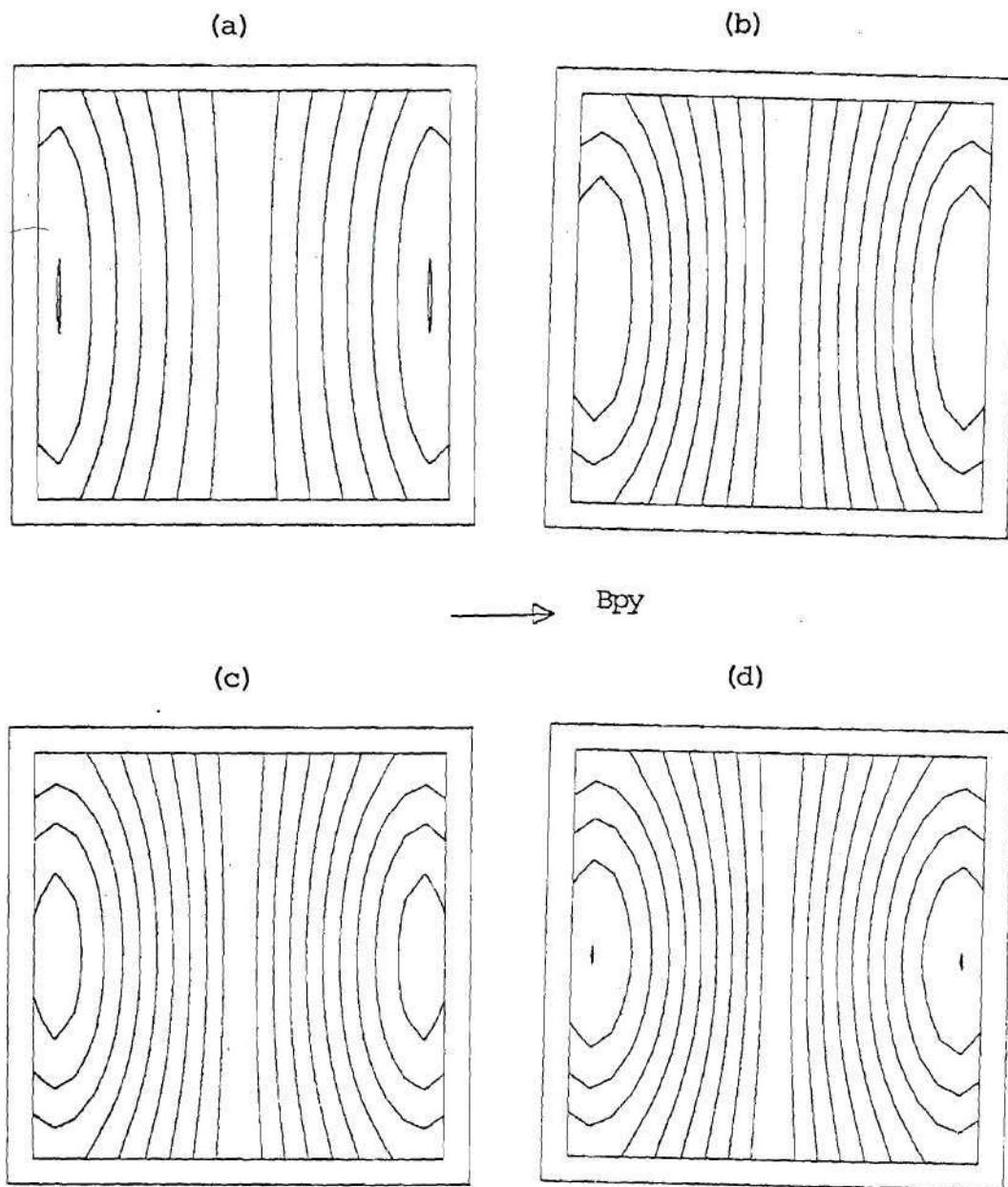


Figure 86. Axial Field Contours at
(a) $L=0.001$, (b) $L=0.005$,
(c) $L=0.010$, (d) $L=0.100$
 $C=1.0$

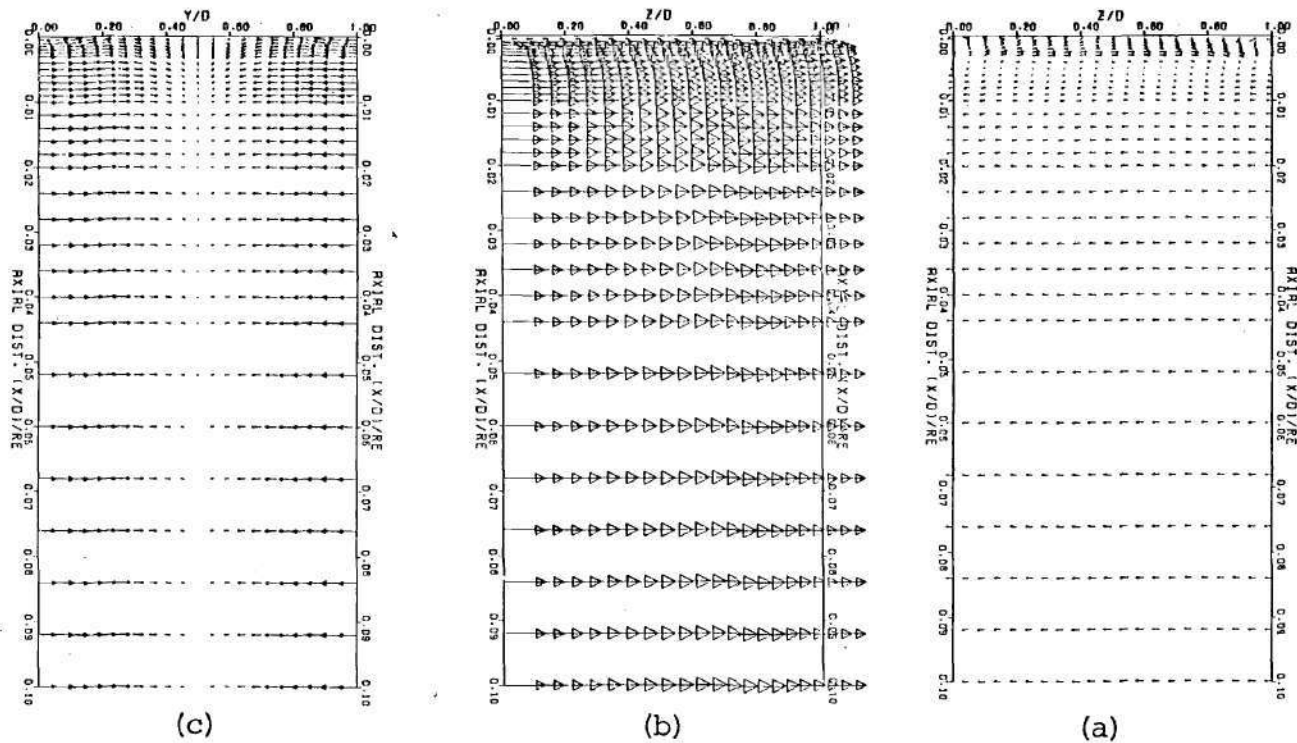


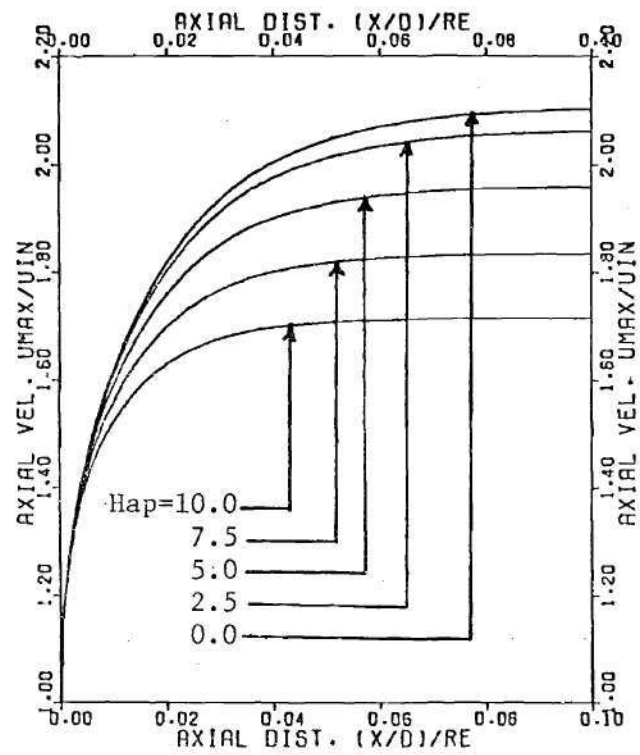
Figure 87. Current Density Vectors in Axial Plane

(a) xz near wall ($Y/D=0.05$)

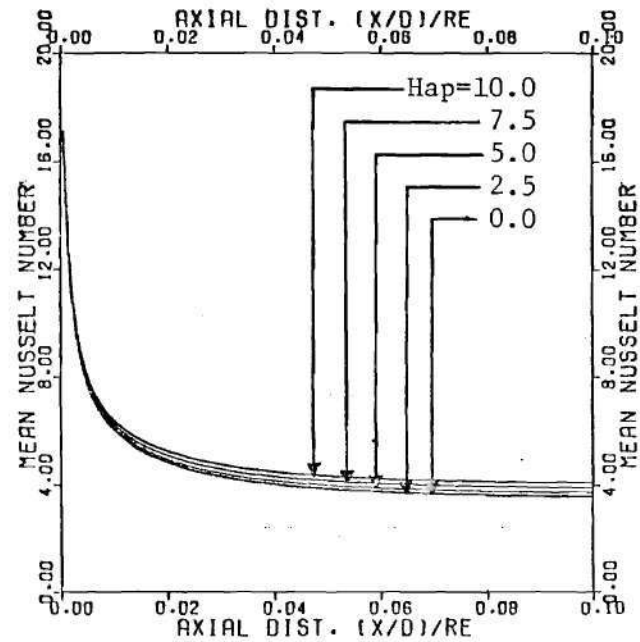
(b) xz at center

(c) xy near wall ($Z/D=0.05$)

$C=1.0$



(a)

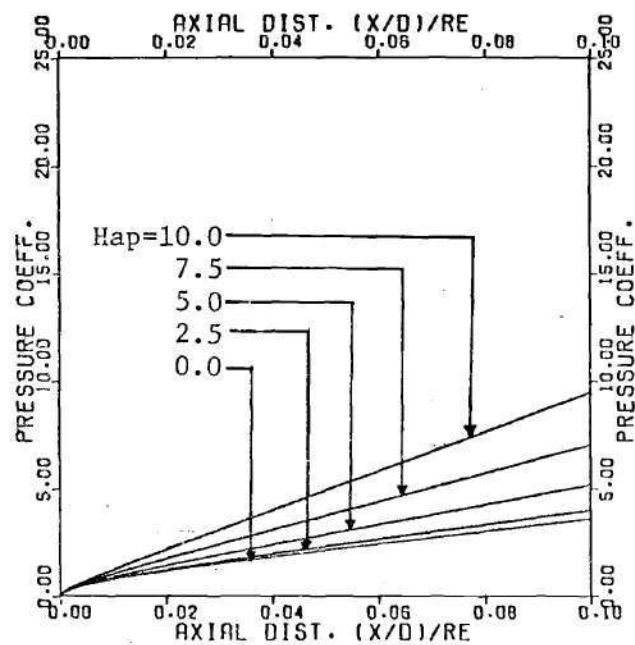


(b)

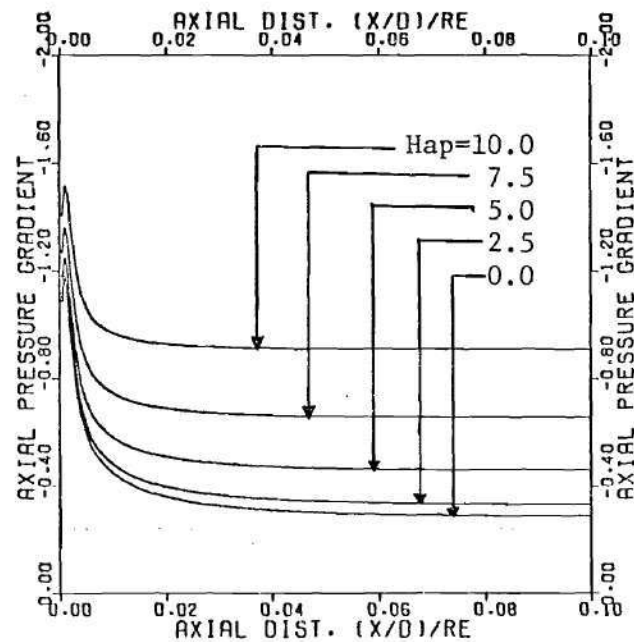
Figure 88. (a) Center-point Axial Velocity Development

(b) Mean Nusselt Number Development

$C=1.0$



(a)



(b)

Figure 89. (a) Pressure Coefficient Development
(b) Axial Pressure Gradient Development

$C=1.0$

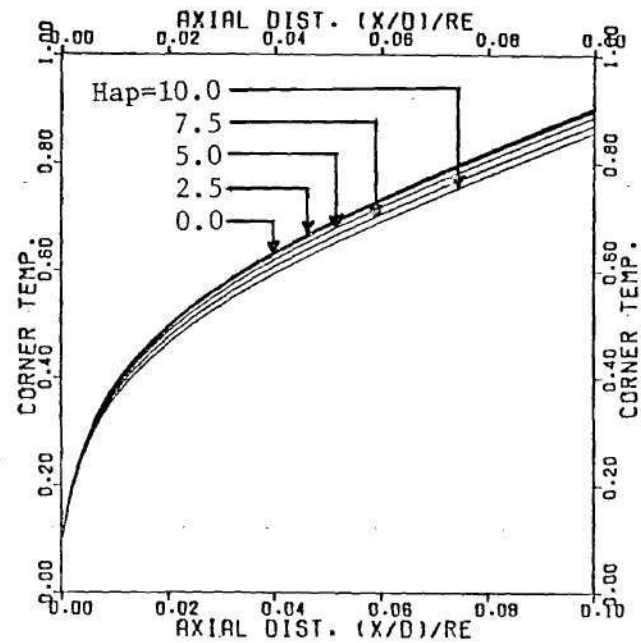
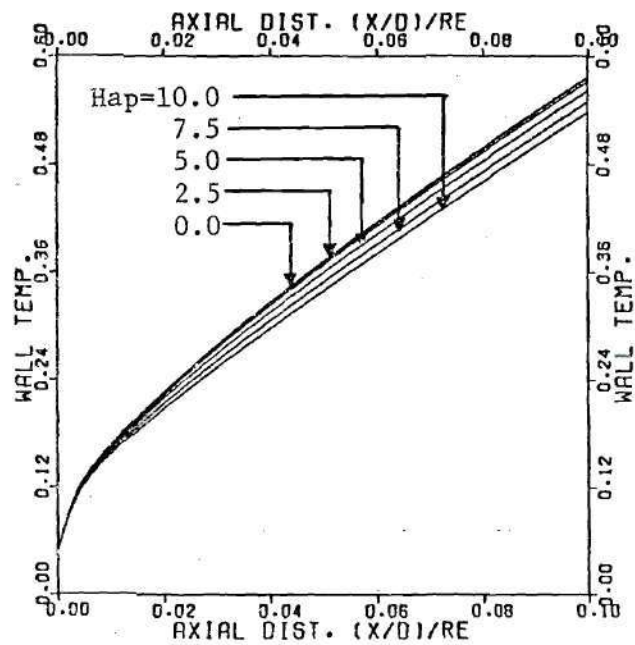


Figure 90. Wall Center and Wall Corner Temperature Development

$C=1.0$

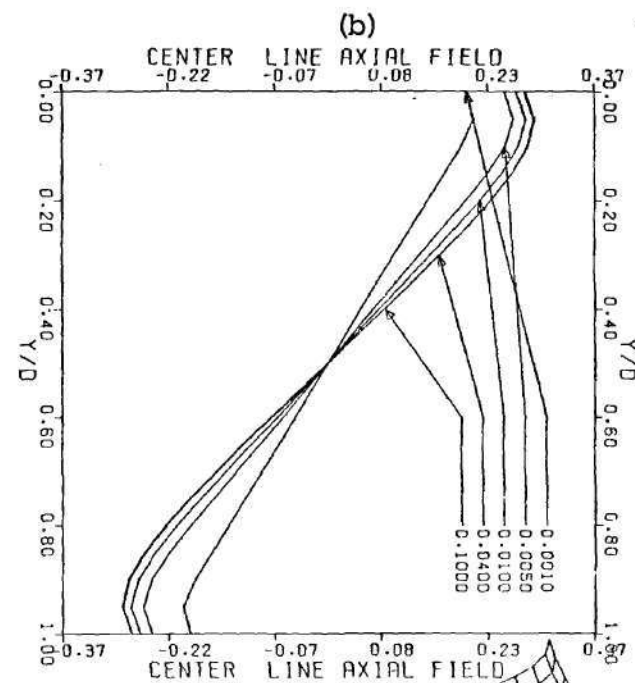
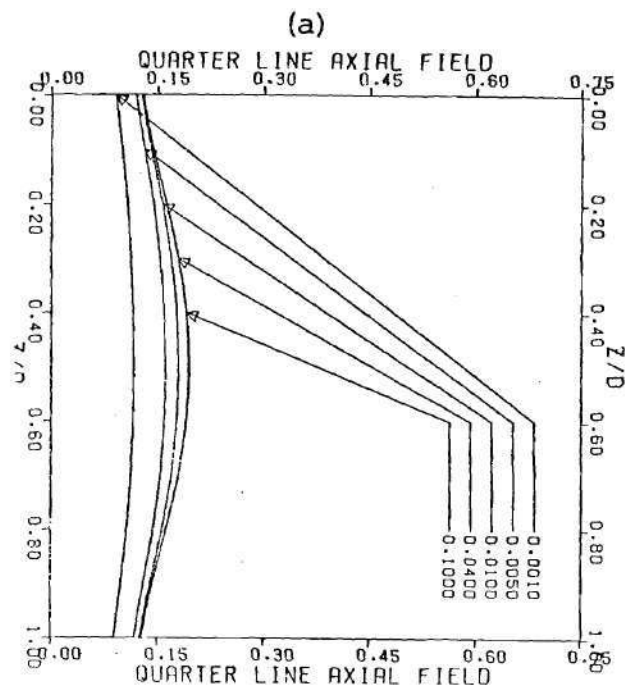
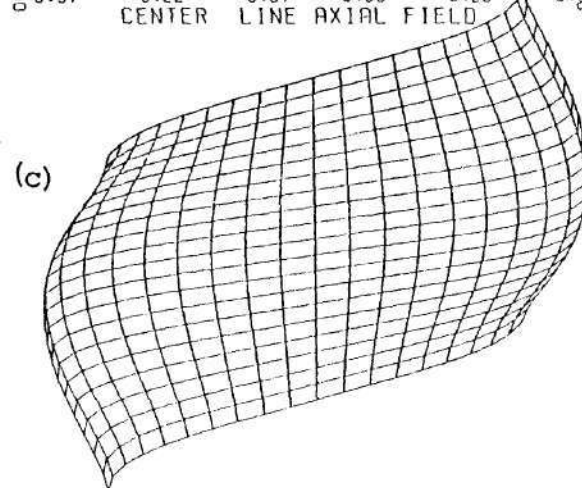
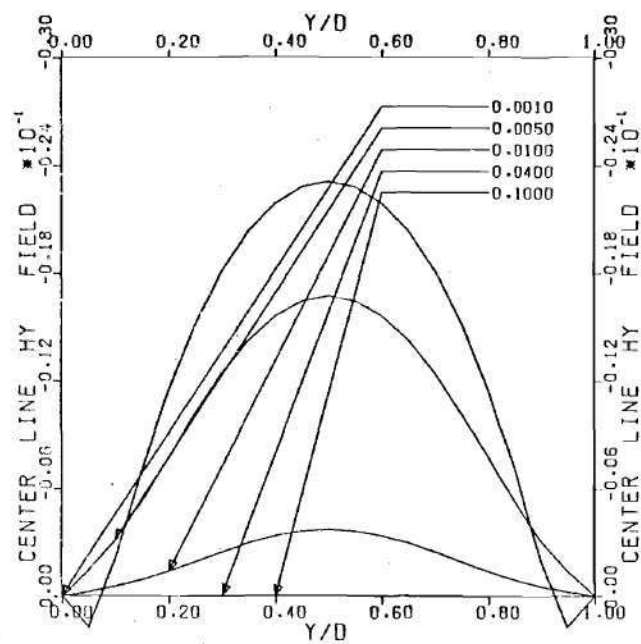


Figure 91. (a) and (b) Axial Field at
Values of L

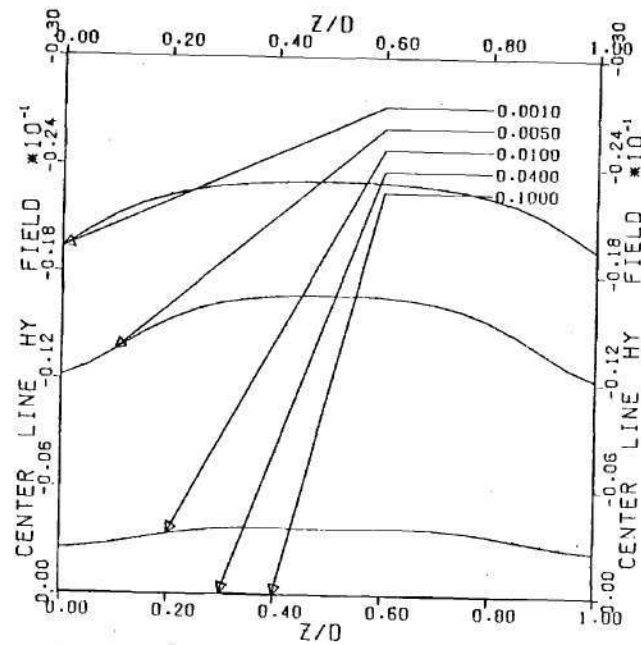
(c) Axial Field Surface at
 $L=0.1$

$C=1.0$





(a)



(b)

Figure 92. (a) and (b) Hy Field at Values of L
C=1.0

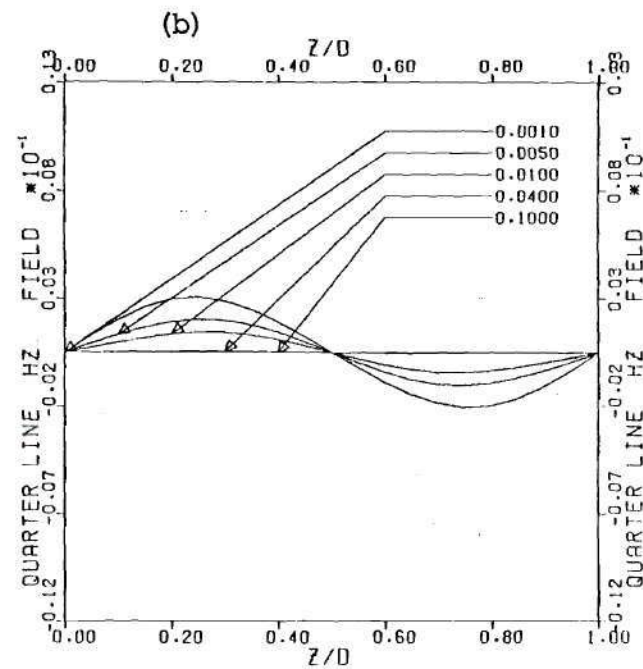
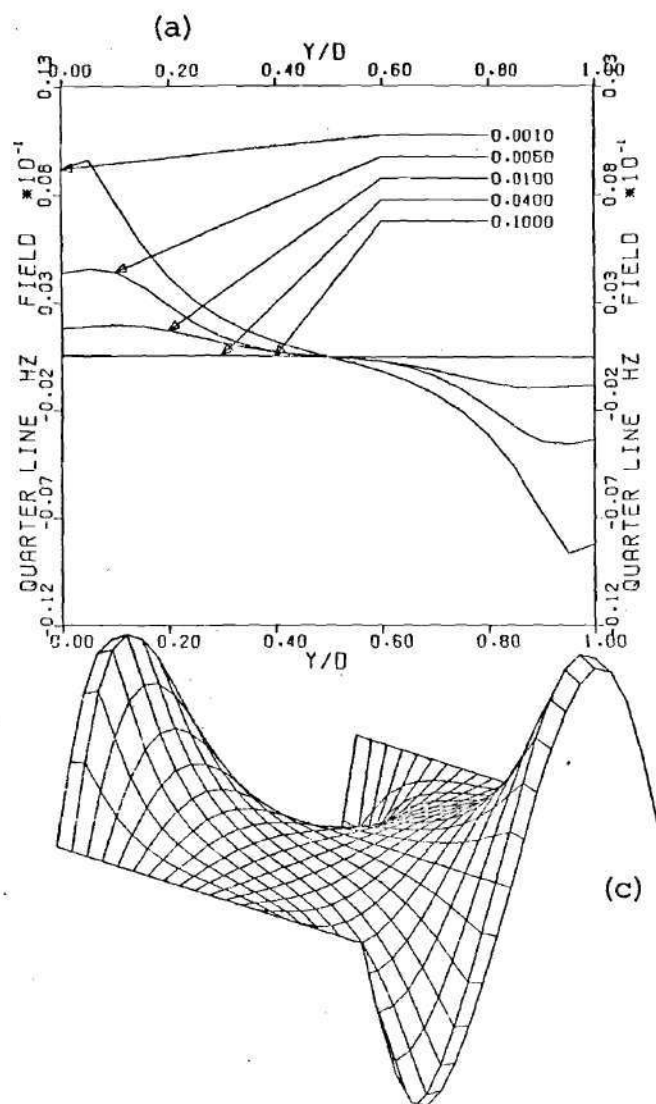


Figure 93. (a) and (b) Hz Field at
Values of L
(c) Hz Field Surface at
 $L=0.1$

$C=1.0$

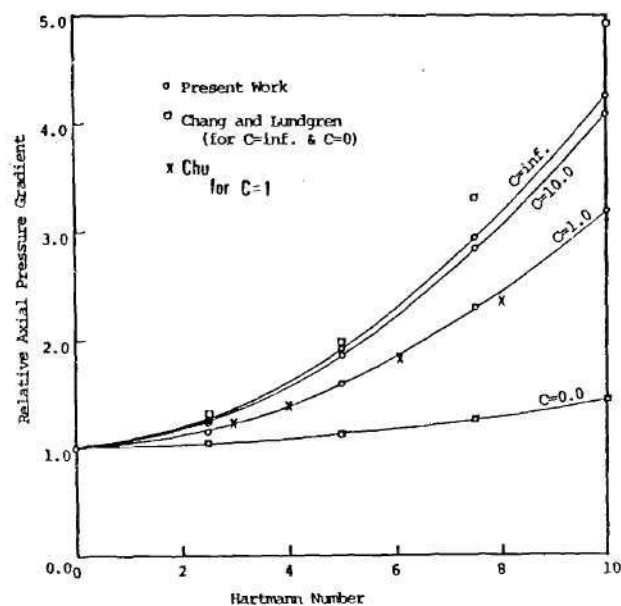


Figure 94.

Comparison of Fully Developed
Relative Axial Pressure Gradient with
work of Chang and Lundgren and work
of Chu

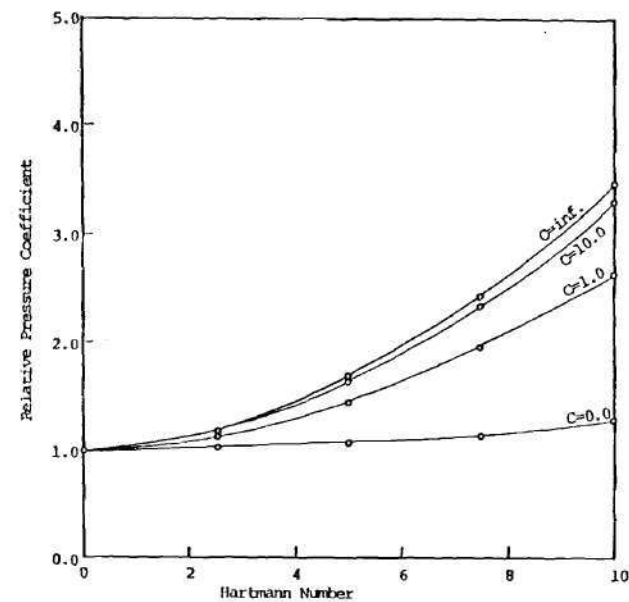
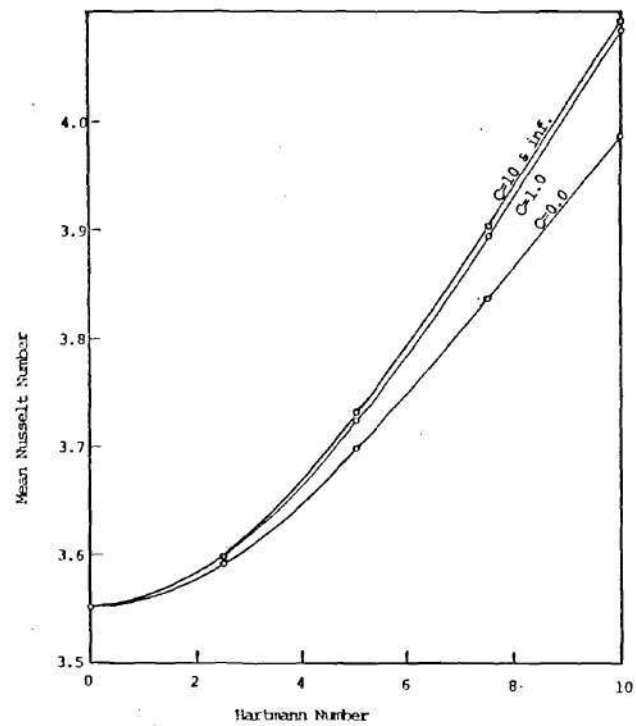
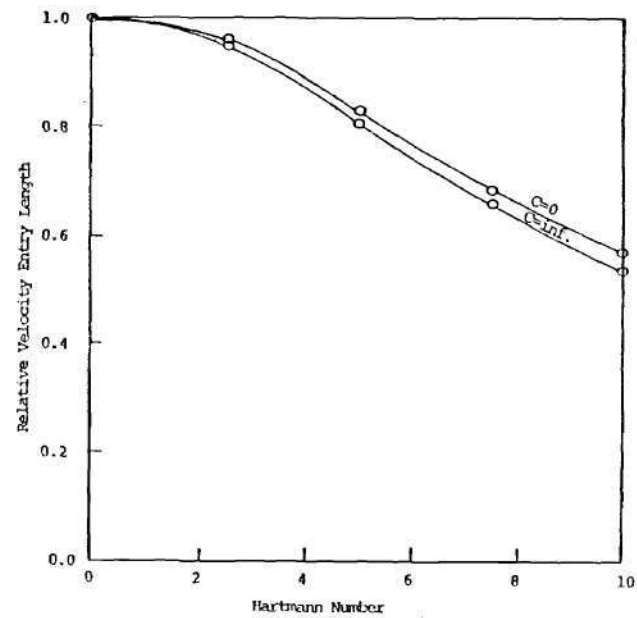


Figure 95.

Fully Developed Relative
Pressure Coefficient



(b)



(a)

Figure 96. (a) Relative Velocity Entry Length
(b) Fully Developed Nusselt Number ($L=0.1$)

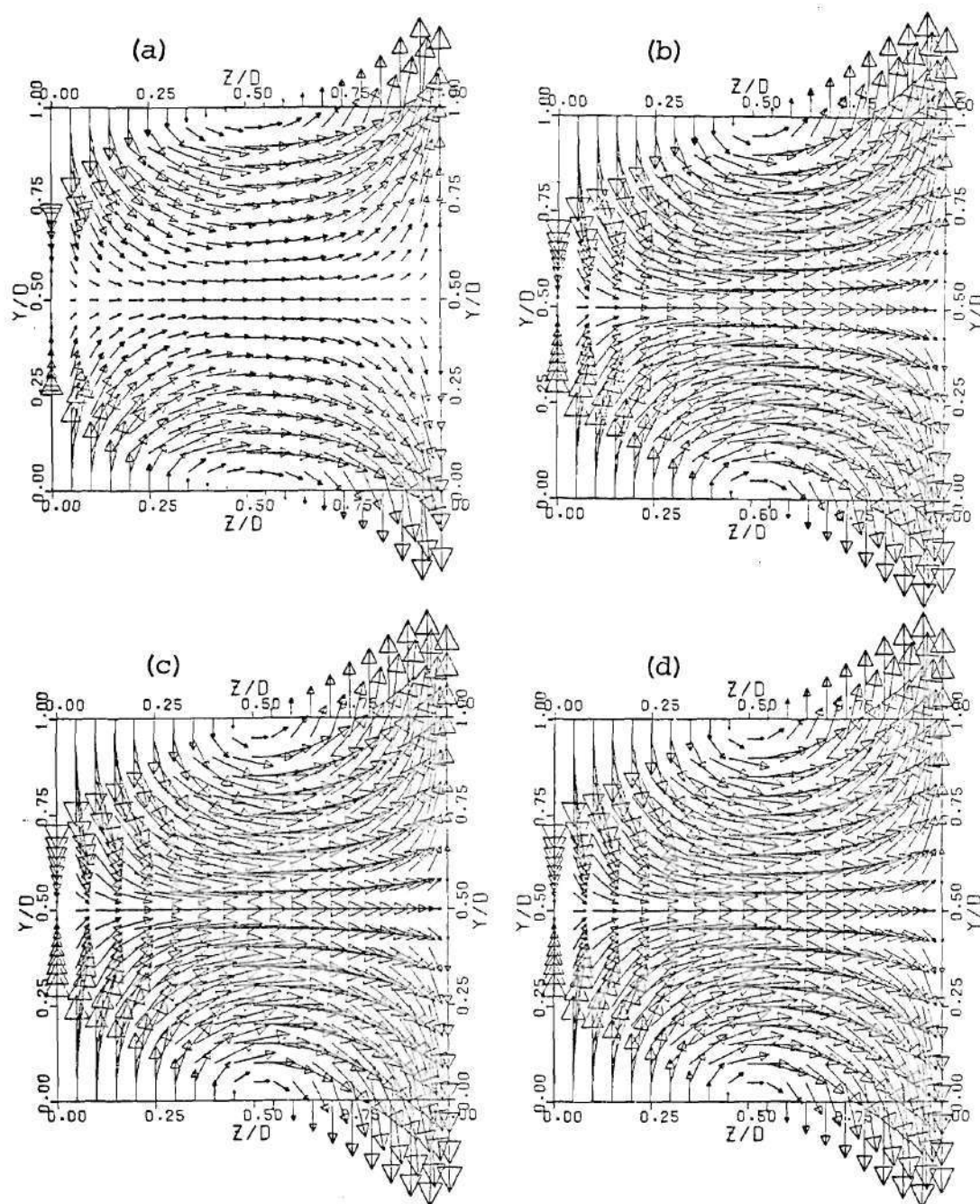


Figure 97. Current Density Vectors at
 (a) $L=0.001$, (b) $L=0.005$,
 (c) $L=0.010$, (d) $L=0.100$

Case A $C=0$ on Parallel Walls and $C=\infty$ on Perpendicular Walls

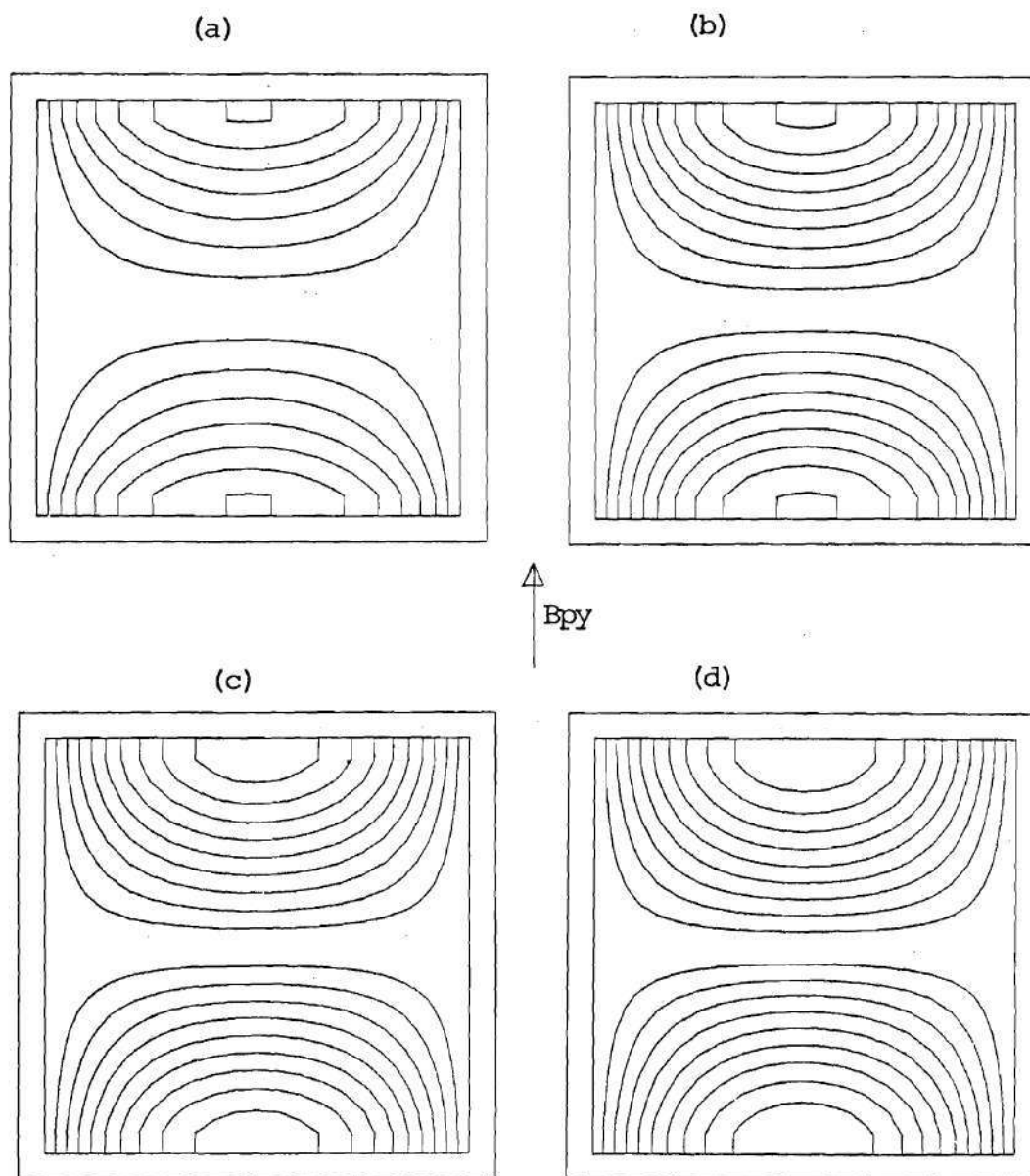


Figure 98. Axial Field Contours at
(a) $L=0.001$, (b) $L=0.005$,
(c) $L=0.010$, (d) $L=0.100$

Case A

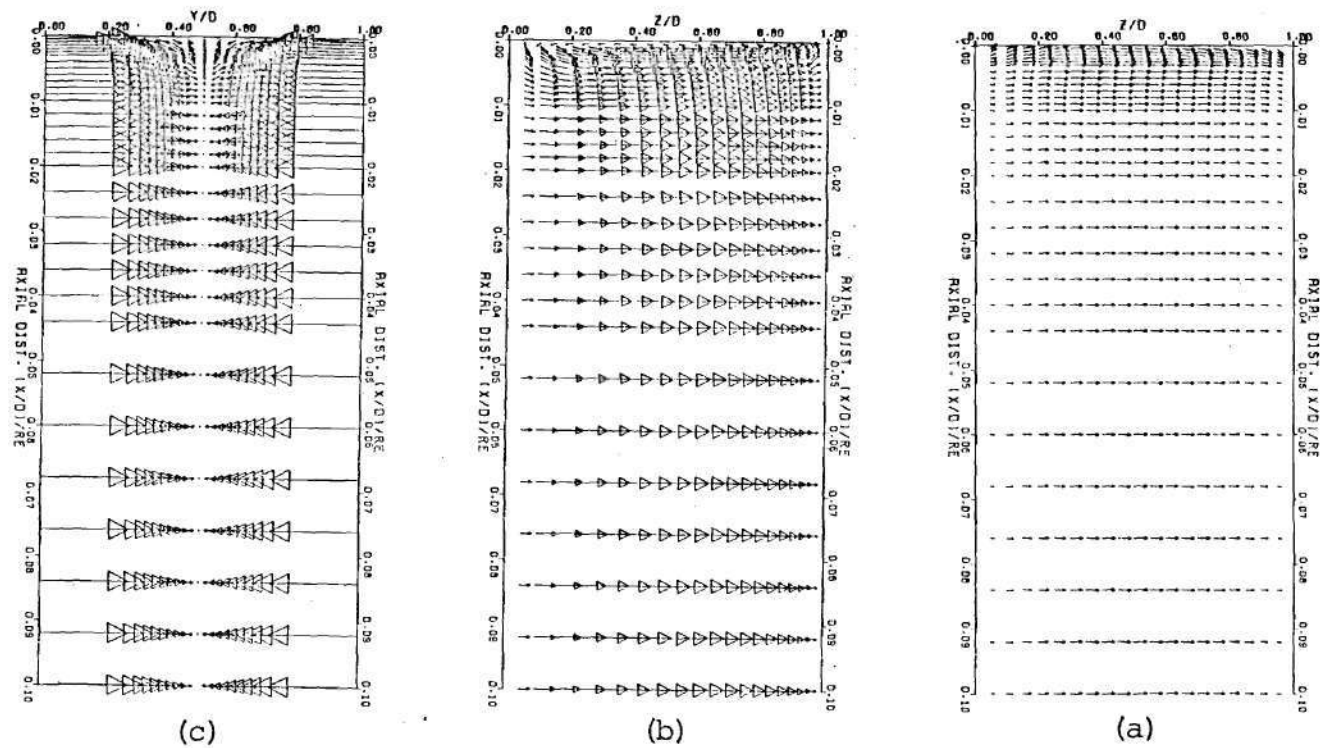


Figure 99. Current Density Vectors in Axial Plane

(a) xz near Wall ($Y/D=0.05$)

(b) xz at Center

(c) xy near Wall ($Z/D=0.05$)

Case A

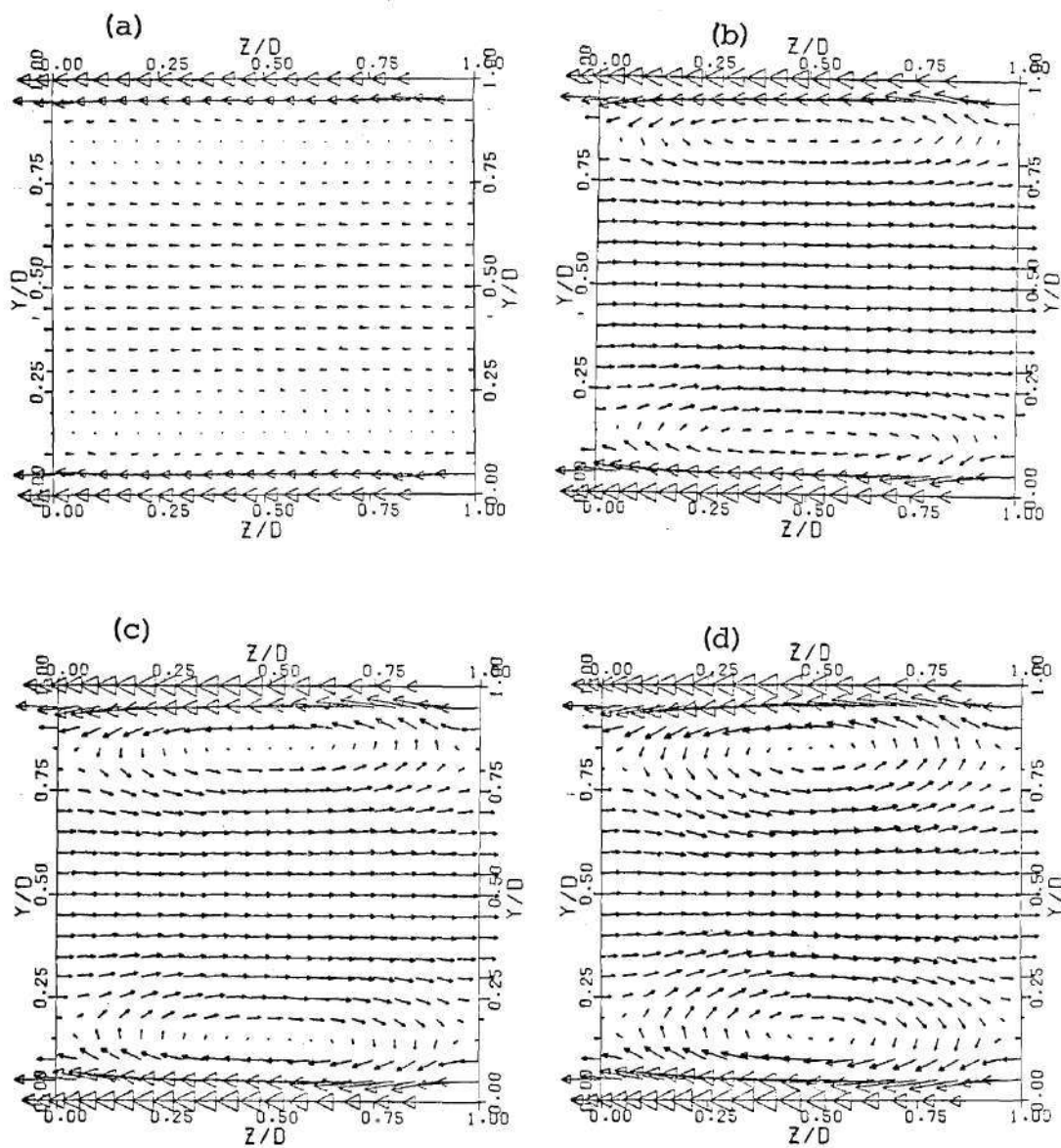


Figure 100. Current Density Vectors at

(a) $L=0.001$, (b) $L=0.005$,

(c) $L=0.010$, (d) $L=0.100$

Case B

$C=\text{inf.}$ on Perp. Walls and $C=0$ on Parallel Walls

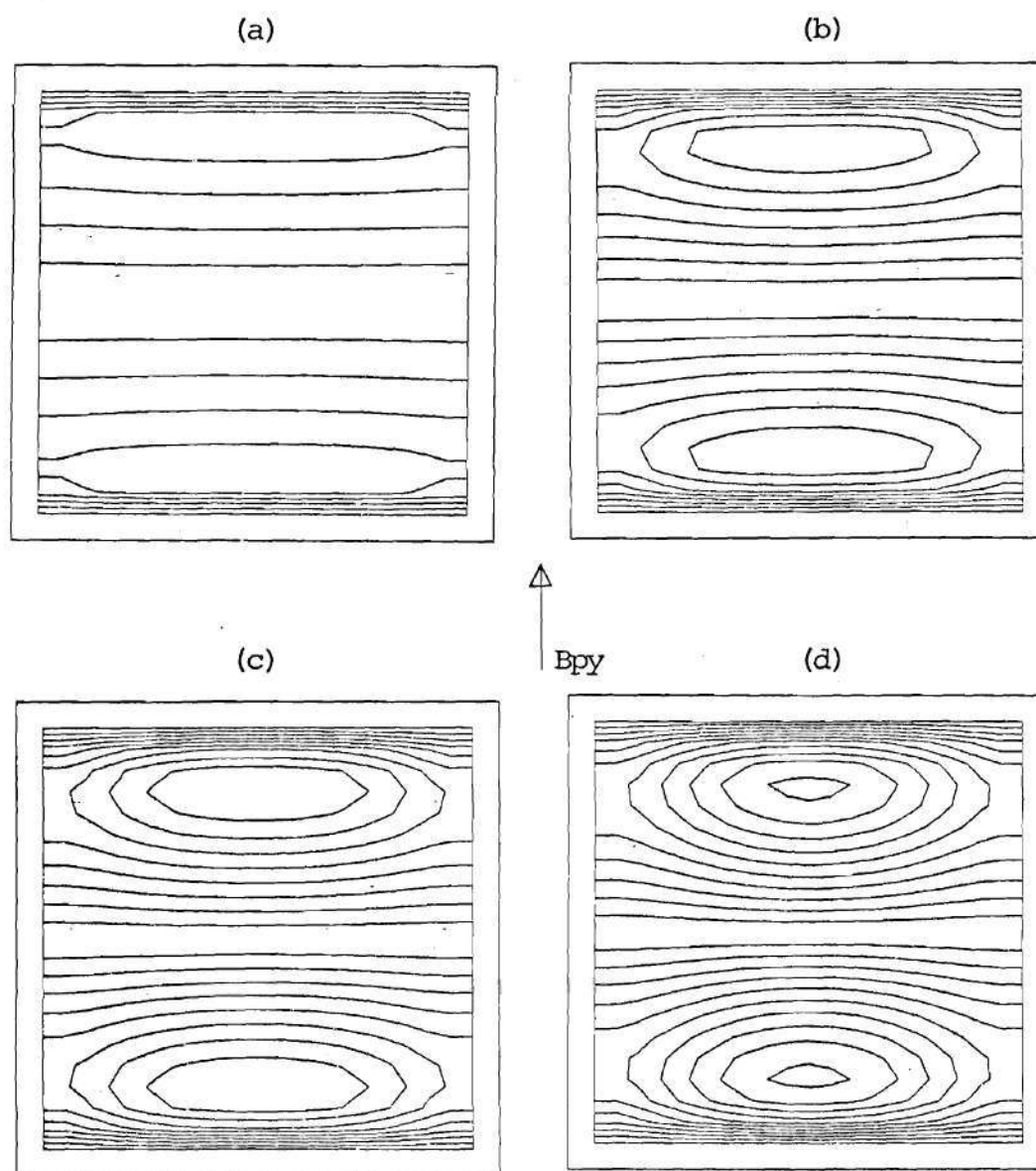
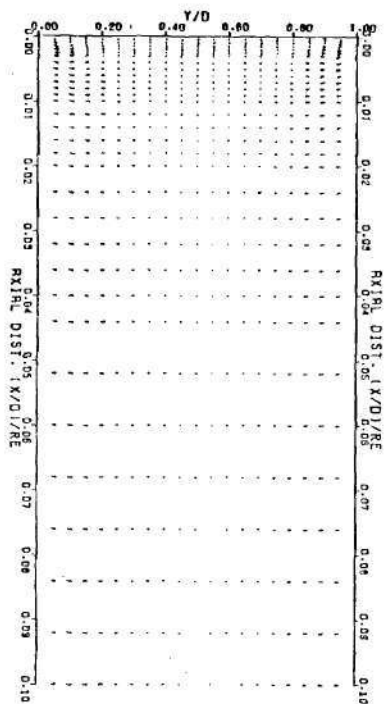
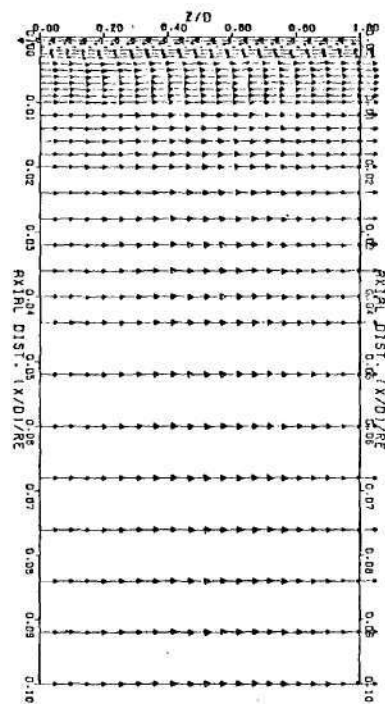


Figure 101. Axial Field Contours at
(a) $L=0.001$, (b) $L=0.005$,
(c) $L=0.010$, (d) $L=0.100$

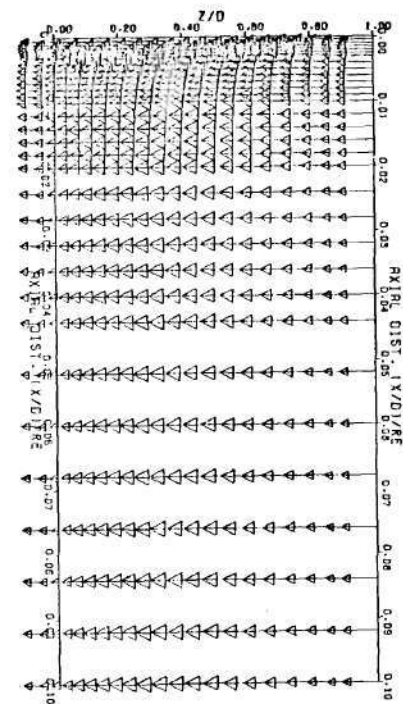
Case B



(c)



(b)



(a)

Figure 102. Current Density Vectors in Axial Plane

(a) xz near Wall ($Y/D=0.05$)

(b) xz at Center

(c) xy near Wall ($Z/D=0.05$)

Case B

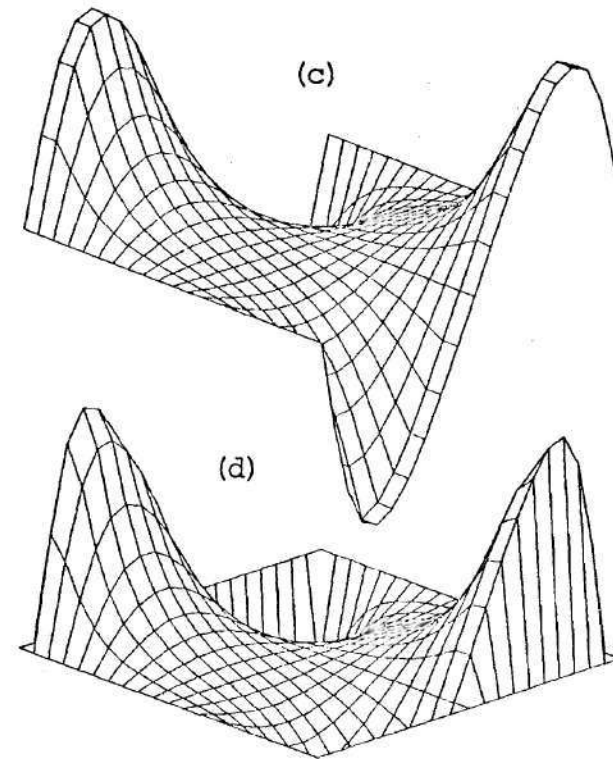
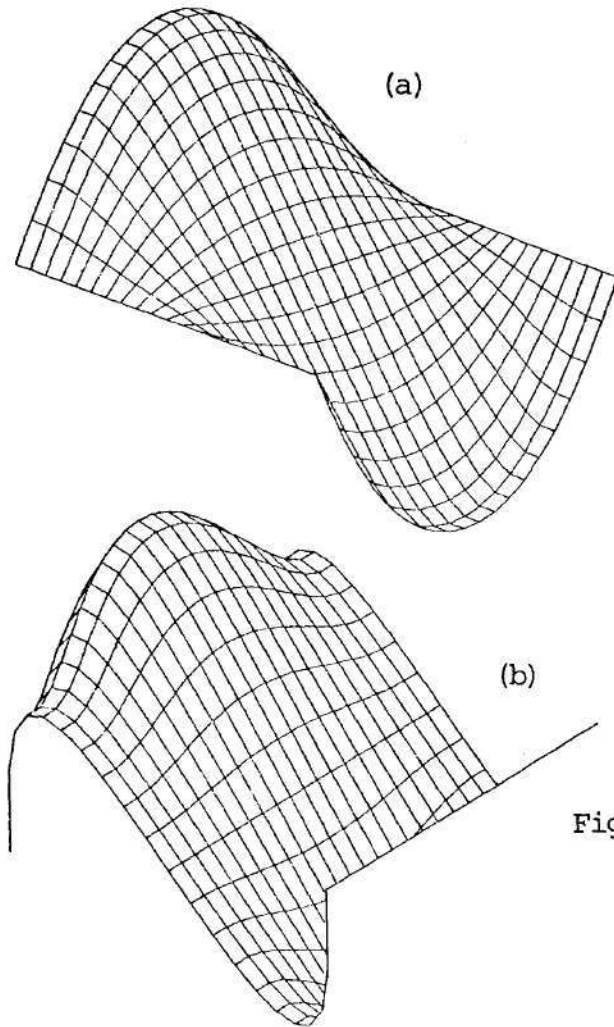


Figure 103. Axial Field Surfaces at $L=0.1$ for
 (a) Case B , (b) Case A
 Hz Field Surfaces at $L=0.001$ for
 (c) Case B , (d) Case A

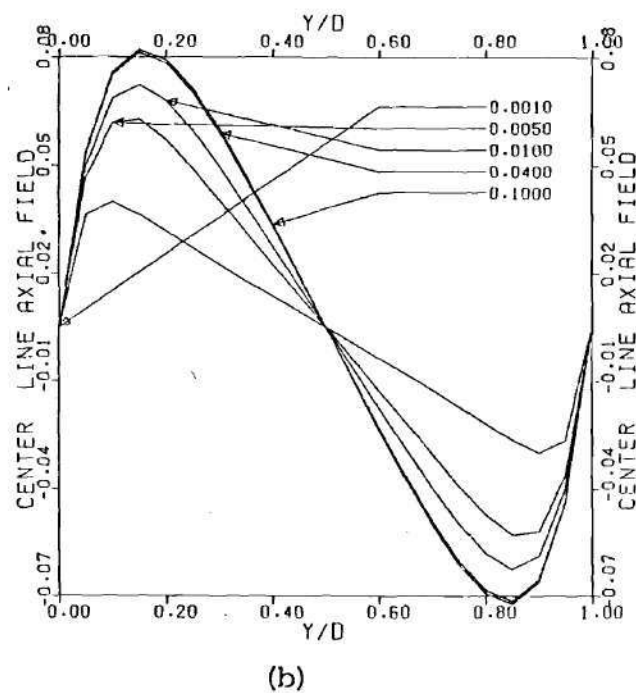
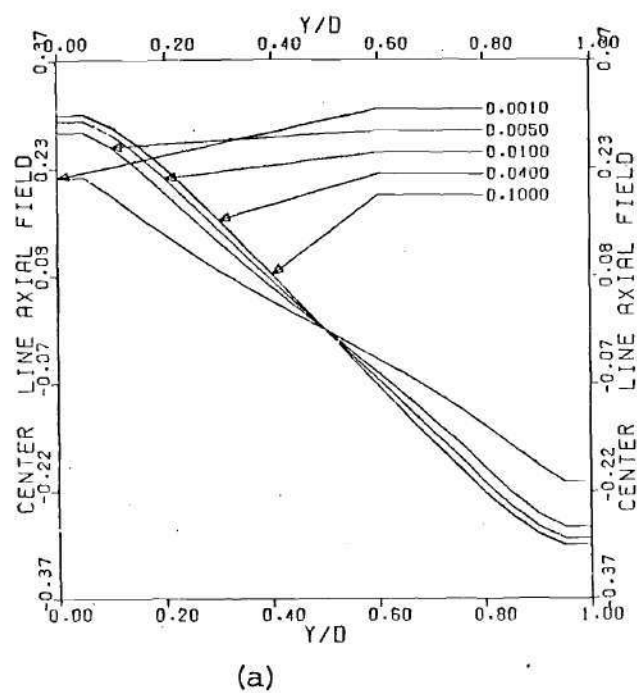
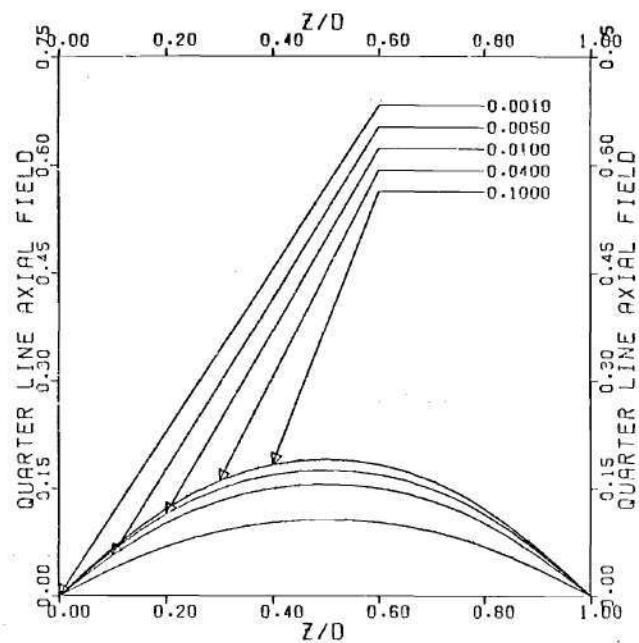
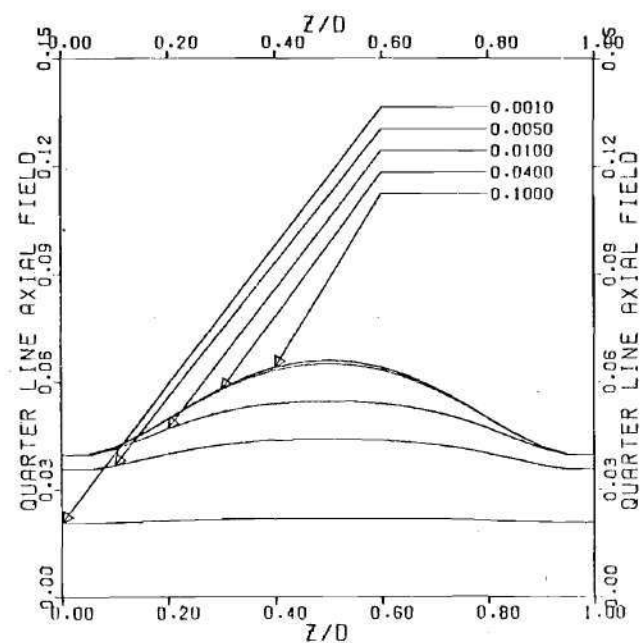


Figure 104. Axial Field at Values of L for
(a) Case A , (b) Case B

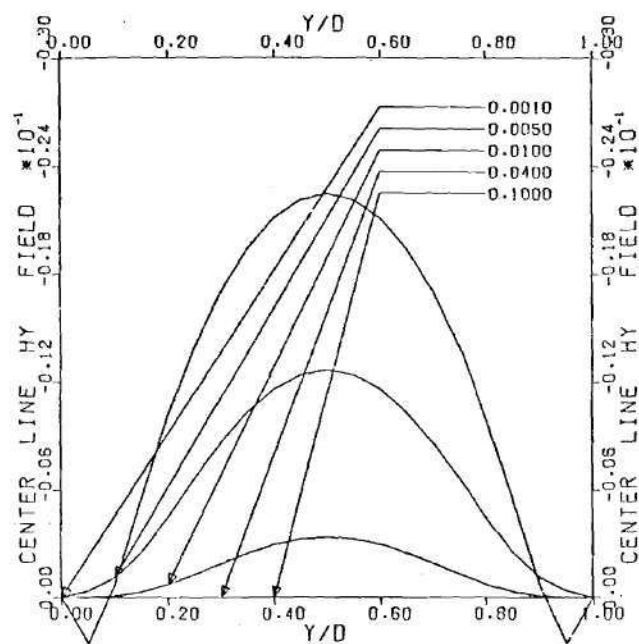


(a)

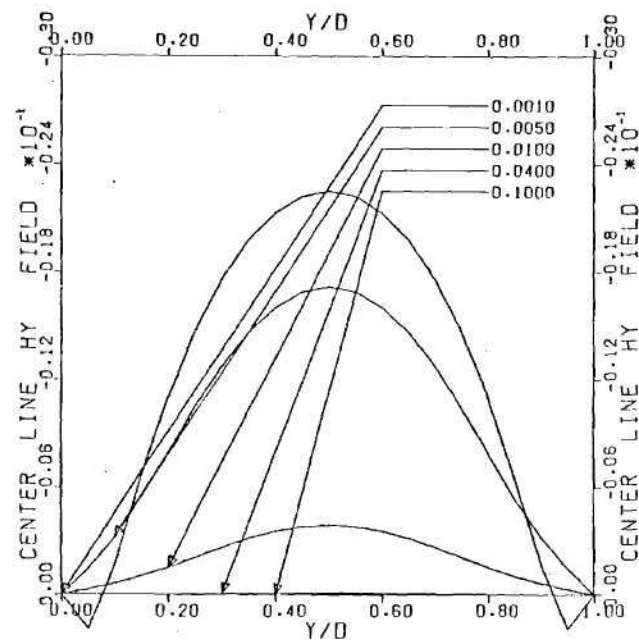


(b)

Figure 105. Axial Field at Values of L for
(a) Case A , (b) Case B

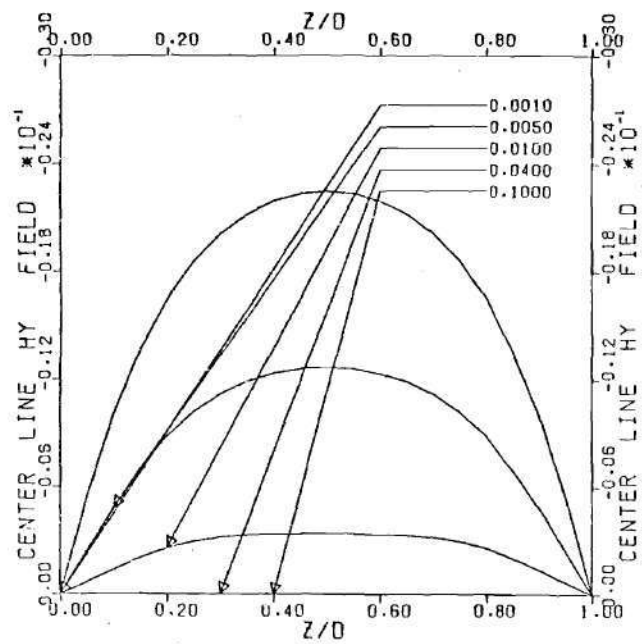


(a)

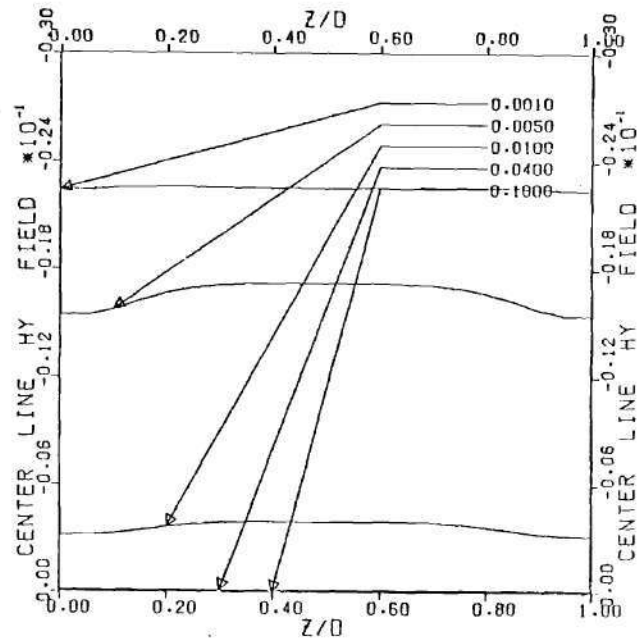


(b)

Figure 106. Hy Field for Values of L for
(a) Case A , (b) Case B

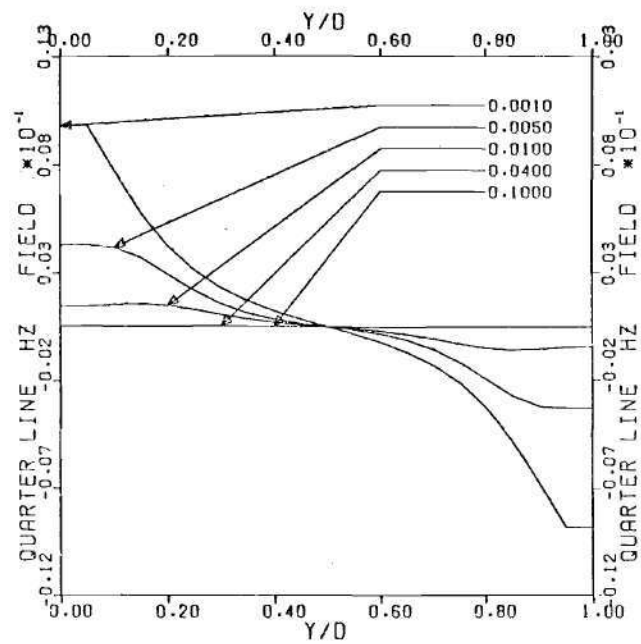


(a)

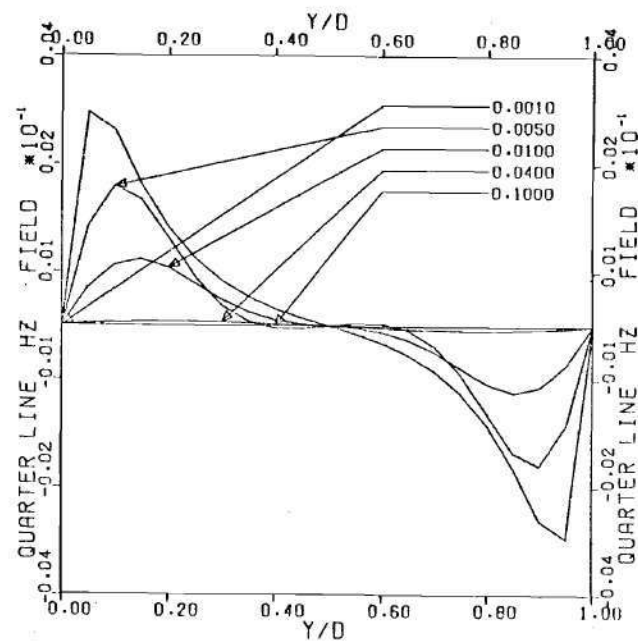


(b)

Figure 107. Hy Field at Values of L for
(a) Case A , (b) Case B

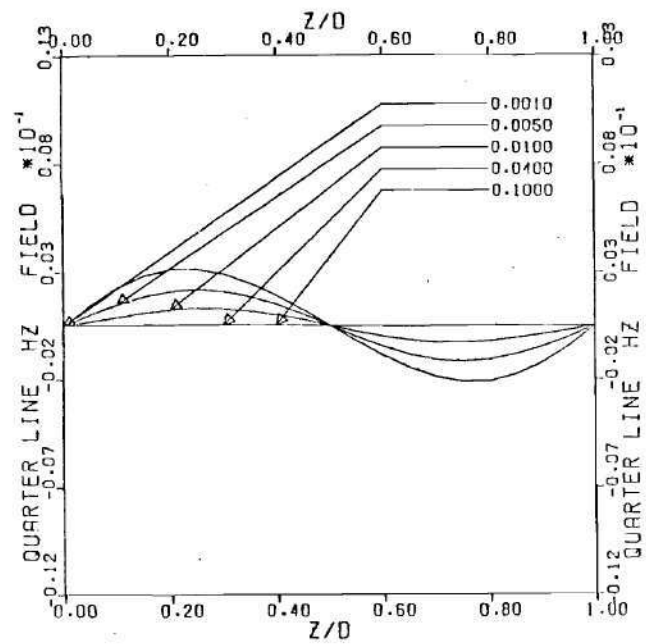


(a)

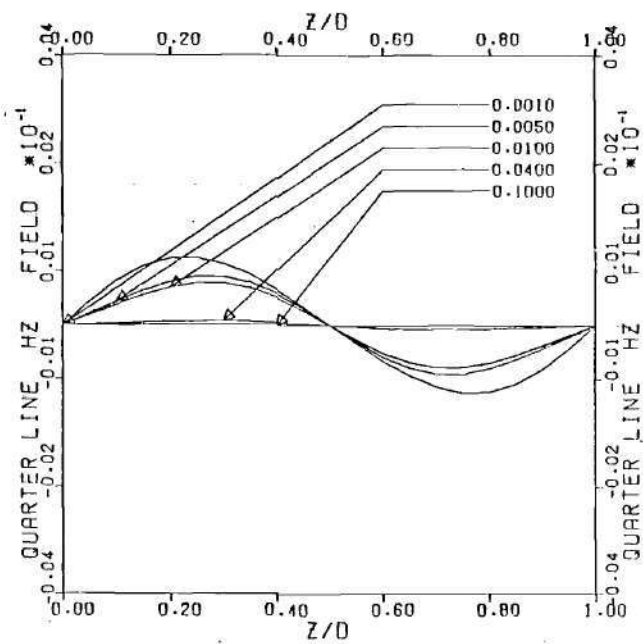


(b)

Figure 108. Hz Field at Values of L for
(a) Case A , (b) Case B



(a)



(b)

Figure 109. Hz Field at Values of L for
(a) Case A , (b) Case B

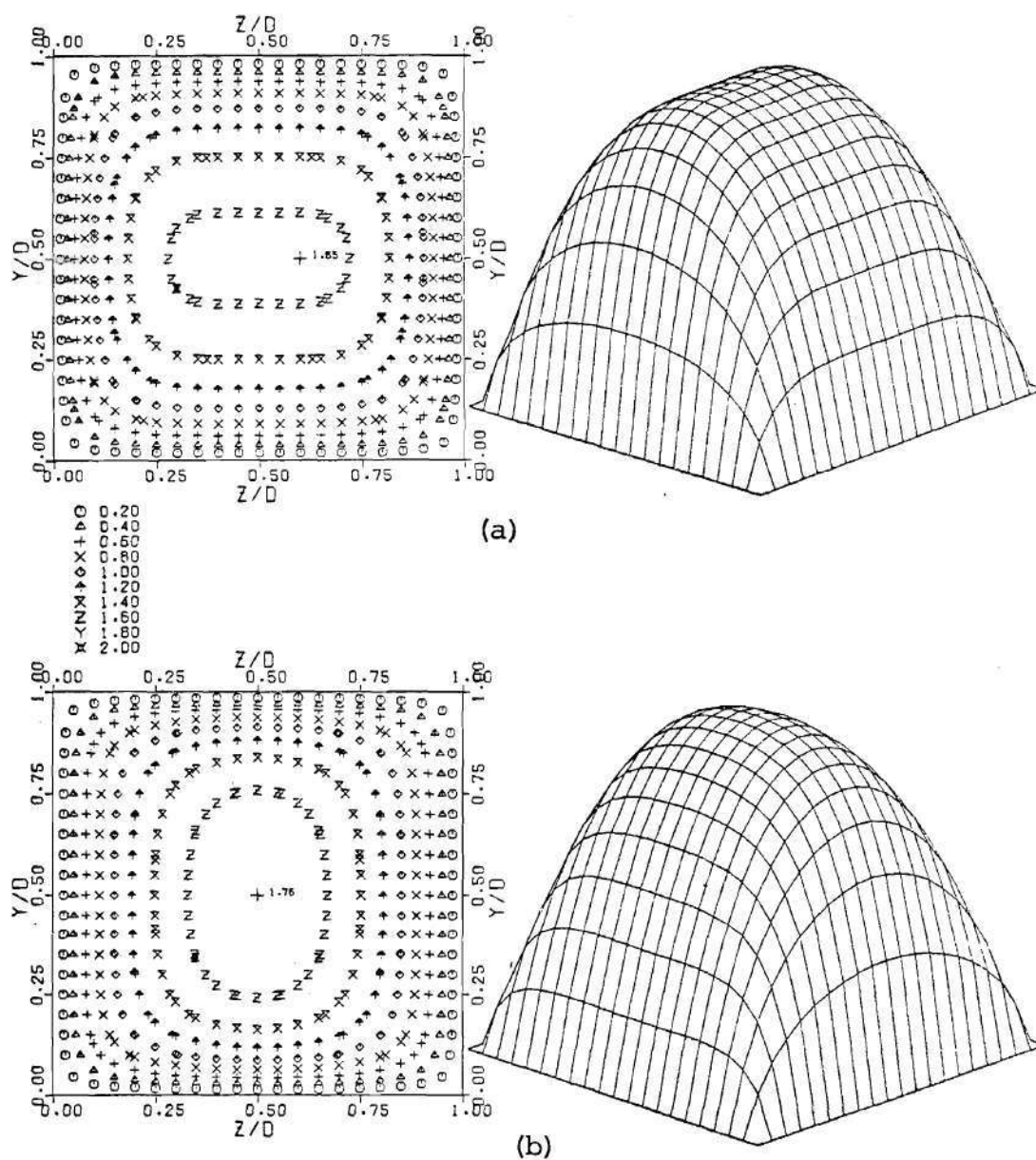


Figure 110. Axial Velocity Contours and Surface at $L=0.1$ for

(a) Case A , (b) Case B

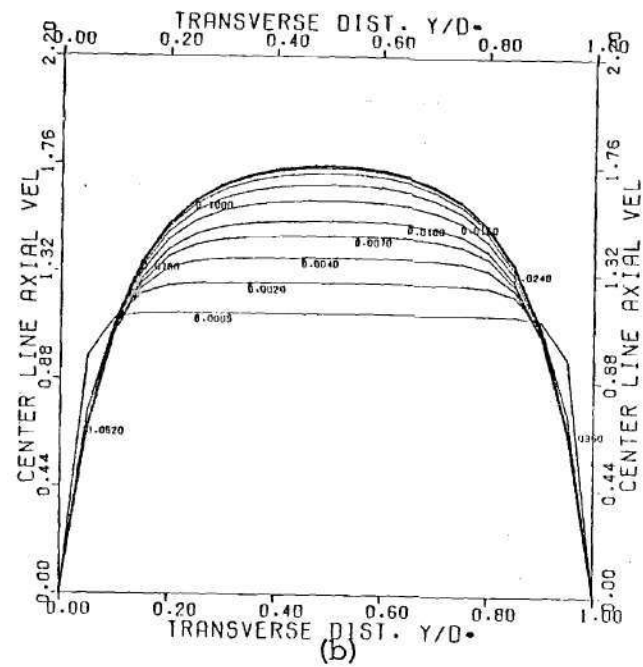
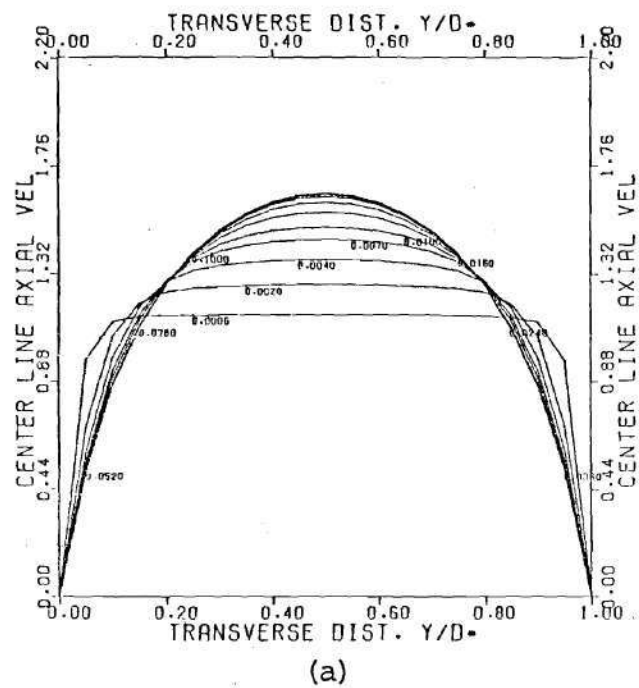


Figure 111. Axial Velocity at Values of L for
(a) Case A , (b) Case B

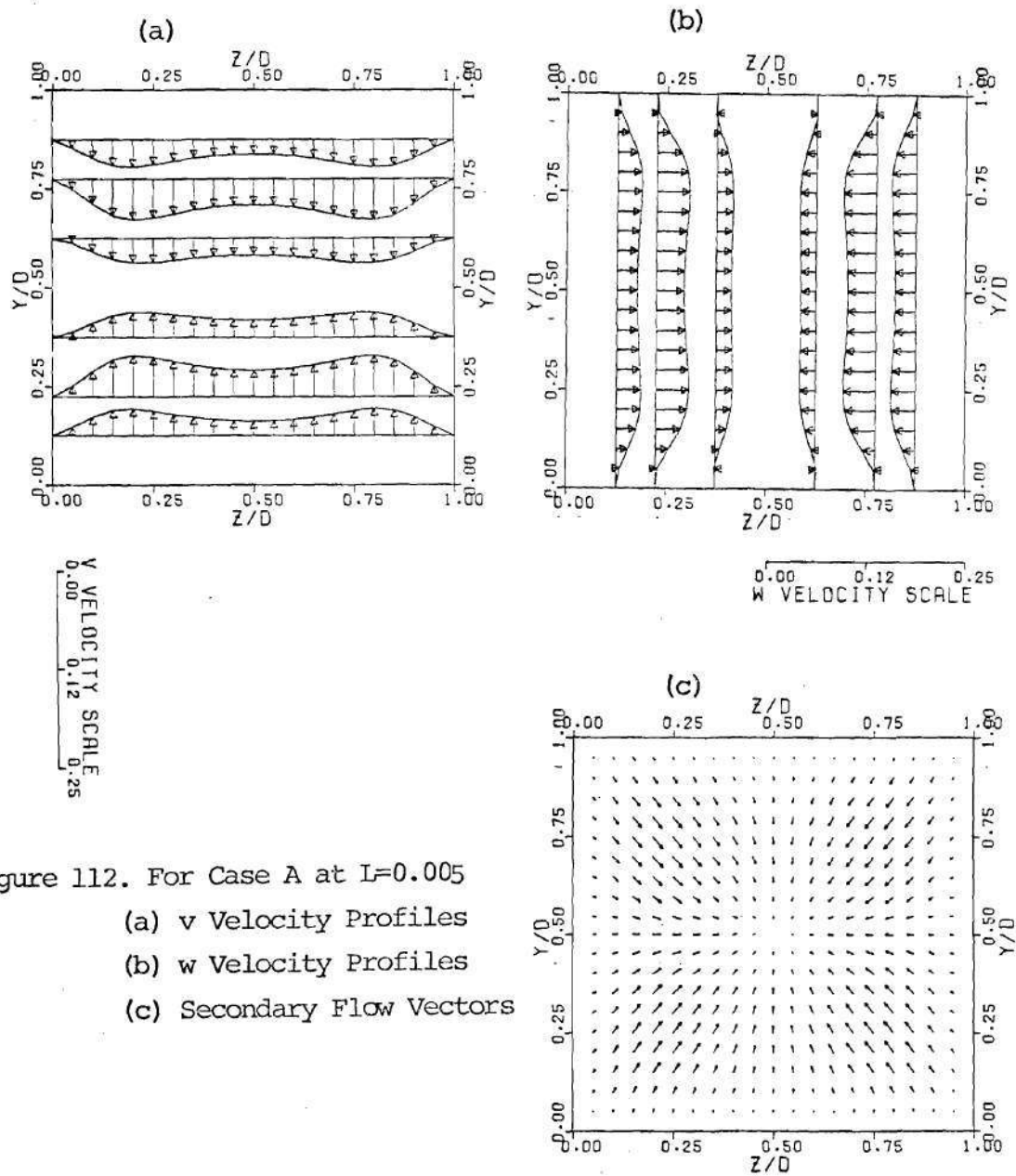


Figure 112. For Case A at $L=0.005$

- (a) v Velocity Profiles
- (b) w Velocity Profiles
- (c) Secondary Flow Vectors

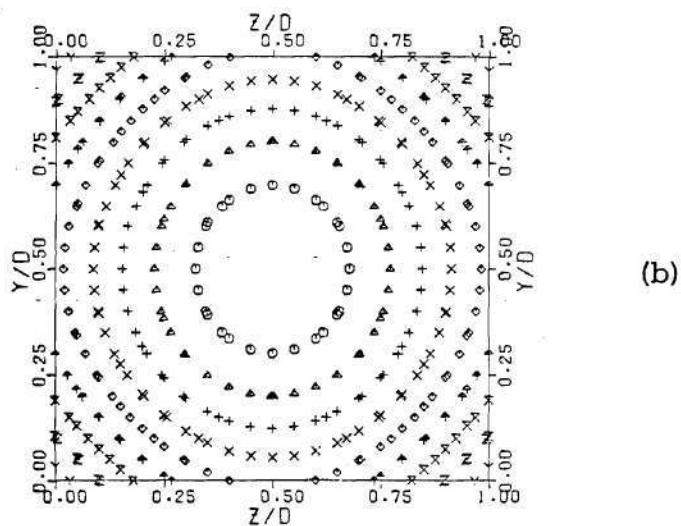
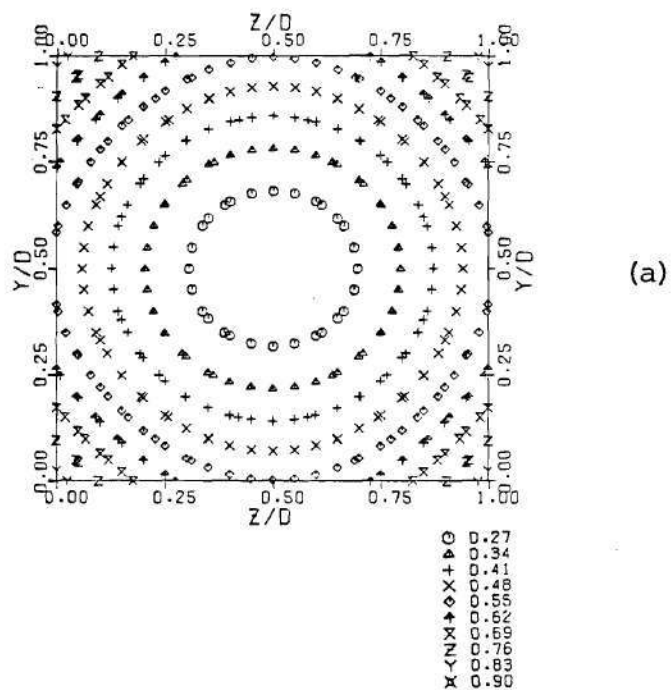


Figure 113. Temperature Contours at $I=0.1$ for
(a) Case A , (b) Case B

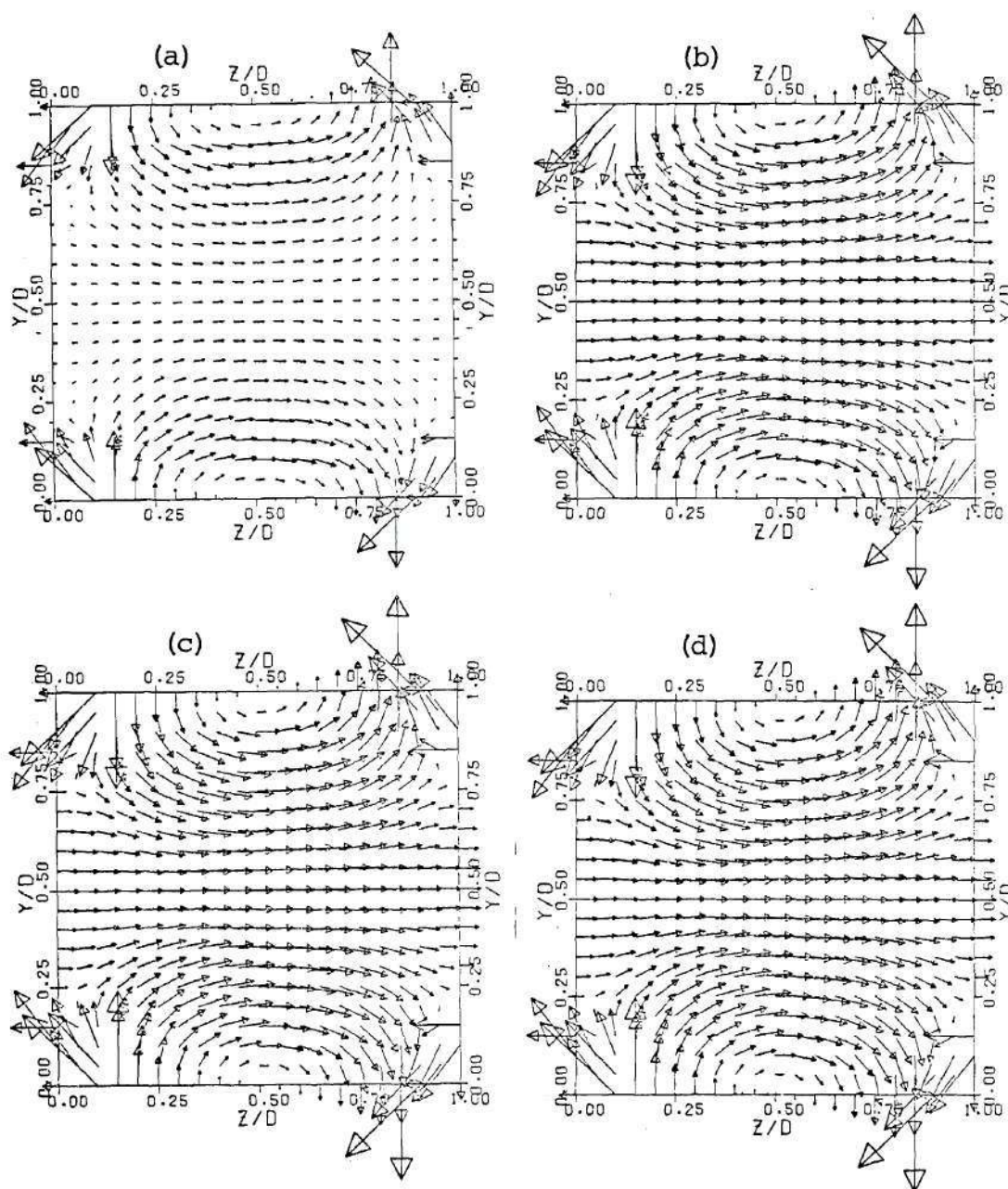


Figure 114. Current Density Vectors at
 (a) $L=0.001$, (b) $L=0.005$,
 (c) $L=0.010$, (d) $L=0.100$

Case C

$C=\infty$ on Walls and $C=0$ on Corners

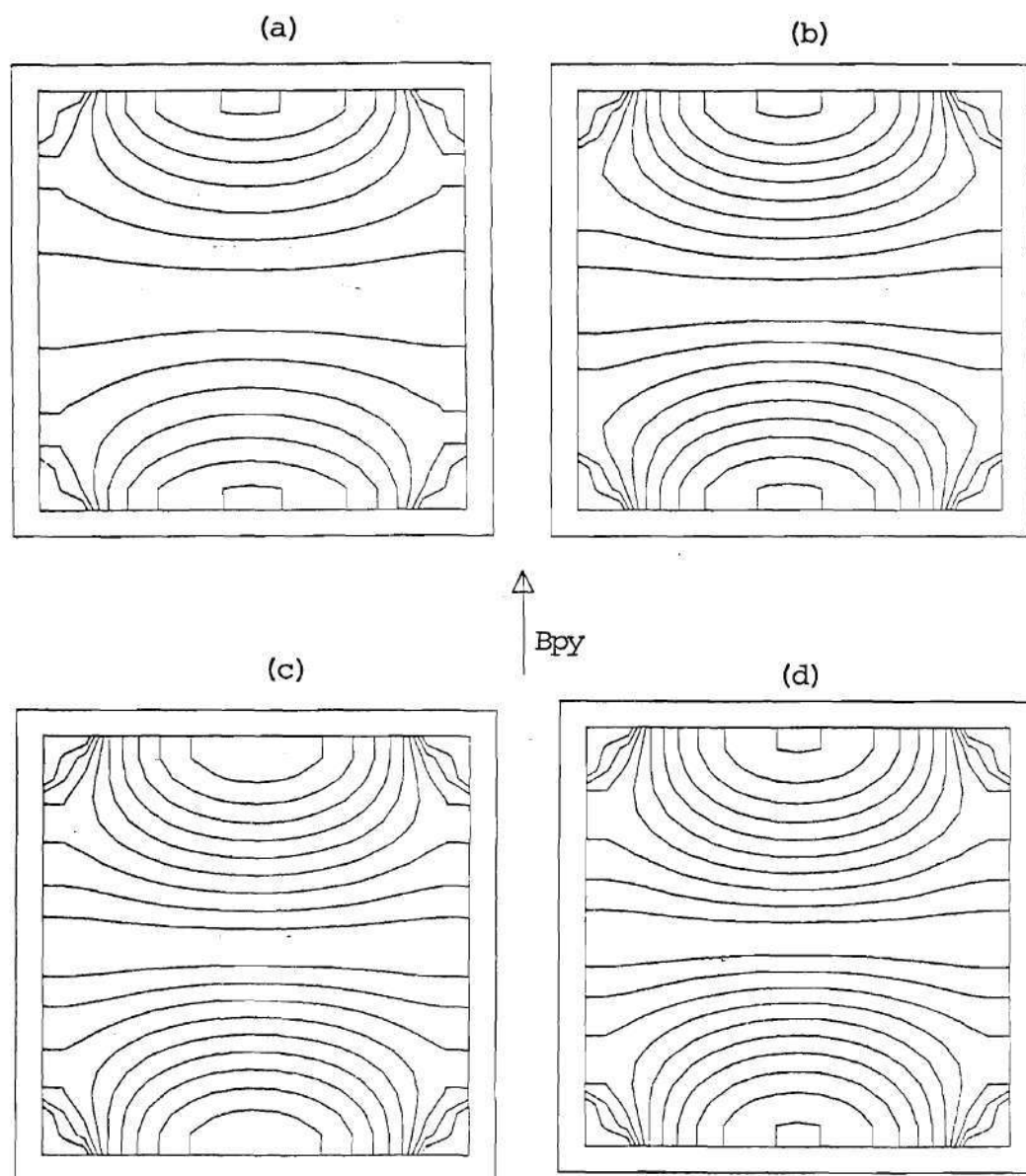


Figure 115. Axial Field Contours at
(a) $L=0.001$, (b) $L=0.005$,
(c) $L=0.010$, (d) $L=0.100$

Case C

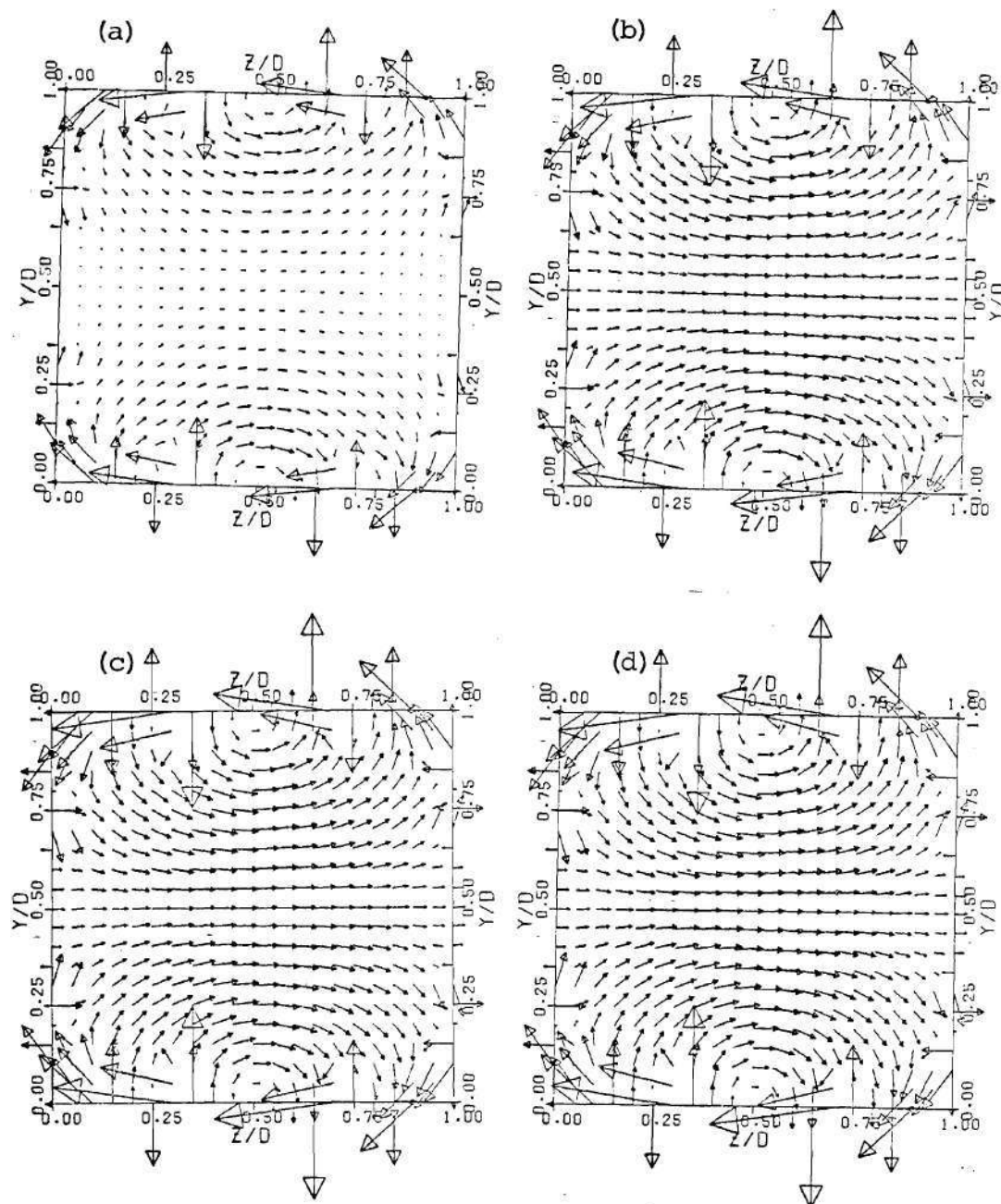


Figure 116. Current Density Vectors at
 (a) $L=0.001$, (b) $L=0.005$,
 (c) $L=0.010$, (d) $L=0.100$

Case D Same as Case C except with Two Insulating Points
 on each Wall

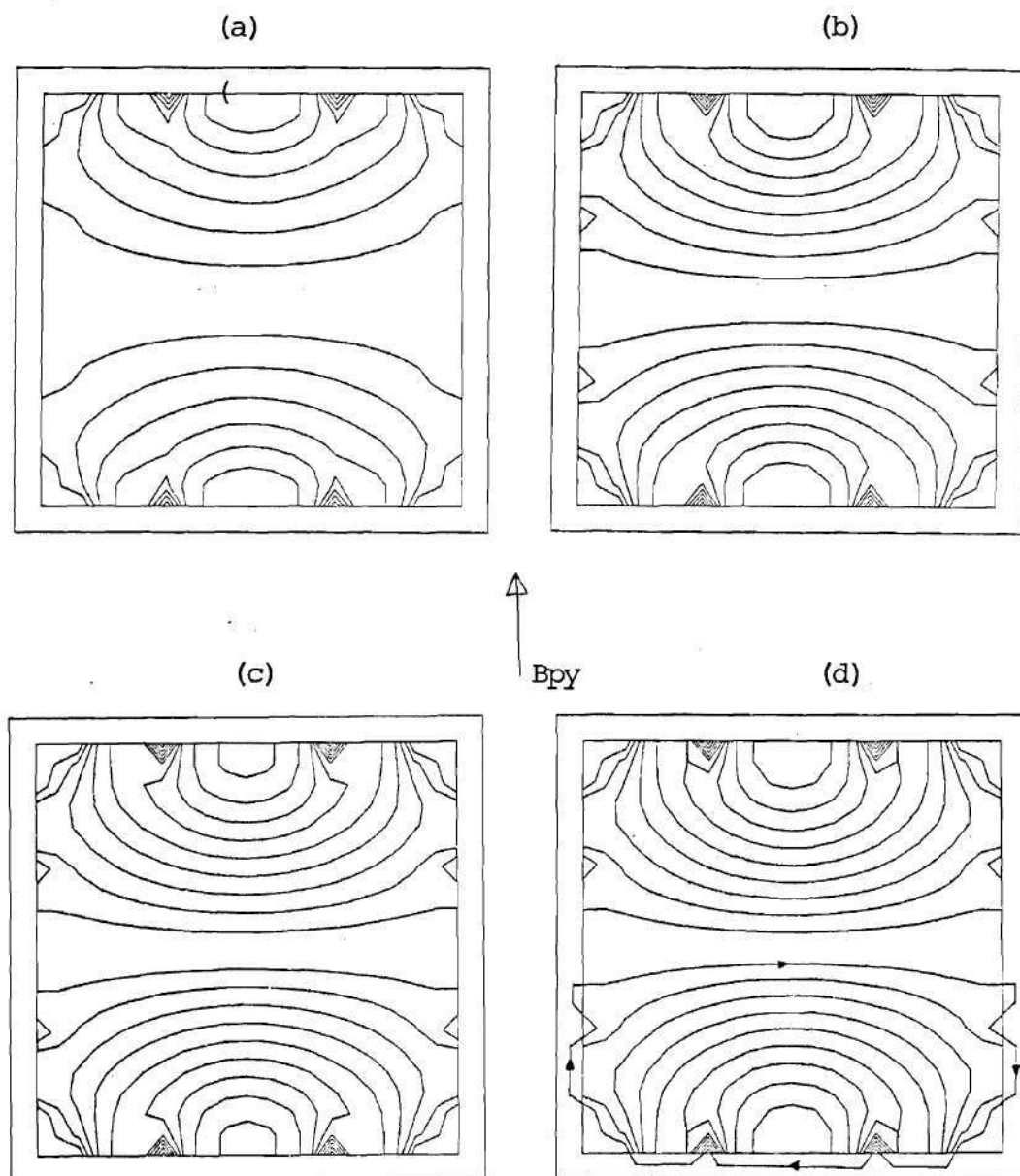


Figure 117. Axial Field Contours at
 (a) $L=0.001$, (b) $L=0.005$,
 (c) $L=0.010$, (d) $L=0.100$

Case D

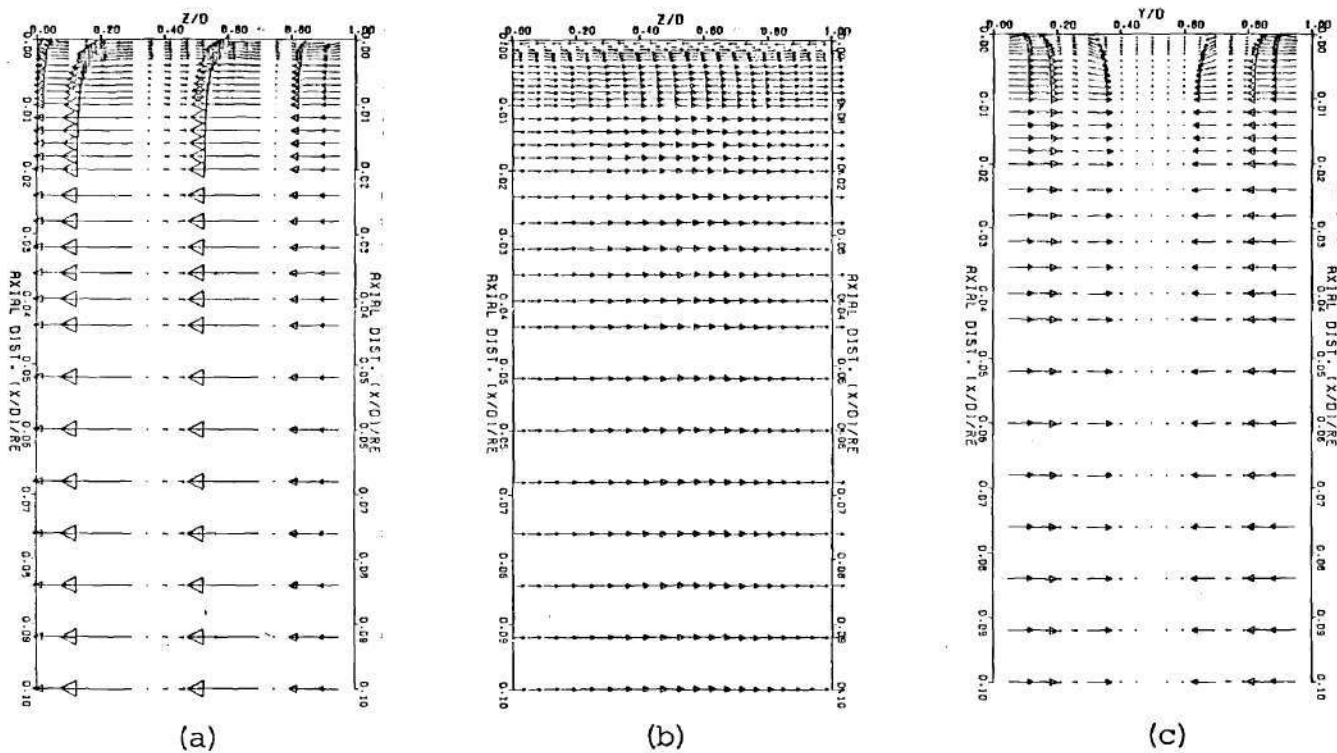


Figure 118. Current Density Vectors in Axial Plane

(a) xz near Wall ($Y/D=0.05$)

(b) xz at Center

(c) xy near Wall ($Z/D=0.05$)

Case D

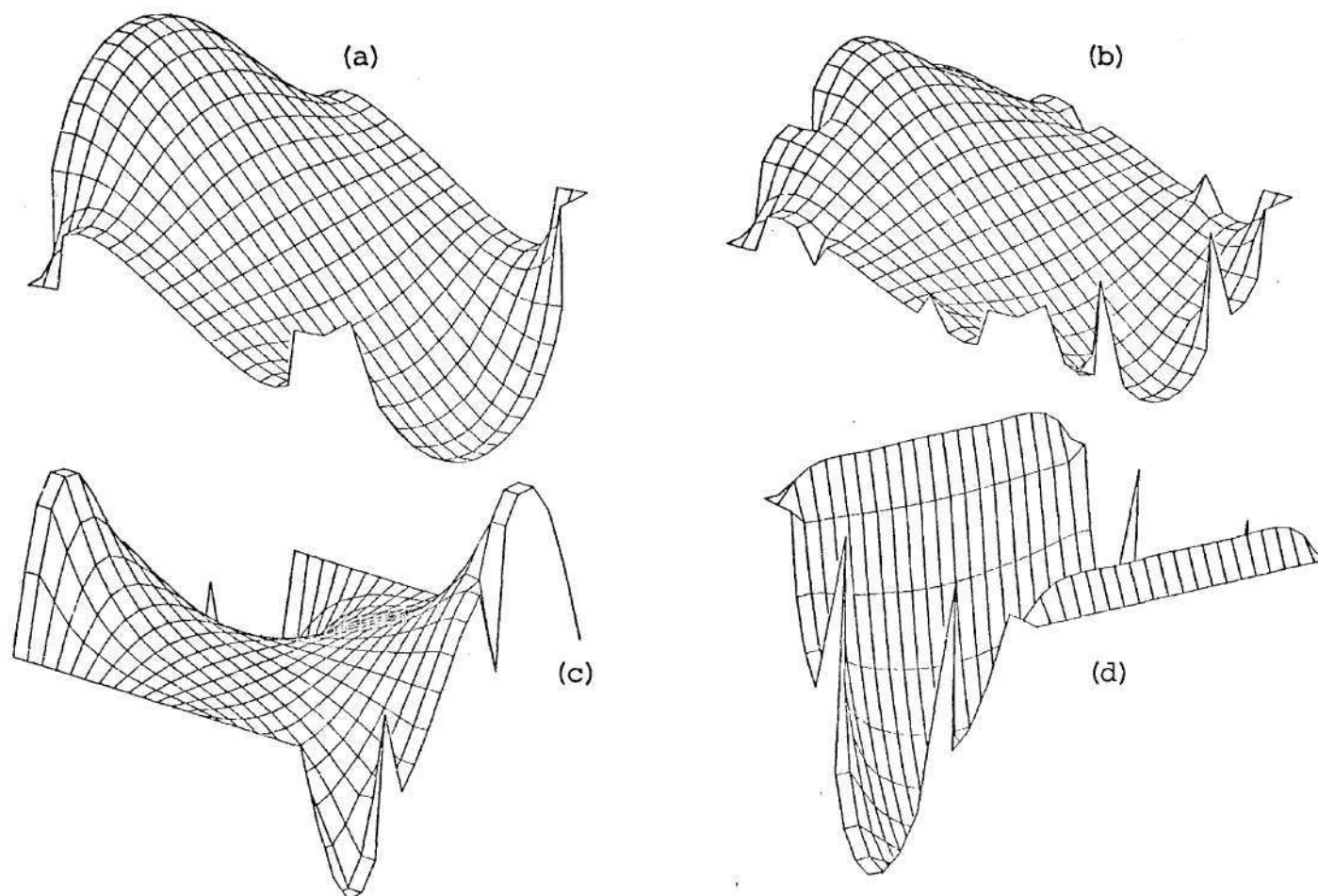


Figure 119. Axial Field Surfaces at $L=0.1$ for (a) Case C , (b) Case D
 (c) H_z Field Surface at $L=0.001$ for Case D
 (d) H_y Field Surface at $L=0.001$ for Case D

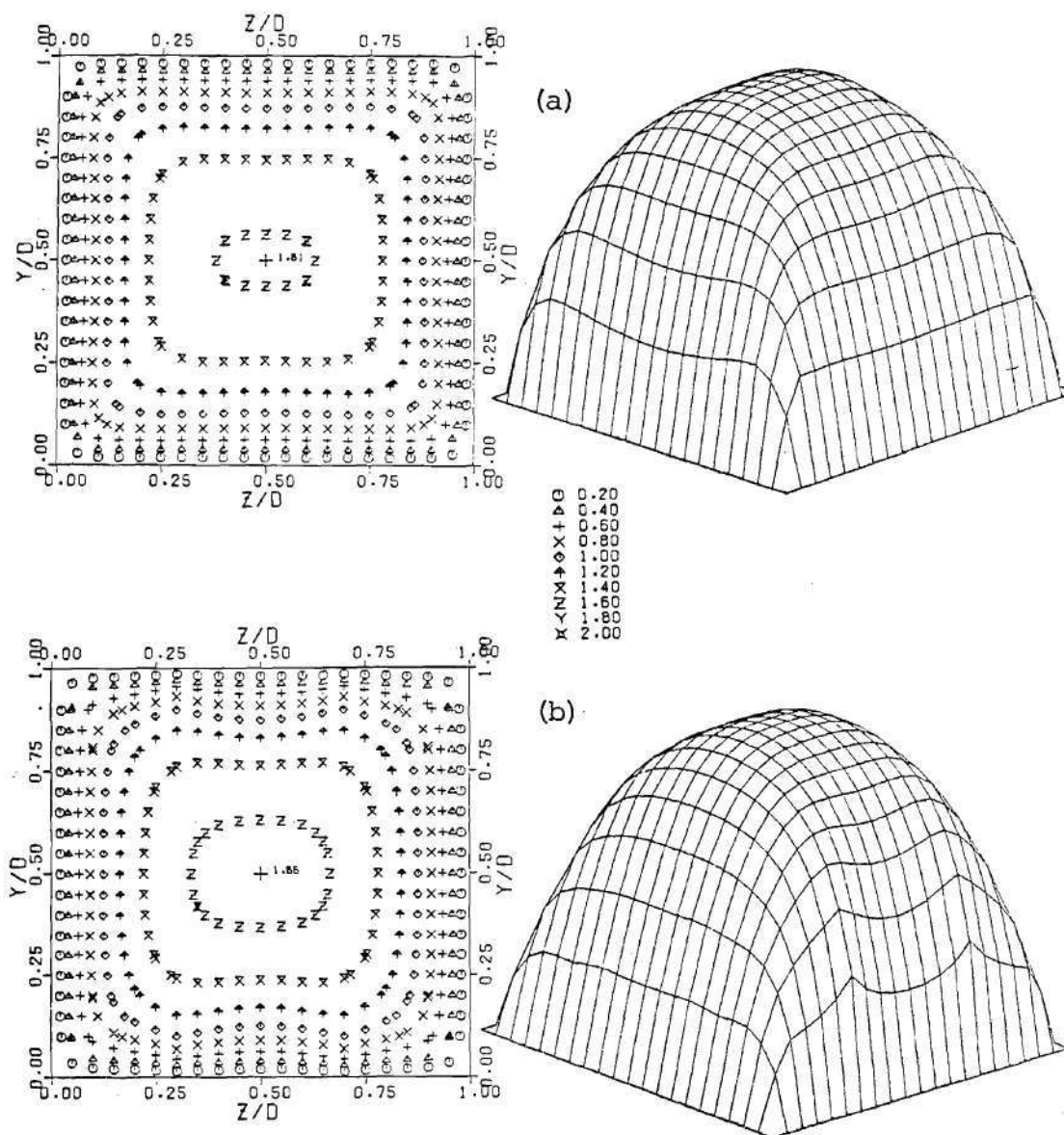


Figure 120. Axial Velocity Contours and Surface at $L=0.1$ for

(a) Case C , (b) Case D

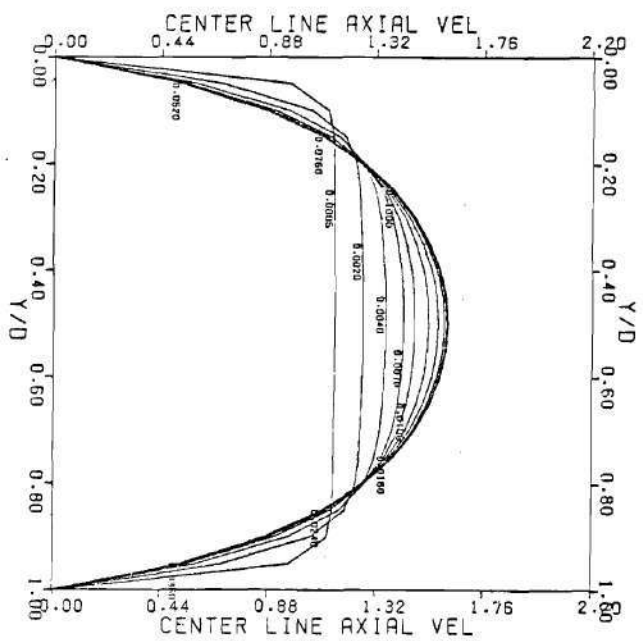
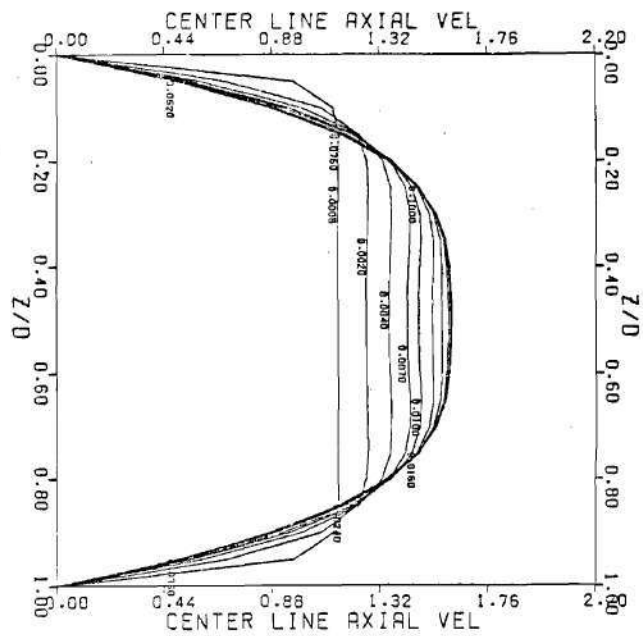


Figure 121. Center-line Axial Velocity at Values of L for Case C

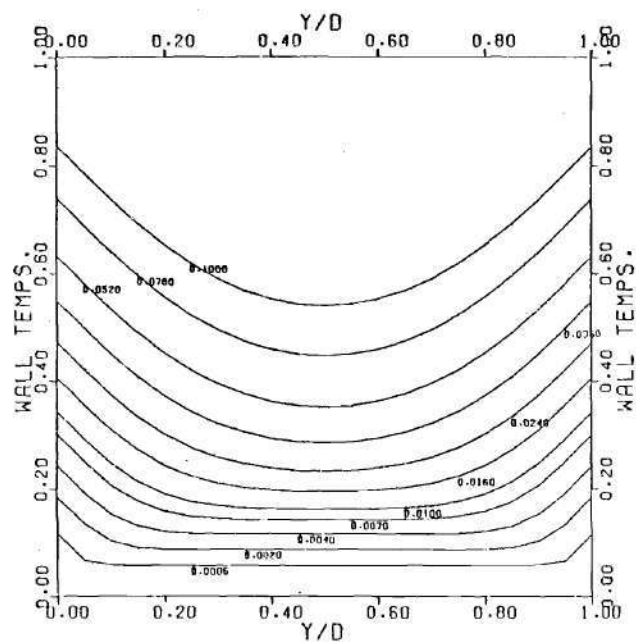


Figure 122.

Wall Temperature at Values of L
for Case C with Constant Wall Heat Flux

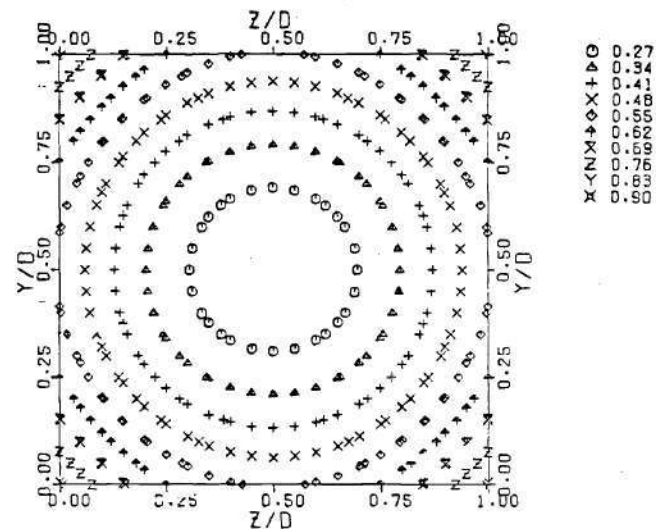
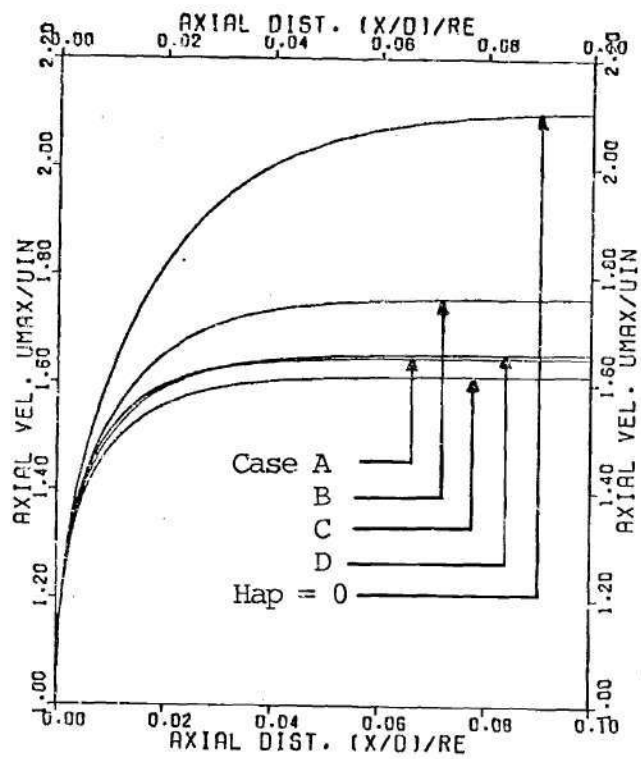
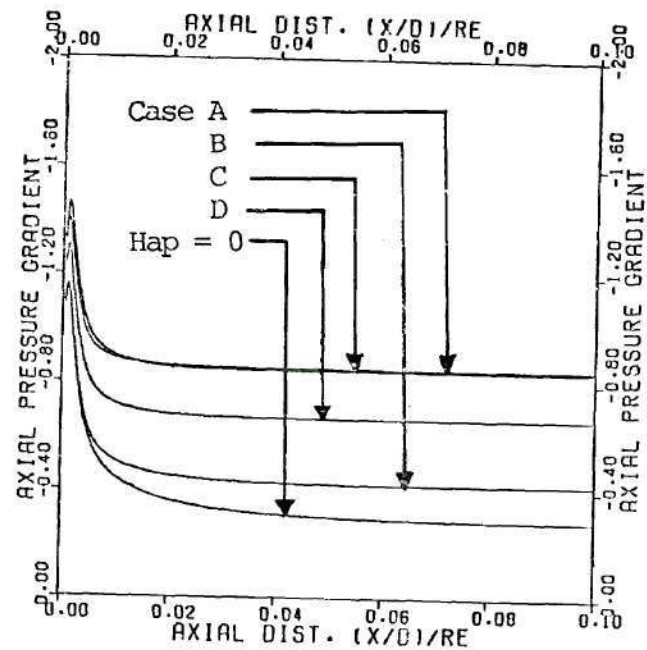


Figure 123.

Temperature Contours at $L=0.1$
for Case C with Constant Wall Heat Flux

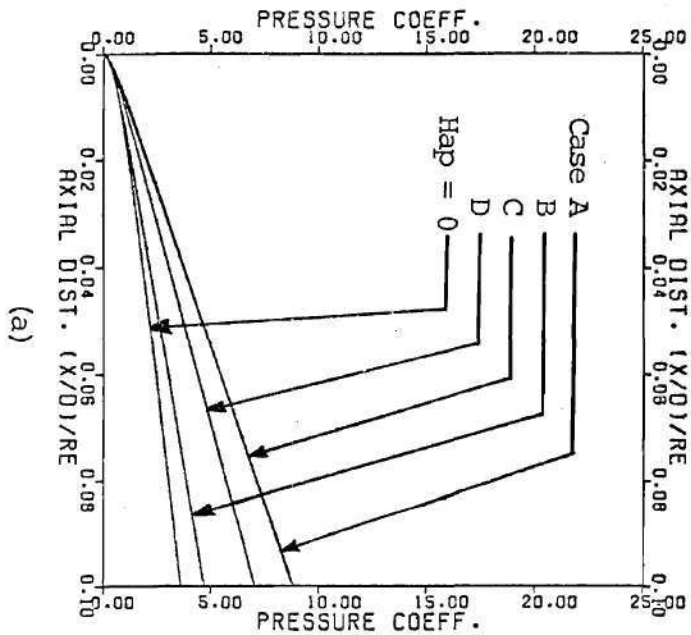


(a)

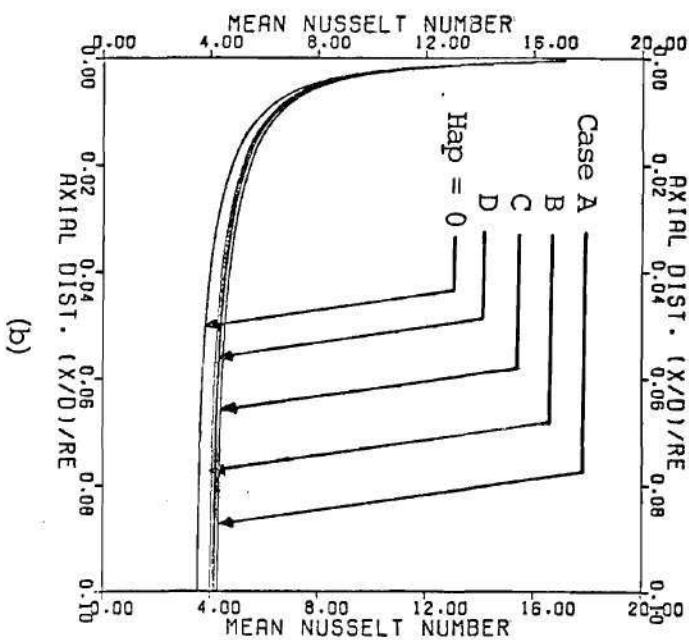


(b)

Figure 124. Case Comparison of
 (a) Center-point Axial Velocity Development
 (b) Axial Pressure Gradient Development



(a)

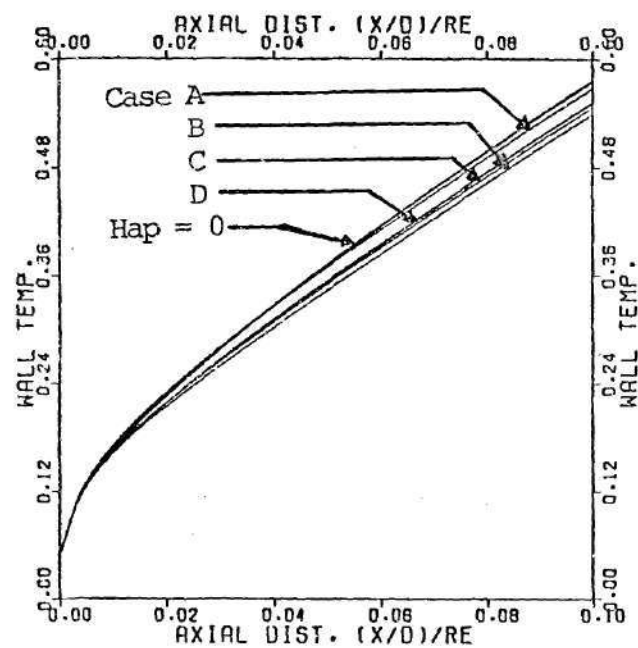


(b)

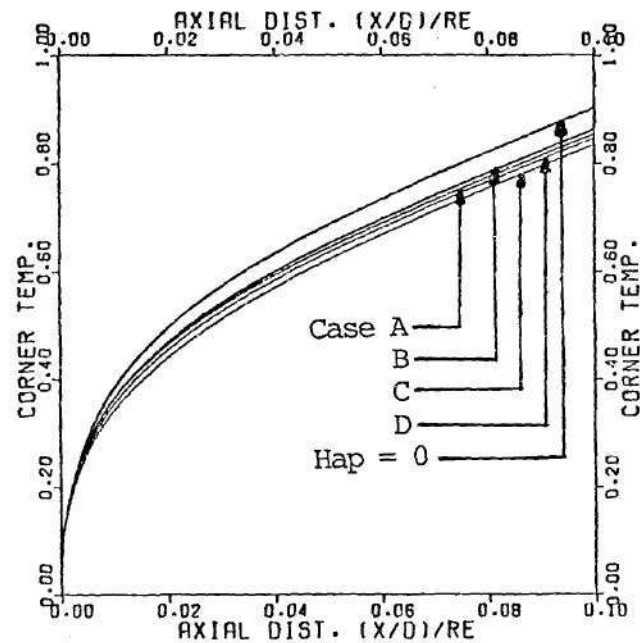
Figure 125. Case Comparison of

(a) Pressure Coefficient Development

(b) Nusselt Number Development



(a)



(b)

Figure 126. Case Comparison of
 (a) Wall Center Temperature Development
 (b) Wall Corner Temperature Development

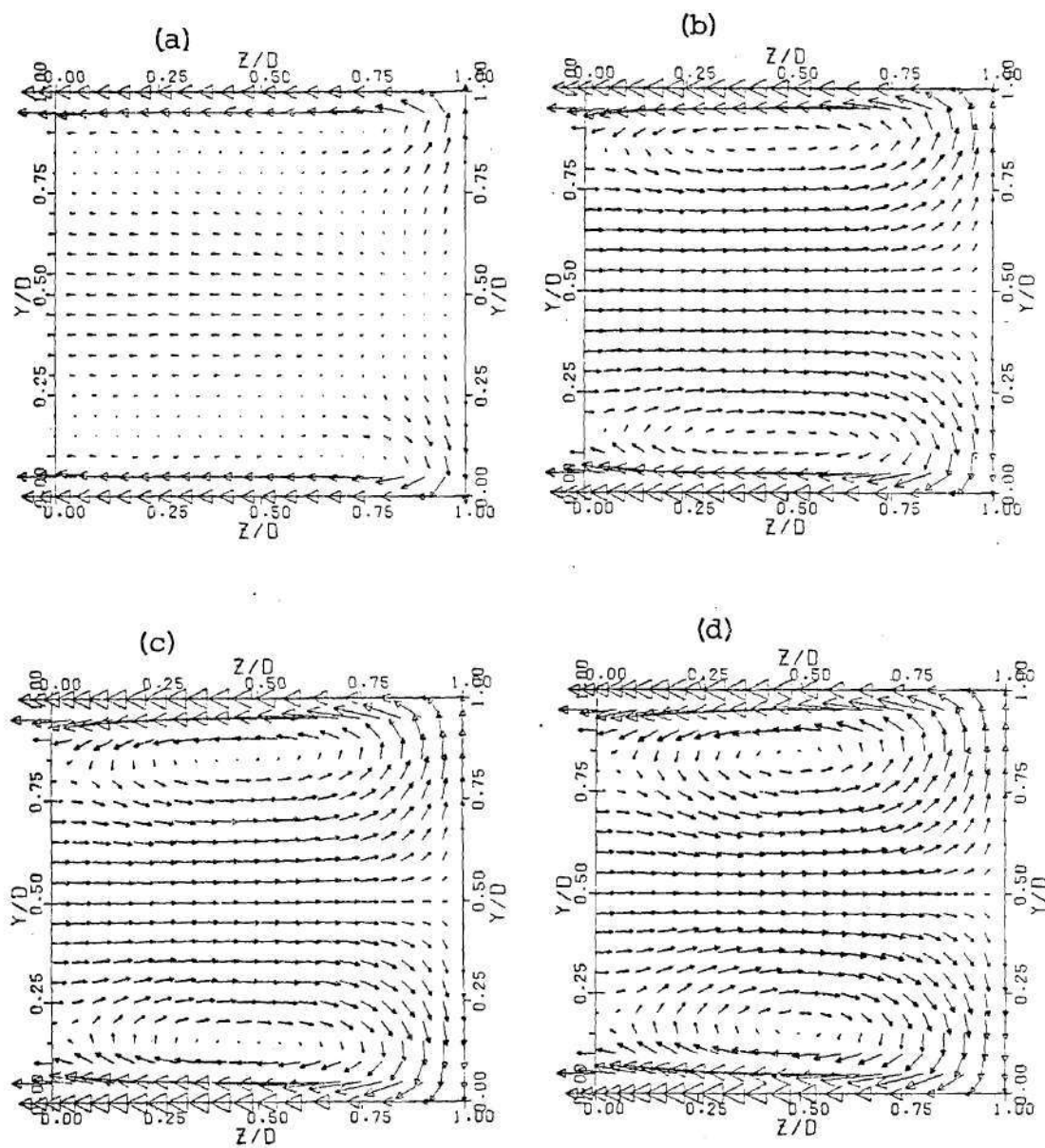


Figure 127. Current Density Vectors at
 (a) $L=0.001$, (b) $L=0.005$,
 (c) $L=0.10$, (d) $L=0.100$

Case E $C=\infty$ on one Parallel Wall and $C=0$ on Remaining
 three Walls

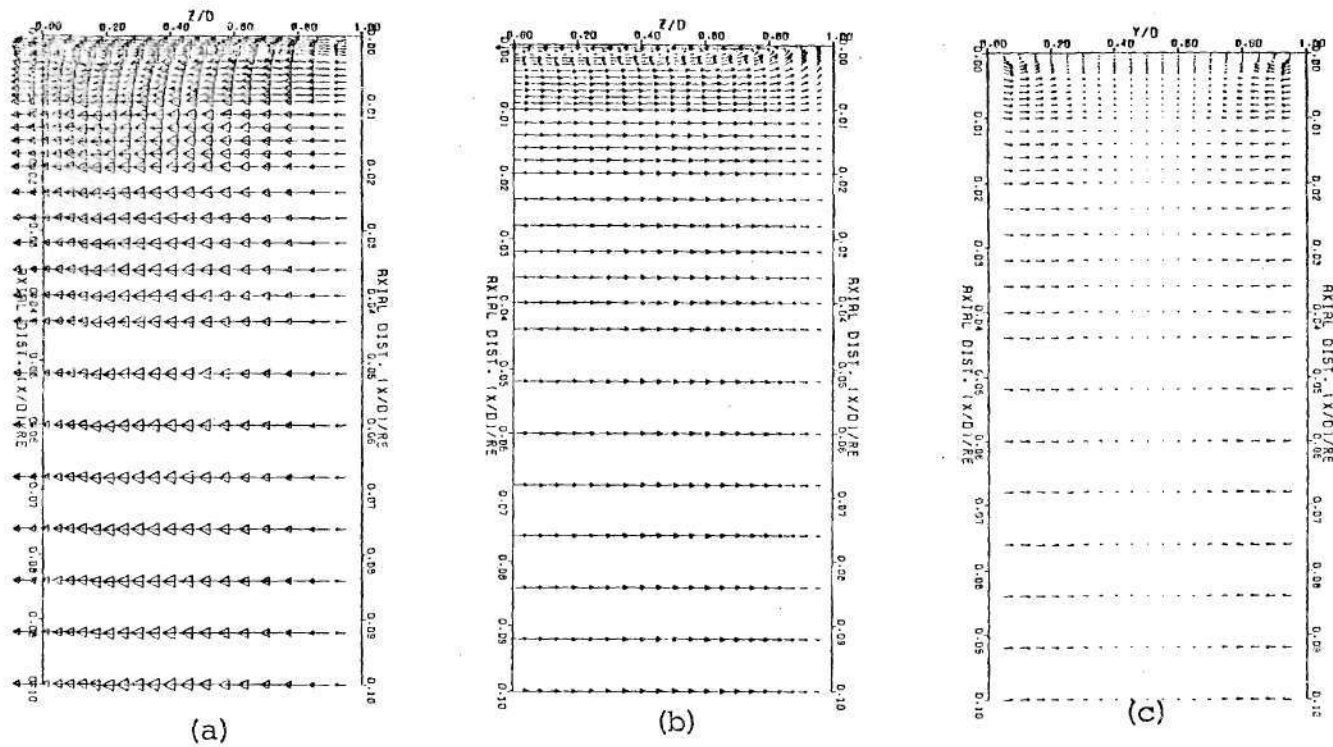


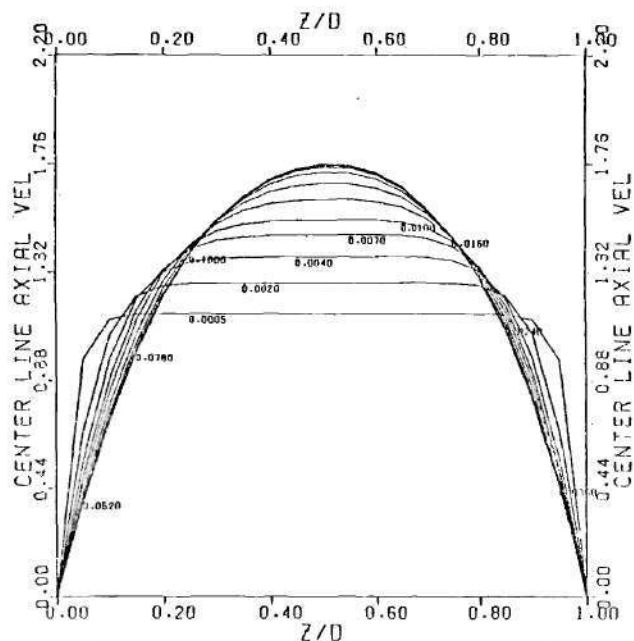
Figure 128. Current Density Vectors in Axial Plane

(a) xz near Wall ($Y/D=0.05$)

(b) xz at Center

(c) xy near Wall ($Z/D=0.05$)

Case E



(a)

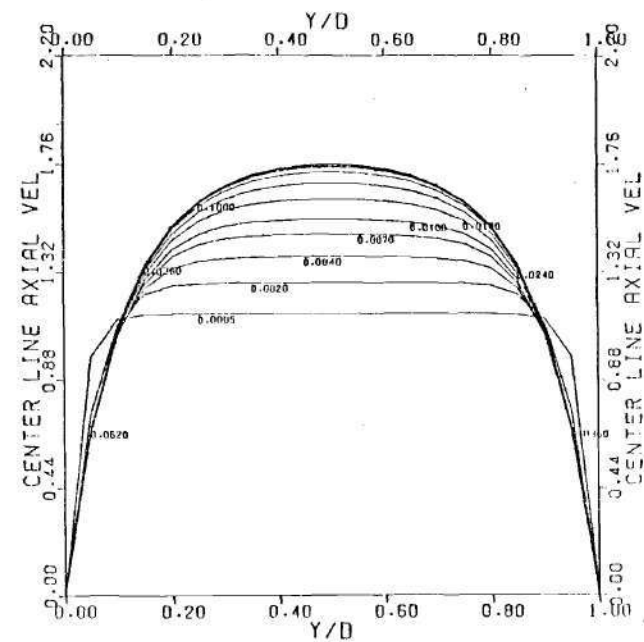


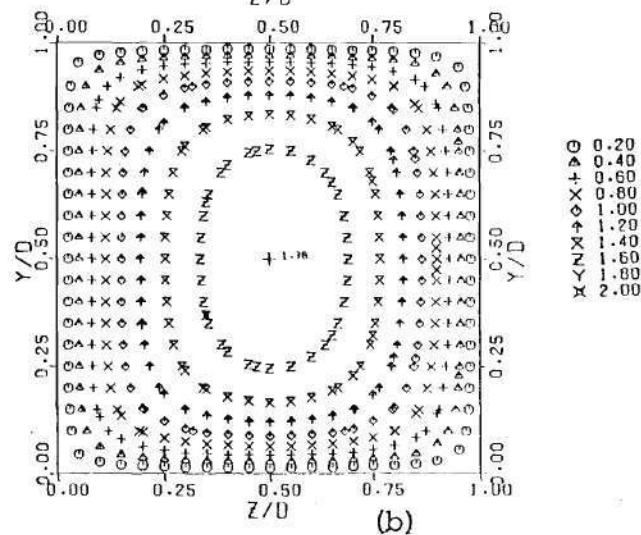
Figure 129.

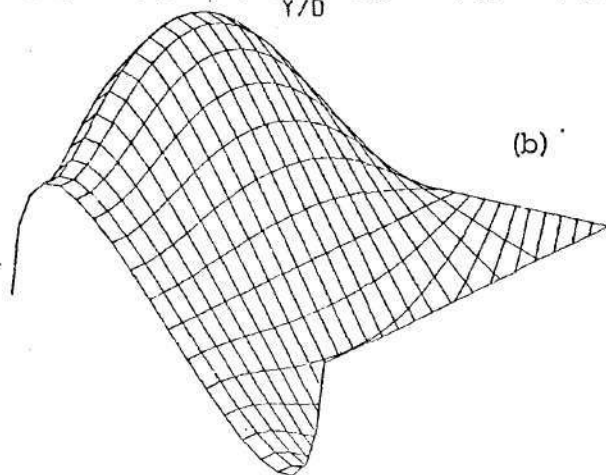
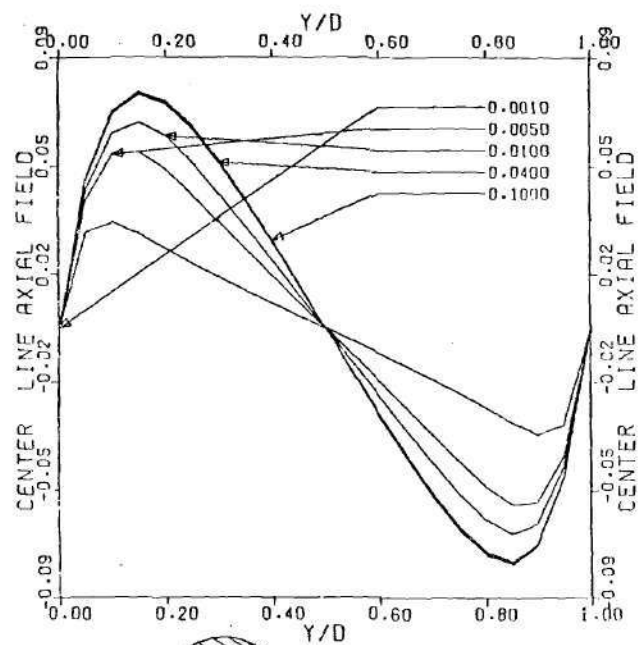
(a) Axial Velocity at Values of L

(b) Axial Velocity Contours at

L=0.1

Case E





(a)

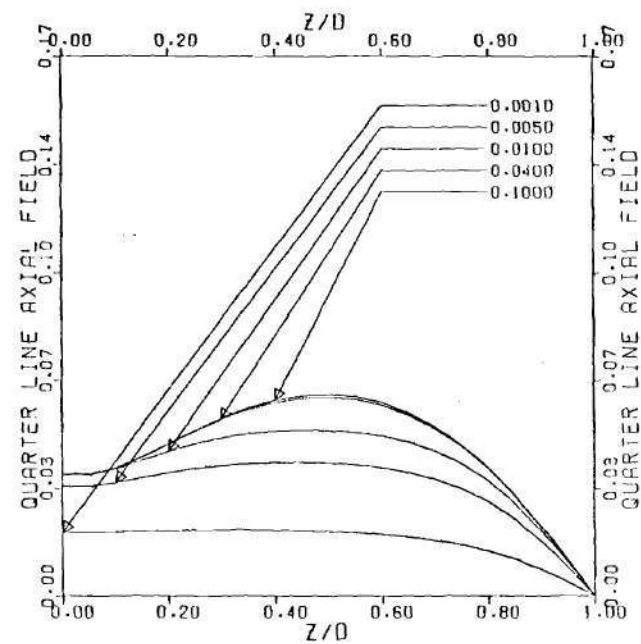


Figure 130.

(a) Axial Field at Values of L

(b) Axial Field Surface at

$L=0.1$

Case E

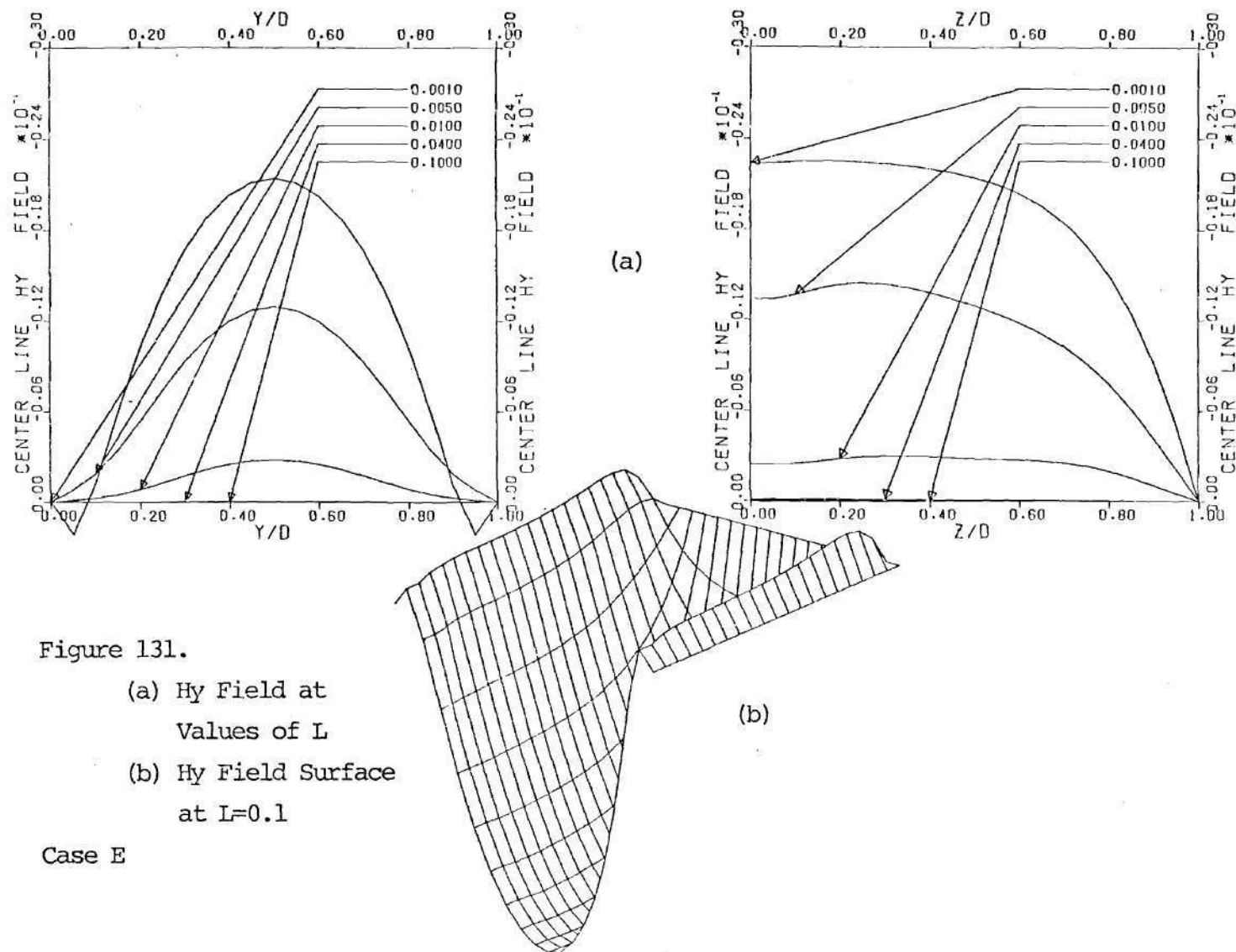


Figure 131.

- (a) Hy Field at
Values of L
- (b) Hy Field Surface
at $L=0.1$

Case E

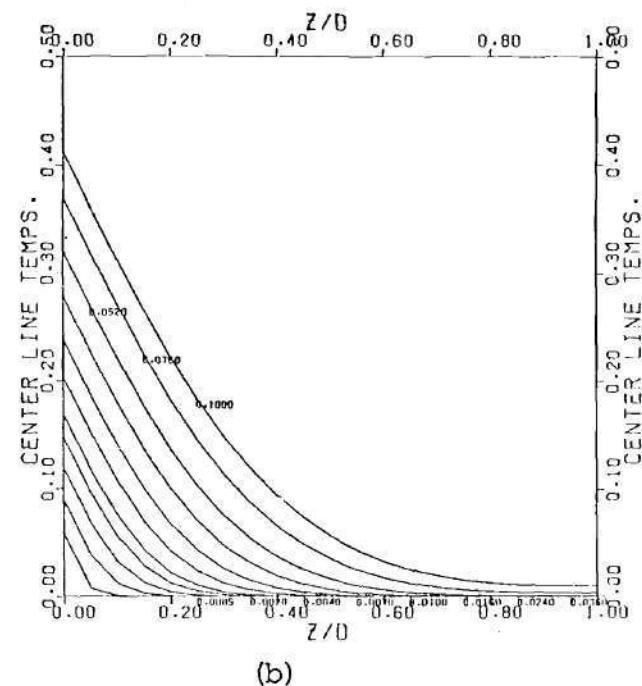
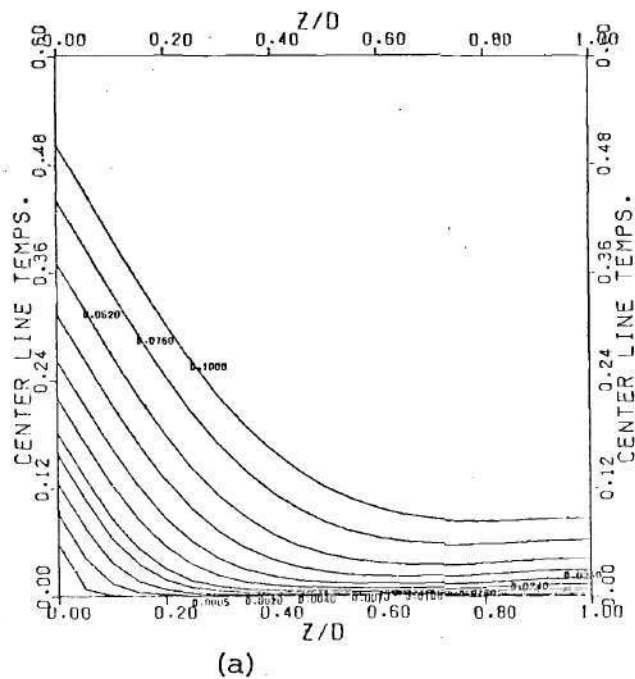


Figure 132. Center-line Temperatures at Values of L for
 (a) Linearly Varying Heat Generation (Internal)
 (b) No Heat Generation

Case E

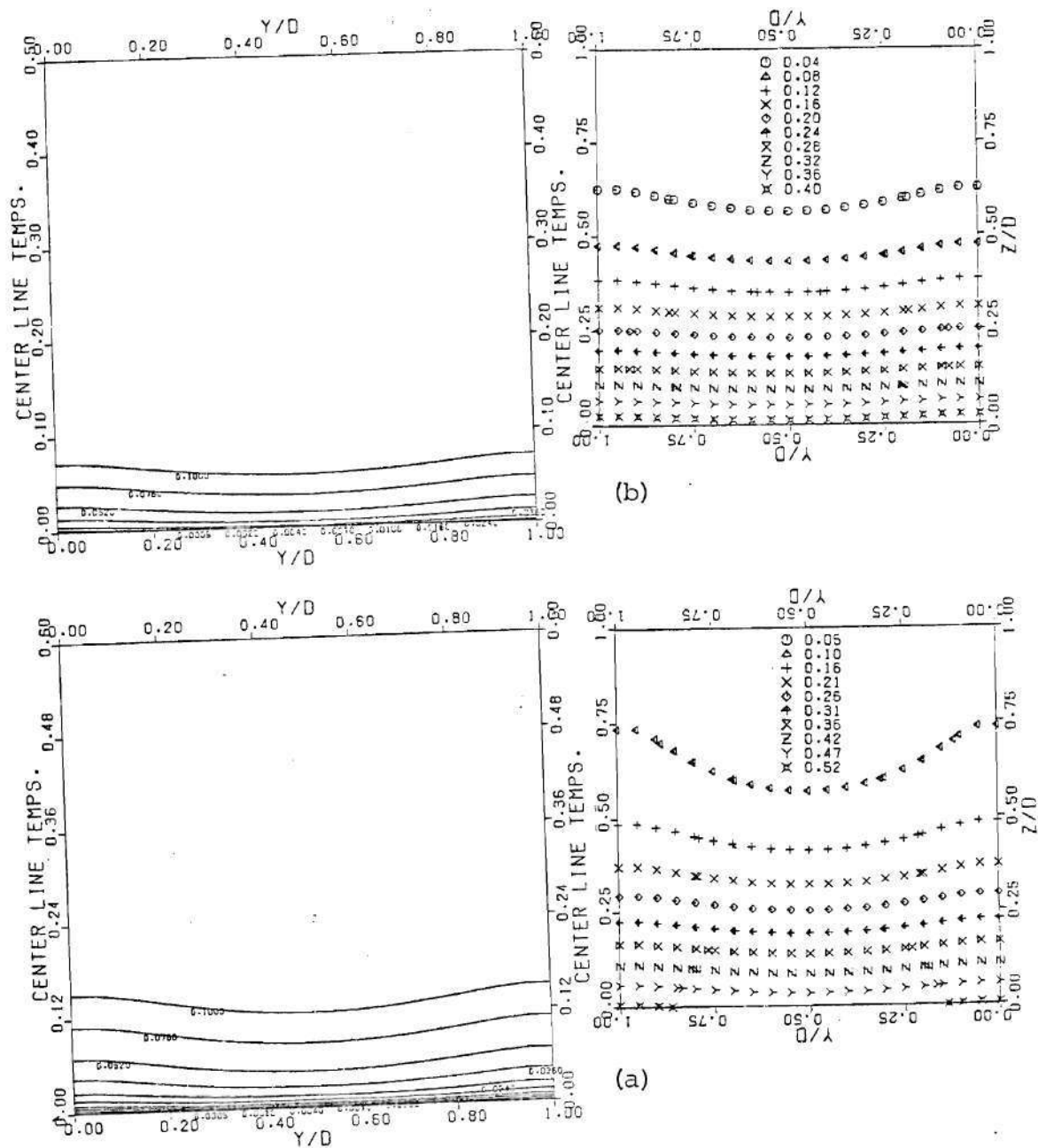
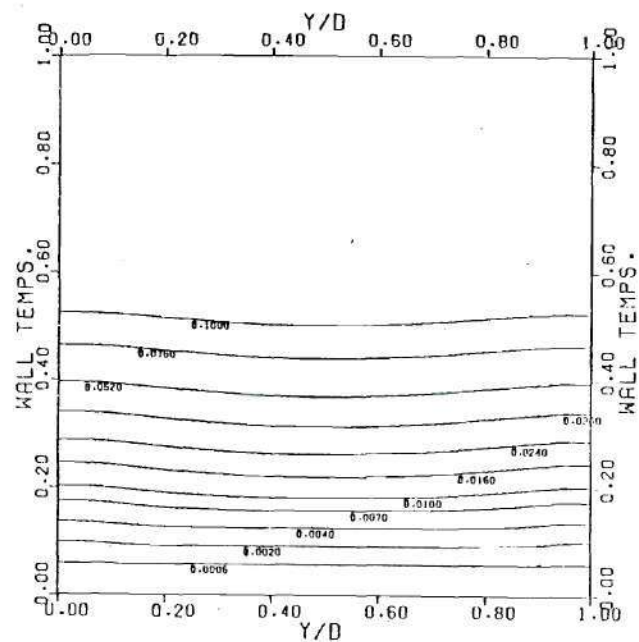
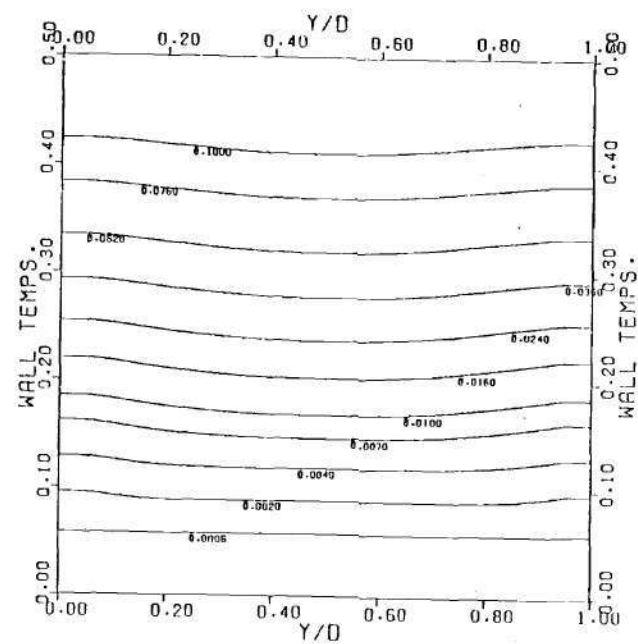


Figure 133. Temperatures at Values of L and Temperature Contours at $L=0.1$ for (a) Linear Internal Heat Generation
 (b) No Internal Heat Generation

Case E



(b)



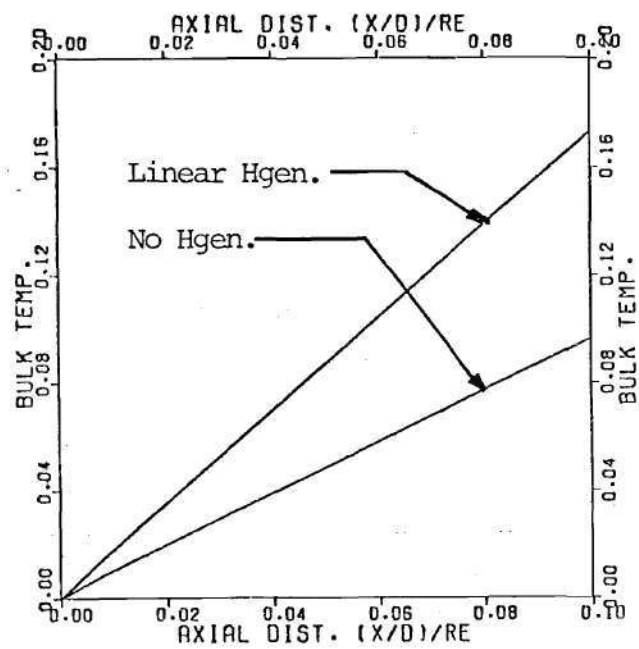
(a)

Figure 134. Conducting Wall Center Temperatures at Values of L for

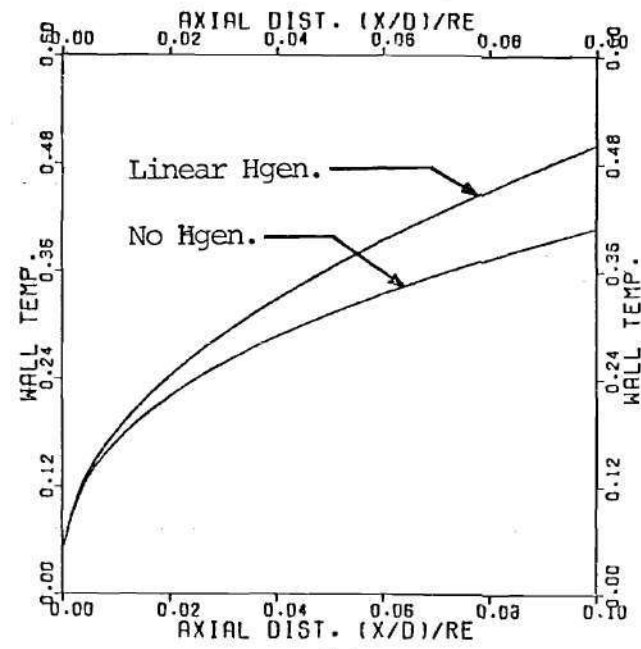
(a) Linearly Varying Internal Heat Generation

(b) No Internal Heat Generation

Case E



(a)



(b)

Figure 135.

(a) Bulk Temperature Development

(b) Conducting Wall Center Temperature Development

Case E

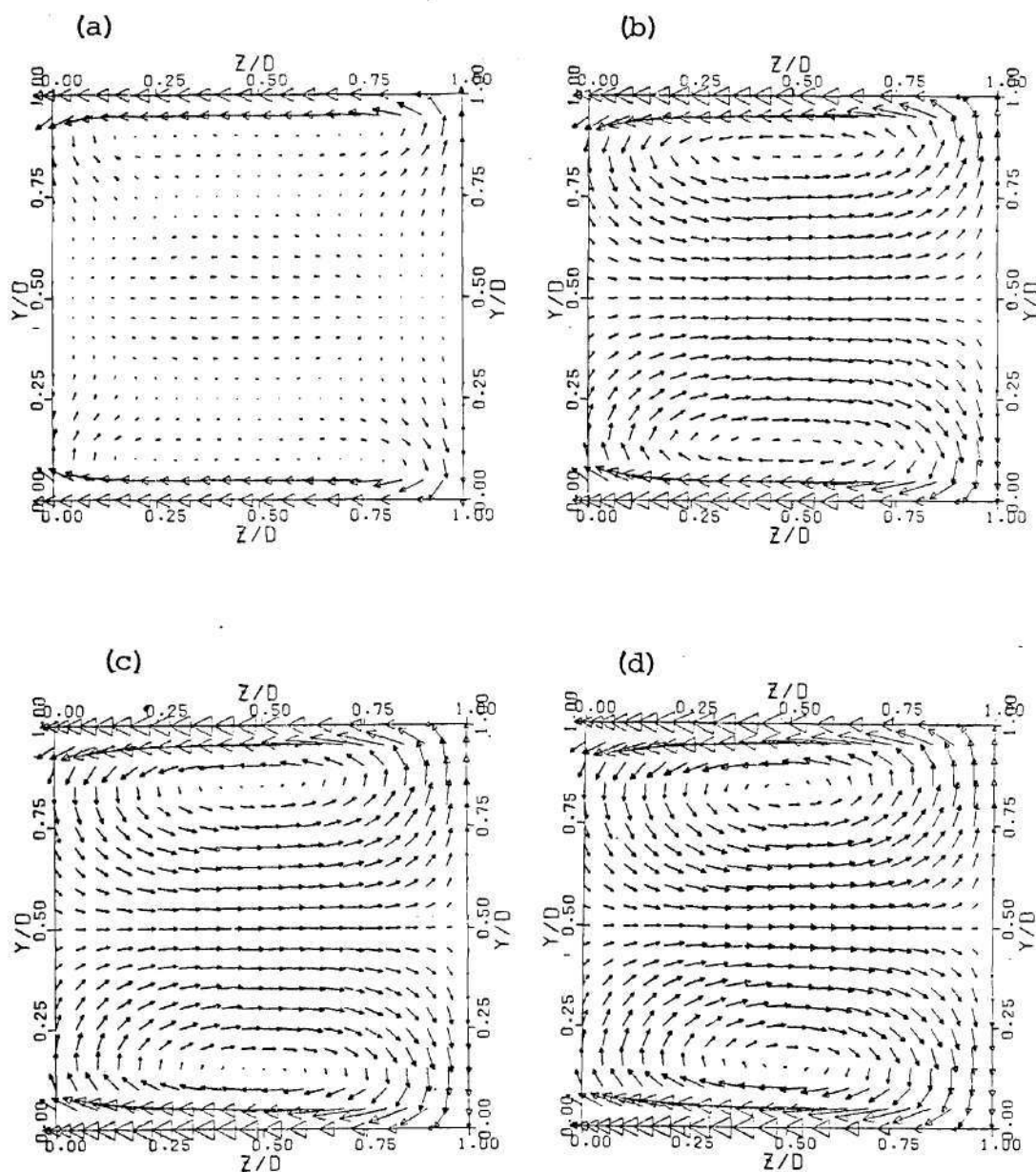


Figure 136. Current Density Vectors for

(a) $L=0.001$, (b) $L=0.005$,

(c) $L=0.010$, (d) $L=0.100$

Case F'

Same as Case E except $C=0.1$ for Conducting Wall

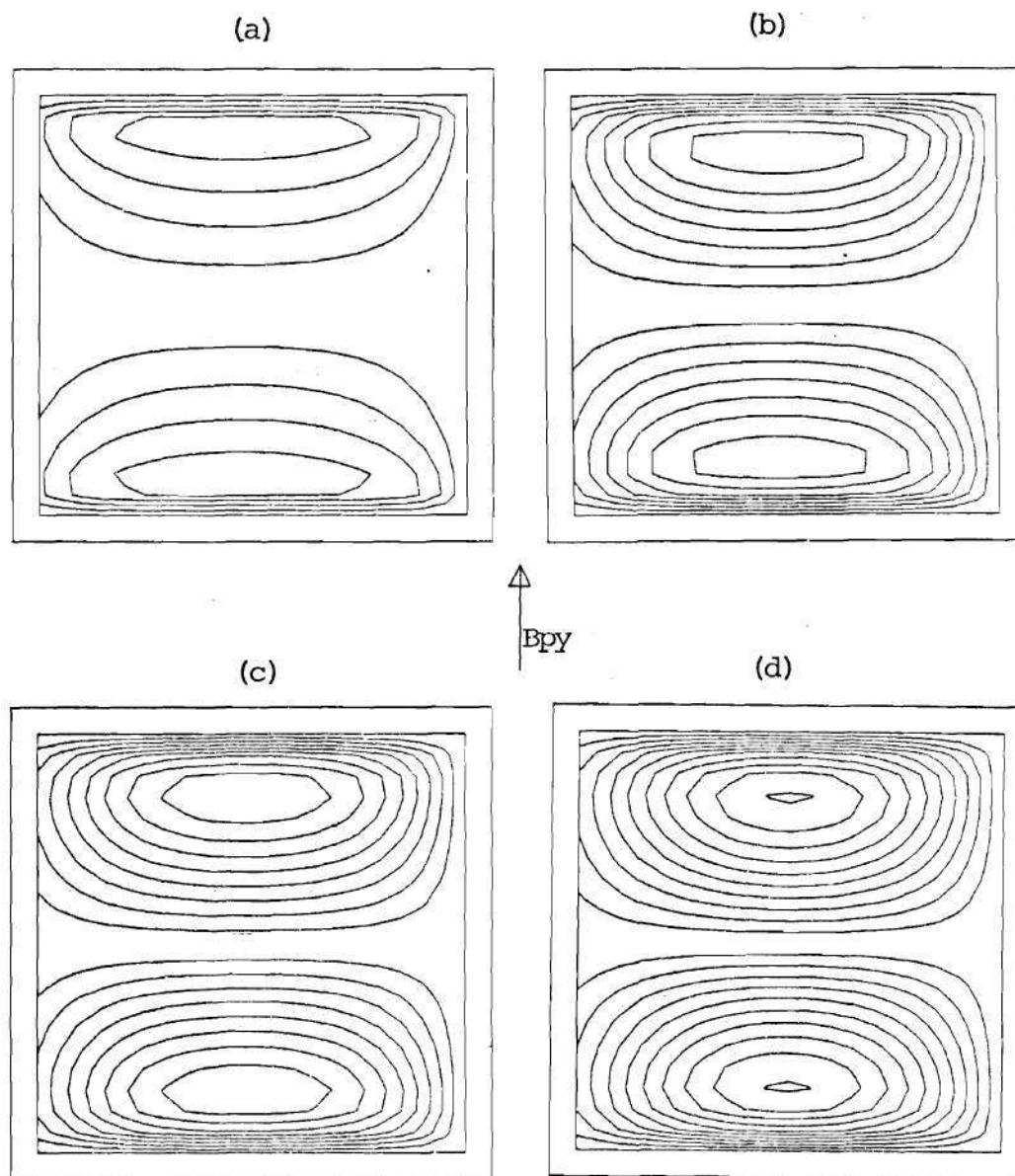


Figure 137. Axial Field Contours for

(a) $I=0.001$, (b) $I=0.005$,
(c) $I=0.010$, (d) $I=0.100$

Case F

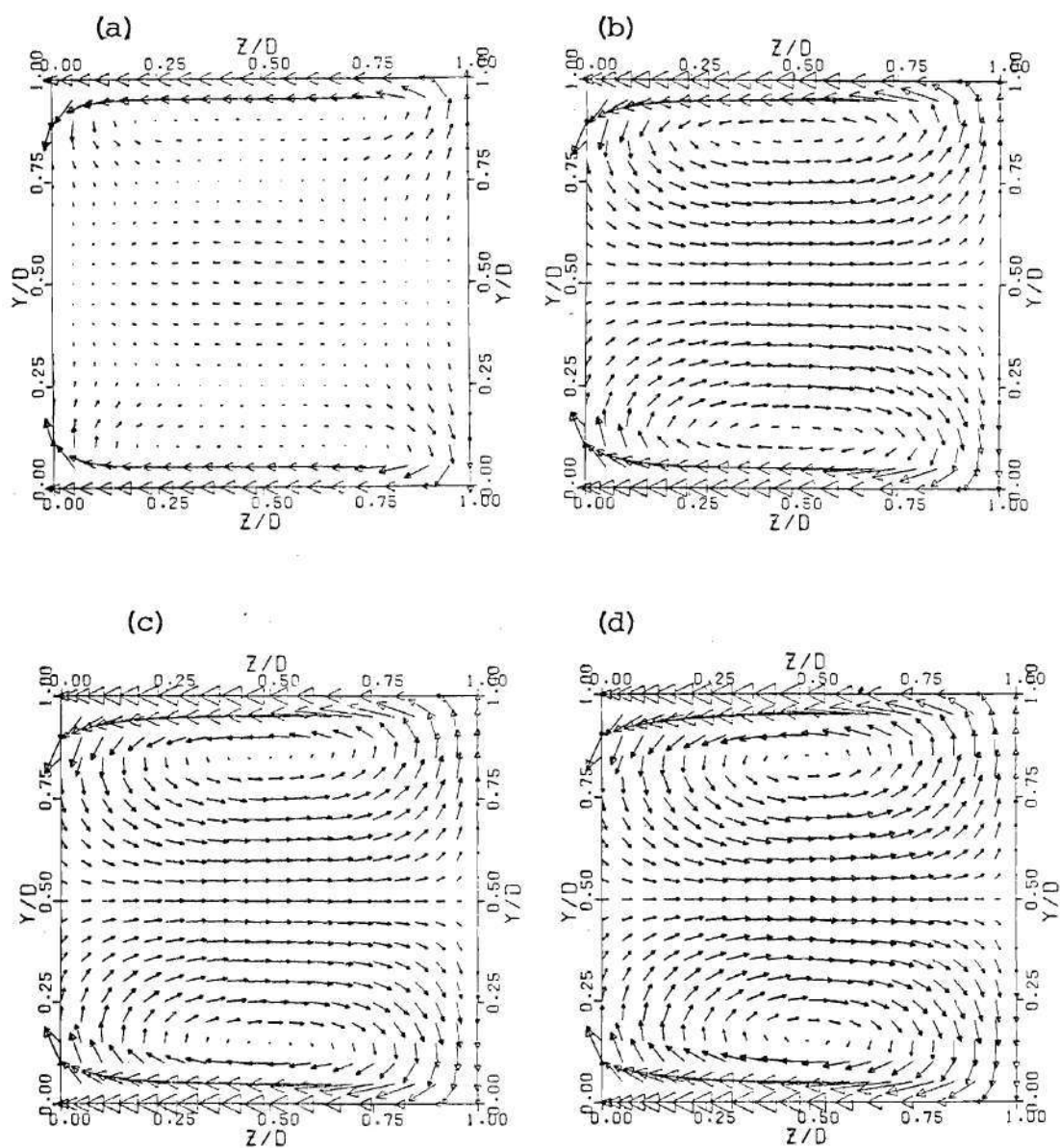


Figure 138. Current Density Vectors at
 (a) $L=0.001$, (b) $L=0.005$,
 (c) $L=0.010$, (d) $L=0.100$

Case G Same as Case F except with Two Corners Insulated

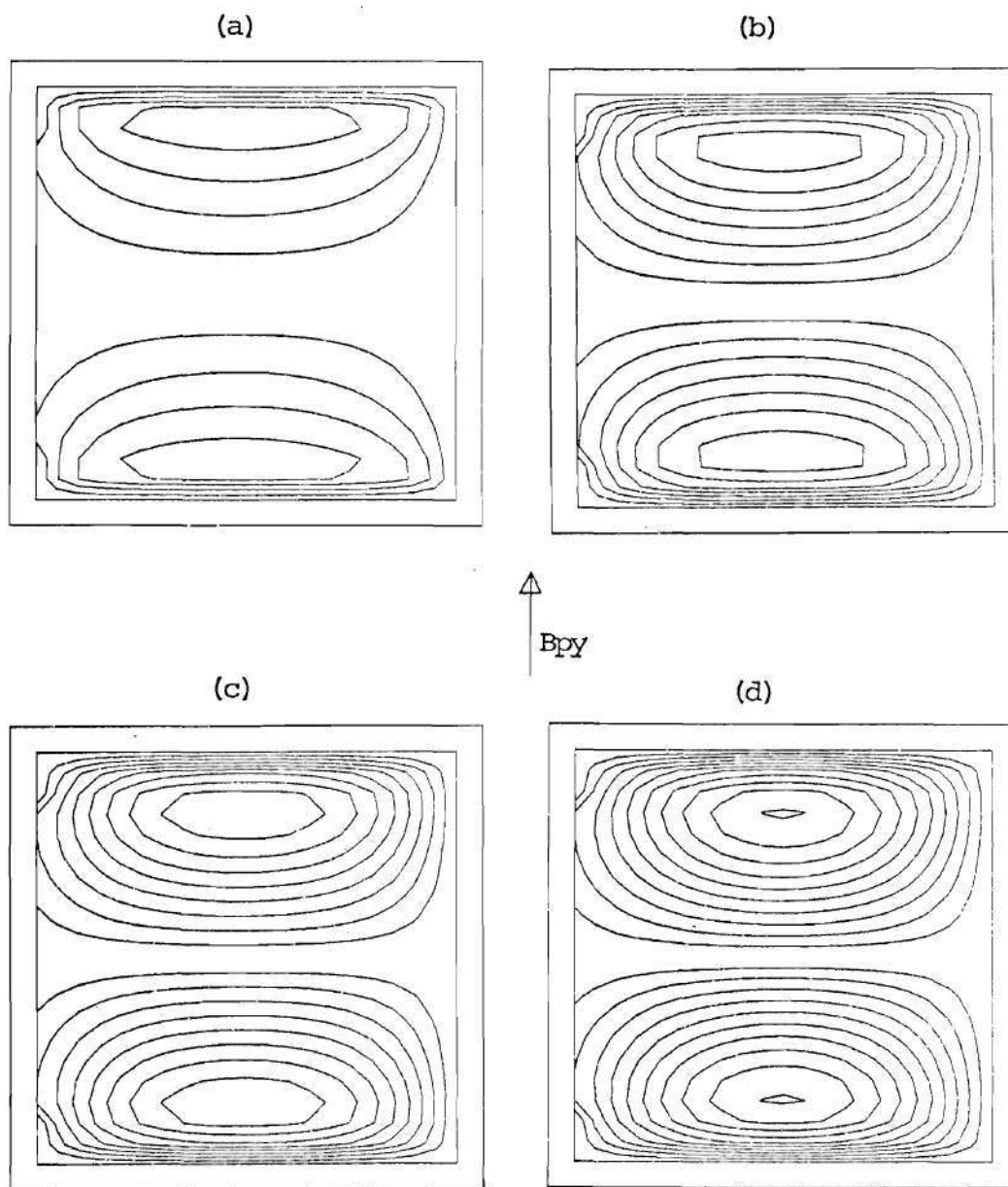


Figure 139. Axial Current Contours at
(a) $L=0.001$, (b) $L=0.005$,
(c) $L=0.010$, (d) $L=0.100$

Case G

CHAPTER VI

CONCLUSIONS AND SUGGESTIONS FOR FUTURE WORK

It is possible to conclude that the three-dimensional MHD entry problem has been solved for low Hartmann number. The accuracy of this solution can be improved by a number of means. First of all, better treatment of the induction boundary conditions, both mathematically and numerically could be imposed. The ideal treatment, however, would involve a separate solution of the induction equation in the duct wall itself, and then the matching of this solution to that in the fluid region in such a way as to satisfy the boundary conditions at the interface. Numerical treatment of the boundary regions can also be improved by such means as specification of slip values at the wall. These slip values are calculated by assuming an appropriate property variation near the wall, e.g. quadratic or exponential.³⁷

No claim is made as to having explicitly solved the Tokamak blanket problem, because this involves much higher Hartmann and Reynolds numbers, and a different formulation and numerical approach would be required. For high Hartmann numbers the flow consists of a core with uniform velocity, and thin boundary layers on the walls. Adequate treatment of these layers, without the use of excessive numbers of mesh points, would require a rather severely varying mesh size. It may be possible to use new hybrid schemes involving finite element nodes in the boundary layer regions for which the errors associated with a severely varying mesh are not so large, coupled with a uniform finite difference grid in the core region.

From these low Hartmann number solutions a number of inferences are possible. First of all, the ideal configuration for heat transfer channels in the Tokamak blanket appears to be one with metallic walls in the direction parallel to the poloidal field, and non-conducting i.e., ceramic, walls in the perpendicular direction. This form of channel will only cause small pressure drop increases over the hydrodynamic case, since it is the conductivity of the perpendicular walls that significantly increases the pressure drop. From a heat transfer point of view this channel is also good, since the main thermal gradient in the blanket will be in the radial direction, i.e. the direction that is perpendicular to the poloidal field, and thus perpendicular to the metallic walls. As a result, the main heat flow will not be affected by the two ceramic walls. If two ceramic walls are not acceptable, appreciable reduction of the pressure drop is also possible by electrically insulating the corners of a metallic duct, and including current breaks, particularly in the walls perpendicular to the imposed field. If the electrical insulator used for the corners is a good thermal conductor e.g., beryllium oxide, significant heat transfer enhancement is associated with this corner insulation.

Owing to the high Reynolds numbers in the Tokamak blanket, the entry region will be rather long. This long entry length will be made even longer by the presence of the toroidal magnetic field along the axis of flow. Thus, the flow is not expected to be fully developed in the length of channel that is in the blanket, and this emphasizes the importance of the entry calculation. Inclusion of the axial field

is the next step to be taken in the development of this method to eventually solve the real blanket case.

Many problems of interest remain to be solved in this area. Flow around a U shaped length of pipe or a right angled bend in the presence of one or two field components is one example. In fact, the solution to the latter could be used as the inlet conditions for the entry problem, to obtain more realistic modeling. The transport of bubbles and voids within liquid metal MHD flow is another. All of the above problems are three dimensional and they could possible be solved with variations of this procedure.

In final conclusion, the recent rejection of lithium cooled blankets by some Tokamak designers in favor of lithium bearing but helium cooled ones, seems unjustified. It appears that the simplifications caused by a lithium cooled blanket are substantial, while the penalties invoked by the same, are small.

APPENDIX A

The complete set of coefficients for all eight equations is presented here.

u Momentum Equation

The equation is,

$$u_{P,D} = A_N u_{N,D} + A_S u_{S,D} + A_E u_{E,D} + A_W u_{W,D} + D^u (\partial \bar{p} / \partial x) + B^u \quad (A.1)$$

where,

$$A_N = A'_N / A'_P, \quad A_S = A'_S / A'_P, \quad A_E = A'_E / A'_P$$

$$A_W = A'_W / A'_P, \quad B^u = B' / A'_P, \quad D^u = D^{u'} / A'_P$$

and,

$$A'_N = T_n^Y - L_n^Y, \quad A'_S = T_s^Y + L_s^Y$$

$$A'_E = T_e^Z - L_e^Z, \quad A'_W = T_w^Z + L_w^Z$$

$$B' = F_U u_{P,U} + S_U$$

$$A'_P = A'_N + A'_S + A'_E + A'_W + F_U - S_P$$

where,

$$F_U = \frac{(\Delta y)(\Delta z)}{\Delta x} u_{P,U}, \quad D^{u'} = -\Delta y \cdot \Delta z$$

$$L_n^Y = \frac{\Delta z}{2} v_{n,U}, \quad L_s^Y = \frac{\Delta z}{2} v_{s,U}$$

$$L_e^z = \frac{\Delta y}{2} w_{e,U}, \quad , \quad L_w^z = \frac{\Delta y}{2} w_{w,U}$$

$$T_n^y = \frac{1}{Re} \frac{(\Delta z)}{\partial y_n}, \quad , \quad T_s^y = \frac{1}{Re} \frac{(\Delta z)}{\partial y_s}$$

$$T_e^z = \frac{1}{Re} \frac{(\Delta y)}{\partial z_e}, \quad , \quad T_w^z = \frac{1}{Re} \frac{(\Delta y)}{\partial z_w}$$

$$S_U = \frac{Y_{Hap}^2}{Re \, Rem} (Hx_n - Hx_s)_U \Delta z - (Hy_{P,D} - Hy_{P,U}) \frac{\Delta y \cdot \Delta z}{\Delta x}$$

$$S_P = 0.$$

v Momentum Equation

The equation is,

$$v_{P,D} = A_{N,N,D}^v + A_{S,S,D}^v + A_{E,E,D}^v + A_{W,W,D}^v + D^v (p_P - p_S)_D + B^v. \quad (A.2)$$

The coefficients are the same as for the u equation except

$$S_U = \frac{Y_{Hap}^2}{Re \, Rem} \left\{ (Hy_{P,D} - Hy_{P,U}) \frac{\Delta y \Delta z}{\Delta x} + (Hx_n - Hx_s)_U \Delta z \right\}$$

and,

$$D^{v'} = -\Delta z.$$

w Momentum Equation

The equation is,

$$w_{P,D} = A_{N,N,D}^w + A_{S,S,D}^w + A_{E,E,D}^w + A_{W,W,D}^w + B^w + D^w (p_P - p_W)_D. \quad (A.3)$$

The coefficients are as for the u equation except,

$$S_U = \frac{Hap^2}{Re \, Rem} \left\{ (Hz_n - Hz_s) \Delta z - (Hy_e - Hy_w) \Delta y \right\} U$$

$$- \frac{Y_{Hap}^2}{Re \, Rem} \left\{ (Hx_e - Hx_w) U \Delta y - (Hz_{P,D} - Hz_{P,U}) \frac{\Delta y \Delta z}{\Delta x} \right\}$$

and,

$$D^{w'} = -\Delta y.$$

Energy Equation

The equation is,

$$\theta_{P,D} = A_N \theta_{N,D} + A_S \theta_{S,D} + A_E \theta_{E,D} + A_W \theta_{W,D} + B^{\theta} \quad (A.4)$$

The coefficients are as for the u equation except,

$$T_n^y = \frac{1}{Re \, Pr} \frac{(\Delta z)}{\partial y_n}, \quad T_s^y = \frac{1}{Re \, Pr} \frac{(\Delta z)}{\partial y_s}$$

$$T_e^z = \frac{1}{Re \, Pr} \frac{(\Delta y)}{\partial z_e}, \quad T_w^z = \frac{1}{Re \, Pr} \frac{(\Delta y)}{\partial z_w}$$

$$S_U = Q/Re \, Pr.$$

Pressure Correction Equation

The equation is,

$$p'_{P,D} = A_{N,D} p'_{N,D} + A_{S,D} p'_{S,D} + A_{E,D} p'_{E,D} + A_{W,D} p'_{W,D} + B^P \quad (\text{A.5})$$

where,

$$A_N = \frac{C^V D^V}{A'_P} \quad , \quad A_S = \frac{C^V D^V}{A'_P}$$

$$A_E = \frac{C^W D^W}{A'_P} \quad , \quad A_W = \frac{C^W D^W}{A'_P}$$

$$A'_P = 2C^V D^V + 2C^W D^W$$

and,

$$B^P = (C^V (v_N^* - v_P^*) + C^W (w_E^* - w_P^*) + C^u (u_{P,D} - u_{P,U})) / A'_P$$

where,

$$C^u = \Delta y \cdot \Delta z \quad , \quad C^V = \Delta x \cdot \Delta z \quad , \quad C^W = \Delta x \cdot \Delta y \quad .$$

Hx Induction Equation

The equation is,

$$Hx_{P,D} = A_{N,D} Hx_{N,D} + A_{S,D} Hx_{S,D} + A_{W,D} Hx_{W,D} + A_{E,D} Hx_{E,D} + B^{Hx} \quad (\text{A.6})$$

The coefficients are as for the u equation except,

$$B' = S_U \quad , \quad F_U = 0$$

$$A'_P = T_n^Y + L_n^Y + T_s^Y - L_s^Y + T_e^Z + L_e^Z + T_w^Z - L_w^Z$$

$$T_n^Y = \frac{1}{\text{Rem}} \frac{(\Delta z)}{\partial y_n} \quad , \quad T_s^Y = \frac{1}{\text{Rem}} \frac{(\Delta z)}{\partial y_s}$$

$$T_e^Z = \frac{1}{\text{Rem}} \frac{(\Delta y)}{\partial z_e} \quad , \quad T_w^Z = \frac{1}{\text{Rem}} \frac{(\Delta y)}{\partial z_w}$$

and,

$$S_U = Y \left[-(v_n - v_s) \Delta z - (w_e - w_w) \Delta y \right] U + (u_n - u_s) \Delta z + (Hy_n u_n - Hy_s u_s) \Delta z \\ + (Hz_e u_e - Hz_w u_w) \Delta y .$$

Hy Induction Equation

The equation is,

$$Hy_{P,D} = A_{N,D} Hy_{N,D} + A_{S,D} Hy_{S,D} + A_{E,D} Hy_{E,D} + A_{W,D} Hy_{W,D} + B^{Hy} . \quad (A.7)$$

The coefficients are the same as for the u equation except,

$$A'_N = T_N^Y , \quad A'_S = T_S^Y$$

$$A'_P = F_U + A'_N + A'_S + A'_E + A'_W - 2L_n^Y + 2L_s^Y$$

and,

$$S_U = Y (v_{D,P} - v_{U,P}) \frac{\Delta y \Delta z}{\Delta x} + \left\{ (Hx_{P,U} \frac{\Delta y \Delta z}{\Delta x} - \Delta z (Hy_n - Hy_s) U \right. \\ \left. - (Hz_e - Hz_w) \Delta y \right\} v_{P,D} - Hx_{P,U} v_{P,U} \frac{\Delta y \Delta z}{\Delta x} \left\{ \right. \\ \left. + ((v_n - v_s) \Delta z + (Hz_e v_e - Hz_w v_w) \Delta y) U .$$

The T's are the same as for the Hx equation.

Hx Induction Equation

The equation is,

$$Hx_{P,D} = A_{N,D} Hx_{N,D} + A_{S,D} Hx_{S,D} + A_{E,D} Hx_{E,D} + A_{W,D} Hx_{W,D} + B^{Hx} . \quad (A.8)$$

The coefficients are the same as for the u equation except,

$$A'_E = T_e^Z, \quad A'_W = T_w^Z$$

$$A'_P = F_U + A'_N + A'_S + A'_E + A'_W - 2L_e^Z + 2L_w^Z$$

and,

$$S_U = \gamma(w_{D,P} - w_{U,P}) \frac{\Delta Y \Delta Z}{\Delta X} + \left\{ (H_{x_{P,U}} \frac{\Delta Y \Delta Z}{\Delta X} - \Delta z (H_{y_n} - H_{y_s})_U \right. \\ \left. - (H_{z_e} - H_{z_w}) \Delta Y w_{P,D} - H_{x_{P,U}} w_{P,U} \frac{\Delta Y \Delta Z}{\Delta X} \right\} + (w_n - w_s) \Delta z \\ + (H_{y_n} w_n - H_{y_s} w_s)_U \Delta z .$$

The T's are the same as for the Hx equation.

BIBLIOGRAPHY

1. Moszynski, J. R., Petrick, M. and Coultas, T. A., "Cooling of Controlled Thermonuclear Fusion Reactors of Toroidal Configurations," Proceedings of a Symposium on the Technology of Controlled Thermonuclear Fusion Experiments and the Engineering Aspects of Fusion Reactors, Austin, Texas (1972)
2. Yih, C., Fluid Mechanics, McGraw-Hill, New York (1969)
3. Marco, S. M., Han, L. S., "A Note on Limiting Laminar Nusselt Number in Ducts with Constant Temperature Gradient by Analogy to Thin Plate Theory," TRANS. ASME, 77:625 (1955)
4. Sparrow, E. M. and Siegal, R., "A Variational Method for Fully Developed Laminar Heat Transfer in Ducts," Journal of Heat Transfer, 157, May (1959)
5. Patankar, S. V. and Spalding, D. B., "A Calculation Procedure for Heat Mass and Momentum Transfer in Three Dimensional Parabolic Flows," Int. J. of Heat and Mass Transfer, 15:1787 (1972)
6. Goldstein, R. J. and Kreid, D. K., "Measurement of Laminar Flow Development in a Square Duct using a Laser-Doppler Flowmeter," J. Appl. Mech., 34:813 (1967)
7. Beavers, G. S., Sparrow, E. M. and Magnuson, R. A., "Experiments on Hydrodynamically Developing Flow in Rectangular Ducts of Arbitrary Aspect Ratio," Int. J. of Heat Mass Transfer, 13:689 (1970)
8. Caretto, L. S., Curr, R. M. and Spalding, D. B., "Two Numerical Methods for Three Dimensional Boundary Layers," Comp. Methods in Appl. Mech. and Engg., 1:39 (1972)
9. Curr, R. M., Sharma, D. and Tatchell D. G., "Numerical Predictions of Some Three Dimensional Boundary Layers in Ducts," Comp. Methods in Appl. Mech. and Engg., 1:143 (1972)
10. Briley, W. R., "Numerical Method for Predicting Three Dimensional Steady Viscous Flow in Ducts," J. Comp. Phys., 14:8 (1974)
11. Ghia, U., Ghia, K. N. and Struderus, C. J., "A Study of Three Dimensional Laminar Incompressible Flow in Ducts," Proceedings of the AIAA 9th Fluid and Plasma Dynamics Conference, San Diego, California (1976)

12. Hartmann, J., Math.-fys. Medd., 15, No. 6(1937)
13. Shercliff, J. A., "Steady Motions of Conducting Fluids in Pipes under Transverse Magnetic Fields," Proc. Camb. Phil. Soc., 49: 136(1953)
14. Chang, C. C. and Lundgren, T. S., "Duct Flow in Magnetohydrodynamics," Zeitschrift fur angewandte Mathematik und Physik, 12:100 (1961)
15. Gold, R. R., "Magnetohydrodynamic Pipe Flow," Journal of Fluid Mechanics, 13:505(1962)
16. Shercliff, J. A., "The Flow of Conducting Fluids in Circular pipes under Transverse Magnetic Fields," Journal of Fluid Mechanics, 1:644(1956)
17. Ihara, S., Tajima, K. and Matsushima, A., "The Flow of Conducting Fluids in Circular Pipes with Finite Conductivity under Uniform Transverse Magnetic Fields," Journal of Applied Mechanics, 34: 29(1967)
18. Chu, W. H., "On MHD Flow in a Rectangular Duct of Arbitrary Conductivity for Arbitrary Hartmann Number," Journal of Applied Mechanics, 36:702(1969)
19. Hunt, J. C. R., "Magnetohydrodynamic Flow in Rectangular Ducts," Journal of Fluid Mechanics, 21:577(1965)
20. Hunt, J. C. R., Stewartson, K., "Magnetohydrodynamic Flow in Rectangular Ducts II," Journal of Fluid Mechanics, 22:565(1966)
21. Hoffman, M. A., and Carlson, G. A., "Calculation Techniques for Estimating Pressure Losses for Conducting Fluid Flows in Magnetic Fields," USAEC Report UCRL-51010(1971)
22. Chu, W. H., "A Numerical Method for Solving General MHD Duct Flow Problems," Journal of Applied Mechanics, 39:47(1972)
23. Wu, S. T., "Unsteady MHD Duct Flow by the Finite Element Method," International Journal for Numerical Methods in Engineering, 6:3 (1973)
24. Shohet, J. L., Osterle, J. F. and Young, F. J., "Velocity and Temperature Profiles for Laminar Magnetohydrodynamic Flow in the Entrance Region of a Plane Channel," Physics of Fluids, 5: 879(1962)
25. Shohet, J. L., "Velocity and Temperature Profiles in the Entrance Region of an Annular Channel for MHD Flow," Physics of Fluids, 5:879(1962)

26. D'Arcy, G. P. and Schmidt, P. S., "Magnetohydrodynamic Entry Flows in Axial Magnetic Fields," Energy Systems Laboratory University of Texas at Austin, Report ESL-6 (1972)
27. Stein, R. P., "Liquid Metal Heat Transfer," in Advances in Heat Transfer, Vol 3, Academic Press, Inc., New York (1966)
28. Achner, P. Y., Mackiewicz, W. V., Fisher, D. L., Yee, D. and Camp, D. C., "Thermophysical Properties of Alkali Metals," USAEC Report AGN-8195 (1968)
29. Gardner, R. A., "Laminar Pipe Flow in a Transverse Magnetic Field with Heat Transfer," Int. J. of Heat Mass Transfer, 11:1076 (1968)
30. Michiyoshi, I. and Matsumoto, R., "Heat Transfer by Hartmann Flow in Thermal Entrance Region," Int. J. of Heat Mass Transfer, 7: 101 (1964)
31. Back, L. H., "Laminar Heat Transfer in Electrically Conducting Fluids Flowing in Parallel Plate Channels," Int. J. of Heat and Mass Transfer, 11:1621 (1968)
32. Regirer, S. A., "Laminar Duct Flow of an Electrically Conducting Fluid in the Presence of a Magnetic Field," Magnetohydrodynamics, 1:5 (1965)
33. Hunt, J. C. R., Hancox, R., "The use of Liquid Lithium as Coolant in a Toroidal Fusion Reactor," UKAEA Report CLM-RL15 (1971)
34. Harlow, F. H., and Welch, J. E., "Numerical Calculation of Time Dependent Viscous Incompressible Flow of Fluid with Free Surface," Physics of Fluids, 8:12, 2182 (1965)
35. Spalding, D. B., "A Novel Finite Difference Formulation for Differential Expressions Involving both First and Second Derivatives," Int. J. for Numerical Methods in Engineering, 1 (1972)
36. Amsden, A. A. and Harlow, F. H., "The SMAC Method: A Numerical Technique for Calculating Incompressible Fluid Flows," Los Alamos Scientific Laboratory, LA-4370 (1969)
37. Patankar, S. V. and Spalding, D. B., Heat and Mass Transfer in Boundary Layers, Second Edition, Intertext Books, London (1970)
38. Miller, J. A., "Laminar Incompressible Flow in the Entrance Region of Ducts of Arbitrary Cross-section," J. Engg. Power, 113 (Jan. 1971)
39. Kays, W. M., Convective Heat and Mass Transfer, McGraw-Hill, New York (1966)

40. Sparrow, E. M., Novotny, J. L., and Lin, S. H., "Laminar Flow of a Heat Generating Fluid in a Parallel Plate Channel," AICHE J., 9:6, 797(1963)
41. Burgraff, O. R., "Analytical and Numerical Studies of Separated Flows," J of Fluid Mechanics, 24:2, 113(1966)
42. "Wisconsin Tokamak Reactor Design Report," UWEDM-68, Vol 1 (1974)

VITA

Shahid Khan was born in Rawalpindi, Pakistan on Nov. 20, 1952. He came to the United States in Sept. 1970 and graduated from the Lowell Technological Institute in June 1973 with a B.S.N.E. He then proceeded to the Georgia Institute of Technology from which he received the M.S.N.E. in Aug. 1974. While at Georgia Tech he was supported by a graduate research assistantship from the School of Nuclear Engineering.